Resurrecting the N = 20 shell closure and upgrades to the TITAN measurement Penning trap

by

Eleni Marina Lykiardopoulou

BSc, Physics, University of Athens, 2016

A THESIS SUBMITTED IN PARTIAL FULFILLMENT
OF THE REQUIREMENTS FOR THE DEGREE OF

Doctor of Philosophy

in

THE FACULTY OF GRADUATE AND POSTDOCTORAL STUDIES
(Physics)

The University of British Columbia
(Vancouver)

December 2023

The following individuals certify that they have read, and recommend to the Faculty of Graduate and Postdoctoral Studies for acceptance, the thesis entitled:

Resurrecting the N = 20 shell closure and upgrades to the TITAN measurement Penning trap

submitted by **Eleni Marina Lykiardopoulou** in partial fulfillment of the requirements for the degree of **Doctor of Philosophy** in **Physics**.

Examining Committee:

Jens Dilling, Professor, Physics and Astronomy, UBC
Supervisor

Douglas A. Bryman, Professor, Physics and Astronomy, UBC
University Examiner

Takamasa Momose, Professor, Chemistry, UBC
University Examiner

Jeremy S. Heyl, Professor, Physics and Astronomy, UBC
Supervisory Committee Member

Kate Jones, Divisional Dean for Natural Sciences and Mathematics, Oakridge National Laboratory
External Examiner

Additional Supervisory Committee Members:

Reiner Kruecken, Professor, Physics and Astronomy, UBC
Supervisory Committee Member

Rob Kiefl, Professor, Physics and Astronomy, UBC
Supervisory Committee Member

Abstract

Experimental investigations of nuclear structure provide a probe to study the strong nuclear force, many properties of which still remain unknown. One powerful way to experimentally investigate nuclear structure is through the mass of the atomic nucleus, as it reveals the binding energy of the nucleus.

In this work, mass measurements of Mg and Na isotopes are carried out and the results indicate, for the first time, a gradual re-emergence of magicity or closed shell behavior for $Z \leq 11$ nuclei at the $N = 20$ island of inversion. The results also discover a previously unknown low-lying isomer, hence a long-lived excited state in ^{32}Na. In addition, complementary work at higher mass numbers which combines mass measurements and decay energies allows us to trace the two-proton dripline between iridium and lead, thus determining the limits of existence for elements with proton numbers $Z = 77 - 82$ on the proton-rich side of the Segrè chart. Comparisons with some theoretical calculations for this work show agreement while others, such as ab initio theory calculations, are currently unable to reproduce effects of the $N = 20$ island of inversion, and will require further developments. Yet the mass measurements serve as important benchmarks.

Beyond studies of nuclear structure via direct mass measurements, this thesis describes the technical developments and improvements to the Measurement Penning Trap (MPET). The Penning trap, an experimental apparatus that uses electric and magnetic fields to determine the atomic mass through the ion's cyclotron frequency, has been upgraded to operate at cryogenic temperatures with the goal to reach storage times on the order of seconds for highly-charged Ions. The aim for this upgrade is an improvement of the achievable precision by an order of magnitude. In addition, simulations and further technical upgrades towards the imple-

mentation of the Phase-Imaging Ion-Cyclotron measurement technique are carried out. With its new capabilities, the TITAN MPET is now able to perform mass measurements of short-lived radioactive isotopes in singly and highly charged states with an unprecedented precision.

Lay Summary

The strong nuclear force, the force the holds together the protons and the neutrons in the atomic nucleus, is extremely complicated to mathematically describe, due to the fact that every proton and neutron in the nucleus interacts with every other proton and neutron at the same time. This mathematical problem, usually referred to as the many body problem, needs to be simplified if a solution is to be found. The simplification of the many body problem happens in conjunction with experiment where theoretical results are compared with experimental values to derive a theory that closely matches experiments.

This work provides a number of newly determined experimental mass values that are compared with theoretical values in order to further our understanding of the nuclear force. In addition, this thesis describes the technical developments and the first tests of a new mass spectrometer that will allow for more precise mass measurements, which are necessary to answer other fundamental questions such as how the heavy elements are produced in our universe.

Preface

This dissertation is a result of three distinct projects with one common denominator: the TITAN experimental facility. The TITAN facility, run by the TITAN collaboration, has been in operation since 2007 and many of the aspects that enabled the successful completion of this thesis have been the result of a 16-year scientific effort. The individual contributions corresponding to each one of the three projects are listed below.

Experimental mass measurements of the neutron-rich Mg and Na isotopes described in Chapter 5:

- The experimental proposal was written by Maxime Brodeur, Thomas Brunner and Jens Dilling in 2015.
- The maintenance and operation of the MR-ToF MS device used for this experiment was performed by Andrew Jacobs, Coulter Walls, Tobias Murboeck, Ali Mollerabimi and Chris Chambers.
- Coulter Walls was responsible for organising the experiment.
- The group leader, Ania Kwiatkowski was responsible for the safety and beam-time approvals for the experiment.
- The people that participated and contributed to data collection and first interpretation of the results were Sakshi Kakkar, Callum Brown, Rane Simpson, Jaime Cardona, Andrew Weaver, Stefan Paul, Alex Ridley, Fernando Maldonado Millan, Dwaipayan Ray, Zach Hockenberry, Sam Porter, John Ash, Yilin Wang, Behnam, Pascal Reiter, Brian Kootte, Annabelle Czihaly,

Andrew Jacobs, Coulter Walls, Ali Mollerabimi, Tobias Murboeck, Chris Chambers and I.

- I was the primary analyzer of the resulted dataset and Coulter Walls was the co-analyzer.
- Communications with collaborators about the direction of the project were performed by me.
- I am the first author of an upcoming publication that describes the results discussed in Chapter 5.

Network calculations determining the two-proton dripline, as described in Chapter 6:

- This work would not had been possible if it wasn't for a previous TITAN experiment which has been published in PRL. In that experiment, I took part in the data collection and I was the second analyzer of the acquired data. I am also a co-author in the publication.
- The idea for the network calculation comes from the published AME2016 evaluation and later, a research proposal by Pascal Reiter.
- The network calculation was conducted by Wenjia Huang with the additional participation of George Audi, Dave Lunney, Andrew Jacobs and me.
- I was responsible for the analysis of the results and the construction and submission of the subsequent publication.
- Feedback and review of the scientific publication was provided by Dave Lunney, Wenjia Huang, George Audi, Jens Dilling, Ania Kwiatkowski, Pascal Reiter, Timo Dickel and Wolfgang Plass.

The publication related to the mass measurements performed at TITAN is: *"Mass Measurements of Neutron-Deficient Yb Isotopes and Nuclear Structure at the Extreme Proton-Rich Side of the N=82 Shell"*, Sönke Beck, Brian Kootte, Irene Dedes, Timo Dickel, A. A. Kwiatkowski, Eleni Marina Lykiardopoulou, Wolfgang R. Plaß, Moritz P. Reiter, Corina Andreoiu, Julian Bergmann, Thomas Brunner,

Dominique Curien, Jens Dilling, Jerzy Dudek, Eleanor Dunling, Jake Flowerdew, Abdelghafar Gaamouci, Leigh Graham, Gerald Gwinner, Andrew Jacobs, Renee Klawitter, Yang Lan, Erich Leistenschneider, Nikolay Minkov, Victor Monier, Ish Mukul, Stefan F. Paul, Christoph Scheidenberger, Robert I. Thompson, James L. Tracy, Jr., Michael Vansteenkiste, Hua-Lei Wang, Michael E. Wieser, Christian Will, and Jie Yang. Phys. Rev. Lett. 127, 112501 (2021).

The subsequent publication that describes the network calculations and its results is: *Exploring the limits of existence of proton-rich nuclei in the Z=70–82 region*, E. M. Lykiardopoulou, G. Audi, T. Dickel, W. J. Huang, D. Lunney, Wolfgang R. Plaß, M. P. Reiter, J. Dilling, and A. A. Kwiatkowski (TITAN Collaboration), Phys. Rev. C 107, 024311 (2023).

The third part of this thesis, which describes the technical upgrades, simulations and commissioning of TITAN's next generation Penning Trap had the following contributions:

- Mel Good and Erich Leistenschneider were responsible for the design of the new spectrometer.
- Erich Leistenschneider, Chris Izzo, Sakshi Kakkar, Sam Porter, Annabelle Czihaly and I were responsible for assembly, installation, and testing of various components and of the overall spectrometer.
- I performed simulations about the feasibility of the PI-ICR technique at TITAN and I ordered and lead the assembly and installation of all necessary hardware and the performance of the new electronic components. During assembly and installation, I was assisted by Sakshi Kakkar, Ivana Belosevic and Andrew Weaver.
- I lead the upgrades, assembly, installation and commissioning that took place from 2021 to 2023.
- The commissioning of the spectrometer in the period 2022-2023, took place by Ivana Belosevic, Sakshi Kakkar and myself.
- Technical support and assistance in the installations was provided by Mel Good. Additional assistance regarding cryogenic components was provided

by Bassam Hitti. Data aquisition support and development that enabled the smooth operation of the spectrometer were performed by Ben Smith and Ivana Belosevic.

- Analysis of the data presented in this thesis was performed by me.

The publication regarding the feasibility of PI-ICR technique is: *"Towards high precision mass measurements of Highly Charged Ions using the Phase-Imaging Ion-Cyclotron-Resonance technique at TITAN"*, Eleni Marina Lykiardopoulou, Christopher Izzo, Erich Leistenschneider, Anna A. Kwiatkowski and Jens Dilling, Hyperfine Interactions 241, Article number: 37 (2020). Subsequent publications regarding the commissioning of the new spectrometer are under way.

Table of Contents

List of Tables

List of Figures

Acronyms

AFG Arbitrary Function Generator

AME Atomic Mass Evaluation

ARIEL Advanced Rare Isotope Laboratory

CKM Cabbibo-Kobayashi-Maskawa

EBIT Electron Beam Ion Trap

EC Electron Capture

EDF Energy Density Functional

EIS Electron Impact Source

FEBIAD Forced Electron-Beam-Induced Arc Discharge

FRIB Facility for Rare Isotope Beams

FT-ICR Fourier-Transform Ion-Cyclotron Resonance

FWHM Full Width Half Maximum

GSI Gesellschaft für Schwerionenforschung

HCI Highly Charged Ions

HFB Hartree-Fock-Bogoliubov

IGLIS Ion Guide Laser Ion Source

IOI Ions of Interest

ISAC Isotope Separator and Accelerator

ISOL Isotope Separation On-Line

LLR Log-Likelihood Ratio

MCP Multiple-Channel Plate

MCSM Monte Carlo Shell Model

ME Mass Excess

MIRACLS Multi Ion Reflection Apparatus For Collinear Laser Spectroscopy

MISTRAL Mass measurements at ISolde using a Transmission RAdiofrequency spectrometer on-Line

MLE Maximum Likelihood Estimation

MPET Measurement Penning Trap

MPIK Max-Planck Institute for Nuclear Physics

MRS Mass Range Selector

MR-TOF MS Multiple-Reflection Time-of-Flight Mass Spectrometers

NMR Nuclear Magnetic Resonance

NQR Nuclear Quadrupole Resonance

OFHPC Oxygen Free High Purity Copper

PBSM Physics Beyond the Standard Model

PI-ICR Phase-Imaging Ion-Cyclotron Resonance

PLT Pulsed Drift Tube

QCD Quantum Chromodynamics

QED Quantum Electrodynamics

RF Radio-Frequency

RFQ Radio-Frequency Quadrupole trap

RGA Residual Gas Analyzer

RIB Radioactive Ion Beam

SA Super-Allowed

SCI Singly Charged Ions

SM Standard Model

TDC Time-to-Digital Converter

TIS TITAN Ion Source

TITAN TRIUMF's Ion Trap for Atomic and Nuclear science

TOF Time-of-Flight

TOF-ICR Time-of-Flight Ion-Cyclotron Resonance

TRC Time Resolved Calibration

TRILIS TRIUMF's Resonant Ionization Laser Ion Source

UHV Ultra High Vacuum

Acknowledgments

This thesis signifies the end of a long journey that began six years ago, when I moved to Canada as a masters student at UBC. Along this journey, Jens, my academic supervisor and Ania, our group leader, have been a constant source of inspiration, help and support. I am eternally grateful to them for their confidence in me, their mentorship and their professionalism. I am also very grateful to the rest of my PhD committee members Reiner, Jeremy and Rob to whom I owe a large part of my academic development. Among my mentors, I couldn't possibly forget Dave from who I hope to have adopted some of his uniquely poetic scientific writing and Theo, my research supervisor during my bachelor degree, who continues to motivate me from distance.

This thesis would not had been possible without the support of Erich and Chris Izzo who trained me in the early days of my PhD and without Ivana who took a lot of weight off my shoulders and with who we achieved some of the beautiful results described in Chapter 7. I also want to explicitly thank Ivana because of her endless scientific curiosity and her unstoppable drive to find solutions. She has always inspired who I try to become. I am also very grateful to Alex, Annabelle and especially Sakshi who I had the honor to train and work with and who taught me so much about how to be a teacher, a mentor and a colleague.

The completion of this journey would not had been possible without so many other group members who were my Vancouver family for all these years: Roshani and Tobias who spent the COVID isolation with me, Eleanor, Brian, Stefan, Andrew J., Pascal, Zach, Ish, Coulter, Ali, Jaime, Yilin, Killian, Chris C., Andrew W. and so many others. Days at TRIUMF would had been a lot more mundane without our volleyball team and our late day practice and a lot more difficult without the

endless support from Mel on all technical aspects.

Aside from TRIUMF, this journey took me to many important stops, which were critical to my professional and personal development and for this I am grateful to Jens, Ania and IsoSIM: my funding scholarship between 2017 and 2020. From my out-of-TRIUMF experiences I want to thank Maxime and Jonas for their hospitality when I visited ISOLTRAP and Mohammad and Alex who welcomed me at D-Wave and taught me with so much patience and care.

As for my out-of-physics companions in this journey, I am eternally grateful to my parents Eleni and Marinos to whom I can't find adequate words to express my gratitude for their continual support and for all the things that they have taught me. I am overwhelmed by my gratitude to my partner Ruben who has loved me and supported me through the stressful parts of my PhD and who has always encouraged my choices. Finally, I couldn't close this section without expressing my gratitude to my pillars of strength: my friends. Babis, Denia, Thelgeia and Ioanna that I left behind but who continue to support me from afar and those who I met here. Alexia, Effie, Nikos, Stelios, Sofia, Kyriaki, Kostas, Sappho, Aris and Ioanna, to whom I owe so many incredible memories from the last six years.

This journey has been an experience that I could never have imagined, and which wouldn't have been possible without all the people mentioned here. Inspired from my mom, I close this section borrowing a poem from Nazim Hickmet and devoting it to all of you who helped me:

The most beautiful sea
hasn't been crossed yet.
The most beautiful child
hasn't grown up yet.
Our most beautiful days
we haven't seen yet.
And the most beautiful words I wanted to tell you
I haven't said yet.

Nazim Hickmet

Chapter 1

Introduction

In the 5^{th} century BC, Democritos and his mentor Leukippos developed the concept that matter is made out of tiny indivisible particles that they named "atoms" [30]. Today, 26 centuries later, we still use the same name to describe the building blocks of our universe.

In Greek, atom ($\acute{\alpha}\tau o\mu o$) refers to something that cannot be split into smaller components. However, we know today, that atoms are constructed of more fundamental particles: the protons and the neutrons that form the atomic nucleus and the electrons that screen the protons' positive charge and make the atom electrically neutral. The studies of the electron cloud and its interaction with the atomic nucleus are governed by the research field of atomic physics, while studies of the atomic nucleus itself are subject to the field of nuclear physics. The protons and neutrons inside the nucleus are composed of quarks and are held together by gluons. Those are today the most fundamental or elementary particles we know, which are studied in the field of Particle Physics.

In the atomic nucleus, Z protons and N neutrons are confined together creating a configuration with a smaller mass or total energy than the one corresponding to the sum of those of the nucleons, and applying Einstein's $E = mc^2$ equivalent. The difference in energy between the two shows how favourable the confined configuration (nucleus) is. This quantity is referred to as the binding energy, given by [151]:

$$BE = [Zm_p + Nm_n - (m(Z,A) - Zm_e)]c^2 \tag{1.1}$$

where $m(Z,A)$ is the mass of the atom[1] with Z protons and N neutrons and $A = Z+N$.

The binding energy plays a central role in nuclear physics, as systematic studies of binding energies in different nuclei reveal information about the underlying nuclear force. Since the early days of nuclear physics, models are being created to explain experimental data. One of the most well-known models is the mass formula [31] based on a liquid drop model [100]. In the liquid drop model, the nucleons are considered to be distributed in a non-compressible volume (like a liquid). The binding energy can be expressed by a number of terms that describe average properties of the nucleus. The result is the semiempirical mass formula [151]:

$$BE = a_V A - a_S A^{2/3} - a_C \frac{Z(Z-1)}{A^{1/3}} - a_{Sym} \frac{(A-2Z)^2}{A} + \delta \tag{1.2}$$

where

$$\delta = \begin{cases} a_P A^{-3/4} & \text{N, Z even} \\ 0 & \text{N or Z odd} \\ -a_P A^{-3/4} & \text{N, Z odd} \end{cases} \tag{1.3}$$

and $a_V, a_S, a_C, a_Sym, a_P$ are free parameters that are adjusted to fits to experimental data.

The first term in Eq. 1.2 is the so called volume term and is derived from the experimental observation that the binding energy per nucleon (BE/A) is approximately constant (see Fig. 1.1). The second term is the surface term and is derived from the fact that nucleons on the surface of the nucleus do not contribute to the overall binding energy as much as those on the interior, as they have fewer nucleons to interact with. The third term considers the Coulomb force between the positively charged protons. The fourth term takes into account that most light stable nuclei have similar numbers of protons and neutrons. This fact doesn't hold for heavy nuclei (more than ≈ 100 nucleons) but since the term is inversely proportional to A, it becomes less important as A increases. Finally, the last term reflects nuclear

[1] Eq. 1.1 ignores the binding energy of the atomic electrons as is it is more than four orders of magnitude smaller than that of the nucleus. Even in cases where a higher precision is achieved or required, the quantity of interest is usually the difference in binding energies between two nuclei, as will be shown later, where the electron binding energies cancel out [151].

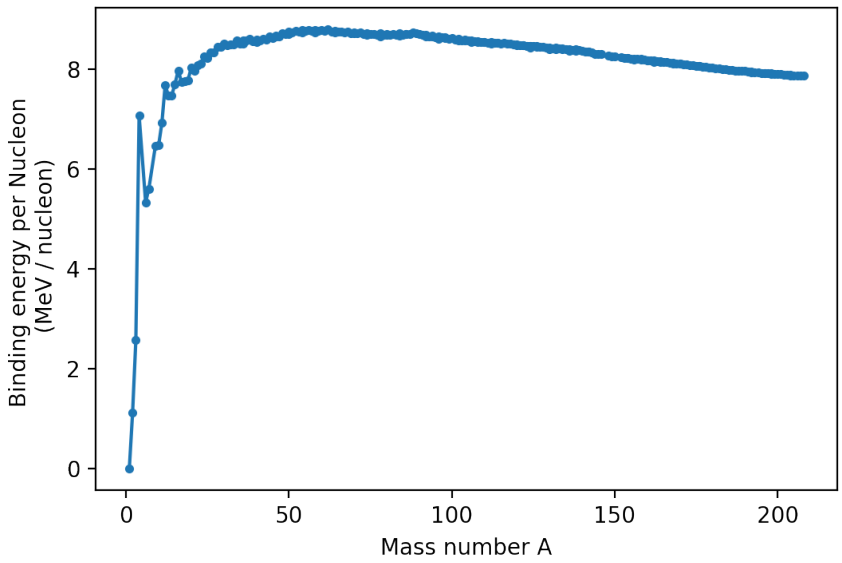

Figure 1.1: Binding energy per nucleon as a function of the mass number A. The binding energy is constant within 1 MeV/nucleon for $A > 10$, though a maximum appears at $A \sim 60$.

pairing, which increases the binding energy of nuclei with even numbers of protons and neutrons as all protons and neutrons are arranged in pairs. The preference of pairing can be simply concluded by the ratio of even-even stable isotopes compared to odd-odd ones which is 161:4 [63] for the currently known ∼270 stable isotopes.

Since the liquid drop model was developed, there have been several other attempts to describe nuclear properties and to model the nuclear force [186]. Much attention, is nowadays directed towards microscopic theories (for example [210, 243, 250]), where the binding energy and other nuclear properties are not derived by macroscopic bulk properties of the nucleus. In the microscopic models, each nucleon in the nucleus is treated separately and the nuclear interaction is tied to the fundamental nucleon-nucleon interaction. The pinnacle of microscopic theories, are the ab-initio (from first principles) theories (for example [250]) where a fully microscopic treatment is used. In other words, the nuclear potential is built by summing the individual interactions of the nucleons thus eliminating the need for

an average (macroscopic) nuclear potential. However, due to limited knowledge of the nuclear interaction, all theories need to be benchmarked against experimental data. As one of the most fundamental properties of an atom, experimental binding energies are key to fine tune microscopic theories, as they reflect all interactions of the nucleons, and can guide one towards a nuclear theory capable to describe and predict properties of all nuclei.

The present thesis begins with a description of basic nuclear structure and the microscopic theories. Chapter 3, motivates the use of mass measurements in revealing nuclear structure effects by determining the binding energy of nuclei. Moreover, an introduction to the production of short-lived radioactive isotopes is given as these are at the center-piece of the experimental investigations. Chapter 4 introduces the TITAN mass measurement facility and its components, while Chapters 5 and 6 report the experimental results derived in this thesis. Finally Chapter 7 (and Appendix 2) describe technical developments which are related to the TITAN Penning trap, and Chapter 8 summarizes the results of this thesis and discusses its scientific impact while providing a future outlook.

Chapter 2

Nuclear structure at the limits of existence

The term "nuclear structure" refers to how protons and neutrons are confined within the nucleus. Currently, there are about 3,000 observed atomic nuclei [88], while it is expected that the total number of individual nuclei in the Universe exceeds 7,000 [88]. Out of these, only about 270 [63] are stable while the rest decay towards more stable configurations. The type of decay depends on the excess (neutron-rich nuclei) or the deficit (neutron-deficient nuclei) of neutrons. Neutron-rich nuclei decay by β^--decay that transforms neutrons into protons while emitting negative beta particles (electrons) and electron anti-neutrinos. Neutron-deficient or proton-rich nuclei transform via β^+-decay or Electron Capture (EC). Heavy (beyond mass $\sim$ 150 u) nuclei often decay via alpha-decay or fission, while other more exotic decay modes (such as proton-decay) can exist but rarely appear (only $\sim 2\%$ of the existing isotopes are known to undergo proton-decay).

Although all radioactive or unstable nuclei decay towards more stable configurations, there are some nuclei which are more strongly bound than others. Fig. 2.1 depicts all observed isotopes as a function of Z and N in what is known as the nuclear chart or Segrè chart [151]. The colormap, on the right, reflects the two-neutron separation energy of each nucleus which is an expression of the relative binding strength:

$$S_{2n} = BE(N,Z) - BE(N-2,Z) \tag{2.1}$$

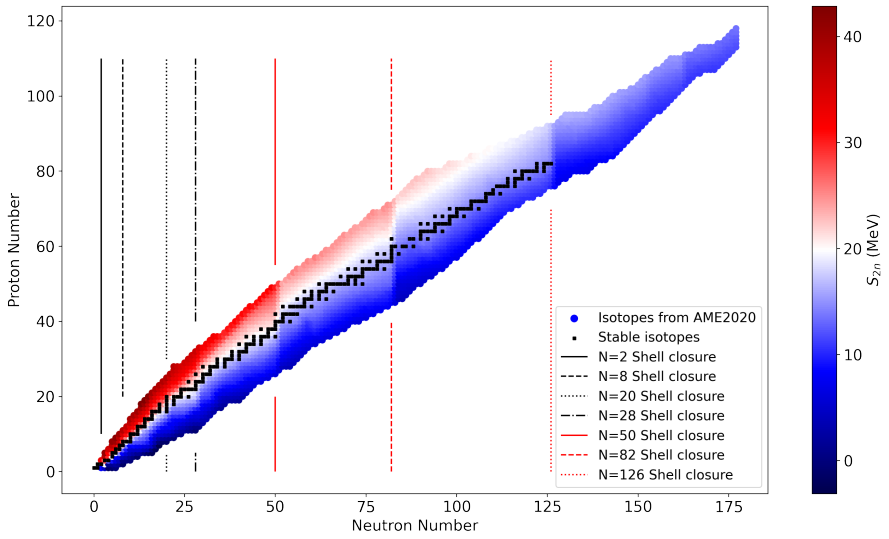

Figure 2.1: The nuclear chart including all observed nuclei. The stable isotopes are depicted with black squares. The color of each isotope corresponds to its two neutron separation energy. The neutron shell closures are represented with vertical lines. The data for this plot were taken from [264].

where $BE(N,Z)$ is the binding energy of a nucleus with N neutrons and Z protons. As can be observed in Fig. 2.1, the S_{2n} is a smooth function of N except for eight neutron number values where a sudden change in S_{2n} appears (indicated by the vertical lines). This sudden change of S_{2n} corresponds to an increased binding strength related to neutron numbers 2, 8, 20, 28, 50, 82 etc. Comparable observations are made for proton numbers. Nuclei with such numbers of protons or neutrons are called magic nuclei [117]. Similarly to atomic physics, with electrons occupying atomic shells, the nuclear shell model, described in detail in the next section, predicts the magic numbers that correspond to fully filled energy shells and therefore are referred to as shell closures. Nuclei with magic proton and/or neutron numbers represent spherical, extra stable configurations.

Nuclear magicity manifests itself in a number of ways in experimental investigations. One way is through neutron and proton separation energies as shown in Fig. 2.1 and Fig. 2.2 (Left). Similarly to the separation energy, shell closures

can be revealed by observing the experimental charge radius (the arranged volume where protons are located inside the nucleus), where sudden changes in the radius correspond to shell closures, as can be seen in Fig. 2.2 (Right) [12], with the assumption that a closed shell corresponds to a compact spherical object and additional nuclei would drastically increase that volume. Another indication of the appearance of a shell closure is the energy of excited states, such as the first 2^+ state of even-Z and even-N isotopes and the ratio between the lowest 4^+ and 2^+ excited states of even-Z and even-N nuclei [151]. Finally, the existence of shell closures can be revealed (not always unambiguously) by determining neutron capture cross sections, the decay energy, and the half-life of isotopes.

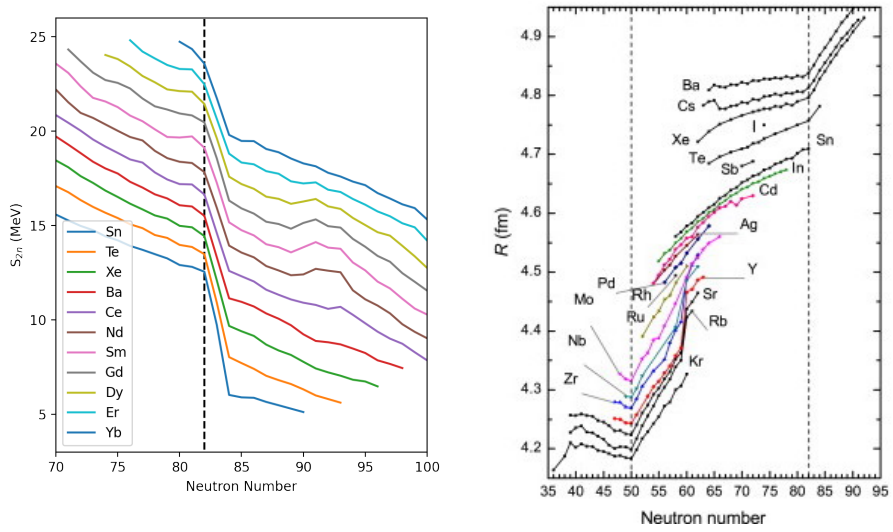

Figure 2.2: Left: Two-neutron separation energies for elements between Sn and Yb. The $N = 82$ shell closure is indicated by the dashed vertical line. Right: Charge radius of elements between Kr and Ba. The $N = 50, 82$ shell closures are shown with dashed lines. Figure taken from [12].

.

2.1 The nuclear shell model

Protons and neutrons are held together in the nucleus by the strong nuclear force. In the quark-level, the strong force is described by Quantum Chromodynamics (QCD) [248] in which the degrees of freedom consist of quarks and their interaction carriers: the gluons. The coupling constant of the strong interaction ($\alpha_S(Q^2)$) that expresses how strongly the quarks couple to the gluons has been shown to be dependent to the energy scale of the system (Q) by a number of different experimental techniques such as deep-inelastic scattering and e^-e^+ annihilation, which are briefly described below.

In deep inelastic scattering [112], a virtual photon is produced by the inelastic scattering of a lepton on a proton. If the photon has enough energy to probe the constituents of the proton, the products of the scattering will be due to electromagnetic interactions (with a coupling constant α) and due to strong interactions (with coupling constant α_S). From the final scattering cross section, the strong coupling constant can be derived as a function of the energy of the incoming particles.

In e^-e^+ annihilation [112], two beams of energetic electrons and positrons collide producing quark-antiquark pairs. This process is electromagnetic and by measuring its cross section, the cross section ratio R between $e^-e^+ \rightarrow q\bar{q}$ and the well-known $e^-e^+ \rightarrow \mu^-\mu^+$ can be derived. However, the process is not purely electromagnetic as gluons can be emitted from the quark or antiquark ($e^-e^+ \rightarrow q\bar{q}g$). As this is the result of the strong force, the ratio R also depends on α_S. Therefore, by measuring the cross-section ratio of these two processes, the strong interaction coupling constant can be derived as a function of the eletron-positron collision energy.

The experimental techniques described above have shown that the strong interaction coupling constant increases with decreasing the energy scale of the system. Since the perturbation expansion, necessary to apply QCD to low-energies, is expressed in powers of α_S [32], a perturbative expansion in the nuclear physics energy scale ($Q < 1$ GeV) is not meaningful. Therefore, nuclear structure has always relied on phenomenological or semi-phenomenological approaches to describe how protons and neutrons compose the atomic nucleus.

In the phenomenological description, a proton (or neutron) in the nucleus ex-

periences a short-distance attractive potential due to the strong interaction. In addition, protons, due to their positive charge, experience a repulsive Coulomb force, while both protons and neutrons experience a centrifugal force that depends on their angular momentum. These three forces give rise to the typical phenomenological nuclear potential that can be seen in Fig. 2.3 and it is usually referred to as the mean field:

$$V(r) = \begin{cases} -V_0(1+e^{(r-R)/\alpha})^{-1} + kq/r + 1(l+1)\hbar^2/2mr^2, & r \geq R \\ -V_0(1+e^{(r-R)/\alpha})^{-1} + kq/r\left(1-\frac{1}{2}\left(1-\frac{r}{R}\right)^2\right) + 1(l+1)\hbar^2/2mr^2, & r \leq R \end{cases} \tag{2.2}$$

where $R = R_0 A^{1/3}$ is the nuclear radius, A is the mass number of the nucleus, R_0 = 1.2 fm [151] is a proportionality constant, q is the charge of the nucleus, V_0 is the depth of the nuclear potential well (usually 50 MeV), α is a parameter related to the skin thickness (4αln3) which is depicted in Fig. 2.3, m is the mass of the nucleus, l is its angular momentum and k is the Coulomb constant.

Due to their fermionic nature, the nucleons in a nucleus occupy discrete energy levels in the nuclear potential that can be derived by solving the Schrodinger equation for a nucleon in a mean field potential V($\vec{r}$):

$$-\frac{\hbar^2}{2m}\nabla^2\psi(\vec{r}) + V(\vec{r})\psi(\vec{r}) = E\psi(\vec{r}) \tag{2.3}$$

where $\psi(\vec{r})$ is the wavefunction and E is the energy of the nucleon. The resulting energy levels describe the structure of a particular nucleus and contribute to the general picture that we refer to as nuclear structure. One of the most important results of this process is that the resulting energy levels are arranged in groups with large energy gaps between them. We refer to the occupation number before a large energy gap as a magic number because a large amount of energy is required for a nucleon to transition to a higher energy level. The solution of the Schrodinger equation (Eq. 2.3) with the mean field potential of Eq. 2.2 results in the magic numbers 2, 8, 20, but unfortunately it does not reproduce other experimentally observed magic numbers (50, 82, 126).

In 1949, Mayer [176] and Jensen [117], inspired by the atomic spin-orbit interaction, showed that the full set of magic numbers can be predicted if a nuclear

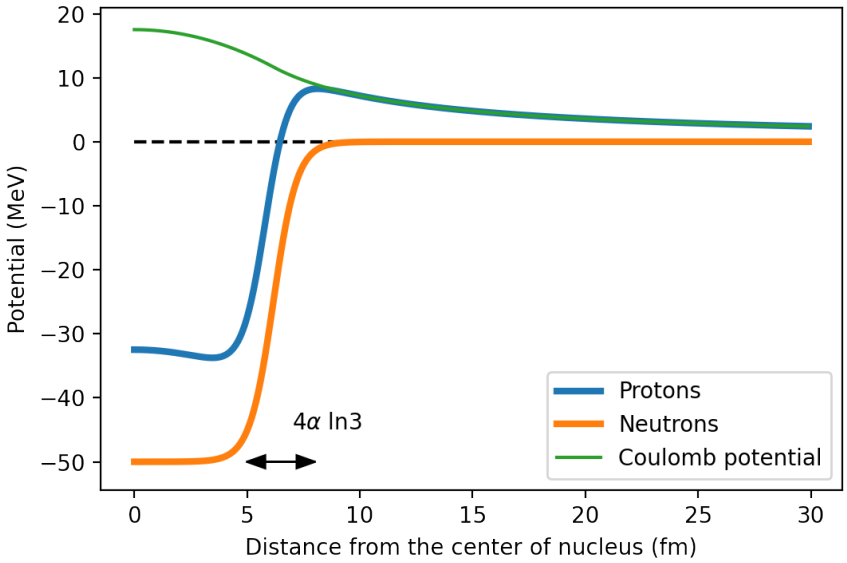

Figure 2.3: A simplified form of the potential experienced by protons (blue) and neutrons (orange). For the nuclear potential, a Wood Saxon potential is used. The green line represents the Coulomb potential experienced by the protons. For this Figure the parameters of ^{120}Sn were used.

spin-orbit potential is included in the calculation:

$$V_{LS} = V_{SO}(r)\vec{l}\cdot\vec{s} \tag{2.4}$$

where $V_{SO}(r)$ is an adjustable parameter, $\vec{l}$ is the angular momentum operator and $\vec{s}$ is the spin operator. The spin-orbit interaction has the ability to split levels of the same angular momentum number $\vec{l}$ into levels with the same total angular momentum $\vec{j} = \vec{l} + \vec{s}$ which changes the energy level structure resulting from Eq. 2.2 according to Fig 2.4.

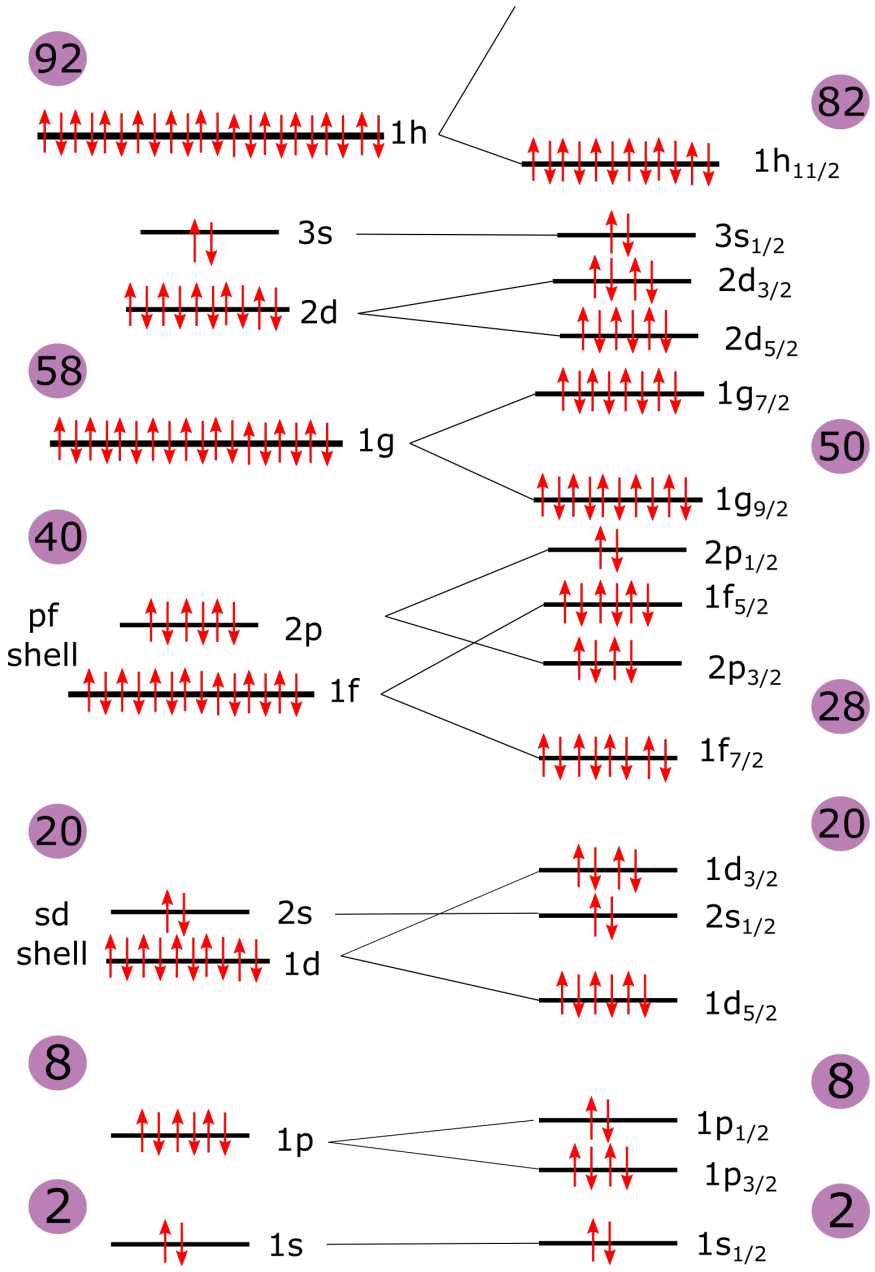

Figure 2.4: Schematic of the energy levels produced by the nuclear shell model before (left) and after (right) including the spin-orbit term. The numbers in purple represent the magic numbers predicted in each case.

2.2 Exotic phenomena in the neutron rich side of the nuclear chart

A few decades after the conception of the nuclear shell model [176], it was realized that although the model was able to accurately predict properties of stable nuclei, its predictions were deviating from experimental data far away from stability. Experimental studies of binding energies [256], charge radii [123] and the excitation energy of the first 2^+ state [71] in Na and Mg isotopes near $N = 20$, gave the first evidence. This resulted in a hypothesis that the $N = 20$ shell closure vanishes for neutron-rich nuclei.

In the first theoretical work that followed the experimental evidence, Wildenthal and Chung [270] concluded that the observed features cannot be explained with nuclei occupying the sd-shell which supported the idea that some of the neutrons in the nucleus must be occupying orbitals in the pf-shell [51]. Theoretical calculations then showed that the phenomenon can be explained by 2 particle - 2 hole excitations (2p2h) from the $1d_{5/2}$ to the $1f_{7/2}$ orbital [265] associated with non-spherical nuclei, a property which is demonstrated via large quadrupole deformation values [191]:

$$Q = e\sum_{i=1}^{A}(3z_i^2 - r_i^2) \tag{2.5}$$

where e is the charge of the electron, (z_i, r_i) are the position coordinates of the ith nucleon and A is the mass number of the nucleus. Due to the fact that in the studied nuclei the 2p2h configuration has a lower energy than the 0p0h, the region of the nuclear chart with $N = 20$ and $Z \approx 12$ was named the island of inversion.

The particle-hole configuration is often referred to as an intruder configuration because of the negative parity $1f_{7/2}$ level intruding the positive parity levels of the sd-shell. A schematic of the normal configuration in comparison to the intruder configuration can be seen in Fig. 2.5.

The emergence of the island of inversion is now attributed to the tensor force between protons and neutrons [199]:

$$V_T = (\vec{\tau}_1 \cdot \vec{\tau}_2)([\vec{s}_1 \cdot \vec{s}_2]^{(2)} \cdot Y^{(2)})f(r) \tag{2.6}$$

where $\vec{\tau}$ is the isospin and $\vec{s}$ is the spin of the nucleons, $[\vec{s}_1 \cdot \vec{s}_2]^{(2)}$ the coupling of

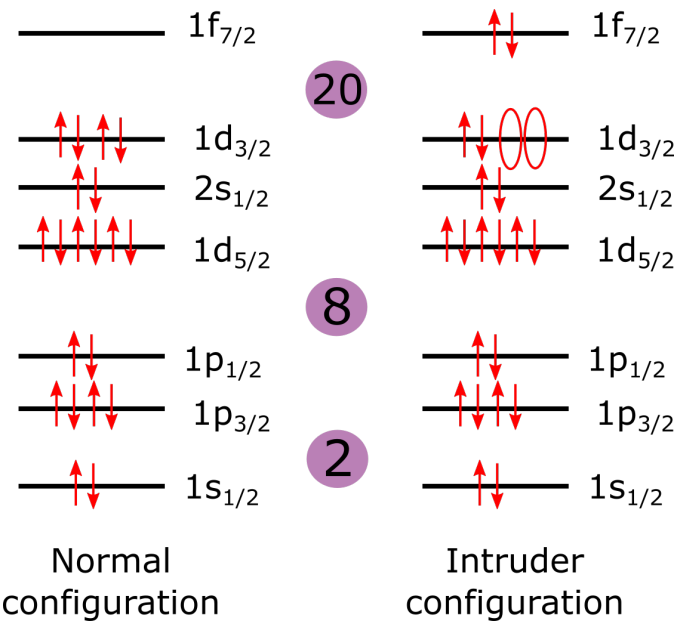

Figure 2.5: Schematic of energy levels that the neutrons occupy in the normal configuration (left) and in the intruder configuration (right)

.

the two operators $\vec{s}_{1,2}$ to an angular momentum 2, Y are the spherical harmonics and $f(r)$ is a function of the relative distance r. As demonstrated in [199], the tensor force causes a shift in the energy levels which is either attractive or repulsive depending on the angular momentum of the valence neutrons and protons. The interaction between the two orbitals is attractive if $j_p = l - 1/2$ and $j_n = l' + 1/2$, or vice versa, where l, l' the orbital angular momentum number of the proton and the neutron respectively.

Today, 50 years after the first experimental result that led to the discovery of the $N = 20$ island of inversion, a number of other islands have been observed [26, 77, 253] as well as the emergence of new magic numbers [97, 134, 200, 247, 267] on the neutron rich side of the nuclear chart. The next section further describes the $N = 20$ island of inversion which is the most relevant to the experimental data presented in this thesis.

2.2.1 The island of inversion at $N = 20$

Due to the fact that the $N = 20$ island of inversion was the first one discovered it has been extensively studied during the last fifty years. Nuclear reaction studies have been used to study deformation and collectivity in Mg [94, 125, 135, 179, 182, 271], Na [83, 208], Ne [147, 179, 277], F [62, 220] and Si [124, 180] isotopes. Laser spectroscopy [50], β-Nuclear Magnetic Resonance (NMR) [17, 175] and β-Nuclear Quadrupole Resonance (NQR) [17] have been used to determine the spin and the electromagnetic moments of the nuclei in the island of inversion [120, 121, 150, 192, 276, 278, 279]. Gamma-ray spectroscopy has been employed to study the excitation levels of the nuclei in the island of inversion [27, 78–81, 101, 194]. Mass measurements have been used to determine the binding energy [57, 103, 155] and half-life studies (for example [66]) have been used to obtain an estimate of the binding energy of the nuclei in the island of inversion.

The $N = 20$ island of inversion extends in proton number from fluorine [81, 220] to aluminum [119–121, 240, 276], as can be seen in Fig. 2.6. The aluminum isotopes are described by a combination of the normal configuration and intruder configurations thus constituting the northern border of the island of inversion. The southern border is currently defined by the fluorine isotopes, however, it is suspected that it might extend to the oxygen isotopic chain, towards the neutron dripline [220]. Whether or not ^{28}O is in the island of inversion is particularly interesting not only because it is a doubly magic ($Z = 8$, $N = 20$) nucleus according to the conventional nuclear shell model but also because it is located beyond the neutron dripline [88], where nuclei become neutron unbound.

Binding energies in the region of $Z = 20$ reveal the island of inversion by a kink in the two-neutron separation energy in the Mg isotopes, as can be seen in Fig. 2.7. For $Z < 13$, there is no sudden drop in S_{2n} that would indicate a shell closure at $N = 20$. In addition, the Mg and Al isotopic chains intercept at $N = 21$, an effect that does not align with the smoothness of the mass surface and the predictions of the nuclear shell model.

This effect is amplified when looking at the neutron shell gap Δ_{2n}, which expresses an empirical estimate of the energy gap between two nuclear shells. The island of inversion is demonstrated by a drop of the empirical shell gap below the

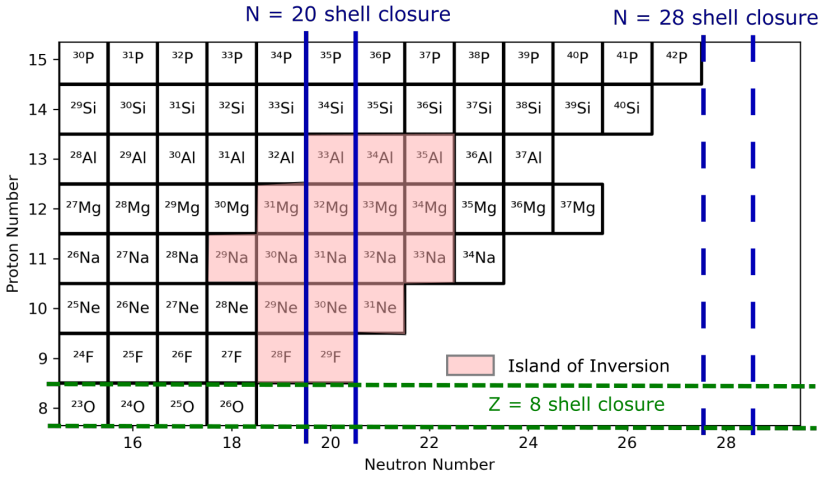

Figure 2.6: Schematic of the N=20 island of inversion.

.

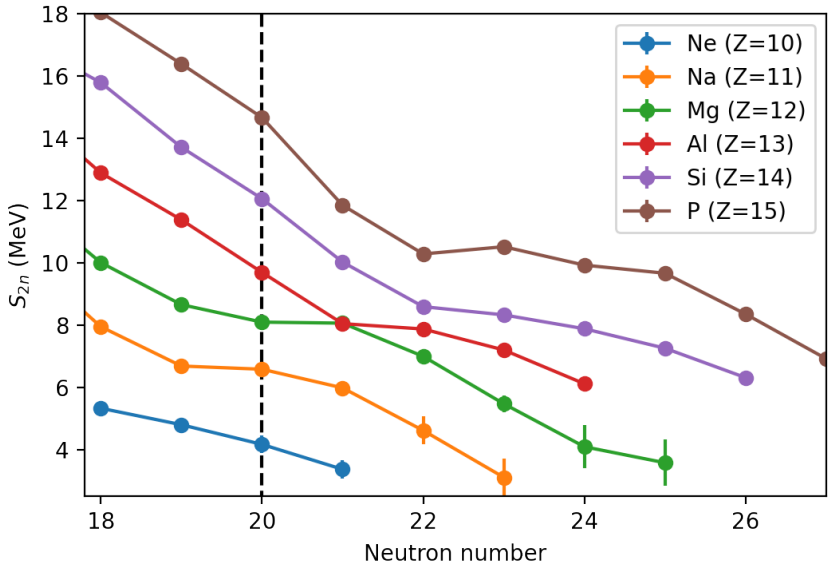

Figure 2.7: Two neutron separation energy as a function of the neutron number in the neighbourhood of the $N = 20$ island of inversion.

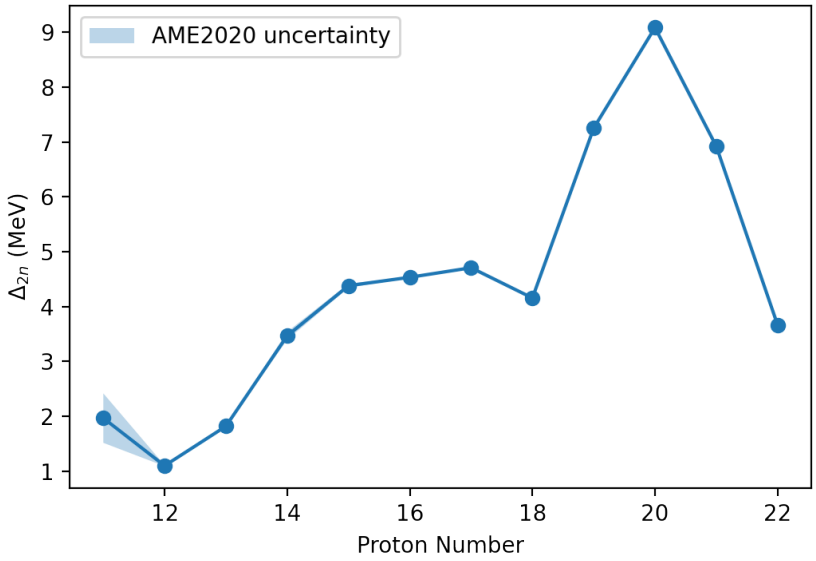

Figure 2.8: The two-neutron shell gap as a function of the proton number for the $N = 20$ isotones. The maximum Δ_{2n} corresponds to the doubly magic ^{40}Ca while the minimum corresponds to ^{32}Mg. The area filled with light blue represents the 1σ uncertainty derived from literature values published in [264].

regular ≈ 4 MeV level that appears for singly-magic nuclei. The Δ_{2n} value seems to reach a minimum at ^{32}Mg and there are signs of increase of the empirical shell gap for ^{33}Na, as can be seen in Fig. 2.8, which could suggest a recovery of the N = 20 magic number towards the dripline. However, the large uncertainty in the Δ_{2n} of ^{33}Na along with the results from nuclear reactions do not exclude the possibility of the island of inversion extending to the dripline ($N = 8$).

The eastern border of the island of inversion is presently unknown due to experimental inability in producing and measuring isotopes beyond $N = 23$. Nevertheless, it is proposed that the $N = 20$ island of inversion extends all the way to $N = 28$ and thus merges with the $N = 28$ island of inversion [54]. An initial verification to this effect has been resulted from in-beam gamma ray spectroscopy [80] and lately from half-life and gamma ray measurements at the Facility for Rare Iso-

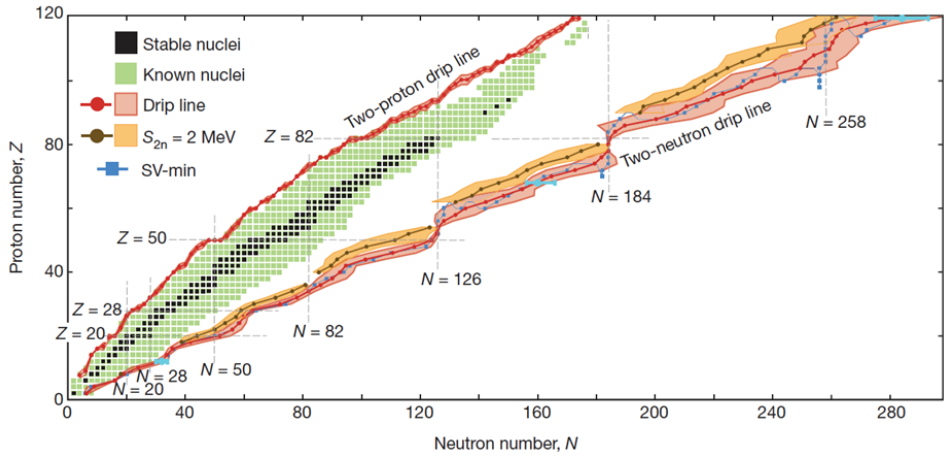

Figure 2.9: The proton and neutron driplines. Figure taken from [88].

.

tope Beams (FRIB) [66, 173]. However, more experimental results are necessary to verify if the merging of the two islands of inversion takes place.

2.3 Limits of existence of proton-rich nuclei

Nuclear existence ends when the nucleus has no capacity to hold additional neutrons or protons. The number of protons and neutrons that define the limits of nuclear existence are expressed by two main driplines; the neutron dripline and the proton dripline. These determine the point at which the one-proton (neutron) separation energy:

$$S_p = \big(-m(Z,A)+m(Z-1,A-1)+m(^1\mathrm{H})\big)c^2 \tag{2.7}$$

$$S_n = \big(-m(Z,A)+m(Z,A-1)+m(n)\big)c^2 \tag{2.8}$$

becomes negative and therefore a nucleon is emitted from the nucleus. This in turn means that adding more nucleons results in an unbound system, since their binding energy (Eq. 1.1) becomes positive.

Although the one neutron dripline is far from what can currently be reached experimentally, the one-proton dripline can be accessed, as can be seen in Fig. 2.9.

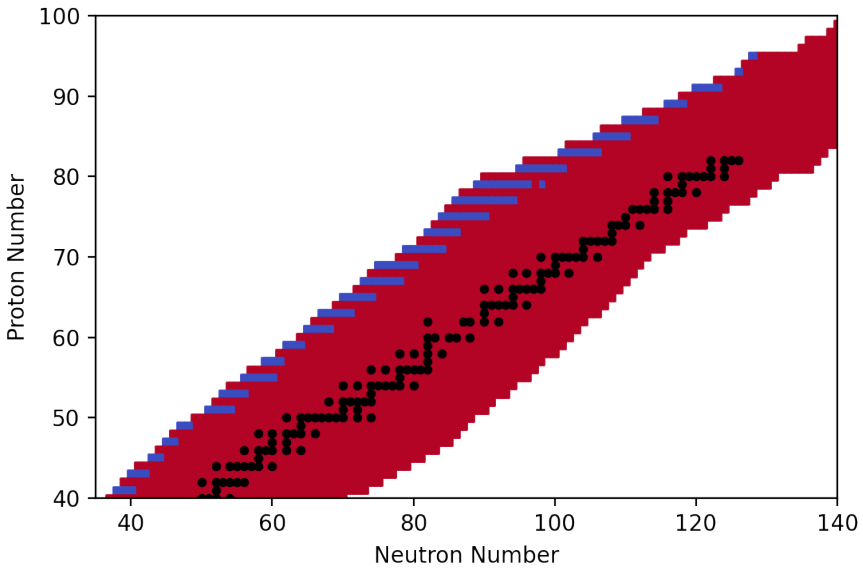

Figure 2.10: Nuclear chart, indicated are one-proton bound (red) and one-proton unbound (blue) nuclei. Data taken from [264].

The first proton unbound nuclei were discovered as early as the 1980s [122, 234] and by now we have more than 50 experimentally verified one-proton emitters [264]. The one-proton unbound nuclei in the region of $Z = 40 - 100$ can be seen in Fig. 2.10 in blue.

Fig. 2.10 is an example of effects stemming from nuclear pairing: identical nucleons (protons or neutrons) have a lower energy when their spins are paired rather than when they are unpaired. Therefore, the one-proton dripline, sets the limits of existence only for odd-Z nuclei, as those have an unpaired proton and therefore will primarily decay with one-proton emission. On the other hand, elements with an even number of protons contain only protons with paired spins. Therefore, due to the additional energy required when breaking the pair, it is more energetically favourable to emit a pair of protons than a single proton. Spontaneous emission of a pair of protons is determined by the two-proton dripline. Similarly to the one-nucleon dripline, it determines the point of which the two proton separation energy,

given by:

$$S_{2p} = \big(-m(Z,A) + m(Z-2,A-2) + 2m(^1\mathrm{H})\big)c^2 \tag{2.9}$$

becomes negative and therefore the point at which two nucleons are simultaneously or sequentially emitted from the nucleus. The theoretical two-proton dripline for even-Z can be seen in Fig. 2.9. The first two-proton decay was observed in ^{45}Fe [107, 203] and today the two-proton dripline up to Kr ($Z = 36$) is determined.

2.3.1 One- and two-proton radioactivity

Unlike neutrons, protons in the nucleus experience both an attractive mean field potential and a long-range repulsive Coulomb potential as can be seen in Eq. 2.2. The result of these two potentials is an attractive potential-well followed by a positive barrier, known as the Coulomb barrier, a schematic of which can be seen in Fig. 2.3. Due to the Coulomb barrier, protons with positive binding energies (thus unbound) cannot escape the nucleus unless they tunnel through the barrier.

Similarly to Gamow's theory for alpha decay [151], these unbound protons have a finite probability of tunnelling through this barrier with an average time of [110]:

$$\tau \propto e^{aZ/\sqrt{|S_p|}} \tag{2.10}$$

where Z is the proton number of the daughter nucleus, $a = ke^2$, e is the proton charge, k is the Coulomb constant and S_p is the one-proton separation energy. This unique property of proton-rich nuclei was proposed in the 1960s as proton radioactivity by Goldansky [108], Zeldovich and Karnaukhov and it is the reason why it is possible to experimentally observe nuclei past the proton-driplines.

The description becomes more complicated for the case of two-proton radioactivity. In this situation, there are two possible scenaria: a) a three-body decay where the two emitted protons have no correlation between them but are emitted simultaneously or b) a di-proton ($^2_2\mathrm{He}^0$) decay where a pre-formed $^2_2\mathrm{He}^0$ cluster tunnels through the Coulomb barrier and then decays outside the barrier. These two descriptions are referred to as "pure two-proton decay". In addition, it is possible that two protons are emitted sequentially from the nucleus. To discriminate between pure and sequential two-proton decays, Goldansky defined the true two-

proton emission [108] as the case where

$$S_p > 0 \quad \text{and} \quad S_{2p} < 0. \tag{2.11}$$

Moreover, he defined the threshold half-life $t_{1/2} \sim 10^{-12}$ s to separate the case of two-proton radioactivity from particle-unstable nuclei.

The region in the nuclear chart between the one-proton dripline and $t_{1/2} \sim 10^{-12}$ s is referred to as the Litorral Shallow of the sea of instability [193]. For light and medium nuclei ($Z \leq 50$, $A \leq 130$), the Littoral Shallow is narrow (only contains few isotopes) because the Coulomb barrier is proportional to Z and hence relatively low, thus not including many unbound energy levels, but as the atomic number Z increases, so does the width of the Littoral Shallow.

However, as the potential barrier increases, so does the tunnelling time, according to Eq. 2.10 and therefore the half-life of the proton-unbound isotopes. In such cases, alpha-decay has proven to be faster than the proton decay and because of that, it becomes the primary decay mode of heavy nuclei ($Z \geq 50$, $A \geq 130$). Olsen et al. [195], suggest that sequential two-proton decay is suppressed for $Z > 82$, while pure two-proton decay is suppressed for $Z > 52$. In agreement with that finding, Neufcourt et al. [190], uses specific nuclear models with Bayesian analysis to predict the heaviest two-proton emitter to exist. They conclude that nuclei with $Z > 54$ have a small ($p < 0.4$) probability for pure two-proton decay.

Nevertheless, the existence of two-proton radioactivity in heavy nuclides still remains to be experimentally verified and the competition between two-proton and alpha decay needs to be explored and tested.

2.3.2 Thomas-Ehrman shifts

Thomas-Ehrman shifts [64], which are shifts in the energy levels of unbound proton states, appear or are predicted to appear in proton-rich ($Z > N$) nuclei, such as ^{39}Sc [64] and they depend on the orbital angular momentum l of the unbound proton states [13]. The effect can be visualized by looking at the nuclear potential for different angular momentum quantum numbers as shown schematically in Fig. 2.11.

In the case of a proton with $l = 1$ (p-orbital), the wavefunction of the last pro-

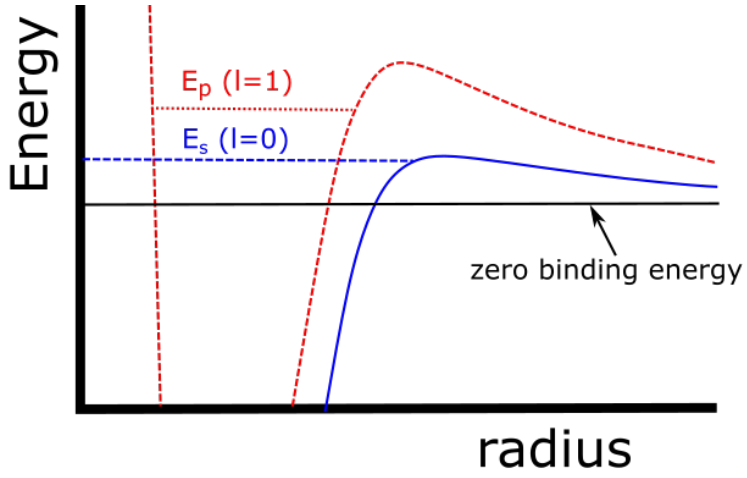

Figure 2.11: Schematic of the energy level of an unbound proton for two different angular momentum numbers. Picture adapted from [13].

ton is well-confined within the nuclear potential due to the large Coulomb barrier created by the combination of the Coulomb interaction and the centrifugal force. This overlap between the wavefunction of the core nucleus and the unbound proton results in an energy level E_p for the unbound proton as shown in the schematic of Fig. 2.11.

In contrast, in the case of the *s*-orbital ($l = 0$), the smaller Coulomb barrier, created in the absence of a centrifugal force, and the larger radius of the potential, allow for a broader wavefunction for the unbound proton and therefore a smaller overlap between the wavefunction of the unbound proton and the one of the core nucleus. As a result, the energy of the unbound proton is lower than that for the *p*-orbital, as shown in Fig. 2.11.

Thomas-Ehrman shifts are determined through the excitation energies of proton unbound states [258] and the separation energies of proton unbound ground states [193]. The effect was first seen in the 1950s by Thomas [258] and Ehrman [82]. They compared the first excited states of two mirror nuclei: ^{13}C and ^{13}N. If the energy levels are corrected as if there was no Coulomb interaction between the protons, the energy levels between protons and neutrons should be almost identical

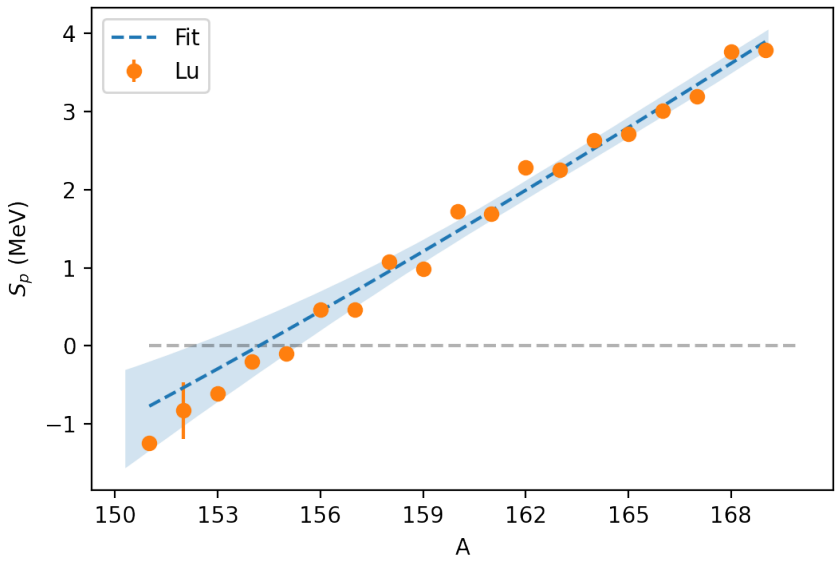

Figure 2.12: Example of the a TE fit for the lutetium isotopes.

due to isospin symmetry[1]. Instead, in the case of ^{13}C and ^{13}N, they were apart by 750 keV, leading to the conclusion that the two wavefunctions have different degrees of overlap in each case and giving rise to the Thomas-Ehrman shift.

The Thomas-Ehrman shift has since been discovered in numerous light nuclei by studying mirror nuclei. However, for $Z > 50$, there are no longer mirror pairs which can be used for comparison, as the nuclear chart deviates from the $N = Z$ line and more neutrons need to be added to the nucleus to gain stability. A different way to look for Thomas-Ehrman shifts for heavy nuclei was developed by Novikov et al. [193]. In this approach, the one-proton separation energy is fitted as a function of the neutron (N) or the mass (A) number for a number of nuclei close to the proton dripline (provided that there are no changes in nuclear structure such as shell closures and deformation), as can be seen in Fig. 2.12. The fit function, given

[1] In reality, isospin symmetry is also broken by the difference in mass between the proton and the neutron.

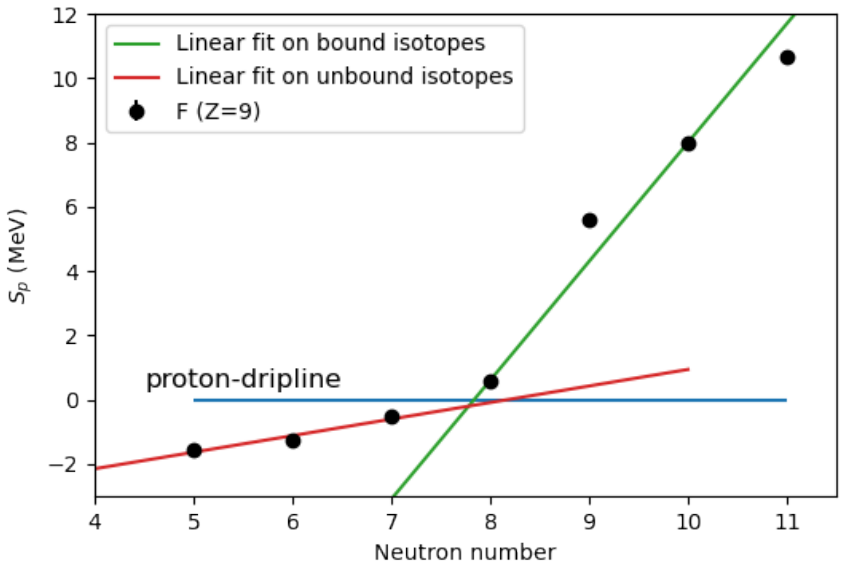

Figure 2.13: Example of the change in the slope of the one-proton separation energy for bound versus unbound nuclei. Here linear fits were applied instead of Eq. 2.12 to highlight the change in the slope between bound and unbound separation energies and to account for the limited number of isotopes.

by:

$$S_p = a + \frac{b}{A^{1/3}} + \frac{c}{A} \tag{2.12}$$

where a, b, c fitting parameters, is a simplification of the liquid drop model formula. If there is a Thomas-Ehrman shift in the element of interest, then there will be an abrupt change in the one-proton separation energy [193] between bound ($S_p > 0$) and unbound ($S_p < 0$) nuclei and therefore a deviation from the S_p predicted by the liquid drop model due to the extra binding that comes from the reduced wavefunction overlap. The change in the slope of S_p for the unbound fluorine isotopes that are known to demonstrate Thomas-Ehrman shifts [64] supports this new method and can be seen in Fig. 2.13.

2.4 Evolution of the nuclear shell model

Since the 1950s significant effort has been devoted to improving the nuclear shell model of Mayers [176] and Jensen [117] in order to predict features such as new magic numbers and islands of inversion. The emergence of such effects is attributed to the residual interaction: a two-body or higher order effect that is not captured in the mean field potential of the individual particle shell model.

The ideal way to to fully describe the properties of a nucleus is to start from the most fundamental theory: QCD [248]. However, QCD is non-perturbative and therefore it cannot be used in the energy scale that concerns the nucleons. Hence, all theories that describe nuclear structure have, to this date, some roots in an effective field theory (for example [243]).

Ab initio theory (for example [250]), is the most fundamental class of nuclear theories, and it is the one with the most ties to QCD. Following ab initio theories, there is the class of effective field theories that derive nuclear properties by solving the Hartree-Fock-Bogoliubov (HFB) equations [280]. The rest of the present section describes the fundamental assumptions and approaches of the two theories as well as their advantages and disadvantages.

2.4.1 Ab initio techniques

Unlike all other techniques, ab initio theories are the first fully microscopic theories that do not contain any mean field components in the nuclear potential. One class of ab initio theories is the VS-IMSRG theory [250], where the nuclear potential is derived from chiral effective field theory [266] with nucleonic and pionic degrees of freedom, due to the non-perturbative character of QCD. It mostly contains two-nucleon terms that describe the exchange of one-pion (leading order), two-pions (next to leading order) and so on. In certain cases three-body forces are needed to bring the theory in better agreement with experimental data.

Except from their closer ties to QCD, ab initio theories also owe their name to the lack of parameters that require adjustment from experimental observables. However, this is not completely true. Ab initio theories are not calibrated using measured binding energies and charge radii as will be seen for other theories in the next section, but they use data from nucleon-nucleon scattering to define the

nucleon-nucleon interaction. In addition, ab initio three-body forces do include free parameters, the values of which are derived from simple nuclear systems such as ^{3}H and ^{3}He [163]. More specifically, the free parameters of the three-body force component are varied until the resulting binding energies, charge radii, quadrupole moments as well as other nuclear properties match the experimental values observed in light nuclei [188].

After the nuclear potential has been determined, nuclear properties are derived by exact diagonalization of the many-body Hamiltonian:

$$\Big(\sum_{i=1}^{A}\frac{p_i^2}{2m_i}+\sum_{i<j}V_{ij}+\sum_{i<j<k}V_{ijk}\Big)\Psi=E\Psi \tag{2.13}$$

where p_i the momentum of nucleon i, V_{ij} the two-body interaction, V_{ijk} the three body interaction (if included), E the energy eigenvalues and Ψ the many body wavefunction. The many body wavefunction is given by the Slater determinant of the single particle wavefunctions (usually expanded in the harmonic oscillator basis)

$$\Psi(r_i,i=1,..,A)=\frac{1}{\sqrt{A!}}\begin{vmatrix}\phi_1(r_1) & \phi_1(r_2) & ... & \phi_1(r_A)\\ \phi_2(r_1) & \phi_2(r_2) & ... & \phi_2(r_A)\\ \vdots & \vdots & \ddots & \vdots\\ \phi_A(r_1) & \phi_A(r_2) & ... & \phi_A(r_A)\end{vmatrix} \tag{2.14}$$

which is used to ensure antisymmetric wavefunctions.

Unfortunately, exact diagonalization is extremely difficult due to the fact that the parameter space increases exponentially with the system size. Despite the computational challenges, theories like the No Core Shell Model [187] have achieved predictions of nuclear systems of up to $A \approx 20$ (for example [61]). A way to overcome the computational limitations is to divide the parameter space into a core, a valence space, and the outside space, as can be seen in Fig. 2.14. The core usually contains a closed shell nucleus (for example ^{40}Ca), to ensure that there will be no excitations from the shells within the core, while the valence space contains open shells and some lower excitation levels. This approach has accelerated the progress of ab initio theories and it has enabled ab initio caluclations for nuclei as heavy as ^{132}Sn [181]. However, calculations are in many cases restricted to proton

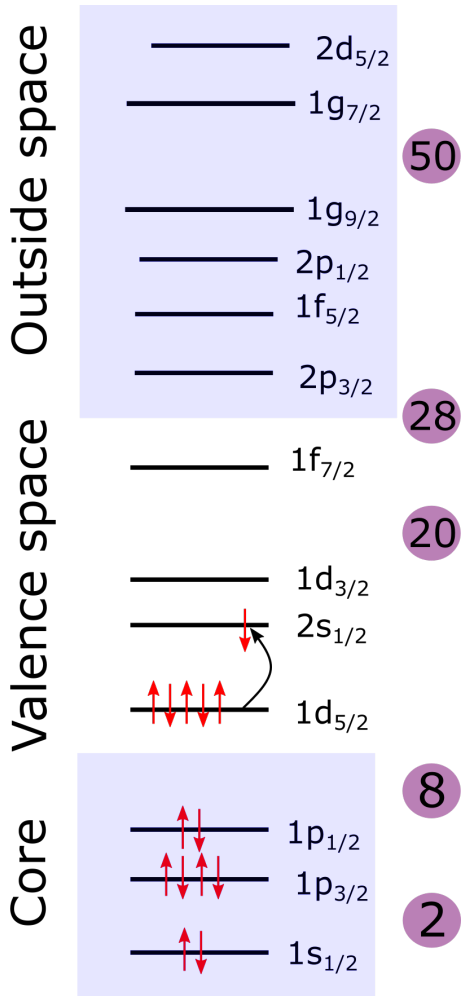

Figure 2.14: Separation of the parameter space into core, valence space and outside space in ab initio calculations of medium-mass nuclei.

and neutron numbers close to shell closures due to computation limitations related to many valence energy levels.

2.4.2 Effective field theories

Before the emergence of ab initio interactions and before the chiral effective field theory was established, the most realistic nuclear interactions were derived from

effective field theories, such as [243]. In such theories, the Energy Density Functional (EDF) $\mathscr{E}$ contains two and three-body terms that describe how the two-body interaction is influenced by other nucleons [243].

Unlike the ab initio theories that solve the many-body Schrodinger equation, the effective field theories solve the Hartree-Fock-Bogoliubov (HFB) equations [280] that are derived using the variational principle on the energy density functional [254]:

$$\frac{\delta}{\delta \phi_i}(\langle \Psi | \mathscr{E}_{tot} | \Psi \rangle - E) = 0 \tag{2.15}$$

where ϕ_i is the single particle wavefunction of nucleon i, Ψ is the antisymmetrized wavefunction, $\mathscr{E}_{tot}$ is the total energy density functional and E is the ground state energy of the system. The total wavefunction is also constructed from the Slater determinant (Eq. 2.14) of the single particle wavefunctions which are usually expanded in the harmonic oscillator basis.

The advantage of the HFB equations is that they can be used to calculate the entire nuclear chart without issues related to computational limitations. In addition, due to decades of improvement they are significantly more precise than ab initio calculations [249]. However, they are not fundamental. Although they can calculate correlations between nucleons, their potential has a mean field component, and there are several parameters that need to be calibrated from experimental data. Two of the main nuclear field theories are the ones employing Skyrme interactions [243] and those employing the Gogny interaction [69]. These two theories have been used to interpret the results of this thesis in Chapter 6, which motivates a more detailed look at their features.

The Skyrme interaction

In its general form, the Skyrme density functional is given by [249]:

$$E = \int d^3 r n(\mathscr{E}_{kin} + \mathscr{E}_{Skyrme} + \mathscr{E}_{Skyrme,odd}) + E_{Coulomb} + E_{pair} + E_{cm} \tag{2.16}$$

where n the nucleon density, $\mathscr{E}_{kin}$ the kinetic energy functional, $E_{Coulomb}$ the Coulomb energy, E_{cm} a center of mass correction, E_{pair} the pairing effect that accounts for

the residual interaction which arises from valence nucleons and $\mathscr{E}_{Skyrme}, \mathscr{E}_{Skyrme,odd}$ the Skyrme energy functionals:

$$\begin{aligned} n\mathscr{E}_{Skyrme} = & \frac{B_0 + B_3 n^\alpha}{2} n^2 - \frac{B'_0 + B'_3 n^\alpha}{2} \tilde{n}^2 + B_1(n\tau - \mathbf{j}^2) - B'_1(\tilde{n}\tilde{\tau} - \tilde{\mathbf{j}}^2) \\ & - \frac{B_2}{2} n\Delta n + \frac{B'_2}{2} \tilde{n}\Delta\tilde{n} - B_4 n\nabla\cdot\mathbf{J} - (B_4 + B'_4)\tilde{n}\nabla\cdot\tilde{\mathbf{J}} + \frac{C_1}{2}\mathbf{J}^2 - \frac{C'_1}{2}\tilde{\mathbf{J}}^2 \end{aligned} \tag{2.17}$$

$$\begin{aligned} n\mathscr{E}_{Skyrme,odd} = & -\frac{C_0 + C_3 n^\alpha}{2}\boldsymbol{\sigma}^2 + \frac{C'_0 + C'_3 n^\alpha}{2}\tilde{\boldsymbol{\sigma}}^2 + \frac{C_2}{2}\boldsymbol{\sigma}\Delta\boldsymbol{\sigma} - \frac{C'_2}{2}\tilde{\boldsymbol{\sigma}}\cdot\Delta\tilde{\boldsymbol{\sigma}} \\ & - C_1\boldsymbol{\sigma}\cdot\boldsymbol{\tau} + C'_1\tilde{\boldsymbol{\sigma}}\cdot\tilde{\boldsymbol{\tau}} - B_4\boldsymbol{\sigma}\cdot(\nabla\times\mathbf{j}) - (B_4 + B'_4)\tilde{\boldsymbol{\sigma}}\cdot(\nabla\times\tilde{\mathbf{j}}) \end{aligned} \tag{2.18}$$

Although a detailed description of individual terms in equations 2.17, 2.18 lies outside the scope of this thesis (for more information see: [249]), it is important to note that all C and B parameters are free parameters of the model that are determined from fits to experimental data, giving rise to numerous Skyrme parametrization as discussed later on.

In addition, it needs to be noted that the densities n, τ, j, J, σ are functions of the single particle wavefunctions $\phi_i, i = 1,..,A$, and the occupation numbers u_i, with the latter necessary in order to take into account the residual interaction. By using the variational principle in with respect to ϕ_i and u_i one derives the mean field (Hartre-Fock-HF) and pairing (Bogoliubov-B) equations respectively. The resulting HFB equations are solved numerically to derive the desired nuclear properties.

The parameters C and B are adjusted to experimental data, such as binding energies and charge radii. Different parametrizations arise from the choice of different experimental data sets. For example, the SLy4 [55] parametrization was derived with a bias towards neutron rich nuclei in order to focus on nuclear astrophysics studies, the SV-min parametrization [144] was developed using spherical nuclei and the UNEDF0 [149] included deformed nuclei [88]. The precision of the resulting binding energies from HFB calculations are of the range of 0.5 MeV to 1.2 MeV [149].

The Gogny interaction

The Gogny interaction [69] is similar to the Skyrme interaction, as they are both effective interactions and determine nuclear physics parameters by solving the HFB equations. A significant difference between them is that while the Skyrme interaction has zero range ($V_{eff}(\vec{r}_1,\vec{r}_2) = 0$ if $\vec{r}_1 \neq \vec{r}_2$, where V_{eff} the effective potential and $\vec{r}_1,\vec{r}_2$ the positions of two interacting nucleons), the Gogny interaction has a finite range as can be seen from the first term of the Gogny effective potential:

$$\begin{aligned} V_{12} = \sum_{j=1}^{2} e^{-(\vec{r}_1-\vec{r}_2)^2/\mu_j^2}(W_j + B_j P_\sigma - H_j P_\tau - M_j P_\sigma P_\tau) + \\ t_3(1+x_0 P_\sigma)\delta(\vec{r}_1-\vec{r}_2)\left[\rho\left(\frac{\vec{r}_1+\vec{r}_2}{2}\right)\right]^\alpha \\ + iW_{LS}\nabla\delta(\vec{r}_1-\vec{r}_2)\times\nabla\delta(\vec{\sigma}_1+\vec{\sigma}_2) \\ + (1+2\tau_{1z})(1+2\tau_{2z})\frac{e^2}{|\vec{r}_1-\vec{r}_2|} \end{aligned} \tag{2.19}$$

Due to its finite range, the Gogny interaction can be used to derive the intensity of the pairing correlations between the nucleons [210]. Similarly to the Skyrme interaction, the parameters $\mu, W, B, H, M, x_0, t_3, \alpha$ and W_{LS} are free parameters that are adjusted with the help of experimental data. Finally, the Gogny Hamiltonian has been updated (5DCH model) to allow rotational and vibrational degrees of freedom and thus to account for collectivity [210], which is the model used in the framework of this thesis.

Chapter 3

Mass spectrometry of exotic ions

The binding energy of a nucleus can act as a probe for nuclear structure effects, as discussed in Chapter 2. The binding energy can be experimentally determined by measuring the atomic mass of a nucleus: a quantity related to its binding energy. The atomic mass can be expressed as:

$$m = Zm_p + Nm_N + Zm_e - BE_n/c^2 - BE_e/c^2 \tag{3.1}$$

where Z is the number of protons or electrons, N is the number of neutrons, m_p, m_n, m_e are the masses of protons, neutrons and electrons respectively and BE_n, BE_e are the binding energies of the nucleons and the electrons. The goal of mass spectrometry of exotic ions is to provide high precision binding energies by measuring the mass of short-lived and exotic atoms, as motivated in Chapter 2.

The present chapter begins with a description of the techniques used to produce radioactive isotopes, it continues with some fundamental quantities and procedures of exotic mass spectrometry and it ends with some of the most common techniques applied for measurements of the masses of radioactive species.

3.1 Production of exotic ions

In exotic mass spectrometry, the quantity that is being measured is the ionic mass, due to the convenience of manipulating and creating beams of charged particles using electric and magnetic fields.

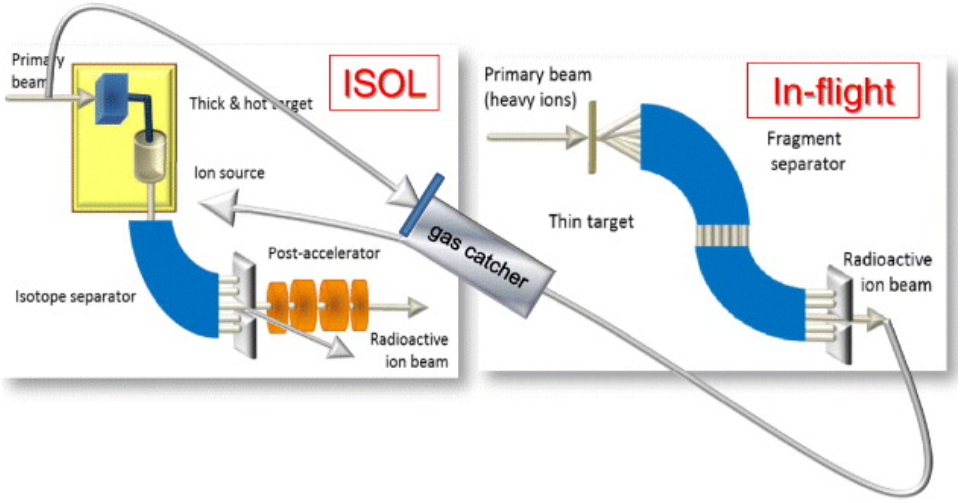

Figure 3.1: Schematic of the ISOL and In-flight separation techniques. Figure from [35].

Exotic ions are produced and studied in Radioactive Ion Beam (RIB) facilities, where a RIB can be generated typically by two different techniques [35]. The two production techniques used in RIB facilities are the In-flight separation and the Isotope Separation On-Line (ISOL) technique [35]. Fig. 3.1 shows a schematic of the two techniques.

In the ISOL technique [215], a light primary beam (usually protons) impinges on a thick ($\approx$ 20 cm) target of a high-Z material. In the target, a number of different nuclei are created through spallation, fragmentation and fission reactions, depending on the material of the target. The new nuclei effuse through and diffuse out of the target, where they are in a neutral state. The element of interest is ionized by some method, for example surface [10] or laser ionization [170] and the Ions of Interest (IOI) are extracted using a strong electric field, typically 10-60 kV. In practice, more than one element is ionized and therefore, a dipole magnet (mass separator) [42] is used to separate the IOI from the ions which are not of interest, hence background. However, background ions and molecules with a similar mass-to-charge ratio as the IOI are able to pass through the dipole magnet and therefore remain as background. The range of mass-to-charge ratios that can pass through the mass separator is determined by the resolving power of the dipole magnet and

	ISOL	In-flight separation
Projectile examples	p,d	Kr, Xe, U
Projectile energy [MeV/u]	500-1400	50-2000
Target thickness [g/cm^2]	10-100	1
From production to delivery	$\approx$ ms-h	$<$100ns

Table 3.1: Characteristic parameters of the ISOL and the In-flight production techniques.

it is discussed for the ISAC-I mass separator in Chapter 4.

The In-flight separation technique [105] employs a primary beam of heavy ions (such as those in Table 3.1) that impinges on a thinner target resulting in in-flight projectile fragmentation. Post fragmentation, the IOI are separated and transported with a fragment separator (for example [239]). Some of the key parameters of the two techniques can be seen in Table 3.1.

The two techniques are to an extent complimentary because although the ISOL technique offers pure high intensity beams, it cannot provide extremely short-lived species ($t < 1ms$) due to ms-scale diffusion times of the ions from the thick target. On the other hand, In-flight separation suffers from a beam cocktail that cannot be efficiently separated but can provide isotopes with significantly shorter half-lives thus being more suitable for isotope discovery. In addition, the In-Flight technique has the advantages of being independent of target chemistry and not requiring ion sources to ionize the isotopes. Finally, as can be seen in Fig. 3.1, the two methods can be combined by coupling a so-called gas-catcher [231] after the in-flight separator.

The ISOL technique for exotic isotope studies is currently used at CERN-ISOLDE [215], GANIL SPIRAL [167], and ISAC TRIUMF [25], while the In-flight separation technique is employed at NSCL/FRIB [257], RIKEN [252] and GSI [105]. These three In-flight facilities also use gas-catchers.

3.2 Fundamentals of exotic mass spectroscopy

Two fundamental quantities in exotic mass spectrometry are the precision of a mass measurement and the resolving power of the mass spectrometer. The precision δm,

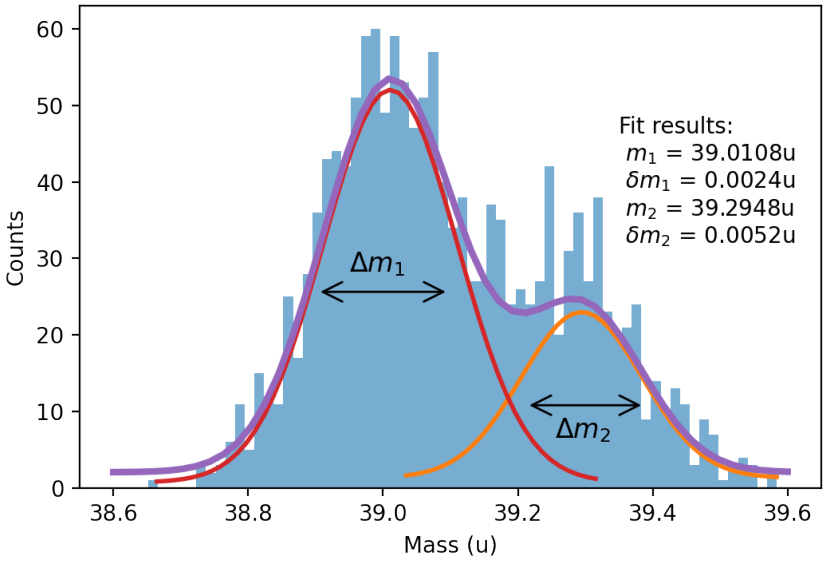

Figure 3.2: An example of two simulated overlapping mass peaks fitted with Gaussian distributions. The FWHM and the fit parameters are noted on the figure.

refers to the uncertainty in the determination of an ion's mass, while the resolving power refers to how well two species with similar masses, such as those in Fig. 3.2, can be separated. The resolving power can be calculated as:

$$R = \frac{m}{\Delta m} \tag{3.2}$$

where Δm is the Full Width Half Maximum (FWHM) of the mass distribution, as shown in Fig. 3.2. Relative precision ($\delta m/m$) and resolving power are related as:

$$\frac{\delta m}{m} \propto \frac{1}{R\sqrt{N}} \tag{3.3}$$

where N is the number of collected statistics.

There are two main methods for mass spectrometry of exotic ions: direct and indirect mass spectrometry. In indirect mass spectrometry, the mass of the ion

is determined from a known decay energy and the mass of the decay progenitor. The technique is useful in unknown territories of the nuclear chart (with extremely rare combinations of protons and neutrons) where half-lives and RIB production yields are small. However, for indirect mass measurements to be accurate, a good understanding of the energy levels of a nucleus is required as decays to unknown excited or isomeric states can cause incorrect assignments and mass values.

Direct mass measurements, rely on the measurement of the inertial mass of the ion. Direct mass spectroscopy itself, contains three main subcategories: mass measurements with Storage rings [22, 38, 281], Time-of-Flight Mass Spectrometers [59, 164, 204, 237, 272] and ion traps [18, 74, 75, 89, 140, 225]. The following sections describe the latter two, which are employed at the TRIUMF's Ion Trap for Atomic and Nuclear science (TITAN) experiment [75].

3.3 Multiple-Reflection Time-of-Flight Mass Spectrometry

Multiple-Reflection Time-of-Flight Mass Spectrometers (MR-TOF MS) is a subcategory of Time-of-Flight (TOF) mass spectroscopy which allows the determination of the mass of an ion by measuring its TOF through an approximately field free region. If the ions travel with a non-relativistic speed and $\vec{v}(z=0)=0$, the TOF relates to the mass as:

$$t = \int_0^L \sqrt{\frac{m}{2q}(V_0 - V(z))^{-1}}dz \propto \sqrt{\frac{m}{q}} \tag{3.4}$$

where L is the total path length, m is the mass of the ion, q is the charge of the ion, V_0 is the electric potential at $z=0$ and $V(z)$ is the electric potential along the path z.

In TOF mass spectrometry, the resolving power of an TOF device is given by:

$$R = \frac{m}{\Delta m} = \left(\frac{t}{\Delta t}\right)^2 \tag{3.5}$$

where t the total flight path of the ion and Δt the spread in the TOF distribution. Therefore, the larger the flight path the better the resolving power that can be achieved in a TOF device. For this reason, TOF devices in Mass Spectroscopy

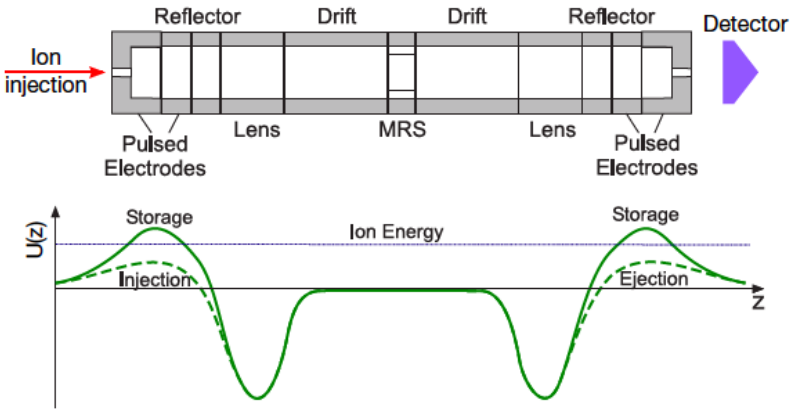

Figure 3.3: Top: Simplified schematic of an MR-TOF MS device. Bottom: The voltages applied to a typical MR-TOF MS device. Picture from [163].

have evolved into MR-TOF MS since a long path in a well controlled and compact device has many advantages. In an MR-TOF MS device, the flight path of the ions can be arbitrarily extended by repeatedly reflecting them between two electrostatic mirrors which are located approx. 30 cm apart, as can be seen in the schematic of Fig. 3.3.

A MR-TOF MS device is a fully electrostatic ion trap that consists of a set of two electrostatic mirrors separated by an approximately field-free drift region, as can be seen in Fig. 3.3. Once the ions are in the spectrometer, they are reflected between the mirrors for a number of times thus extending the flight path length of the ions. Once the required path length has been reached, to achieve the required resolving power, the ions are extracted to a particle detector where their TOF is recorded. A typical spectrum on the TOF detector can be seen in Fig. 3.4, where the ions have undergone 659 reflections, reaching a resolving power of 380,000. The mass of the species in Fig: 3.4 can be calculated through their TOF using [21]:

$$m/q = \frac{c(t-t_0)^2}{1+Nb} \tag{3.6}$$

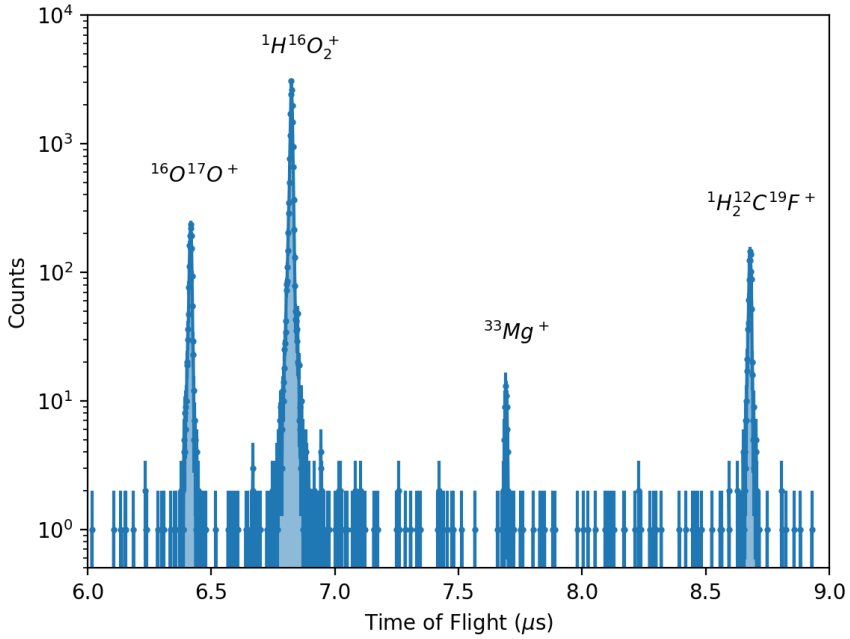

Figure 3.4: Time-of-Flight spectrum from the TITAN MR-TOF MS. The ions have undergone 659 reflections, resulting in a resolving power of 380,000.

where t the TOF of the ion, N the number of reflections, and t_0, b and c fitting parameters that are unique to each MR-TOF MS device. Parameters t_0, b and c are calibrated prior to a mass measurement using ions of well known masses.

Due to their short-cycles (few ms) and their non-scanning measurement principle, MR-TOF MS devices are ideal in detecting short-lived isotopes ($5ms < t < 50ms$) with very low production yields ($< 1pps$) and in achieving high signal to background ratios ($1 : 10^6$) [217]. Their success and performance relies on some of the following aspects.

3.3.1 Isochronicity

The relative properties of two ions of the same mass in an MR-TOF MS system prior and after one mirror reflection can be described by a transfer matrix [273],

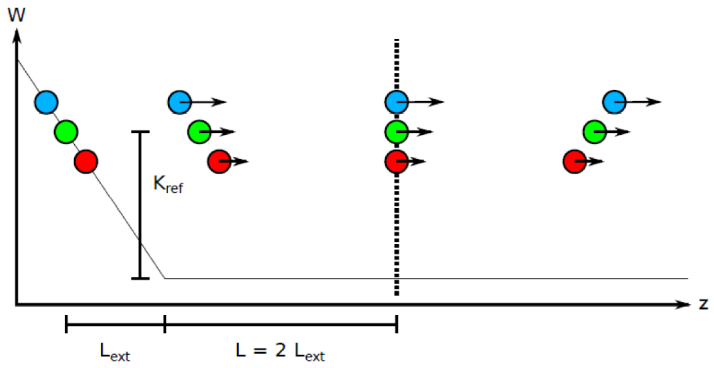

Figure 3.5: Schematic of the electric potential of the ion injection into the MR-TOF MS mass analyzer. A Time Focus point is shown with a vertical dashed line. Figure from [127].

such as the one shown in [274]. The transfer matrix describes the evolution of the ions' position, angle, relative energy and relative TOF over time. The relative TOF deviation $\delta t' = t'_2/t'_1 - 1$ after one mirror reflection, where t'_1 and t'_2 the TOF of ion 1 and ion 2 respectively, as derived from the transfer matrix, is proportional to [274]:

$$\delta t' \propto (\delta t|\delta K)\delta K + \delta t \tag{3.7}$$

where $\delta t'$ is the TOF deviation after a mirror reflection, δt is the TOF deviation before a mirror reflection and $\delta K = K_1/K_2 - 1$ is the relative energy deviation between the two ions. In order to achieve a high TOF resolution and hence a high mass resolution, the MR-TOF MS system needs to be isochronous [274]:

$$(\delta t|\delta K) = 0 \tag{3.8}$$

resulting in minimum TOF spread, as can be seen from Eq. 3.7.

This is achieved by shaping the accelerating potential that transfers the ions inside the field-free region, which is often referred to as the mass (or TOF) analyzer. As can be seen in Fig. 3.5, ions starting from a earlier starting point inside the potential (blue) will experience a larger field gradient and thus will acquire a larger acceleration, allowing them to catch up with the slower ions that started earlier, at

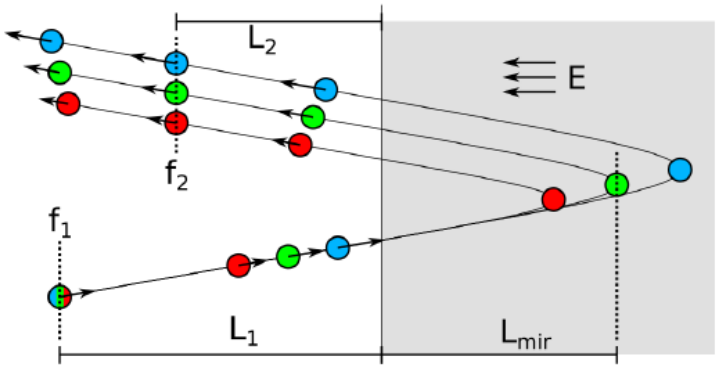

Figure 3.6: The trajectories of ions of different kinetic energies during a reflection from the mirror electrodes. In the mass analyzer, all ions with the same m/q are focused in certain focus points (f_1, f_2) determined by the electrostatic voltages applied to the electrodes. Figure from [127].

the time focus point (depicted with a vertical line). When the same ions arrive at the position of the mirror (Fig. 3.6), due to their larger energy, they will penetrate further, thus increasing their turn-around time which allows them to arrive at the second Time Focus point (f_2) at the same time with the rest of the ions after one turn, as can be seen in Fig. 3.6.

Using the isochronicity requirement, the primary time focus, which is depicted on Fig. 3.5, is achieved for

$$L = 2L_{ext}$$

while the secondary time focus, depicted in Fig. 3.6, requires that

$$L_1 + L_2 = 4L_{mirr}$$

where L_{ext} and L_{mirr} are the path lengths in the injection and reflection electric fields and L_1, L_2 and L are the path lengths in the field-free region (see [127] for a derivation).

In this way, the TOF spread remains controlled and a minimum TOF spread is achieved at the detector, leading to maximum resolving power.

3.3.2 Ion bunch size

Other important components for the successful operation of an MR-TOF MS device are the initial conditions of the ions, as can be seen from the parameter δt in Eq. 3.7. Ions need to enter the MR-TOF MS device in "bunches": an ensemble of ions with well-defined spatial and energy distributions. That is achieved by coupling the MR-TOF MS device with a preparation system, here a Radio-Frequency (RF) cooler-buncher trap [118] that creates ion bunches with a well defined energy, using buffer-gas cooling. Certain MR-TOF MS devices, such as the TITAN MR-TOF MS, have multiple RF cooler-bunchers which enable even further optimization of the bunch size.

The dependence of the resolving power on the ion bunch size is visible in Fig. 3.7, for the Multi Ion Reflection Apparatus For Collinear Laser Spectroscopy (MIRACLS) MR-TOF MS [238]. Lack of cooling, in this case laser Doppler cooling, results in significant transmission losses due to the large beam size and can be devastating for measurements of rare isotopes. Buffer-gas cooling, reduces the size of the ion bunch and results in higher transmission. Finally, further improvements in the ion bunch size can be achieved by Doppler cooling in a Paul trap, which has shown a 4.6 times increase in resolving power in MR-TOF MS measurements compared to buffer gas cooling alone [238].

3.3.3 Contamination

Another key aspect for the successful operation of MR-TOF MS devices is the absence of unwanted ions or molecules in the original bunch, referred to as beam contamination, or in a neutralized form in the trap, referred to as background contamination.

The presence of contaminants in the ion bunch can have two major consequences. First, if the IOI and the contaminant are sufficiently close in mass then they might not be resolved, thus reducing the precision and accuracy of the mass measurement. The second consequence of high rates of contamination in the ion bunch is that the contaminants can Coulomb interact with the IOI and thus cause systematic shifts in the TOF. An example of the mass shift as a function of the number of ions per ion bunch can be seen in Fig. 3.8, where a 4σ deviation can be

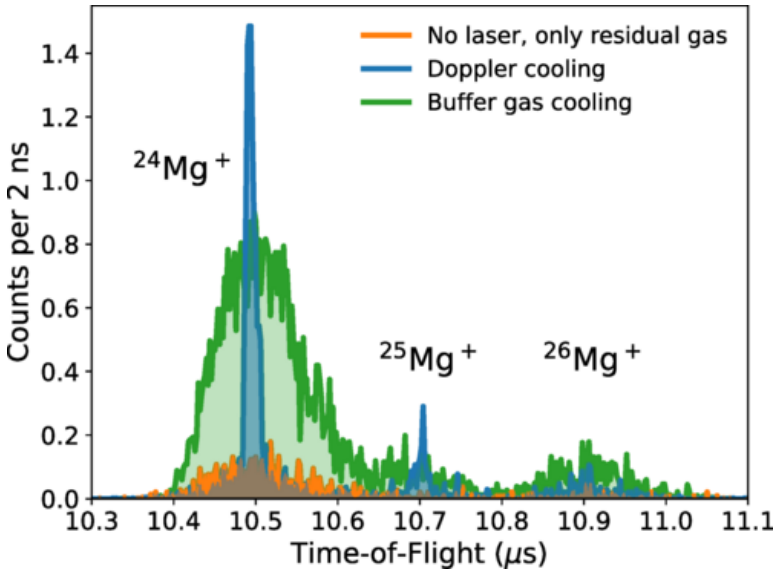

Figure 3.7: Time-of-Flight distributions in the MIRACLS MR-TOF MS for different ion bunch preparations. The effect of cooling is indicated by the width of the peak without (green) and with (blue) Doppler laser cooling. Figure from [238].

observed for an increase in beam intensity by a factor of ten.

High concentrations of background gasses in an MR-TOF MS device are responsible for neutral atom-ion collisions between ions and background molecules and a transfer of kinetic energy. As a result, the ion bunch size increases causing the reduction of resolving power and precision and in some cases, the loss of stored ions.

There are a number of techniques applied to reduce contamination in MR-TOF MS devices. A common way is the use of a central segmented electrode in order to deflect unwanted species [72]. This electrode is referred to as the Mass Range Selector (MRS) and it is used to deflect non-isobaric contaminants based on the m/q dependence of the ion velocity leading to a different number of turns in the system than the ion of interest. The voltage applied to the MRS is reflective at all times except when the IOI is about to pass through. Its location among the other electrodes of an MR-TOF MS can be seen in the schematic of Fig. 3.3. Alternatively, the electrostatic mirrors or the central drift tube of the MR-TOF MS can be shortly

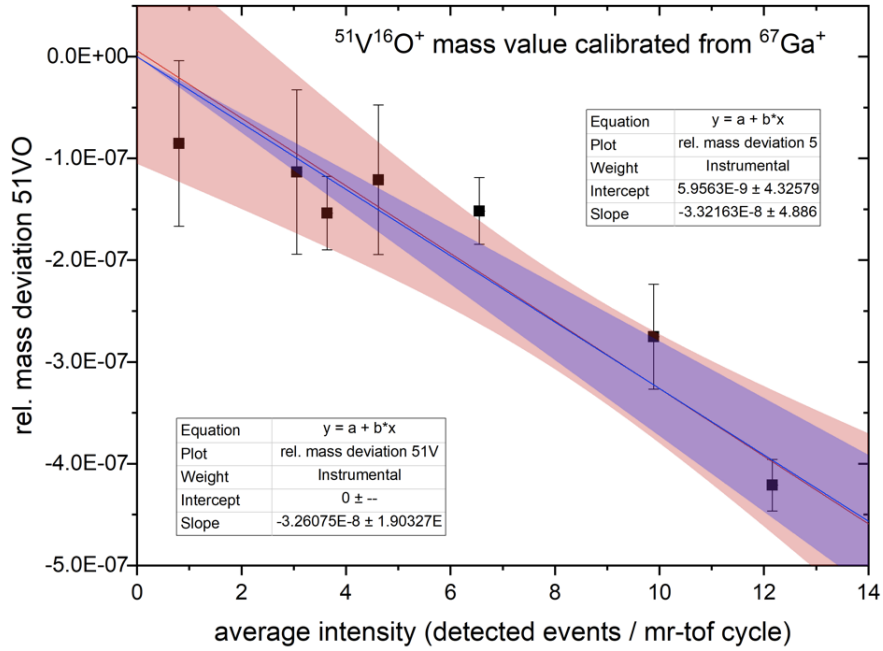

Figure 3.8: The effect of ion-ion interactions in the measured mass value of $^{51}V^{16}O^{+}$ using the TITAN MR-TOF MS. Figure taken from [206].

opened, raised [131, 268] or repeatedly pulsed [227] to remove unwanted species.

Although it is desired to remove non-isobaric contaminants from the trap, the beam contamination can still remain high due to isobaric contaminants. For this reason, a new technique to reduce isobaric contamination has been developed. The new technique, called Mass Selective Retrapping [29], relies on separating the ion bunch in the MR-TOF MS and retrapping in the buffer-gas-filled Radio-Frequency Quadrupole trap (RFQ). Only the subset of the initial ion bunch that contains the ions of interest are captured and preserved for further measurement. TITAN is the only experiment that currently uses the technique and more details are provided in Chapter 4.

Over the last ten years, due to their non-scanning measurement approach and their fast cycles, MR-TOF MS devices have proven to be ideal for mass measurements of short-lived, low production exotic isotopes with their relative measure-

ment precision reaching few-10^{-8} [227]. However, although Eq. 3.5 indicates a resolving power that scales with the time of flight, actual MR-TOF MS devices show a saturation of resolving power for $N \approx 700$. The next section focuses on the causes of the saturation of the MR-TOF MS resolving power.

3.3.4 Challenges of MR-ToF MS systems

Perhaps the most challenging aspect of increasing the MR-TOF MS's resolving power is the stability of power supplies for the electrostatic ion optics elements. Although temporal voltage drifts can be corrected using a reference ion of well-known mass [21], random voltage fluctuations or voltage "ringing" following fast switching of voltages can have a large impact on the peak width.

Voltage "ringing" [130] occurs when a power supply does not settle smoothly to the set voltage but instead fluctuates before reaching it [21]. This effect is one of the primary sources of MR-TOF MS systematic errors as ion bunches that are well separated experience a different amount of "ringing" depending on their position when the voltage switch occurs. Fig. 3.9 shows a histogram of the TOF distribution of $^{133}Cs^{+}$ ions that were stored in the TITAN MR-TOF MS for different durations ($\Delta t_{stor} = 7\mu s$). Different storage times correspond to ion bunches located at different positions in the MR-TOF MS when the voltages of MR-TOF MS extraction optics is switched, and the systematic uncertainty related to this effect can be estimated by the width of the TOF distribution in Fig. 3.9.

To reduce the effects of voltage "ringing" and power supply fluctuations, passive (RC filters [127, 227]) and active voltage stabilization as well as temperature stabilization [227] of the power supplies are applied.

One method to increase resolving power based on Eq. 3.5 is by increasing the ion's flight path. However, as the storage time in the MR-TOF MS increases, so do the number of collisions with the background gas, which result in peak broadening. Therefore, longer storage times require better vacuum conditions. This is achieved by very effective differential pumping (where small orfices separate vacuum sections in the system, introducing reduced gas flow from one section to the other between the MR-TOF MS vacuum section and the helium-filled Paul traps [127]. At this point, more developments are needed to increase the number of reflections to

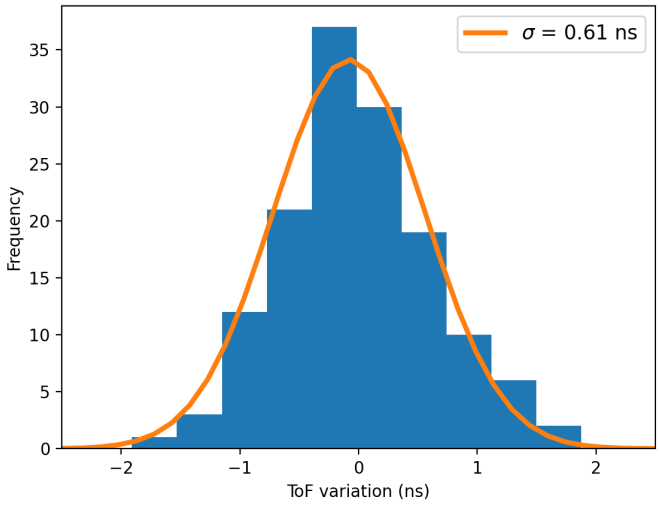

Figure 3.9: Histogram of the TOF dstribution of $^{133}Cs^{+}$ ions extracted at different times from the TITAN MR-TOF MS. By extracting ions at different times, systematic effects from switching the electrostatic mirrors can be studied. In an ideal case, the TOF distribution would be a delta function.

$N > 700$.

Although the MR-TOF MS is now the spectrometer of choice for extremely low-yield, short-lived isotopes, its aforementioned limitations set a limit in the precision that can be achieved. In order to reach relative precisions below 10^{-7}, the Penning trap mass spectrometer method is preferred.

3.4 Penning Trap Mass Spectrometry

The Penning trap method was conceived and first developed by Hans G. Dehmelt (Nobel prize in Physics 1989) in 1959 [7] to study the magnetic moment of the electron. Since its first conception, the Penning trap has been utilized in a number of different fields to answer a plethora of questions. A non-exhaustive list of modern applications of Penning traps in physics include: ion preparation [232], tests of Quantum Electrodynamics (QED) [33, 251], quantum computing [48], the study of antimatter [11, 20] and mass spectrometry [34]. Penning traps were

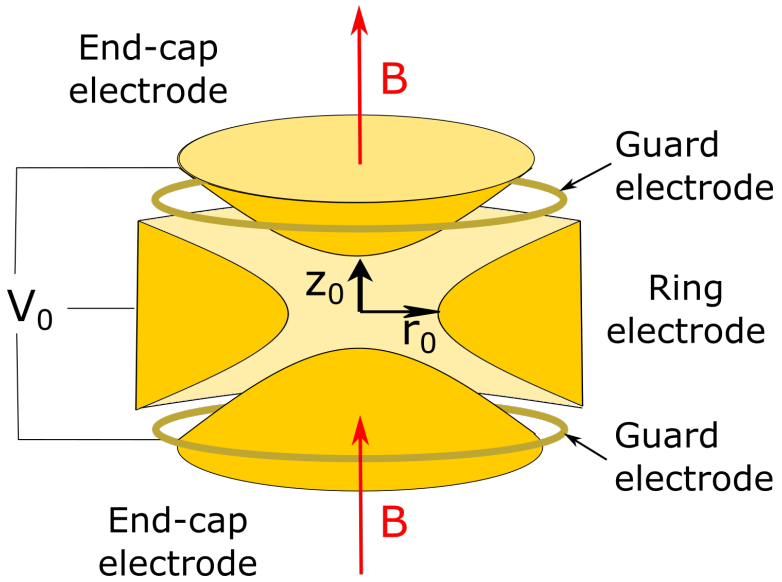

Figure 3.10: Schematic of a hyperbolic Penning trap. The characteristic trap dimensions are indicated.

first introduced as mass spectrometers of rare isotopes in the late 1980s [36] at ISOLTRAP [143]. Today, there are seven systems operational: TITAN [75], CPT [233], LEBIT [225], ISOLTRAP [143], JYFLTRAP [89], SHIPTRAP [74] and TRIGATRAP [140] around the world that use Penning traps for mass spectrometry of rare species while more systems are currently being constructed (as for example the PIPERADE [18] Penning trap at GANIL).

A Penning trap is formed by the combination of a strong magnetic field for radial confinement and a weak quadrupolar electric field for axial confinement. The quadrupolar electric field can be described as [76]:

$$V(r,z) = \frac{V_0}{4d^2}(2z^2 - r^2) \tag{3.9}$$

where V_0 the voltage difference between two neighbouring electrodes that can be seen in Fig. 3.10, and $d = \sqrt{z_0^2/2 + r_0^2/4}$ a characteristic dimension of the trap. The parameters z_0 and r_0 are characteristic of the trap geometry and are shown in Fig. 3.10.

The quadratic potential of Eq. 3.9 can be achieved by two main geometries: a trap with finite hyperboloid electrodes as shown in Fig. 3.10, or a trap with cylindrical electrodes. The first trap geometry has the advantage of creating quadratic potential that requires only minor corrections, and hence can be operated with a total four electrodes. However, the hyperbolic electrodes are challenging to manufacture. On the other hand, cylindrical Penning traps are easy to manufacture but the quadrupolar electric field is significantly more difficult to achieve [34].

A hyperbolic Penning trap usually consists of four main electrodes:

- The Ring electrode that is typically segmented for ion manipulation through excitations. The method is described in the sections below.
- A set of two end-cap electrodes that are responsible for the axial confinement.
- A set of two tube electrodes that allow ions to enter and exit the trap.
- A set of two guard electrodes that are used to optimize the trap potential shape to approach ideal field conditions.

The principle of mass measurements using Penning traps relies on the fact that in the presence of a strong magnetic field, ions revolve with their cyclotron frequency:

$$\nu_c = \frac{qB}{2\pi m} \tag{3.10}$$

where q is the charge of the ion, B is the magnetic field strength and m is the mass of the ion. However, due to the imprecise knowledge of the magnetic field and due to magnetic field fluctuations and variations, the mass of the IOI is determined through the frequency ratio R:

$$R = \frac{m_{IOI}}{m_{ref}} = \frac{\nu_c^{ref}}{\nu_c^{IOI}} \tag{3.11}$$

of the cyclotron frequency of the IOI and that of a different isotope with a well known mass m_{ref}. The measurement of the reference frequency ν_c^{ref} acts as a calibration of the magnetic field strength.

3.4.1 Ion motion in an ideal Penning Trap

Ions that are only trapped by the magnetic field, have a frequency inside the trap that is equal to the cyclotron frequency of Eq. 3.10. However, due to the presence of the quadrupolar electric field, the trapped ion's motion is modified and can be described by three eigenmotions: the reduced cyclotron motion with frequency ν_+, the magnetron motion with frequency ν_- and the axial motion with frequency ν_z:

$$\nu_\pm = \frac{\nu_c}{2} \pm \frac{\nu_c}{2}\sqrt{1-2\left(\frac{\nu_z}{\nu_c}\right)^2} \tag{3.12}$$

$$\nu_z = \frac{1}{2\pi}\sqrt{\frac{qV_0}{md^2}} \tag{3.13}$$

provided that the confinement condition:

$$1-2\left(\frac{\nu_z}{\nu_c}\right)^2 > 0 \tag{3.14}$$

is satisfied.

The resulting motion from the superposition of the three eigenmotions can be seen in Fig. 3.11, where the slow radial motion corresponds to ν_-, the fast radial motion corresponds to ν_+ and the axial motion corresponds to ν_z.

The three eigenfrequencies follow the Brown-Gabrielse theorem [46] according to which:

$$\nu_c^2 = \nu_+^2 + \nu_-^2 + \nu_z^2 \tag{3.15}$$

with,

$$\nu_+ >> \nu_z >> \nu_- \tag{3.16}$$

From Eq. 3.12, the cyclotron frequency can expressed as [46]:

$$\nu_c = \nu_+ + \nu_- \tag{3.17}$$

a property widely used across Penning trap experiments to determine the true cyclotron frequency from the reduced cyclotron and magnetron frequencies.

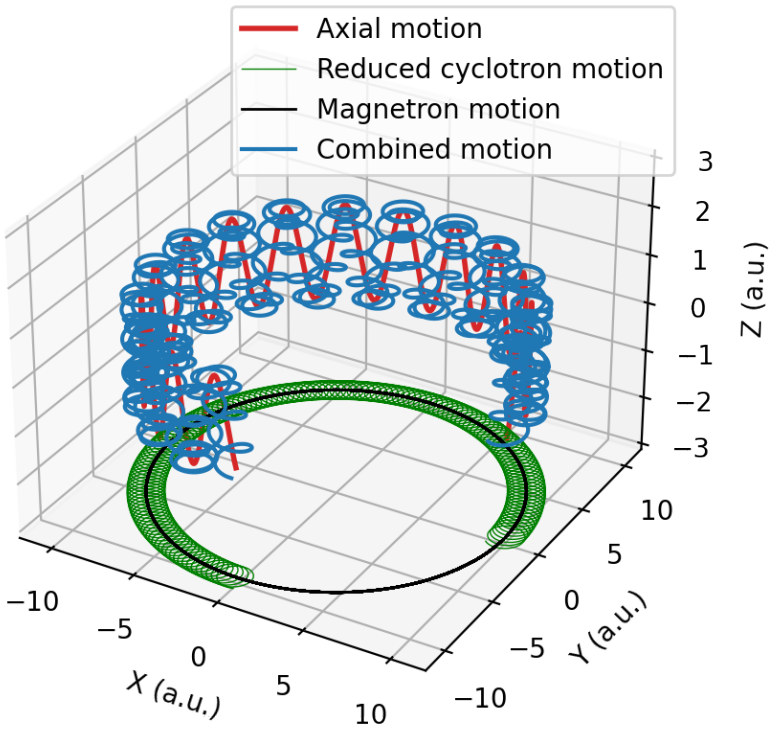

Figure 3.11: Shown is the simulation of the motion in the Penning trap. Each eigenmotion is depicted by a different color, while their superposition is shown in blue.

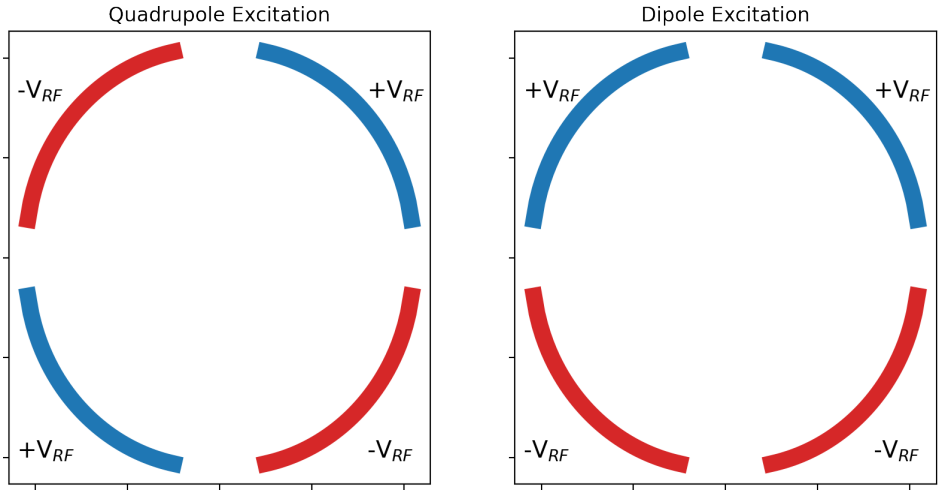

Figure 3.12: Schematic of the applied voltages in a quadrupole (left) and dipole (right) excitation, shown in colour is the polarity of applied voltages.

3.4.2 Ion manipulation

In order to measure the cyclotron frequency of an ion stored in a Penning trap, it is necessary to manipulate the stored ion, including its radius and eigenfrequency. Controlling these properties is achieved by Radio-Frequency Dipole, Quadrupole and higher-order pulses applied to the segmented trap electrodes, some of which can be seen in Fig. 3.12.

Dipole pulses

The simplest pulse that is applied for ion manipulation is a single square dipole pulse of duration T_{dip}. The applied RF field is of the form:

$$u_{RF}(t) = V_{RF} sin(\omega t + \phi) \tag{3.18}$$

where V_{RF} is the RF voltage amplitude, $\omega = \omega_{\pm}$ and $\phi = 0, \pi$, as can be seen in Fig. 3.12 (right).

The result of a dipole pulse at $\omega_{RF} = \omega_{\pm}$ is a resonant increase of the ion's

radius and kinetic energy [261]:

$$r = \frac{C_{1,\rho} V_{RF} T_{dip}}{Bd} \tag{3.19}$$

where $C_{1,\rho}$ is a geometry parameter [261].

In Penning trap mass spectrometry, dipole pulses serve a number of purposes. They can be used to prepare the ion in a pure magnetron r_- or reduced cyclotron r_+ radius or they can be used to selectively drive unwanted contaminants away from the trap centre, ultimately driving them into the confining electrode where they are lost. This process is referred to as dipole cleaning [153].

Quadrupole pulses

Quadrupole pulses constitute an essential element of of Penning trap mass spectrometry. A Rabi quadrupole excitation consists of a single square pulse of duration T_{quad}, as can be seen in Fig. 3.13 (top). The difference from the dipole pulse is that opposite segments of the ring electrode are supplied with an RF of the same phase as can be seen in Fig 3.12 (left).

The amplitudes of the reduced cyclotron (r_+) and the magnetron motion (r_-) during a quadrupole excitation are described by [156]:

$$r_\pm(t) = \left(r_\pm^0 cos(\omega_B t) \mp \frac{1}{2} \frac{r_\pm^0 [i(\omega_{RF} - \omega_c)] r_\mp^0 k_0^\pm}{\omega_B} sin(\omega_B t) \right) e^{i/2(\omega_{RF} - \omega_c)t} \tag{3.20}$$

where $r_\pm^0$ are the initial reduced cyclotron and magnetron radii, ω_{RF} is the applied RF frequency,

$$\omega_B = \frac{1}{2} \sqrt{(\omega_{RF} - \omega_c)^2 + k_0^2} \tag{3.21}$$

and

$$k_0 \simeq \frac{V_{RF}}{2d^2} \frac{q}{m} \frac{1}{\omega_+ - \omega_-} \tag{3.22}$$

If $\omega_{RF} = \omega_c$, Eq. 3.20 simplifies to:

$$r_\pm(t) = r_\pm^0 cos\left(\frac{k_0}{2} t\right) \mp r_\mp^0 e^{i\Delta\phi} sin\left(\frac{k_0}{2} t\right) \tag{3.23}$$

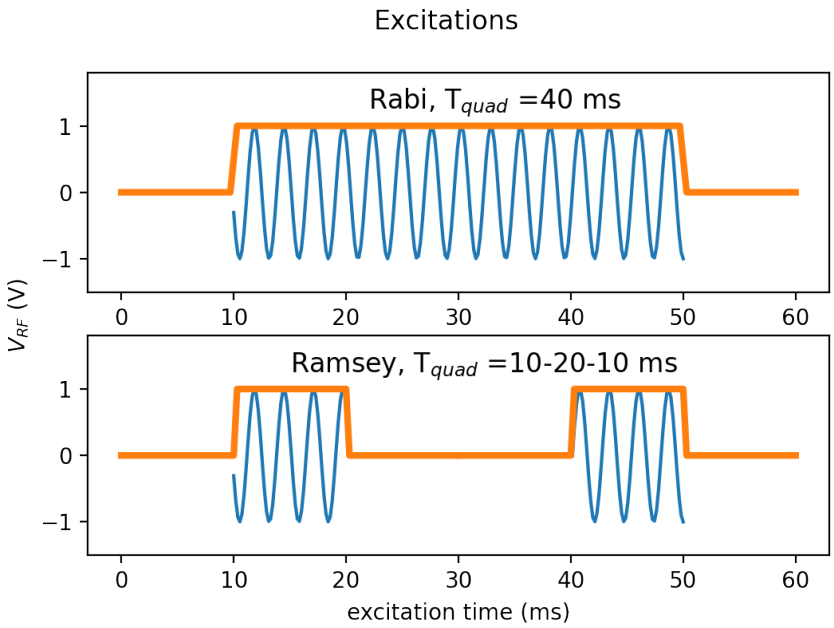

Figure 3.13: Schematic of the excitation pulses applied during a Quadrupole Rabi (single-pulse) [156] excitation (top) and a Ramsey (double-pulse) [213] excitation (bottom).

where $\Delta\phi$ corresponds to the phase difference:

$$\Delta\phi = \phi_{RF} - (\phi_+ + \phi_-) \tag{3.24}$$

Eq. 3.23 results in a beat pattern between the magnetron and the reduced cyclotron motion with period T_{quad}. One full conversion from magnetron to reduced cyclotron frequency occurs for:

$$\frac{k_0}{2} T_{quad} = \frac{\pi}{2} \rightarrow T_{quad} = \frac{\pi}{k_0} = \frac{2\pi m d^2}{q V_{RF}} (\omega_+ - \omega_-) \simeq \frac{2d^2 B\pi}{V_{RF}} \tag{3.25}$$

and it is independent of the type of trapped ion. Eq. 3.25 determines the excitation time required for a successful conversion if $\omega_{RF} = \omega_c$ and for a predefined V_{RF}.

Due to the fact that $\omega_+ >> \omega_-$, a full conversion of an ion in the magnetron motion ($r_-^0 \neq 0$, $r_+^0 = 0$) to an ion in the reduced cyclotron motion significantly

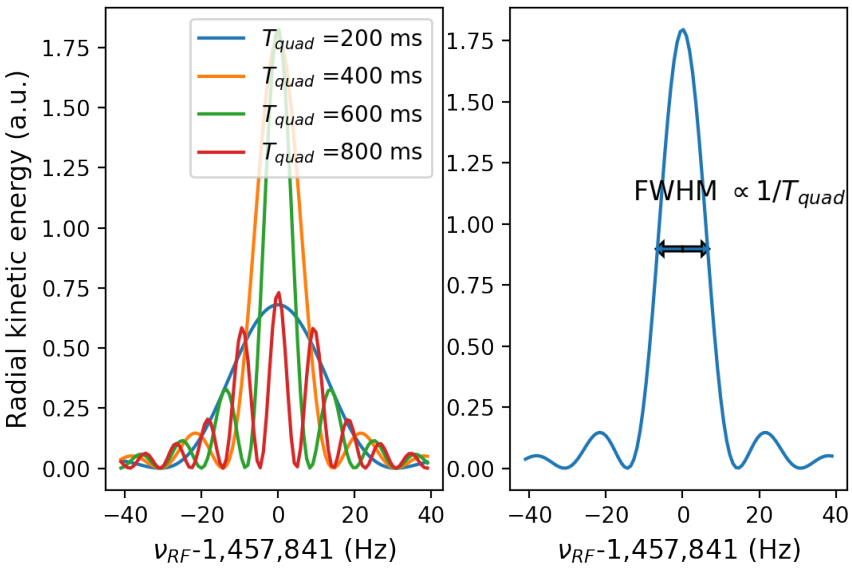

Figure 3.14: Left: Calculation of the radial kinetic energy of $^{39}K^{+}$ ions for different conversion times. Right: The radial kinetic energy profile for one full conversion and the dependence of the FWHM of the central maximum to the excitation time T_{quad}.

increases the ion's radial kinetic energy:

$$E_r \propto \omega_+^2 r_+^2 = \frac{\omega_+^2 k_0^2}{4} \frac{sin^2(\omega_B t)}{\omega_B^2} \tag{3.26}$$

if $\omega_{RF} = \omega_c$, as can be seen in Fig. 3.14 (right). Fig 3.14 (left) also shows the radial kinetic energy lineshape for excitation times that do not correspond to a full conversion. The blue line shows an underconverted resonance while the rest show examples of overconverted resonances.

Therefore, an unknown cyclotron frequency (and hence mass), can be precisely determined by determining the RF frequency at which a full conversion between the two eigenfrequencies takes place.

The precision of the frequency measurement is proportional to the FWHM of the central fringe of the lineshape, which is inversely proportional to the excitation

time T_{quad}, as can be seen in Fig. 3.14 (right). This proportionality between the FWHM and T_{quad} comes from the Fourier transform of the applied RF pulse and would approximate a delta function for an infinite pulse. Consequently, the longer the quadrupolar excitation the better the precision and resolving power. However, extending the duration of the excitation of the measurement can be difficult for multiple reasons, some of which are:

- Poor vacuum conditions in the trapping region.
- Short half-life of the trapped ion.
- Stability of electrostatic system.

The next two sections describe alternative techniques that have been developed and are used to improve the results of the traditional quadrupole excitations.

Ramsey pulses

Ramsey excitation schemes were first developed in magnetic resonance experiments in 1949 [213, 214]. Prior to this development, the standard method was a Rabi-type approach [211] to expose the ions to two superimposed magnetic fields that are present in the same volume of space. In Ramsey type measurements, ions are exposed to a sequence of different magnetic field configurations with a well-defined phase relation [152].

In 1992, the Ramsey technique was applied in mass spectroscopy [37] where the idea of the spatial sequence of magnetic fields is transformed into a time sequence of quadrupole pulses at the cyclotron frequency, as can be seen in Fig. 3.13 (bottom). In mass spectrometry, Ramsey excitations offer a reduction of $\sim 30\%$ to the FWHM of the central fringe [76] of Fig. 3.14, thus improving the precision and resolving power of Penning trap spectrometers. However, Ramsey pulses have not fully replaced Rabi ones due to the sometimes ambiguous position of the central minimum. As a result, they usually follow an initial Rabi-type measurement.

Octupole pulses

Higher order excitations are proven to be beneficial for certain mass measurements. The LEBIT [222] and SHIPTRAP [74] mass spectrometers have investi-

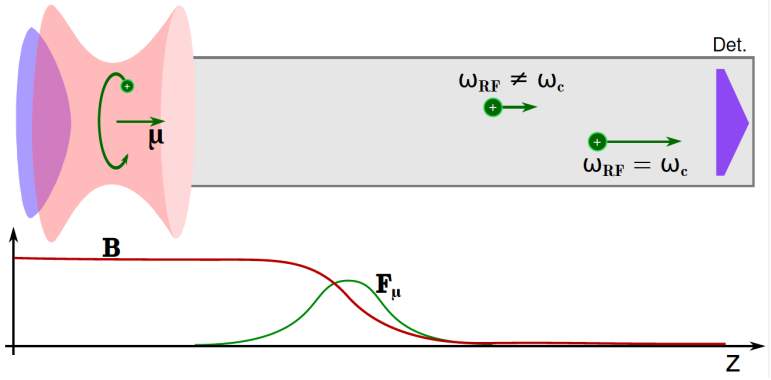

Figure 3.15: Schematic of the principle of the TOF-ICR technique. Due to the magnetic moment of the ions and the magnetic field gradient, resonant ions experience a larger axial force. Figure taken from [163].

gated the use of octupole pulses instead of quadrupole pulses and they both agree in a ten-fold increase in resolving power [84, 224]. However, unlike in the case of quadrupole pulses, the conversion frequency shows a strong dependence on the initial conditions of the ion motion [224] thus making the technique more susceptible to systematic errors, or requiring more preparation time for the ions to be well localized.

3.4.3 Detection techniques

Mass measurements in Penning traps rely either on the measurement of the true cyclotron frequency, or the measurement of the individual eigenfrequencies. The three main methods for determining the frequency in on-line mass spectrometry are described below.

Time-of-Flight Ion-Cyclotron-Resonance technique

The Time-of-Flight Ion-Cyclotron Resonance (TOF-ICR) technique [156] is a scanning approach which requires repeated measurements under constant conditions and relies on detecting the radial kinetic energy of the ions as a function of the applied RF frequency as was shown in Fig. 3.14.

After a full conversion of the ion motion from ν_- to ν_+ using a quadrupole

excitation, the voltage of the trap's extraction end-cap is lowered and the ions are accelerated out of the trap towards a particle detector, as can be see in the schematic of Fig. 3.15. As they travel towards the detector, they experience the gradual decrease of the magnetic field (see Fig. 3.15, lower graph). The magnetic field gradient interacts with the ion's magnetic moment resulting in an axial force

$$\vec{F} = -\vec{\mu}\nabla\vec{B} = \frac{E_r(\omega_{rf})}{B}\hat{z}\cdot\nabla\vec{B} \tag{3.27}$$

which results in an increase of the axial energy of the ions and a reduction in the TOF of the ions between the trap and the detector.

The detected TOF depends on the applied RF frequency, and can be described and fitted by [156]

$$ToF = \int_{z_0}^{z_f} \Big(\frac{m}{2(E_0 - qV(z) - \vec{\mu}(\omega_{RF})\cdot\vec{B})}\Big)^{1/2} dz \tag{3.28}$$

where E_0 is the total initial energy of the ion and $V(z)$ and $B(z)$ are the voltage and magnetic field experienced by the ion from the trap (z_0) to the detector (z_f). An example of a TOF resonance fitted with Eq. 3.28 can be seen in Fig. 3.16.

The precision of a mass measurement performed using TOF-ICR with Rabi or Ramsey pulses is given by [37, 156]:

$$\frac{\delta m}{m} = C\frac{m}{qBT_{quad}\sqrt{N}} \tag{3.29}$$

where the proportionality constant C depends on the excitation scheme used. Although C depends heavily on the quality of the resonance, a simple comparison between Ramsey and Rabi excitations performed for ^{76}Rb with Measurement Penning Trap (MPET) [90], results in $C_{Rabi} = 27$ and $C_{Ramsey} = 8$.

Despite being very robust, the TOF-ICR technique suffers from a number of disadvantages. First of all, it is a scanning technique, and thus a large number of off-resonance ions (50:1 off- to on- resonance ions) need to be detected in order to construct a TOF resonance. Although this is not a concern for stable isotopes, it constitutes a potential problem for experiments with radioactive species from RIB facilities. In addition, as mentioned before, the precision and resolving power

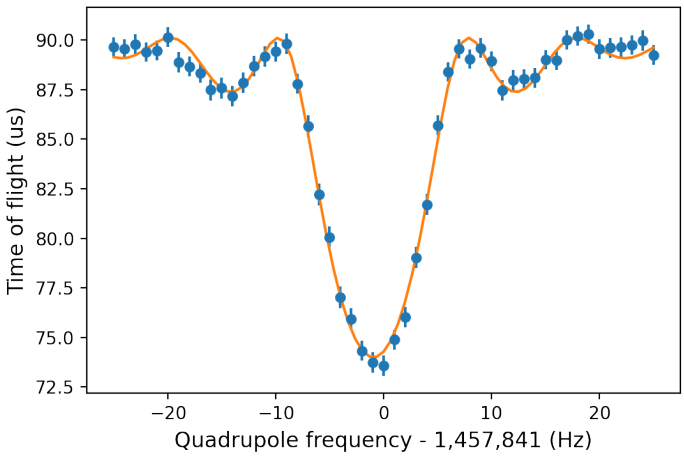

Figure 3.16: TOF-ICR resonance of $^{39}K^{+}$ ions, excited with a t = 100 ms quadrupole excitation pulse. The orange line indicates a fit to the experimental data using Eq. 7.7.

of TOF-ICR is limited by the length of the excitation time applied, which itself is limited by the isotope's half-life and the storage conditions in the trap, typically connected to the vacuum, since collisions and charge exchange with background molecules negatively affect the resonance shape. The following two techniques are developed to overcome the need for high statistics in TOF-ICR, showing advantages to TOF-ICR under certain circumstances.

Phase-Imaging Ion-Cyclotron-Resonance

The Phase-Imaging Ion-Cyclotron Resonance (PI-ICR) technique is an alternative to the TOF-ICR technique and it was first developed by SHIPTRAP [85].

In PI-ICR, the cyclotron frequency of the trapped ions is measured by projecting the ion motion on a position sensitive charged particle detector located outside the strong magnetic field. The measurement starts by injecting the ions at the center of the Penning trap, where the center location has been previously determined. The ions are excited to a radius with a dipole pulse at either the magnetron or the reduced cyclotron eigenfrequency. After a well-defined time of free evolution at that particular frequency, the ions are extracted and their position is recorded. An

example of the projected images on the position sensitive detector can be seen in Fig. 3.17. From the corresponding phase ϕ between the location created by ions at the magnetron frequency and those at the reduced cyclotron frequency, the true cyclotron frequency can be calculated as follows [86]:

$$\nu_c = \nu_+ + \nu_- = \frac{\phi + 2\pi(n_+ + n_-)}{2\pi t_{acc}} \tag{3.30}$$

where t_{acc} is the time of free evolution in the trap and $n_\pm$ is the number of full revolutions of the ions in the reduced cyclotron and magnetron motions respectively.

The resolving power of the PI-ICR technique is given by:

$$R_{PI-ICR} = \frac{\nu_c}{\Delta\nu_c} \simeq \frac{\nu_+}{\Delta\nu_+} = \frac{\pi\nu_+ t_{acc} r_+}{\Delta r_+} \tag{3.31}$$

where r_+ the radius of the reduced cyclotron motion and Δr_+, one standard deviation of the spacial ion distribution for the ions at the reduced cyclotron motion.

The PI-ICR technique offers a factor of 40 better resolving power and a factor five better precision compared to TOF-ICR for singly charged ions [85]. In addition, it reduces the time required for a measurement since scanning of RF frequencies is no longer required, thus lowering the necessary number of detected ions. This offers an efficient use of rare isotopes and is less susceptible to temporal fluctuations of the experimental conditions.

However, the PI-ICR technique has higher demands for alignment between the magnetic field axis and the trap axis [197] and for more stable trap voltages [86, 197]. For example Orford et al. [197] report a 30^{o} shift in the reference phase due to a 1 mV drift over the course of a 24 hours. The technique also requires a more complicated detection apparatus in order to record the position of the ions which is more expensive. Today, more and more mass measurement Penning trap experiments are contributing to further development and advancement of this technique [86, 136, 189, 197].

Fourier-Transform Ion-Cyclotron-Resonance technique

The TOF-ICR and PI-ICR techniques allow relative precisions of up to few 10^{-9}. In many cases, as for example tests of QED [251], a higher relative precision is

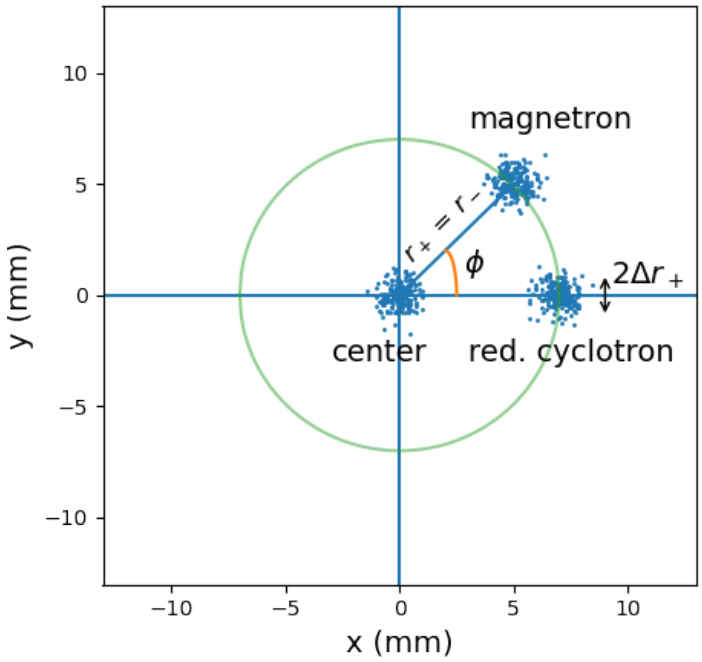

Figure 3.17: PI-ICR schematic. The groups of scattered points represent ion spots with positions (x_i, y_i). Ion spots after no excitation (center), magnetron excitation (magnetron) and reduced cyclotron excitation (red. cyclotron) are shown. The cyclotron frequency is determined from the phase between the latter two spots, while its uncertainty is determined from the radius of excitation (represented with the green line) and the position spread ($2\Delta r_+$) of the ion spots.

required. The technique of choice to reach a precision of 10^{-10} is the Fourier-Transform Ion-Cyclotron Resonance (FT-ICR) technique [76]. The FT-ICR technique is not destructive, allowing the ions eigenfrequencies to be probed continuously while the ion is confined. This is achieved by coupling one of the trap electrodes to an LC circuit with a resonant frequency similar to the storage frequency of the trapped ions, as can be seen in Fig. 3.18 (top).

The ion signal appears as a reduction to the LC circuit's noise signal (Fig. 3.18

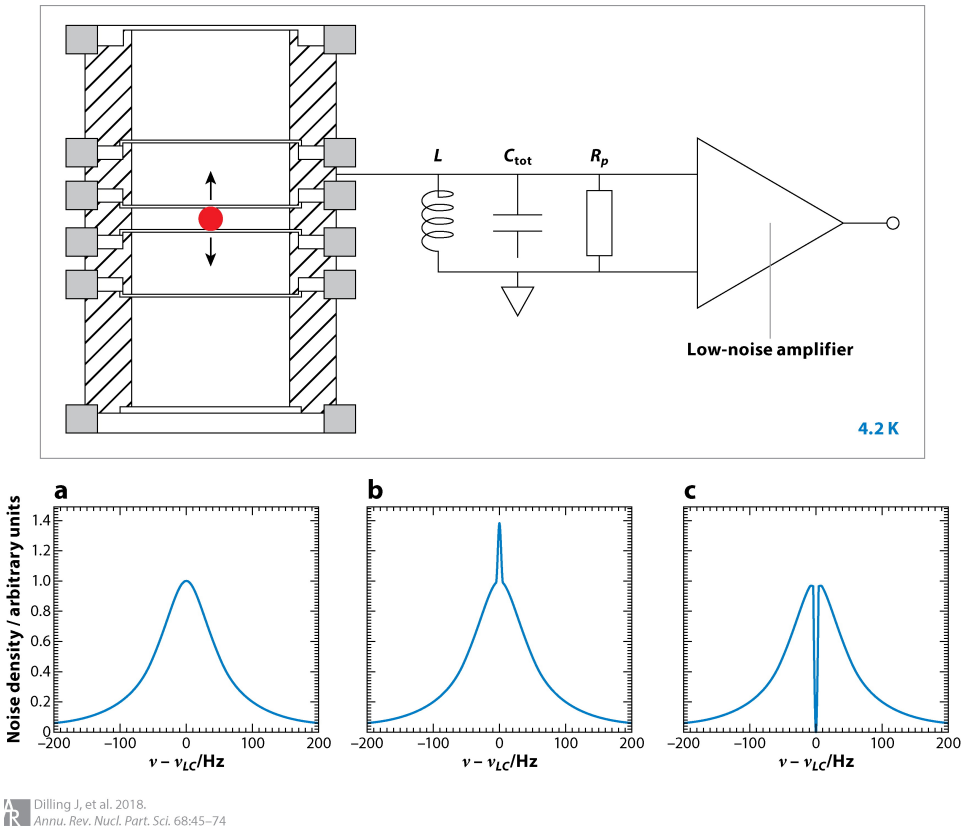

Figure 3.18: Top: FT-ICR schematic. Bottom: a) Noise spectrum of the resonant circuit without ions stored in the trap. b) Noise spectrum superimposed with the signal from a non-resonant trapped ion. c) Noise spectrum superimposed with the signal from a resonant ion. Figure taken from [76].

(c)). The signal to noise ratio (S/N) is determined by [126]:

$$S/N \sim Nq\frac{\rho}{\rho_0}\sqrt{\frac{\nu}{\Delta\nu}}\sqrt{\frac{Q}{kTC}} \tag{3.32}$$

where N is the number of ions, q is the charge state ρ/ρ_0 is the radius of the ions' orbit relative to the trap radius, $\nu/\Delta\nu$ is the ratio of the ions frequency and the spectral width, $Q = R\sqrt{C/L}$ is the quality factor, T is the temperature and C is the capacitance of the circuit.

In order to achieve a significant signal-to-noise ratio, the ambient noise needs to be low. This is achieved by cooling both the electrodes and the circuit, typically by immersing them in liquid helium and by using a circuit with a high quality factor. In addition, in order to further improve the signal the ions can be prepared in higher charge states ($q > 1$).

Although the FT-ICR technique offers a great advantage, a number of challenges need to be addressed. One of the most significant challenges is that it is limited to long-lived ions, as its resolving power scales with the storage time (Fourier limited) and therefore the ion's half-life, making the technique uncommon in rare isotope studies (with an exception being the Single ion Penning Trap [113]). In addition, the high quality factor circuits that are used in order to reduce the noise, result in a narrow-band spectrum which reduces the range of ion frequencies at which the circuit is sensitive to. As a result each isotope requires a custom circuit making the technique inflexible and in general not applicable for studies of different species.

3.4.4 Ion motion in a realistic Penning Trap

An ideal trap assumes infinite hyperbolic surfaces without imperfections as well as absolute vacuum. A real existing Penning trap cannot be constructed using infinite or perfectly hyperbolic electrodes and cannot trap ions in absolute vaccum. In addition, there can be misalignments between the magnetic field axis and the trap axis [197] and magnetic non-uniformities [45]. All these effects distinguish a real Penning trap from the description of a theoretical Penning trap and modify the motion of the trapped ion. The corresponding aspects of the real Penning trap, relevant to measurements, systematic effects and mitigation, are described in detail below.

Finite hyperbolic electrodes and geometry imperfections

Due to the finite size of the hyperbolic electrodes and the holes in the end-cap electrodes, necessary for injection and extraction of ions, the resulting electrostatic potential includes non-quadratic, higher-order terms, such as octupole and dode-

capole contributions [45]:

$$V_4(r,z) = C_4\Big(\frac{V_0}{2d^4}\Big)[z^4 - 3z^2r^2 + \frac{3}{8}r^4] \tag{3.33}$$

$$V_6(r,z) = C_6\Big(\frac{V_0}{2d^6}\Big)[z^6 - \frac{15}{2}z^4r^2 + \frac{45}{8}z^2r^4 - \frac{5}{16}r^6] \tag{3.34}$$

These non-harmonic terms induce shifts in the ion's frequencies thus resulting in systematic uncertainties.

The contribution of non-quadratic terms can be minimized with the use of "correction" electrodes. In the system used at TITAN, these are the Guard electrodes and the Tube electrodes. A procedure has been developed to optimize the effectiveness and is called "Trap compensation" [44]. It is performed to empirically determine the optimal settings for these correction electrodes. There are two steps to achieve it. The first step is dipole compensation [28] where the reduced cyclotron frequency is measured for different amplitudes of axial oscillations. The axial oscillations in the trap depend on the ion's axial kinetic energy and their amplitude can be controlled with the time at which the trap closes to trap the ions (capture time) as can be seen in Fig 3.19. If the ions are not in the center of the trap when the voltages of the trap switch from the open to the closed configuration, the ions experience a voltage gradient that increases their axial energy.

The optimal potentials, in terms of dipole compensation, are achieved when the shift in the reduced cyclotron frequency is minimal for different capture times. Fig 3.20 shows an example of the reduced cyclotron frequency shift for different capture times and different correction voltages. Each voltage setting is fitted with a quadratic function $y = \alpha t^2 + \beta t + \gamma$, where t is the capture time and α, β, γ are fit parameters. The set of quadratic parameters $[\alpha_i, \alpha_{i=1}, ..]$ derived from different voltage settings can be linearly fitted and the optimal guard or tube voltage is found by solving the linear equation for $\alpha = 0$. This method results in a set of optimal values instead of a single optimal value as was shown in [45].

In order to determine the optimal V_{guard} and V_{tube}, a second step is needed [45]. This requires the measurement of the true cyclotron frequency for different conversion times of a quadrupole resonance. Here, the position of the centroid of the quadrupole resonance is measured for different Tube and Guard voltages.

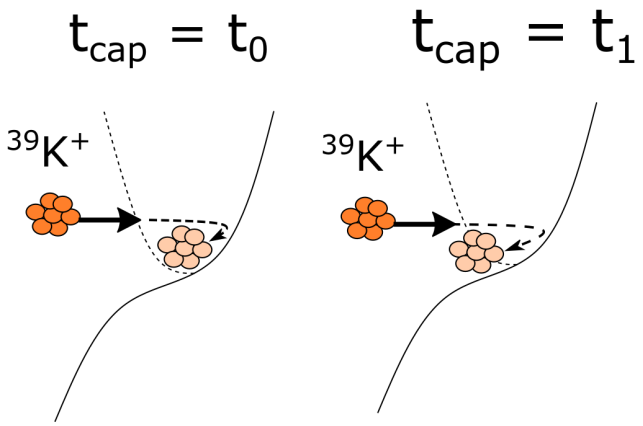

Figure 3.19: Schematic of description of axial oscillations due to imperfect trapping. Left: The injection end-cap voltage rises when the ions are at the center of the trap thus the ions are not experience the voltage switch. Right: The injection end-cap voltage rises when the ions are decentralized and closer to the injection side of the trap. The ions sense the voltage gradient, which results in an increase of their axial energy. The excess axial energy causes the ions to axially oscillate while trapped.

Similarly, the optimal settings are found when the shift in cyclotron frequency is minimal for different conversion times. The result is also a set of optimal V_{guard} and V_{tube}. Now, by taking the intersection of the sets determined with the two methods, the optimal V_{guard} and V_{tube} is identified.

Real vacuum conditions

In the theoretical Penning trap, radioactive ions can be stored for as long as their nuclear lifetime allows without any disturbance. However, that requires one particle to be stored in the absence of any other particles in the trap, charged or neutral. However, real traps are affected by the existing vacuum conditions, and hence the residual gases that are not removed out of the trap volume and molecules outgassing from the trap surfaces.

These molecules interact with the trapped ions and when the Coulomb interaction between the electrons of the molecule and the trapped ion, which scales with

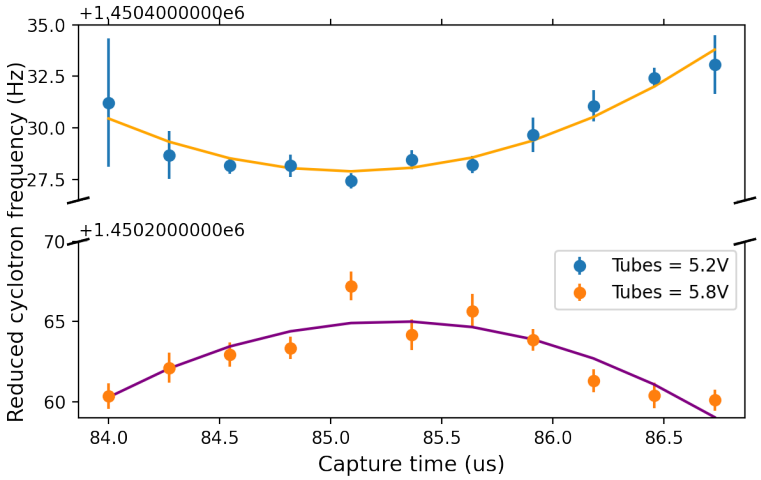

Figure 3.20: Reduced cyclotron frequency variation for different capture times and for two different voltage values of the Tube electrodes in the TITAN Penning Trap. The tube voltages that are displayed in the legend are amplified by a 20x-amplifier before being applied to the trap electrodes. The ions trapped and excited are $^{39}K^{+}$ ions.

the charged state of the trapped ion, becomes larger than the binding energy of those electrons, charge exchange between the molecule and the ion takes place. This is typically detrimental since ions of different charge states have significantly different cyclotron frequencies and therefore cannot be used for a single coherent mass measurement.

Collisions with background gas atoms or molecules have primarily the effect of disturbing the ion trajectories and reducing the energy of the ions. This can be seen in the simulation results depicted in Fig. 3.21 by the increase in the TOF (blue histogram) when increasing the collision rate. This effect is usually called damping as it reduces the ion motion, similar to the cooling process employed in the RF cooler trap. In the TOF-ICR technique, this effect is reflected in the data-analysis in the form of a damping force $\vec{F} = -\delta m\vec{u}$ [156], with

$$\delta = \frac{q}{m}\frac{1}{M_{ion}}\frac{p/p_N}{T/T_N} \tag{3.35}$$

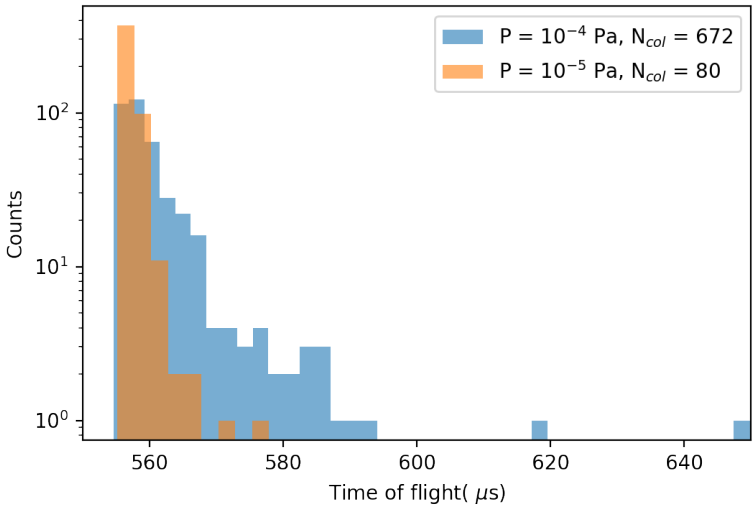

Figure 3.21: SIMION simulated TOF distribution for ions trapped under different pressures. The pressure and the number of collisions are displayed in the legend. The storage time of the ions is 500μs.

where M_{ion} is the reduced ion mobility, m is the mass of the trapped ion, p is the pressure in the trap, T is the temperature of the background gas and p_N, T_N are the normal pressure and temperature. At TITAN the typical background composition in the Penning trap is dominated by N_2, H_2, H_2O and CO_2. This is described in detail in Chapter 7.

In order to minimize the effects of non-ideal vacuum, ion traps operate under Ultra High Vacuum (UHV) conditions ($P < 10^{-7}$ Torr) and are manufactured from materials that have low outgassing rates (mainly metals and ceramics with outgassing rates smaller than 10^{-7} mbarns^{-1}cm^{-2}/h [158]). For further reduction of background gas molecules, the system can be operated at lower temperatures as demonstrated in Chapter 7.

Other aspects of the real Penning trap

The material out of which Penning traps are constructed also requires significant consideration. The material requirements for Penning trap electrodes include

being non magnetic, in order to not affect the uniformity of the magnetic field which would result in systematic errors in the determination of the ions' cyclotron frequency. The material used for our system is Oxygen Free High Purity Copper (OFHPC) [222]. We use copper because it is non-magnetic and we choose oxygen-free copper instead of regular copper because the lack of oxygen reduces the oxidation rate of the copper and because it results in better thermal conductivity [163]. However, the copper on the surface of the trap can still oxidize, by forming ionic bonds with oxygen molecules that have not been pumped out of the vacuum system. This is problematic as copper oxides are not electrical conductors and therefore they can accumulate charge as they are insulated from the biased trap electrode [116]. These charged areas that are created as a result of copper oxidation are known as "patch effects" and can compromise the shape of the electric field [116] that the trapped ions are exposed to. In order to prevent such effects, the Penning trap electrodes are gold plated due to gold's higher ionization energy that results in a smaller reaction rate with oxygen. Moreover, gold plating achieves high thickness and uniformity in the application process, maintaining the original geometry of the electrodes. The gold plated TITAN Penning trap system can be seen in Fig. 3.22.

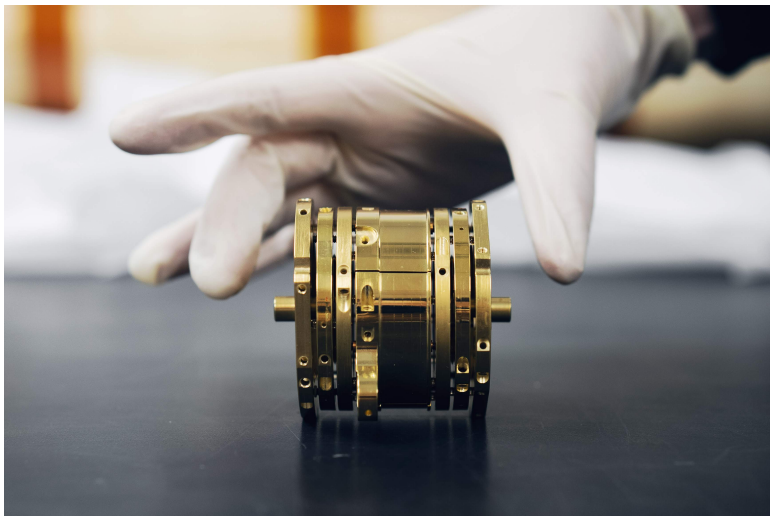

Figure 3.22: The TITAN Measurement Penning Trap is made of OFHP copper and it is coated with a thin silver and gold layer to prevent oxidation.

Chapter 4

The TITAN experimental setup

TRIUMF's Ion Trap for Atomic and Nuclear science (TITAN) [75] (Fig. 4.1) is one of eight trap-based mass measurement experiments for short-lived nuclei operating worldwide[1]. Similarly to other facilities, TITAN uses a series of ion traps to prepare the ions before the final mass measurement. These preparation systems include a Radio-Frequency Quadrupole trap, a Multi-Reflection Time-of-Flight Mass Separator/Spectrometer and a Measurement Penning Trap. Uniquely from all other online mass experiments, the TITAN experiment also utilizes an Electron Beam Ion Trap for charge breeding of ions. Charge breeding is used to boost the precision of Penning trap mass measurements [90] and for decay-spectroscopy experiments [162].

This chapter focuses on the ion traps constituting TITAN and how their operation can be combined to provide high-precision mass measurements of low-yield, short-lived ions.

4.1 ISAC at TRIUMF

TITAN is located at the Isotope Separator and Accelerator (ISAC) Hall [25] at TRIUMF. ISAC is a RIB facility based on a proton beam with up to 520 MeV energy and up to 100 μA of current [40], from the TRIUMF 520 MeV cyclotron [65].

[1] The other seven are: LEBIT [222] at FRIB, Big-RIPS [237] at RIKEN, ISOLDE [143] at CERN, SHIPTRAP [74] at GSI, FRS [205] at GSI, TRIGATRAP at Mainz [111] and JYFLTRAP [148] at the University of Jyvaskyla.

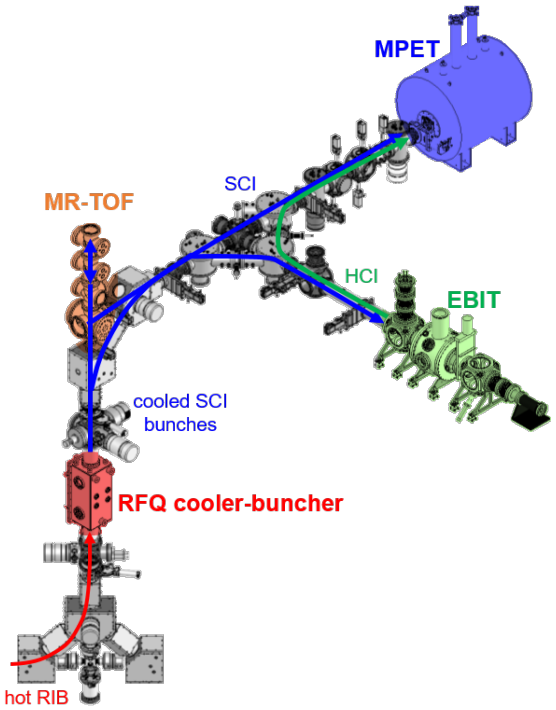

Figure 4.1: The TITAN experimental apparatus. Indicated in color are the different ion traps. The lines and arrows along the beamline indicate the path of Singly Charged (SCI) and Highly Charged Ions (HCI).

In the ISAC target stations [40] the proton beam impinges on an ISOL target [43], which can be made of different materials, with two of the most common ones being Ta and U. Spallation, fragmentation and fission reactions are induced by the protons, resulting in the production of a number of stable and radioactive species. Fig. 4.2 shows the measured production yields of elements produced using UC_x targets (top) and Ta targets (bottom) with a variety of ion sources, in units of particles-per-second. The high production rate of proton-rich heavy isotopes ($Z \geq 70$) shown in Fig. 4.2 is a result of the spallation reactions which remove either protons or neutrons from the nucleus. For heavy-Z target materials, such as Ta and U, the number of neutrons is much larger than the number of protons and therefore it is more likely that neutrons will be emitted, creating, as a result proton-rich nuclei.

The simplest way to ionize the reaction products is by heating the target to a

temperature ($T_{target} \approx 2000^{o}$C) which facilitates thermal field ionization. In addition, these conditions speed up diffusion of the reaction products in the target and leads to ionization of chemical elements with low ionization energies (such as alkali metals). Ionization of elements with higher ionization potential (for example noble gases) is achieved with the use of a Forced Electron-Beam-Induced Arc Discharge (FEBIAD) source [41]. Element-selective ionization can be achieved using laser ionization techniques, for example with TRIUMF's Resonant Ionization Laser Ion Source (TRILIS) [170].

Once ionized, the ions are accelerated electrostatically to an energy of 20 keV. This process results in a beam cocktail containing a number of species. The most common species are surface-ionized alcali metals as well as molecules such as certain fluorides (for example SrF) that have low ionization energies [139, 141]. The contamination rates and variety increases when using ion sources capable of ionizing species with higher ionization potentials ($E_{ionization} = 5 - 7$ eV), such as the FEBIAD ion source [41]. In order to separate the ion of interest from contaminant ions, ISAC utilizes a dipole separator magnet [42] that separates ions based on their mass to charge ratio (m/q) as can be seen in the schematic of Fig. 4.3. The ISAC mass separator has a resolving power of [42]:

$$R = \frac{m}{\Delta m} \approx 2,000 \tag{4.1}$$

capable of generating overall isobarically pure beams. As can be seen from Eq. 4.1, the separation is more effective for lower mass numbers, as $\Delta m = m/2000$, thus offering better beam purity but also requiring better optimization of the magnet settings, so that the IOI is not "cut" by the magnet.

After separation using the dipole magnet, the radioactive beam from ISAC is delivered to low-energy experiments, such as TITAN, or it is re-accelerated for reaction studies in ISAC-II [25].

4.2 TITAN Radio-Frequency Quadrupole

The first unit within the TITAN experiment, which receives the mass separated beam is the TITAN RFQ. The TITAN RFQ [47] is a linear Paul trap that is used to cool and bunch the continuous radioactive beam from ISAC.

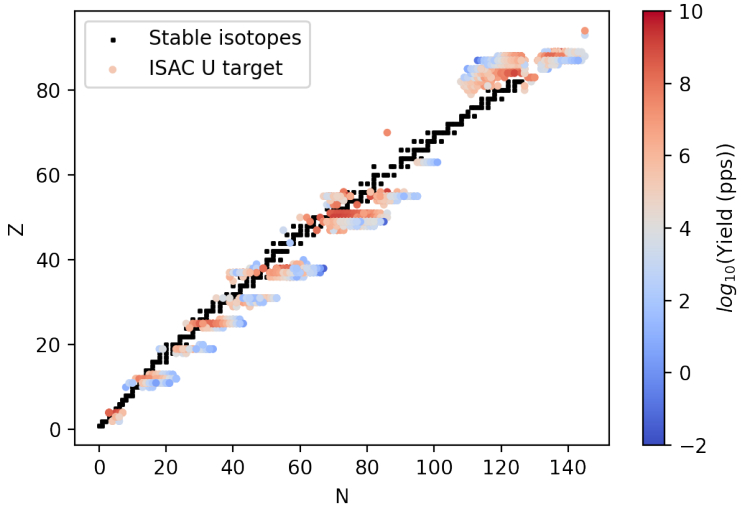

(a) Measured yields for Uranium Carbide ISAC targets

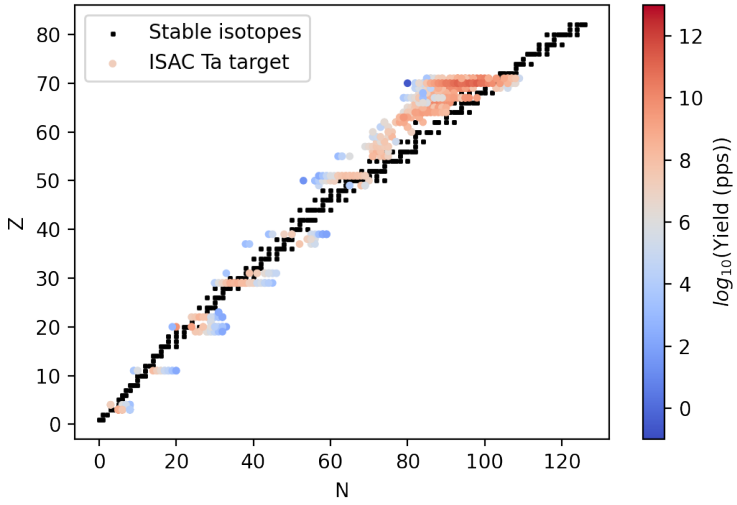

(b) Measured yields for Tantalum ISAC targets

Figure 4.2: Yields of isotopes produced at ISAC for different target materials. Yield data taken from: [1].

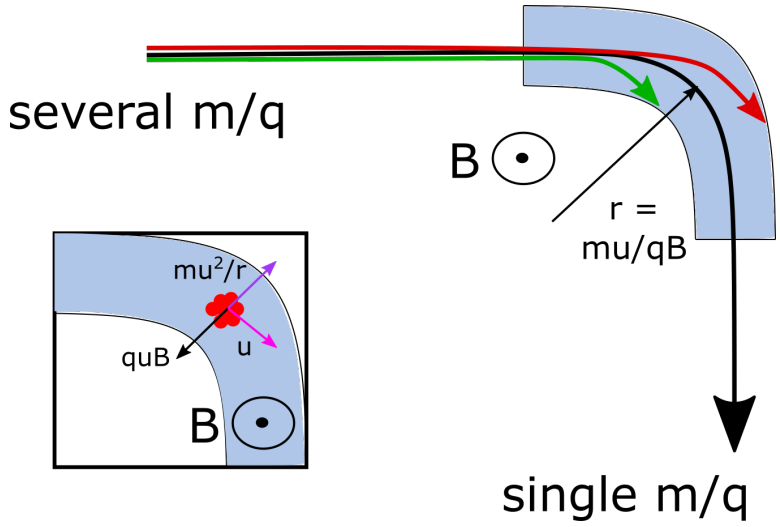

Figure 4.3: Schematic of a dipole separator magnet. The field strength is selected so that only species with a unique m/q are transported though. The inset shows the forces that an ion experiences in the dipole mass separator.

The shape of the voltage of the RFQ electrodes, shown in Fig. 4.4, along with collisions with the helium buffer gas, allow the confinement of ions into well-localized groups (FWHM $\approx$ 50 [47]-500 [217] ns spread in TOF), usually referred to as "bunches".

In order to store ions in the RFQ, three-dimensional confinement is achieved by an alternating radial potential and a static axial potential. In a quadrupolar field, such as the one employed in the TITAN RFQ [47], the motion of the ions is described by the Meissner equations [177, 245]:

$$\frac{d^2u}{d\zeta^2} \pm h^2 u = 0 \tag{4.2}$$

for $0 < \zeta \leq \pi/2$ and $\pi/2 < \zeta \leq \pi$ respectively, with:

$$u = \frac{\omega^2 x}{4} \tag{4.3}$$

Element	Mass (u)	V_{pp} (V)	Freq. (kHz)	q
Na	23	230	1015	0.474
Al	27	240	960	0.471
K	39	252	820	0.470
Rb	85	295	600	0.471
Cs	133	325	500	0.478

Table 4.1: Confinement Paremeters for the TITAN RFQ for singly charged ions. The parameter q_u is derived from the Meissner equations (Eq. 4.2).

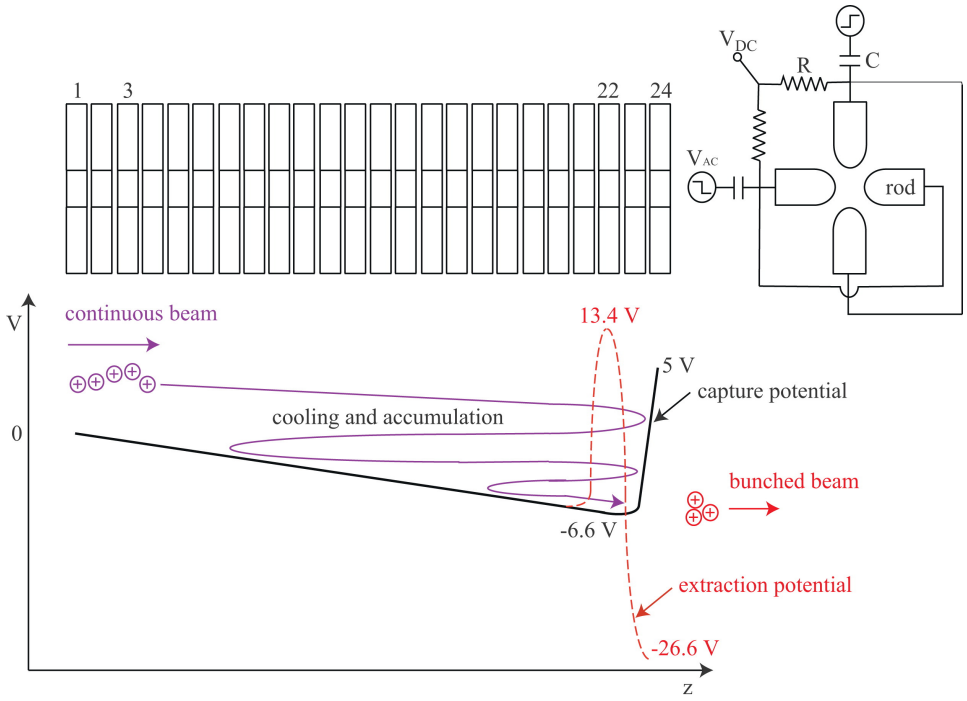

Figure 4.4: Top: Schematic of the TITAN RFQ. Bottom: The axial voltages and the principle of accumulation and cooling using buffer gas. Figure from [47].

$$q = \frac{4ZeV}{m\omega^2 r_0^2} \tag{4.4}$$

and $h = \sqrt{2q}$, $\zeta = \omega t/2$. In Eq. 4.4, V is the amplitude of the RF potential, r_0 is a dimensional parameter of the trap and ω is the radial frequency of the RF potential.

In a linear Paul trap, the alternating radial potential is created by supplying an

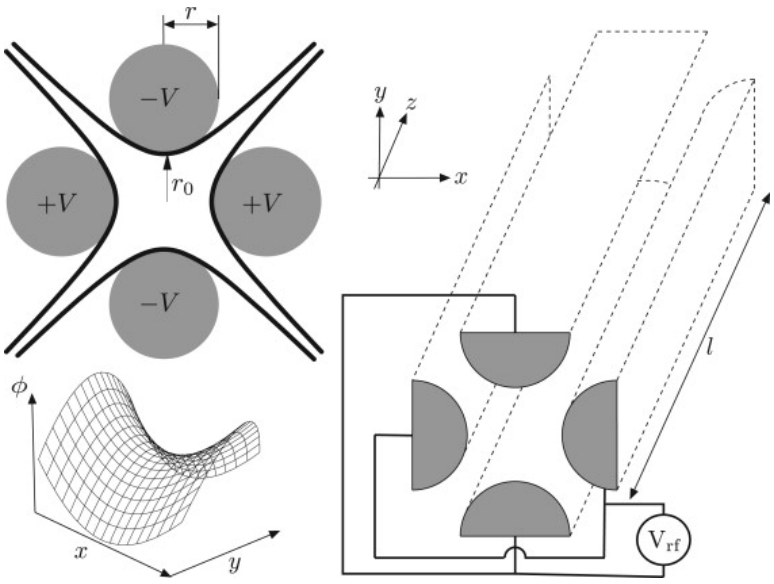

Figure 4.5: Top left: A cross section of an RFQ trap showing its characteristic dimensions. Bottom left: The radial potential of a linear Paul trap. Right: Three-dimensional schematic of a Paul trap. Figure from [47].

RF voltage to four axially segmented rods as can be seen in Figures 4.4 and 4.5. The result is a harmonic saddle-shaped potential which depending on the phase focuses the ions in the x or y direction as can be seen in Fig 4.5. The frequency and the voltage of the radial alternating potential depends on the mass and charge of ions being stored in stable conditions and consequently allows one to use these parameters to tune the system as a mass filter. The typical values used during this work and can be seen in Table 4.1 for the TITAN RFQ.

The TITAN RFQ is floated on a high voltage platform at 20 kV to in order to stop the 20 keV beam supplied from ISAC. Floating the trap system allows TITAN to achieve axial confinement by only a 20 V local DC voltage in addition to the floating potential as can be seen in the plot of Fig. 4.4. The high-voltage platform acts as an offset to all local potentials and hence simplifies the use of low voltage power supplies.

Cooling of the ions in the RFQ is achieved with the use of He gas at a pressure of $\approx 10^{-2}$ Torr [118] at room temperature. The trapped ions elastically collide with

inert gas particles until they thermalize with the helium and the ions accumulate at the minimum of the potential well (Fig. 4.4). Cooling times at $P \approx 10^{-2}$ Torr pressure are of the order of 1-10 ms [118].

Located underneath the RFQ setup is a thermal ion-source which provides stable, singly-charged alcali ions to TITAN for commissioning and testing purposes.

Ions are extracted from the RFQ by switching the voltages applied to the last segment of the RFQ, as can be seen in the plot of Fig. 4.4 (red dashed line). The extraction energy of the ions is determined by the difference in the electric field from the RFQ, floating at high voltage, to the next optical element, the pulsed drift tube (PB5). PB5 is located at the exit of the RFQ and between the 20 kV and the 0 V sections of the TITAN beamline, as can be seen in Fig. 4.6. The kinetic energy of the ions past the PB5 drift-tube is determined by:

$$E_k^f = E_k^0 + q(V_{RFQ} - V_{PB5}) \tag{4.5}$$

where E_k^0 is the initial kinetic energy of the ions, V_{RFQ} = 20 kV, the voltage of the RFQ bias and V_{PB5} = 17.8 kV (for MPET) or 18.3 kV (for MR-TOF MS), the voltage applied to PB5. While the ions are within PB5, its voltage switches from 17.8 kV (or 18.3 kV) to ground, so that ions are essentially in a field-free region and don't gain any additional kinetic energy from the potential difference between the PB5 high voltage setting (17.8 kV or 18.3 kV) and the rest of the beamline at ground. The overall transfer efficiency of the TITAN RFQ is $50-80\%$ depending on the ions trapped and the quality of the tune of the RIB, coming from the ISAC target. Due to the complexity and flexibility of the ISAC system using new targets and extraction optics, every time TITAN receives beam, the beam needs to be optimized. The RFQ decouples the TITAN system from the ISAC ion transport and provides essentially identical and reproducible conditions of the ion bunches once delivered by the RFQ system.

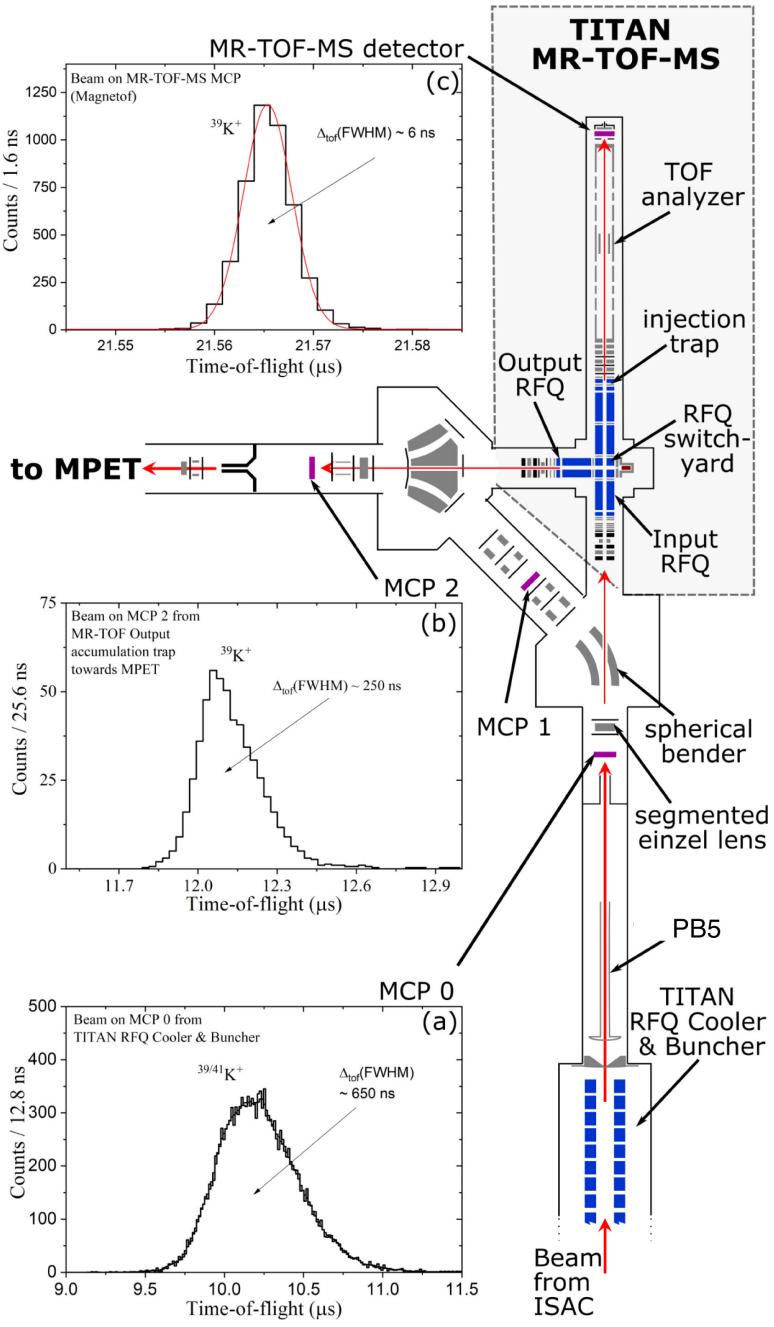

Figure 4.6: Schematic of the TITAN RFQ to MR-TOF MS beamline. The insets (a)-(c) show the TOF distribution of the ions after various stages of cooling along the beamline. Cooling is achieved by the TITAN RFQ and the MR-TOF MS RFQs. Figure from [217].

4.3 TITAN Multi-Reflection Time-of-Flight Mass Separator/Spectrometer

The TITAN MR-TOF MS has been designed and built at the Justus Liebig University Giessen [129] and it has been in operation at TITAN since 2017. It was designed based on the MR-TOF MS system installed at the FRS Ion Catcher [205] at Gesellschaft für Schwerionenforschung (GSI) with the additional unique capability of mass selective retrapping. The system and functions are described in the following sections.

The TITAN MR-TOF MS consists of an RFQ transport system, the TOF analyzer and a TOF detector as can be seen in Fig. 4.6. Under vacuum conditions, the pressure in the system is $2 \cdot 10^{-8}$ Torr while when operated with He buffer gas, the pressure in the RFQ transport section is $2 \cdot 10^{-2}$ Torr. The pressure in the TOF analyzer is $1 \cdot 10^{-7}$ Torr. This pressure difference is achieved through strong differential pumping between the RFQ and the TOF analyzer section maintained by a series of turbomolecular pumps [217].

The RFQ transport system ensures optimum beam quality of the ions before injection into the TOF analyzer, which is necessary for achieving a high resolving power. This is achieved by a series of buffer-gas filled RFQ traps as shown in Figures 4.6 and 4.7. Ions extracted from the TITAN RFQ with 1.3 keV of energy are transported to the MR-TOF MS RFQ system where they are first trapped at the input RFQ for about 1 ms [217] as can be seen in Fig. 4.7. Then they are transported to the preparation RFQ where they can be merged with stable ions for calibration purposes. After a 2 ms storage time, the ion bunch is transferred to the injection RFQ for optimal cooling, as can be seen in Fig. 4.7 (c). The size of the beam at various stages of the cooling and bunching process is plotted in Fig. 4.6 (a,b and c).

The ions are injected into the TOF analyzer section by lowering the voltage of the injection RFQ. The TOF analyzer consists of two pairs of four electrostatic mirrors separated by a grounded drift tube as can be seen in the schematic of Fig. 4.8. It is equipped with an MRS electrode in the center of the TOF analyzer which allows cleaning of non-isobaric background as explained in Chapter 3.

Uniquely, the TITAN MR-TOF MS acts as its own isobaric separator. As can be

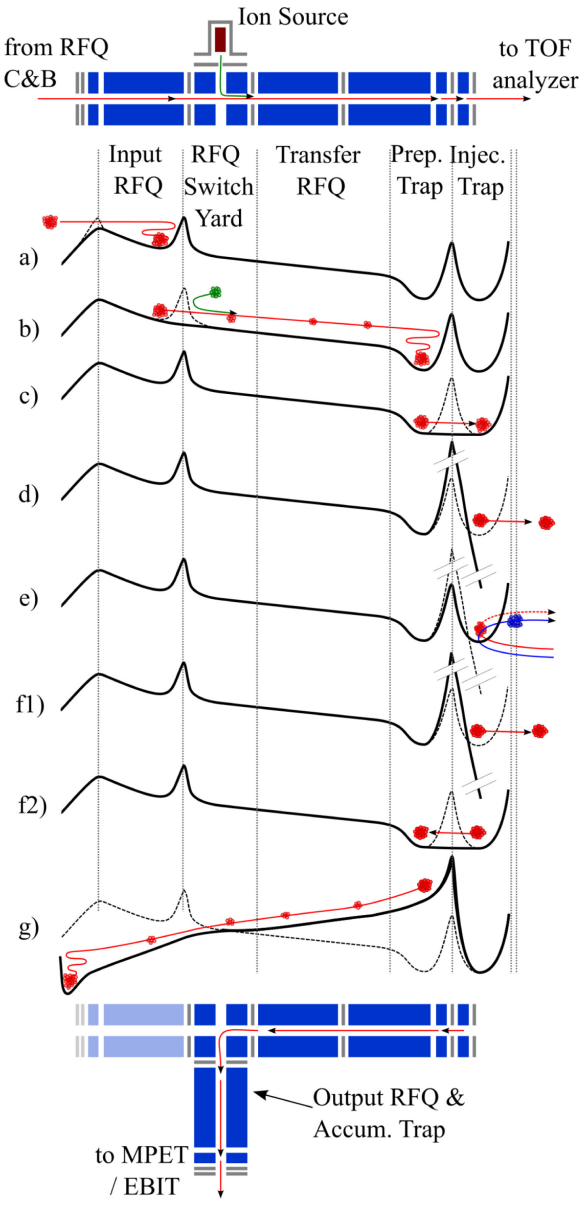

Figure 4.7: Schematic of the MR-TOF MS RFQ transport system. Indicated from (a) to (g) are the individual steps in injecting, cooling, ejecting, selectively re-injecting and extracting ions from the TITAN MR-TOF MS RFQ system. Figure from [217].

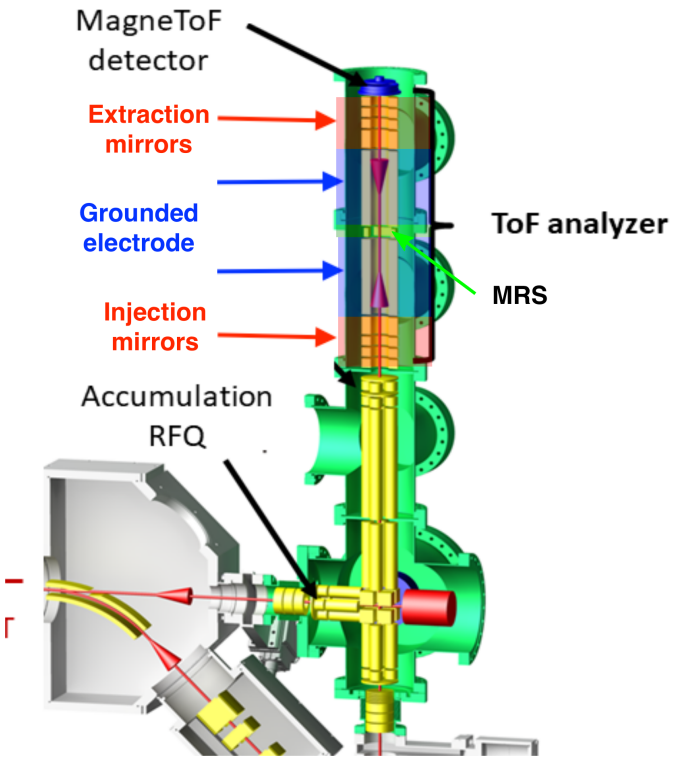

Figure 4.8: Schematic of the MR-TOF MS installed in the TITAN beamline. The ions are cooled in the preparation RFQs before the ToF analyzer. The ToF analyzer that includes the electrostatic mirrors and the MRS is where the ions perform hundreds of revolutions before they are ejected and measured at the MagneToF detector shown at the top of the MR-ToF MS.

seen in Fig. 4.7 (e), after a short number of turns in the TOF analyzer, the IOI (red) can be selectively retrapped in the injection RFQ, while any non-trapped contaminants in the beam (blue) can be expelled. The retrapped beam undergoes a second iteration of cooling in the injection RFQ which removes additional energy spread due to ion-ion interactions with the previously co-trapped contaminants. After a few milliseconds of re-cooling, the ions are ejected from the injection trap (Fig. 4.7 (f1)) and injected to the TOF analyzer for mass separation and for the mass measurement. Due to this unique feature, the TITAN MR-TOF MS is able to operate

at ion-of-interest to contaminant-ion ratios of up to $1:10^6$. Fig 4.9 (a) shows an attempt to measure the mass of ^{151}Yb in the MR-TOF MS without retrapping. Due to the high rate of isobaric contaminants (with a signal to background ratio smaller than 10^{-4}) the mass spectrum is dominated by ^{151}Eu, and ^{151}Yb cannot be identified. In contrast, Fig. 4.9 (b,c) shows a measurement with similar overall statistics (of total number of counts shown) while using the retrapping technique. Due to the fact that retrapping increases the signal to background ratio by suppressing the background ions, and given the limitation that the MR-TOF MS can only measure 1 ion per cycle to avoid systematic errors, this technique allows the MR-TOF MS to reach the required statistics faster than without retrapping. In addition, by removing the background contaminants, it produces cleaner mass spectra allowing for mass measurements using less than 100 total counts.

The TITAN MR-TOF MS normally operates with a repetition rate of 50 Hz, corresponding to a 20 ms cycle. In cases when measuring the mass of isotopes with $t_{1/2} < 20$ ms, the repetition rate can be increased up to 160 Hz to minimize decay losses. The 20 ms cycle is split into two 10 ms sections, where the first 10 ms are dedicated to isobar separation and the second 10 ms section is used for the mass measurement. During the mass measurement part of the cycle, the ions undergo 400-600 isochronus turns that result in resolving powers [217]:

$$\frac{m}{\Delta m} \simeq 400,000 \tag{4.6}$$

The maximum achieved precision of the TITAN MR-TOF MS has been found to be $\delta m/m \sim 10^{-7}$. It is limited by voltage fluctuations in power supplies and ringing of the voltages after fast switching [127]. Ringing occurs when the applied voltage is affected by induction effects from fast switching of nearby high-voltage electrodes. The vacuum enclosure acts as an antena and transmits the induced signal, eventually changing the ground potential and leading to fluctuations of the well-defined potentials of the ion-optics. The overall transport efficiency of the TITAN MR-TOF MS is 15% for radioactive beams [217] and arises from transmission losses in the RFQ section, losses due to collisions with background gas in the TOF analyzer, the non-unity detection efficiency and re-trapping efficiency (when utilized) [217].

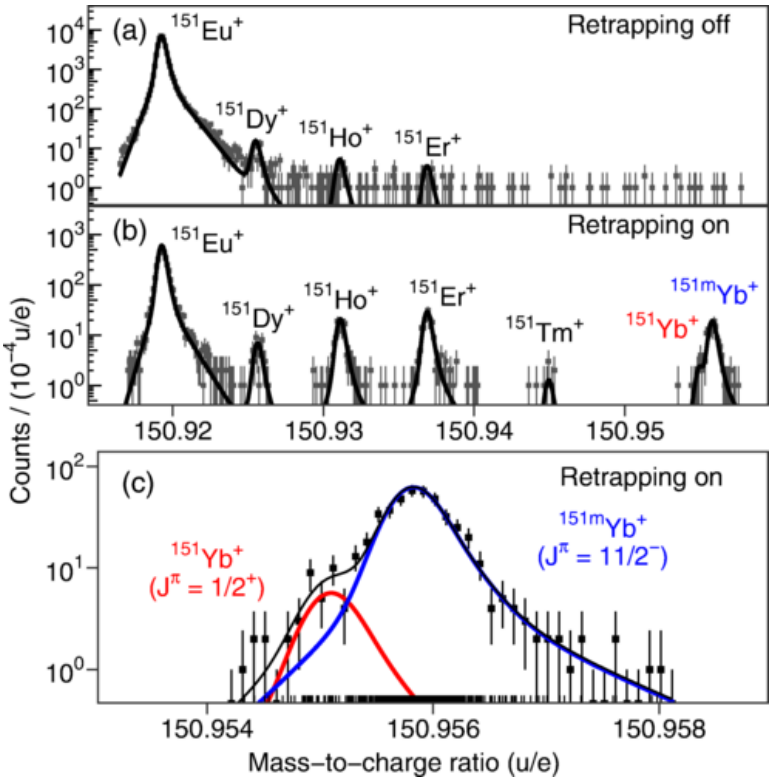

Figure 4.9: MR-TOF MS spectrum of mass 151 u with the goal of measuring the mass or ^{151}Yb. (a) Mass spectrum without the use of retrapping, (b) Mass spectrum with the use of retrapping, (c) The ^{151}Yb peak was found to contain an undiscovered isomer. Figure taken from [29].

4.4 TITAN Electron Beam Ion Trap

A unique characteristic of the TITAN mass experiment, compared to other ion trap systems, is that it provides the ability to measure the mass of both Highly Charged Ions (HCI) and Singly Charged Ions (SCI). The use of HCI in Penning trap mass spectroscopy results in faster or more precise measurements, as Eq. 3.28 implies and as demonstrated for example in [90]. This is due to the fact that the cyclotron frequency increases linearly with the charge q, while the error in the determination of the cyclotron frequency depends on the observation time and it is hence independent of the charge state. Although HCI are utilized in mass measurements of stable and long-lived species (see for example [219]), TITAN is the only experiment

that provides access to charge bred short-lived ions for mass measurements. The instrument enabling this feature is the TITAN Electron Beam Ion Trap (EBIT).

The TITAN EBIT was built at the Max-Planck Institute for Nuclear Physics (MPIK) in Heidelberg [98] and was first used for charge-breeding of rare isotopes at TITAN in 2008. Charge breeding occurs by overlapping singly charged trapped ions inside the EBIT with an intense and dense electron beam, as can be seen in Fig. 4.10. Collisions between free electrons of the electron beam and atomic electrons cause the atomic electrons to be liberated from the atom. This process is repeated until the bound electrons' ionization energy is larger than that of the electron beam energy.

The electron beam is formed by heating a barium cathode located outside the trap. The formed beam is transported into the magnetic field through the trapping region and it is collected by a hollow electrode at the other side of the trap, as seen in Fig. 4.10. The electron beam is compressed and focussed to the center of the trap with the use of a strong magnetic field (up to 6 Tesla) created by a pair of superconducting coils arranged in Helmholtz configuration (Fig. 4.10). Ions are injected into the EBIT trap region from the collector side and are trapped radially by the electron beam and the magnetic field. Axial confinement is achieved by applying a voltage difference between a number of tube electrodes to create a potential well. The central tube electrode contains a number of radial openings to allow for spectroscopic access [159, 166].

The charge state of trapped ions after a charge breeding time t_{CB}, depends on the electron beam current density, radius and energy. An example of how the different charge states are populated as a function of t_{CB} in the TITAN EBIT can be seen in Fig. 4.11. As the charge breeding time increases, the population of ions in higher charge states increases while that of lower charge states reduces. However, if the electron beam energy is not high enough to populate higher charge states, a saturation effect occurs, as seen in Fig. 4.11 (bottom).

Currently, the EBIT electron beam can be operated with energies of up to 66 keV [52], sufficient to produce bare nuclei of up to $Z = 65$ [95]. In addition, a new electron gun has been designed for the TITAN EBIT which will allow for improved electron beam compression and electron beam currents of up to 5 A [52].

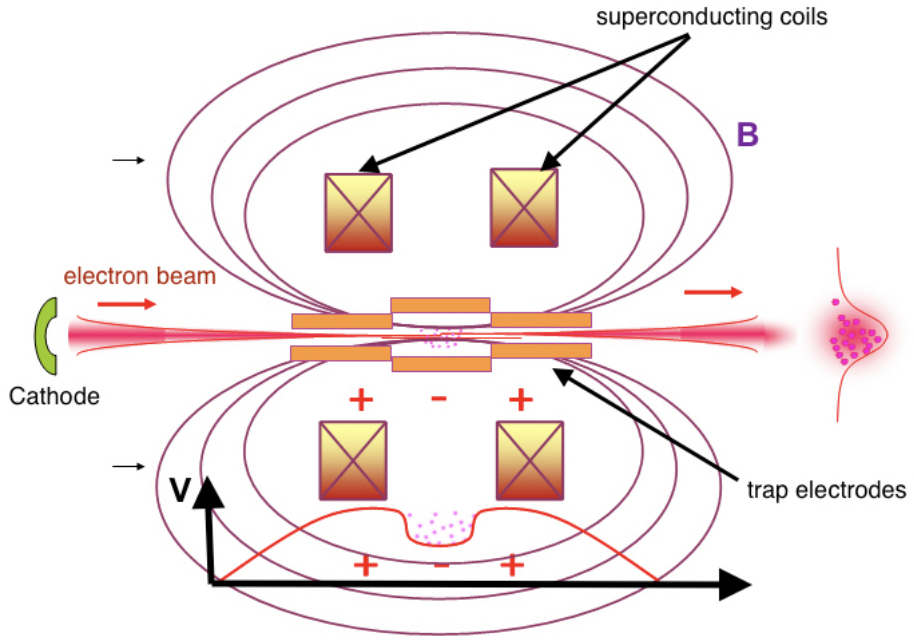

Figure 4.10: Schematic of a cross section of the TITAN EBIT. Shown are the superconducting coils, the magnetic field lines (purple), the ion optics and the applied voltages (red). Also shown is the electron beam (red) produced by the cathode. On the right, a schematic of the overlap between the electron beam and the trapped ions is shown. The overlap between the trapped ions and the electron beam results in electron impact ionization and the production of HCI.

4.5 TITAN Measurement Penning Trap

TITAN MPET is a hyperbolic Penning trap used for high-precision mass measurements of singly and highly charged ions. It currently holds the record of the fastest on-line Penning trap demonstrated by the mass measurement of the neutron-halo ^{11}Li [244], produced via particle fragmentation reactions, with a nuclear half-life of $t_{1/2} = 8.8$ ms. In addition, it was demonstrated that a measurement cycle-time of 5 ms [58], designed to carry out mass measurements of ^{14}Be, produced again via particle fragmentation reactions, can be achieved. In addition, since 2011, it specializes in high-precision mass measurements of short-lived, highly-charged ions

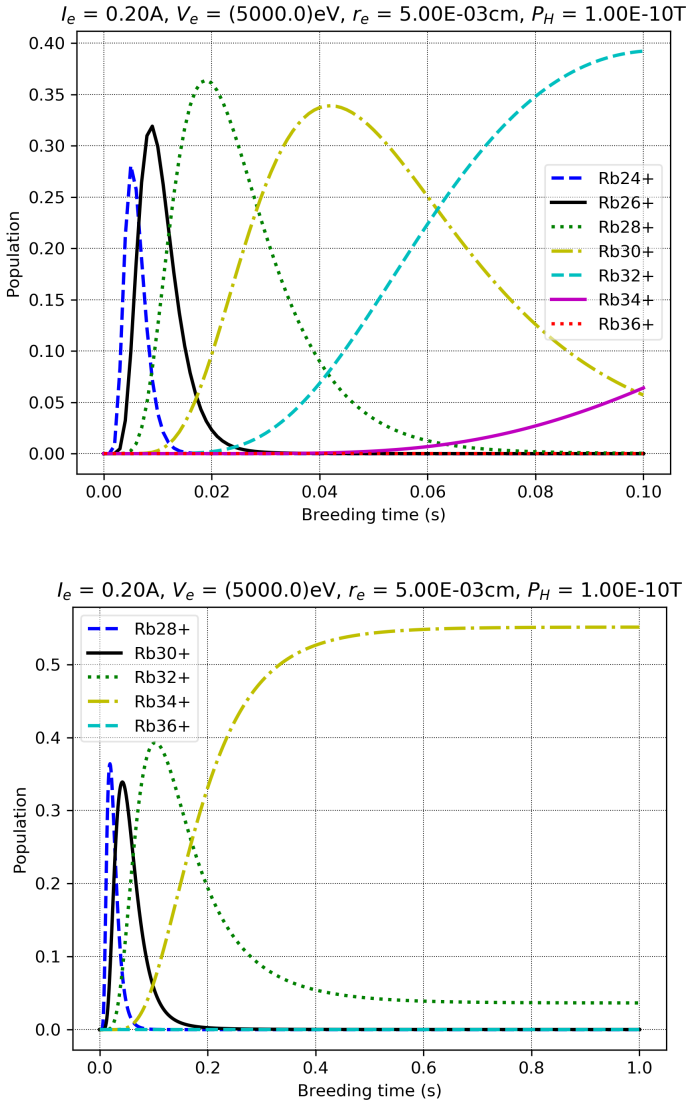

Figure 4.11: Charge breeding simulation as a function of breeding time for ^{74}Rb ions in the TITAN EBIT for an electron beam current $I_e = 200$ mA, an electron beam energy $E_e = 5$ keV, an electron beam radius $r_e = 5 \cdot 10^{-3}$ cm and a trap pressure of $P = 10^{-10}$ Torr. (Top): Charge breeding times from 0 to 100 ms. (Bottom): Charge breeding times from 0 to 1000 ms. The simulation does not account for decay loses and is performed using the simulation code EBIT Simulator for Ionization [226].

[23, 90, 102, 142, 160, 242] provided by the TITAN EBIT. TITAN MPET has been able to achieve relative precisions of $\delta m/m \sim 5 \cdot 10^{-9}$ [154] and it is the spectrometer of choice for $\delta m/m < 10^{-7}$ measurements at TITAN.

From 2008-2017 MPET [45] was operated at room temperature. However, due to charge-exchange interactions between HCI and background gases [163, 165], MPET's vacuum required improvements which were achieved by an upgrade to cryogenic temperatures. At cryogenic temperatures, the charge-exchange effect is greatly minimized as the background gases condense at the trap surfaces and hence improved vacuum conditions are achieved.

CryoMPET has replaced the room temperature system and is located in the bore of a 3.7 Tesla superconducting magnet. The trap electrodes are located at the center of the magnet bore, which corresponds to the most uniform section of the magnetic field (1 part per million in a 2cm· 1cm volume). These electrodes are commonly referred to as the "trap" or the "trap system" in the rest of this thesis while in practice a Penning trap consists of the complete system including the magnet, vacuum system, electrodes, electrical and electronics detection system. For injection and extraction of ions to and from the trap, a series of room-temperature electrodes are located before and behind the trap, as can be seen in Fig. 4.12 and 4.13. The design of CryoMPET along with upgrades and its first commissioning are presented in detail in Chapter 7.

The trap injection structure contains four electrodes, as can be seen in the schematic of Fig. 4.12.

The first two of those: the injection tube (NDT) and injection cone (NDC), are biased to approximately 1000 V and 500 V respectively and are used to optimize the injection of the ions into the Pulsed Drift Tube (PLT). The voltage applied to the PLT switches between two values to adjust the kinetic energy of the beam from 2.2 keV to a few eV. The last element in the injection optics is the Lorentz steerer [223] which is used for focusing the ions at the center of the trap (an example of which can be seen in Fig 4.14) or for preparing them in an initial magnetron motion.

TITAN MPET is able to perform fast measurements due to the use of the Lorentz Steerer electrode [225], as it avoids the need for additional RF manipulation steps and reduces the preparation time. A Lorentz Steerer, is a four-way segmented electrode (Fig. 4.15 (right)) that allows ion preparation in a magnetron radius (r_m)

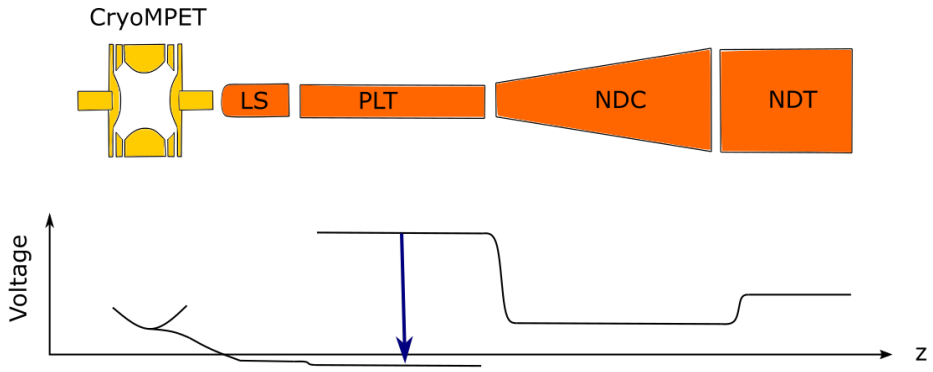

Figure 4.12: Injection optics of CryoMPET. The top of the figure shows a schematic of the geometry of the electrodes, while the bottom shows a schematic of the applied voltage on each of the electrodes.

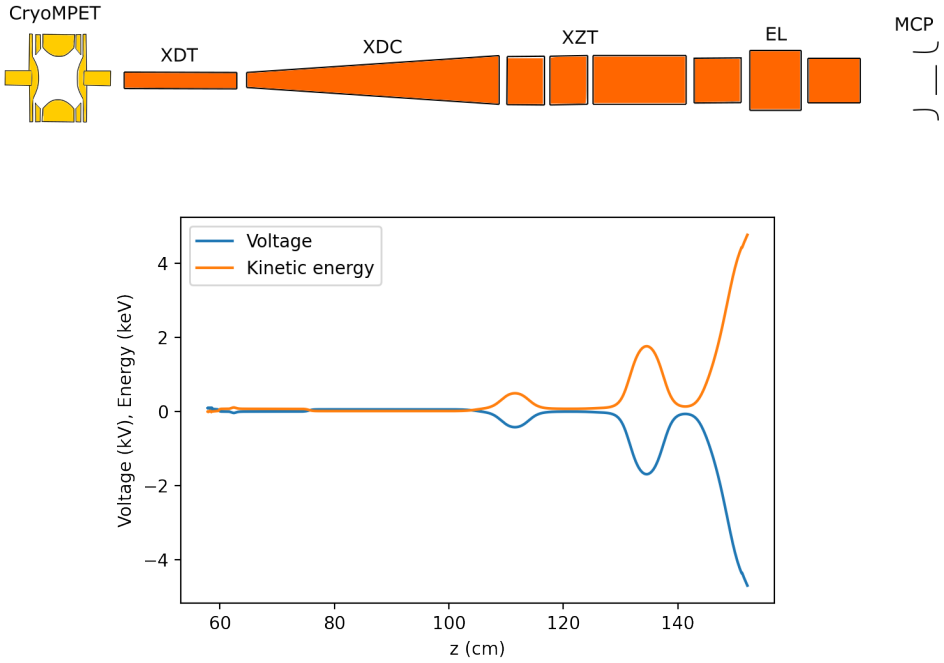

Figure 4.13: Top: Schematic of the extraction optics of CryoMPET, Bottom: Typical extraction voltages and kinetic energy of ions in CryoMPET

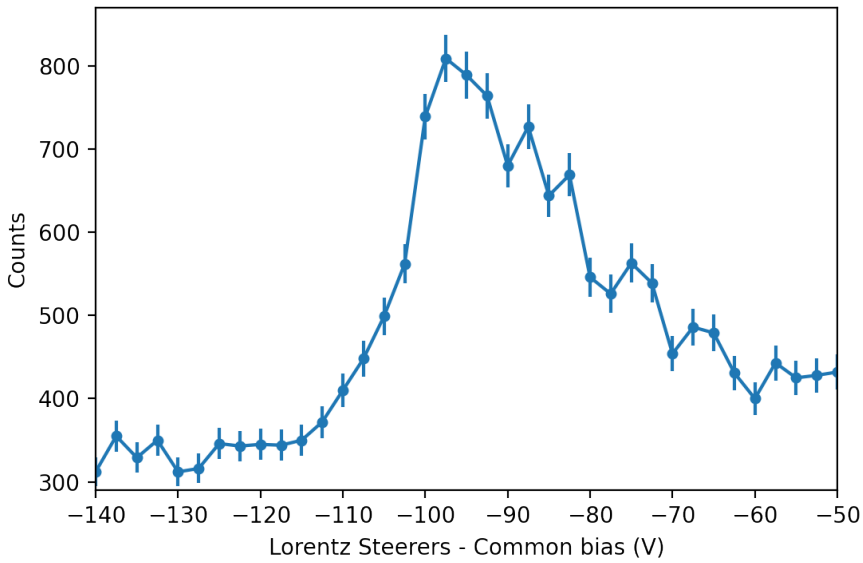

Figure 4.14: Focusing effect created by the common bias of the Lorentz Steerer electrode in CryoMPET: In order for the ions to be efficiently trapped, they need to arrive at the trap with minimum total energy and minimum energy spread. At this setting, which is partially determined from the Lorentz Steerer common bias the maximum trapping efficiency is achieved, as can be seen in the present plot.

upon entering MPET. The Lorentz Steerer electrode is located a few centimeters away from the center of the trap and functions as follows: as the ions fly through the Lorentz Steerer electrode, a voltage difference is applied. The combination of the electric field generated by the voltage gradient and the 3.7 Tesla magnetic field of the superconducting solenoid, results in a Lorentz force $F = |q\vec{E} + q\vec{u}x\vec{B}|$ that prepares the ions at a magnetron radius $r_m = (E/B)t$, where $E = -q\Delta V$ and B, is the magnetic field strength.

In the trap, the ions are captured in a 40 V potential well generated by a bias across the trap electrodes. The ring electrodes of CryoMPET are segmented four-way, allowing the use of dipole and quadrupole excitations as will be demonstrated in Chapter 7.

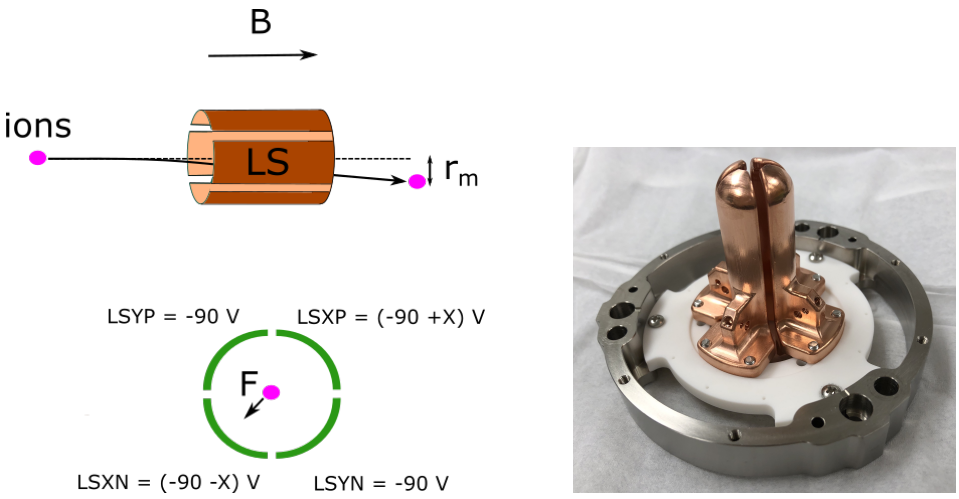

Figure 4.15: Left: Schematic of the principle of the Lorentz Steerer electrode. Upper figure: A schematic of the an ion's tajectory when passing through the Lorentz Steerer. Lower figure: A cross section of the Lorentz steerer electrode with the applied voltaged indicated. Right: The LS electrode of TITAN MPET and its holding structure.

Ions are extracted from CryoMPET by lowering the voltage of the extraction electrodes of the trap. After the ions are extracted from CyoMPET they are accelerated and focused to a position-sensitive Multiple-Channel Plate (MCP) detector, which is approximately 1 m away from the trap. The ion optics' system that focuses and accelerates the extracted beam can be seen in Fig. 4.13 (top). Fig. 4.13 (bottom) shows the typically applied voltages and the corresponding kinetic energy of the ions from the time the ions are extracted until they reach the MCP detector [2].

TITAN MPET currently employs the TOF-ICR technique to measure the cyclotron frequency of the trapped ions and their mass. In order to reduce the overall measurement time and in order to increase the precision that can be achieved, the TOF-ICR technique is currently being replaced by the PI-ICR technique, described in Chapter 3. All necessary simulations and hardware upgrades for the implementation of the PI-ICR technique have been completed and are described in Appendix B.

[2]These voltages are specfic to the TOF-ICR technique. For those appropriate for the PI-ICR technique see Appendix B

Chapter 5

Resurrecting the N = 20 shell closure near the neutron dripline

5.1 Mass measurements of neutron-rich Mg and Na isotopes with the TITAN MR-TOF MS

In the last 30 years, mass measurements within the $N = 20$ island of inversion have been conducted mostly by time-of-flight experiments, namely the SPEG [230] experiment at GANIL, the TOFI [275] experiment at Los Alamos, the Mass measurements at ISolde using a Transmission RAdiofrequency spectrometer on-Line (MISTRAL) [260] experiment at CERN/ISOLDE and more recently the TITAN [75] experiment at TRIUMF.

The masses of the Mg isotopic chain have been precisely measured ($\delta m \leq 50$ keV) by the MISTRAL [171] and TITAN [57] experiments for masses up to 34 u, covering and extending further than the magic number $N = 20$ which is considered to be collapsed [270]. However, scientific motivation for precise mass measurements extends beyond $N = 20$. Recent half-life studies carried out at FRIB [66] suggest that the deformation that begins at the island of inversion extends all the way to ^{38}Mg ($N = 26$). However, due to the large difference between the proton and the neutron numbers of these isotopes, which makes them extremely exotic, the only available results regarding this finding come from lifetime studies [66]

and gamma spectroscopy [80]. As mentioned in Chapter 2, since lifetime studies provide indications rather than definitive results due to the presence of ambiguities, other measurement techniques are necessary to verify and further understand the extent of the region of deformation.

Furthermore, ^{37}Mg is shown to be a neutron halo [146]. In neutron halos, the last neutron(s) are weakly bound to the nuclear core, resembling a halo. Due to the weak binding and small spatial overlap between the last neutron(s) and the core, neutron halos are characterized by small one-neutron separation energies (typically $S_n \leq 1$ MeV) and low orbital angular momentum numbers (typically $l = 0, 1$). In this case, ^{37}Mg, was studied via transfer reactions at RIKEN [146] in order to determine whether it is a halo nucleus. It was found that its one-neutron separation energy is $S_n = 0.22^{+0.12}_{-0.09}$ MeV and that a low angular momentum ($l = 1$) component was necessary to explain the experimental results [146]. Despite the known halo nature of ^{37}Mg after the RIKEN experiments, there is still an important reason for measuring its mass with a higher precision. Due to the large proton to neutron imbalance and due to the low-angular momentum component that arises from its halo nature, ^{37}Mg is an excellent case for testing existing theories. However, the current uncertainty in the one-neutron separation energy ($\sim$ 100 keV) limits this ability. In addition, due to the low mass of ^{37}Mg, there is a plethora of theoretical models that can be used in this region which allows for a wide comparison.

Although the island of inversion has been well-mapped for the Mg and Al isotopes (see for example [120, 155, 182]), less information is available about its southern border. A schematic of the area of the nuclear chart currently considered within the island of inversion can be seen in Fig. 2.6. The masses of ^{31,32}Na isotopes have been measured using the TITAN Penning trap [103] but not with a precision higher than 20-30 keV. Although this precision is sufficient to discover sudden shell changes (typically of the order of few MeV as can be seen in Fig. 2.8), it does not allow the resolution of low-lying isomeric states that can provide important structural information. In addition, the mass of ^{33}Na which has $N =$ 22 neutrons and thus influences the two-neutron shell gap for $N = 20$, has only been measured by the SPEG experiment [133] to a precision of 350 keV and is susceptible to systematic errors. More specifically, ToF-Bρ measurement methods such as the one employed by SPEG are extremely fast ($\sim 1\mu s$) and hence produced

isomeric states are present in the beam that arrives for detection. As these isomeric states do not have enough time to decay and as they cannot be resolved by the spectrometer, they are sources of systematic shifts [230].

With the aim to extend our knowledge of the evolution of the island of inversion, east and south of ^{32}Mg, TITAN carried out mass measurements that took place over two separate measurement campaigns. Both campaigns utilized a UC_x target with the Ion Guide Laser Ion Source (IGLIS) [212] and the TRILIS [161] ion source for the first and the second campaign, respectively. The ion source is highly chemical element sensitive and was setup for laser ionization of Mg isotopes. The extracted isotopes from ISAC were mass separated using the standard isotope separator [42] and delivered to the experimental hall. Once at TITAN, the received RIB beam was cooled and bunched in the TITAN RFQ [47] and then sent to the TITAN MR-TOF MS [217] for mass separation and mass measurement. The measurement cycle varied over the course of the experiment in order to account for the nuclear half-life of the measured species, as can be seen in Tab. 5.1.

The first measurement campaign took place in 2021 and the main goal was the measurement of the neutron halo ^{37}Mg. However, the rate of ^{36}Mg isotopes delivered to TITAN was too low. Instead, the experiment carried out successful measurements of the masses of $^{31-35}$Mg and $^{31-33}$Na. Of the measured masses, we are able to improve the precision of ^{34,35}Mg and $^{31-33}$Na.

The second campaign took place in November 2022 and the main goal was to measure again the mass of ^{37}Mg in a UC_x target and testing an ionization scheme without surface ion suppression from the IGLIS ion source. However, the yield was not improved and the campaign pivoted in the goal to measuring the mass of ^{36}Mg and improving the results for ^{34,35}Mg.

The present chapter provides a brief discussion of the data analysis procedure for data collected with the MR-TOF MS and the treatment of systematic uncertainties. It continues with the description of the experimental results and it closes with a summary of the results and their impact on our knowledge of the island of inversion.

5.2 Data analysis procedure

The data analysis procedure follows multiple steps to determine the measured mass with the maximum precision. The first step is the so-called Time Resolved Calibration (TRC) calibration, that corrects drifts in the ions' TOF, and therefore mass, caused by voltage drifts in MR-TOF MS's power supplies. The TRC calibration is followed by the precise determination of the peak-shape of the mass peaks via a procedure called peak-shape calibration. Finally, all the peaks in the TOF spectrum are fitted simultaneously with the previously determined peak-shape, and their mass values are determined.

As the MR-TOF MS system is based on electrostatic optical elements, changes in the supplied bias of these elements will be reflected in the measured TOF. The bias is provided by static power supplies, yet some variations over time can be found as a slow drift, likely due to ambient conditions. The TRC corrects slow time-of-flight drifts, such as the one in Fig. 5.1 (a). The origin of these drifts are mostly bias changes due to temperature fluctuations and the expansion or compression of the mass analyzer geometry due to temperature drifts [21].

In the TRC, the measurement data are separated in bins of a few seconds in which the parameter b of Eq. 3.6 is being re-evaluated. The re-evaluation takes place using a calibrant of well-known mass that is identified in the mass spectrum. The centroid of the position of the calibrant in each bin is determined with a Gaussian fit and the parameter b is adjusted so that the determined centroid matches the literature mass:

$$b = \frac{\sqrt{\frac{qc}{m_{lit}}}(t_{exp} - t_0) - 1}{N} \tag{5.1}$$

where q is the charge of the ion, c, t_0 are MR-TOF MS calibration parameters which are determined offline, t_{exp} is the TOF of the ions in the MR-TOF MS system and N is the number of isochronous turns that the ions perform while in the MR-TOF MS. Fig. 5.1 (b) compares the peak shape before and after a TRC.

Once the TRC is completed, the mass spectrum is fitted using the EMGfit package [201]. The fitting function is determined using a high-statistics peak of an isotope with well-known mass (typically with $\delta m \leq 1$ keV) in the spectrum. The identity and the mass of the peak needs to be well known so that there are no

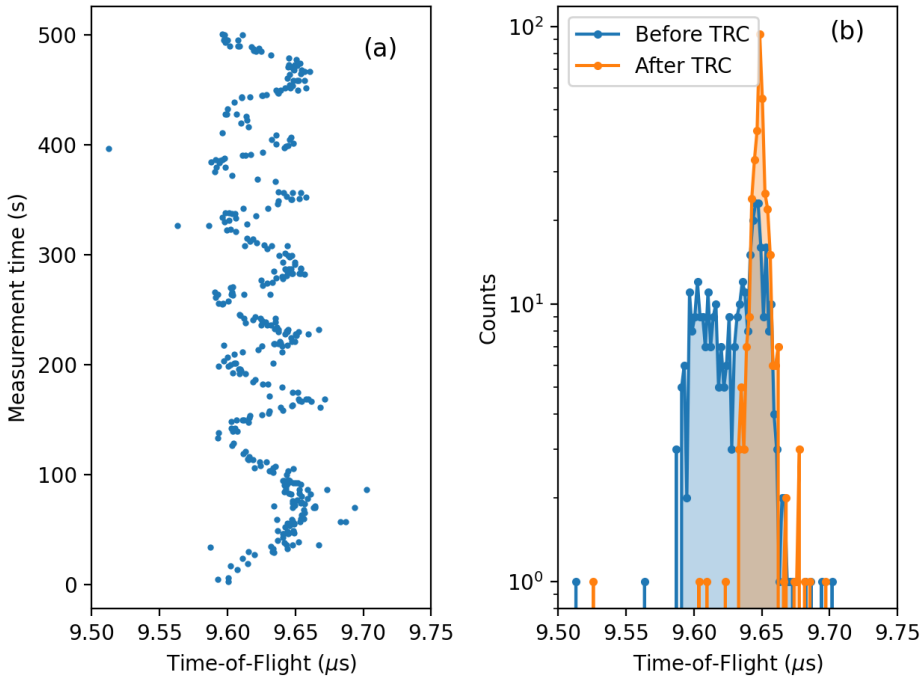

Figure 5.1: (a): TOF drifts of the $^{12}C_3^+$ peak in the mass spectrum of 36 u without a TRC. (b): Comparison of the measured peak before and after TRC.

isomers overlapping with it and possibly altering its shape. In addition, the peak needs to have enough statistics (typically more than 1000 detected ions) so that the EMGfit package converges to the correct fit model. The fit model is an exponentially modified Gaussian function with a varying number of exponential tails on each side of the peak which account for image aberrations, field imperfections and mechanical misallignments. In its most general form, the fit function is given by [209]:

$$\begin{aligned} h_{emg}(x) = \Theta \sum_{i=1}^{m} \frac{\eta_{-i}}{2\tau_{-i}} \exp\left[\left(\frac{\sigma_G}{\sqrt{2}\tau_{-i}}\right)^2 + \frac{x-\mu_G}{\tau_{-i}}\right] \operatorname{erfc}\left[\frac{\sigma_G}{\sqrt{2}\tau_{-i}} + \frac{x-\mu_G}{\sqrt{2}\sigma_G}\right] + \\ + (1-\Theta) \sum_{i=1}^{n} \frac{\eta_{+i}}{2\tau_{+i}} \exp\left[\left(\frac{\sigma_G}{\sqrt{2}\tau_{+i}}\right)^2 - \frac{x-\mu_G}{\tau_{+i}}\right] \operatorname{erfc}\left[\frac{\sigma_G}{\sqrt{2}\tau_{+i}} - \frac{x-\mu_G}{\sqrt{2}\sigma_G}\right] \end{aligned} \tag{5.2}$$

where Θ determines the strength of left- versus right-side exponential tails, $\eta_{\pm i}$ determines the weight of the right- or left-side exponential tail i, $\tau_{\pm i}$ is the standard deviation of the exponential distribution $\pm i$, m,n are the number of exponential tails to the left and to the right of the Gaussian peak and μ_G and σ_G^2 are the mean and variance of the Gaussian distribution. Finally x is the mass-to-charge ratio (m/q) derived from the MR-TOF MS calibration (Eq. 3.6) and h_{emg} is the number of counts that corresponds to each m/q.

The number of exponential tails in the fit is determined by fitting the peakshape calibrant with an increasing number of exponential tails until the minimum Pearson chi-squared χ_P^2 [24] value is reached. Overfitting is avoided by rejecting models for which the parameter amplitudes are consistent with zero within one standard deviation [201]. After the peakshape calibration is complete, the peakshape of all subsequent fits remains fixed.

The next step is to fit the entire mass spectrum with the pre-determined peakshape. The only fit parameters are now the peak centroids and their amplitudes. In contrast to the peak-shape fit which uses a χ^2 minimization to determine the best fit model, the general fitting of the mass spectrum uses the Maximum Likelihood Estimation (MLE) method [24], which minimizes the Log-Likelihood Ratio (LLR) [24],

$$L = 2\sum_{i=1}^{N}[f(x_i) - y_i + y_i ln\Big(\frac{y_i}{f(x_i)}\Big)] \tag{5.3}$$

where $f(x)$ is the fit model, and (x_i,y_i) are the experimental data. The MLE log-likelihood ratio is preferred in this case because it respects the Poisson distribution of counting statistics and thus can be used in cases with few counts ($N \leq 50$). On the contrary, the χ^2 distribution assumes that the data are normally distributed, and therefore cannot be used in cases of low statistics [201].

5.3 Evaluation of systematic uncertainties

There are three major sources of systematic effects impacting measurements performed by the TITAN MR-TOF MS. These sources are: a) TOF fluctuations due to the voltage switching of the MR-TOF MS electrostatic mirrors, b) ion-ion interactions in the MR-TOF MS mass analyzer and, c) systematic effects depending on the

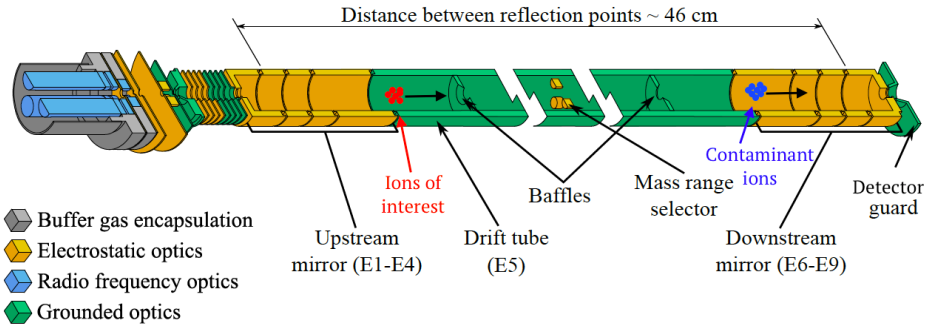

Figure 5.2: Schematic of the TITAN MR-TOF MS. During extraction, ions of different mass that have beem separated in the MR-TOF MS are shown with red and blue. Figure adapted from [241].

block size in the TRC calibration.

The first, and usually dominant, systematic effect is related to voltage instabilities due to voltage switching of MR-TOF MS's electrostatic mirrors. This effect becomes significant for the ejection mirror (Downstream E6-E9 mirror in Fig. 5.2), where species are well separated, as shown in Fig. 5.2 and can therefore experience different voltage values of the mirror electrodes while extracted towards the detector.

The estimation of the effect of mirror voltage switching in this particular experimental campaign was evaluated before the measurement, using a $^{133}Cs^{+}$ beam from the MR-TOF MS ion source. Fig. 5.3 shows the fluctuation of the average time of flight of the $^{133}Cs^{+}$ ions as a function of the opening time of the mirror. The systematic effect is evaluated by calculating the scatter of the average TOF for extraction delays within t $\approx$ [-4,4] μs, where the ions are in the field-free region when the voltage switch occurs. Larger TOF variations as those seen in Fig. 5.3 (Left) for $t > 4\mu s$ and $t < 4\mu s$ are avoided by carefully selecting the extraction delay during the beam-time preparation period.

The histogram of the TOF variation can be seen in Fig. 5.3 (right). The orange line corresponds to a Gaussian fit to the histogram data. From the standard

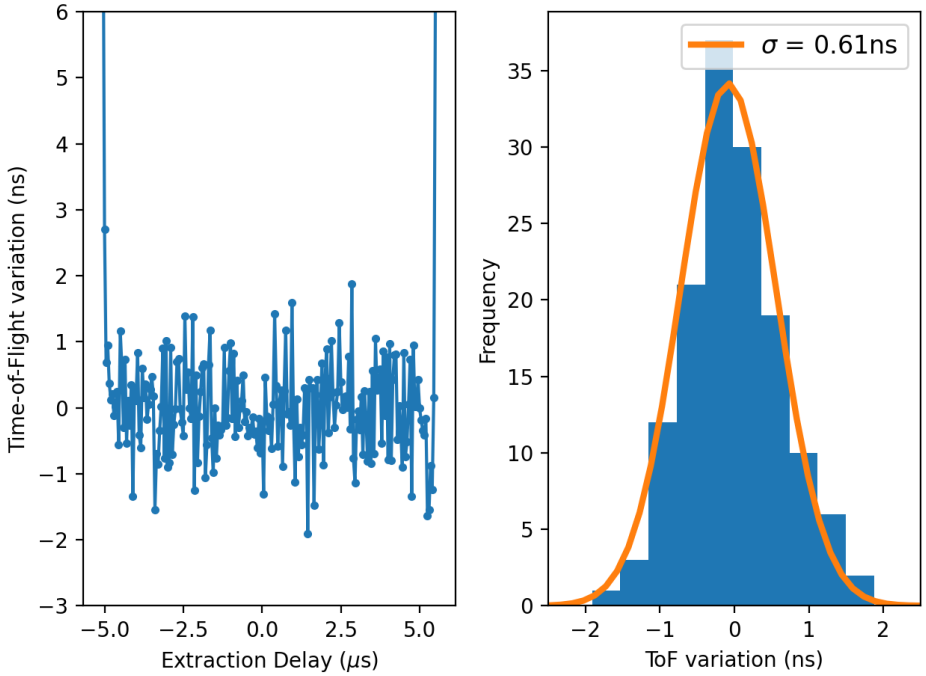

Figure 5.3: Opening mirror scan from the 2021 measurement campaign. Left: TOF variation as a function of the extraction delay. Right: Histogram of the TOF variation for extraction delays within $[-4,4]\mu$s. The orange line corresponds to a Gaussian fit to the data. The standard deviation of the fit corresponds to the systematic error originating from switching voltages.

deviation derived from the fit, the systematic uncertainty can be calculated as:

$$\frac{\delta m}{m}\Big|_{2021} = \frac{\sigma}{t} = \frac{0.61ns}{8ms} = 7.6 \cdot 10^{-8} \tag{5.4}$$

The same analysis for the 2022 measurement campaign results in a systematic uncertainty of:

$$\frac{\delta m}{m}\Big|_{2022} = 1 \cdot 10^{-7} \tag{5.5}$$

where the small difference in the overall uncertainty comes from differences in the optimal voltage settings applied in the two measurement campaigns, which in turn

Mass Number	Campaign	Ions per second	cycle (Hz)	Rel. error	Error (keV)
31	2021	14.94	60	$8.21{\cdot}10^{-9}$	0.24
32	2021	64.50	60	$3.55{\cdot}10^{-8}$	1.06
33	2021	3.94	60	$2.17{\cdot}10^{-9}$	0.07
34	2021	3.49	60	$1.92{\cdot}10^{-9}$	0.06
34	2022	86.90	80	$3.58{\cdot}10^{-8}$	1.14
35	2021	0.64	60	$3.52{\cdot}10^{-10}$	0.01
35	2022	92.34	80	$3.81{\cdot}10^{-8}$	1.24
36	2022	2.00	160	$4.13{\cdot}10^{-10}$	0.01

Table 5.1: Count rates and the corresponding systematic uncertainty due to ion-ion interactions in the MR-TOF MS.

depend on the ambient conditions.

The second source of systematic uncertainty in MR-TOF MS measurements originates from ion-ion interactions in the mass analyzer of the MR-TOF MS. As described in Chapter 3, when a large number of ions are stored in the mass analyzer, the TOF of the ions of interest is influenced by Coulomb interactions between the ions, thus resulting in systematic deviations from the expected TOF. The effect of ion-ion interactions has been investigated in the past [206], revealing a systematic effect of:

$$\frac{\delta m}{m} = 3.3 \cdot 10^{-8} / \text{per detected ion} \tag{5.6}$$

A figure of the ion-ion interaction effect can be seen in Fig. 3.8. Due to the fact that the count rate of most of the measurements in the present two campaigns contained less than 1 detected ion per cycle, as can be seen in Tab. 5.1, the ion-ion interaction systematic effect (Table 5.1) is smaller than the mirror switching systematic effect.

The last systematic effect that needs to be taken into account originates from the TRC. In the TRC, the re-evaluation of the parameter b depends on the binning of the data during the re-evaluation. Here, the TRC systematic uncertainty is evaluated from the mass deviations resulting from TRCs with different binning. An example for ^{33}Mg can be seen in Fig 5.4. The systematic effect due to varying the bin size in the TRC calibration amounts to $\delta m/m \approx 3.7 \cdot 10^{-8}$. The overall systematic uncertainty during this experiment can be seen in Table 5.2 and it has been added in quadrature with the statistical uncertainty of each measured mass in the final

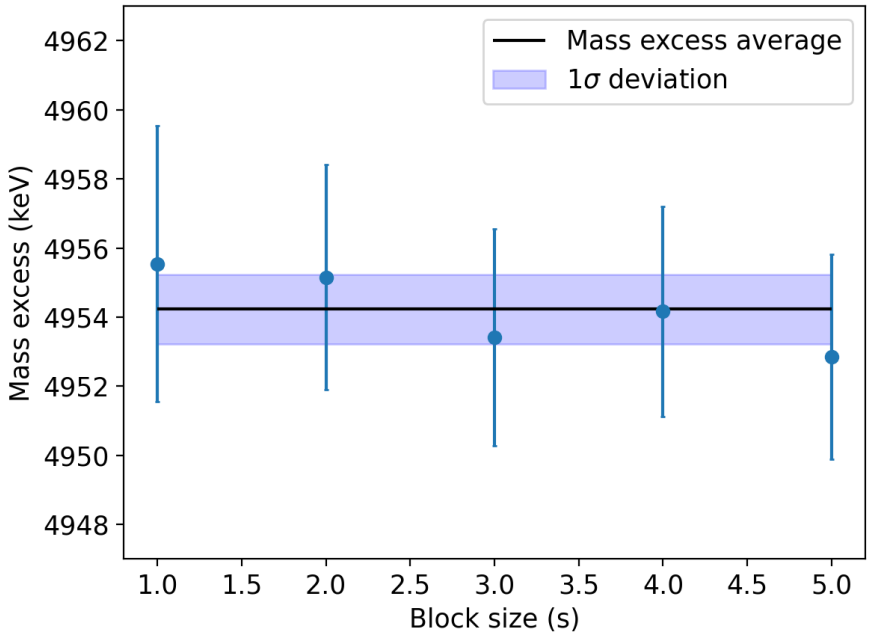

Figure 5.4: Mass excess values of ^{33}Mg derived from TRC calibrations with different bin sizes.

result.

5.4 The sodium isotopic chain

Mg and Na isotopes were measured simultaneously for each mass unit, as Na is co-produced in the UC_x target and is delivered as an isobaric contaminant in the Mg beam. Due to its low ionization energy (5.14 eV), Na can be surface ionized, as the ion source surface typically reads a temperature of $\sim$ 1500^{o}C due to its proximity to the hot target. Post ionization, the Na isotopes are delivered to TITAN as the standard ISAC mass separator has insufficient resolving power to remove the isobaric Na contaminants from the Mg beam.

^{31}Na, was the most dominant species in the 31 u RIB beam, therefore resulting in a the smallest total uncertainty achieved in this experiment. The Mass Ex-

Mass Number	Campaign	Relative systematic error	Final systematic error (keV)
31	2021	$8.40{\cdot}10^{-8}$	2.43
32	2021	$9.08{\cdot}10^{-8}$	2.71
33	2021	$8.37{\cdot}10^{-8}$	2.57
34	2021	$8.37{\cdot}10^{-8}$	2.65
34	2022	$1.12{\cdot}10^{-7}$	3.56
35	2021	$8.36{\cdot}10^{-8}$	2.73
35	2022	$1.13{\cdot}10^{-7}$	3.69
36	2022	$1.07{\cdot}10^{-7}$	3.58

Table 5.2: Total systematic uncertainty for each mass unit. The uncertainty from opening the ejection mirror dominates the total systematic uncertainty in both measurement campaigns.

cess (ME) value and its uncertainty can be seen in Tab. 5.3. Our uncertainty is dominated by the systematic uncertainty of the mirror voltage switching and the result is within 1σ agreement with the literature value, in Tab. 5.3. For the data analysis, $^{1}H_{3}^{12}C^{16}O^{+}$ was used as the TRC calibrant, the peakshape calibrant and the mass calibrant.

^{32}Na was delivered to TITAN at a rate of 0.5 pps. Due to the low count rate of the isobaric species at mass 32 u (total incoming rate was $\approx$ 3 pps), stable beam from MR-TOF MS's thermal ion source was merged with the RIB beam [217]. This allowed us to use $^{39}K^{+}$ as the TRC calibrant, injected at a rate of 56 pps. The achieved resolving power provided by performing the TRC with a high statistics peak, allowed for the resolution of two peaks instead of one in the position where ^{32}Na was expected. The two peaks have been fitted with Eq. 5.2 and based on the fit results, they are separated by 117.6(8.4) keV. The literature value for ^{32}Na lies in-between the two fitted values, as can be seen in Fig 5.5. Possible explanations of the origin of the second peak are described below.

- **Stable or radioactive molecule of mass 32 u:** One of the peaks corresponds to ^{32}Na and one to a stable molecule of mass 32 u. Only the mass of the molecule $^{2}H^{7}Li^{23}Na^{+}$ closely matches the first peak in Fig. 5.5. However, it is too light, and therefore we exclude it from the potential candidates. The possibility of a radioactive molecule was additionally investigated. However,

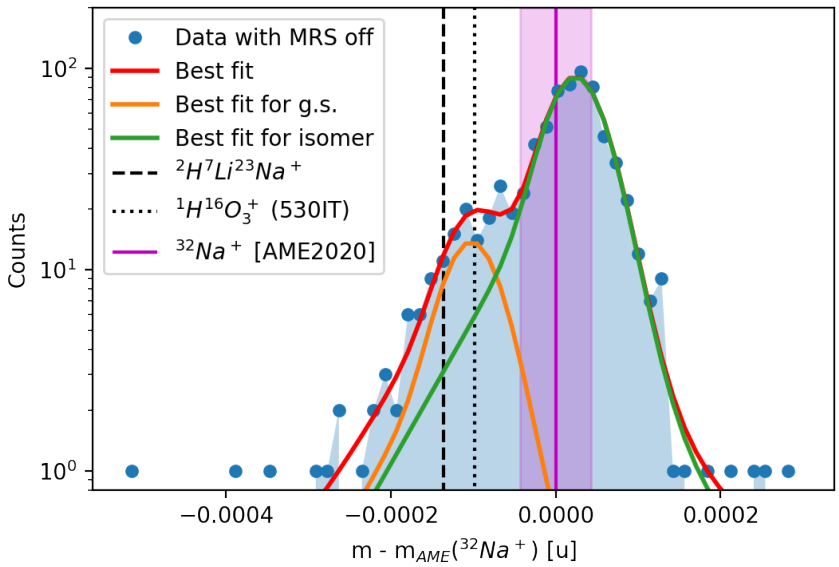

Figure 5.5: The final mass spectrum of $^{32}Na^{+}$. Individual and combined fit lines are shown in orange, green and red respectively. The literature mass of $^{32}Na^{+}$ is marked with purple. Other species with similar m/q are denoted with vertical lines.

no reasonable ($t_{1/2} \geq 10$ ms) molecules were found to match the mass of the peak under discussion.

- **Doubly charged ions:** One of the peaks corresponds to species of ^{32}Na and the other peak to a doubly charged ion of mass 64 u ($m/q = 32$). Since a doubly charged ion ($q = 2e$) with $A = 64$ has the same m/q with a singly charged ion ($q = 1e$) with $A = 32$, a doubly charged ion produced in the ISAC target can be transported and delivered to the MR-TOF MS. Previous MR-TOF MS experiments have detected doubly charged ions produced by ISAC. However, no doubly charged species are observed in the mass spectrum and there are no doubly charged ions that match the mass of either two candidate peaks.

- **Molecules of a different mass:** One of the peaks corresponds to ^{32}Na and one to a stable molecule of mass different from 32 u. As mentioned in

Chapter 3, non-isobaric species are removed from the mass analyzer of the MR-TOF MS using the MRS electrode. However, in order to use $^{39}K^{+}$ as a calibrant the MRS electrode could not be used. Therefore the mass spectrum can contain species of any other mass that performs a different number of turns in the MR-TOF MS. The position of the first peak matches with the position of a $^{1}H^{16}O_{3}^{+}$ molecule at 530 turns, as can be seen in Fig 5.5. As it is explained in the rest of this section, this scenario can be excluded based on an MRS on measurement that followed the main MRS off measurement.

- **Unknown Na isomer:** It is possible that the first peak belongs to the ground state of ^{32}Na and the second peak belongs to an unknown ^{32}Na isomer. This hypothesis would require independent verification of such an isomer.

In order to investigate the third scenario; the presence of a molecule of a different mass, we need a high statistics (N$\geq$ 500 counts in the mass region of question) measurement using the MRS electrode. This was not performed during the experiment as there was no identified scientific interest at this mass. The only spectrum that was taken is a low statistics measurement, that can be seen in Fig. 5.6. This measurement included 86 detected $^{32}Na^{+}$ ions and 344 total ions. Fig. 5.6 shows a single (black) and a double (red) fit on the data of the MRS on measurement. The comparison between the fits and the data favours the existence of two peaks in the spectrum instead of one. As a result, both peaks have to be of $m/q = 32$ and therefore the presence of $^{1}H^{16}O_{3}^{+}$ ($m/q = 49$) can be excluded. However, due to the low number of counts in this measurement, hypothesis testing [9] was performed to further evaluate whether there are two peaks in the spectrum. The result, as described in the next paragraph, verified that there are two peaks in the spectrum and thus excluded scenario three.

Hypothesis testing has been implemented in the EMFGfit package [201]. In our test, the null hypothesis corresponds to the case where there is only one peak in the spectrum while the alternative hypothesis corresponds to having two peaks. A 3σ significance is required in considering which hypothesis is true. The probability is determined as the fraction of times that the simulated LLR exceeds the observed LLR. The simulated LLR is determined with two different methods. The first uses the Monte Carlo method to calculate the LLR distribution from the best-fit model

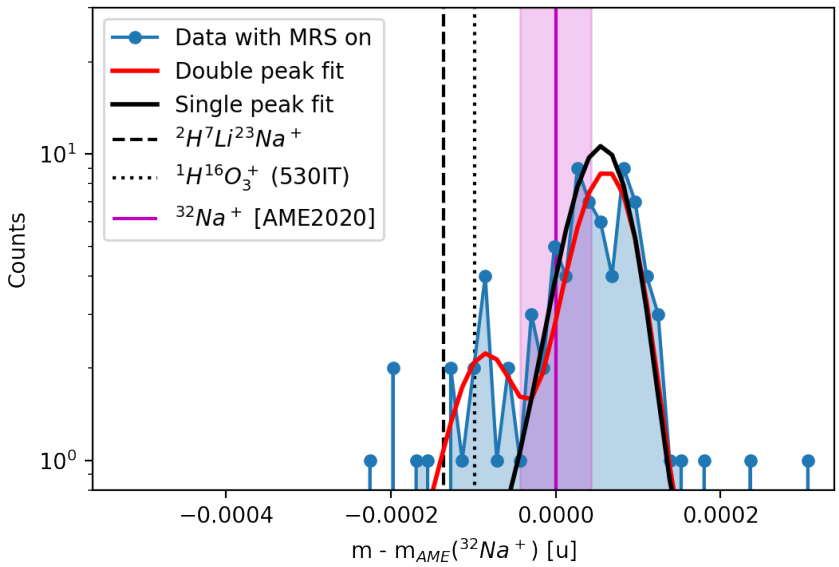

Figure 5.6: Mass 32 u spectrum with MRS on. Fits with a single (black) and a double peak (red) are shown.

of the null hypothesis, while the second method uses Multiple hypothesis testing, where multiple LLR distributions are derived for different positions in the mass spectrum. Plots of the simulated LLR distributions for the two methods compared to the observed LLR value can be seen in Fig. 5.7. The results reveal that there are indeed two peaks in the spectrum with a 4σ significance and therefore, we conclude both species have to be isobaric ($m/q = 32$), with the first peak corresponding to the ground state of ^{32}Na and the second peak corresponding to a low-lying unknown isomer of ^{32}Na, with an excitation energy of 117.6(8.4) keV.

^{33}Na was the last Na isotope that was measured during the experiment. The average count rate was approximately 0.01 pps. In total, we collected 200 counts of ^{33}Na which resulted in determining the mass with an uncertainty of 4.3 keV. $^{1}H^{16}O_{2}^{+}$, produced from MR-TOF MS's Electron Impact Source (EIS) was used as a TRC calibrant and $^{1}H^{32}S^{+}$ was used as the peakshape and mass calibrant. The EIS uses thermally emitted electrons from a tantalum cathode in order to ionize background molecules in the MR-TOF MS vacuum. Our result for the mass of ^{33}Na

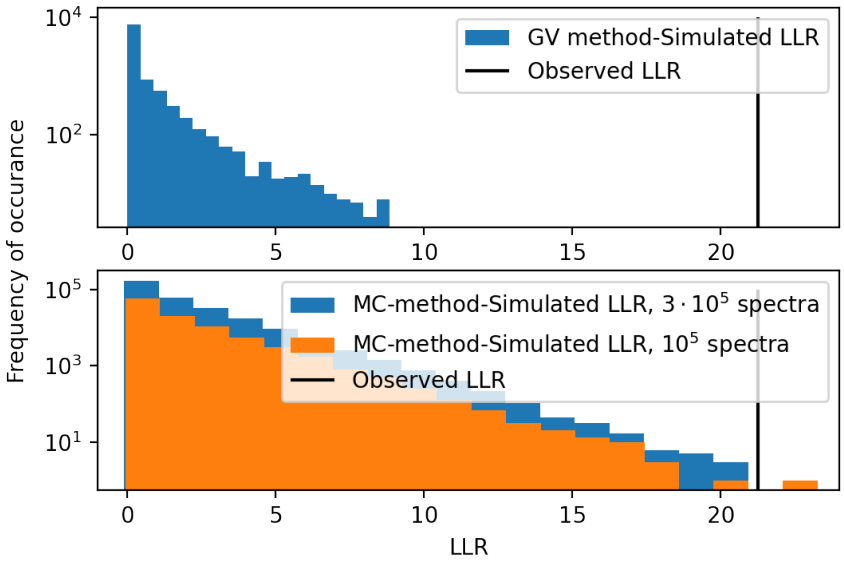

Figure 5.7: Simulated LLR distributions in comparison with the observed LLR value for the Multiple Hypothesis (top) and the Monte Carlo method (bottom).

is in agreement with the literature value published in the 2020 Atomic Mass Evaluation (AME) [264] (AME2020) shown in Table 5.4 [264]) and it improves the precision by two orders of magnitude. A comparison of the results with literature values is shown in Fig. 5.8.

The literature mass values of Na isotopes for masses 31 u and 32 u originate from previous TITAN mass measurements, where the Penning trap was used. The mass values derived from that measurement campaign can be seen in Fig. 5.8 in orange. In both cases, the TOF-ICR method with a 20 ms excitation was used [103], due to the short half-life of the two species ($t_{1/2} = 17.0(4)$ ms for ^{31}Na [114] and $t_{1/2} = 13.2(4)$ms for ^{32}Na [259]). A 20 ms TOF-ICR excitation corresponds to a FWHM ≈ 50 Hz, which corresponds to a resolving power of:

$$R = \frac{m}{\Delta m} = \frac{\nu_c}{\Delta \nu_c} = 36,000 \tag{5.7}$$

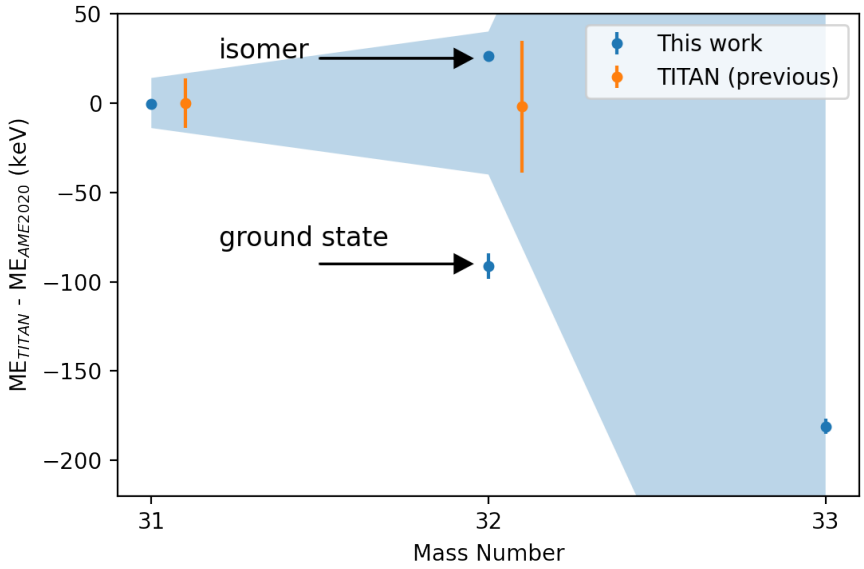

Figure 5.8: Deviation from AME2020 [264] for the Na masses measured in this experiment (blue). Previous mass values from TITAN are plotted in orange and are depicted at a positive offset from the integer mass number for easier comparison with the results of this work. The light blue colored area corresponds to the AME2020 mass uncertainty.

Mass Number	ME (keV)	unc. (keV)	ME$_{AME}$ (keV)	unc.$_{AME}$ (keV)
31	12245.3	2.6	12246	14
32	18548.7	7.7	18640	40
32	18666.3	3.3	18640	40
33	23599.0	4.3	23780	450

Table 5.3: Mass excess value of the Na isotopes measured in this work. The last two columns correspond to literature values from AME2020 [264].

In order to separate a $\sim$120 keV isomer from the ground state, the resolving power needed is $R = 250,000$, which justifies why the isomer was not observed in [103]. Further evidence for the existence of a low-lying isomeric state in ^{32}Na is provided by theoretical calculations [259] which are mention in more detail in the Discussion of Results (Section 5.6).

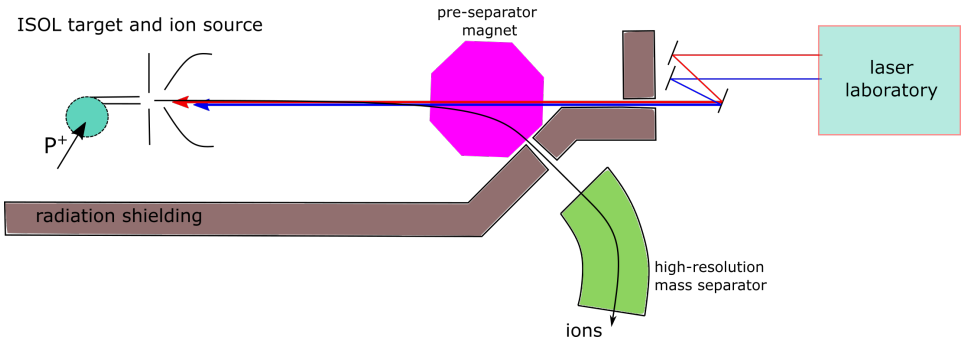

Figure 5.9: Schematic of the TRILIS ion source at ISAC. A two or three step ionization laser scheme is directed through the pre-separator magnet to the isotope production target. Due to their positive charge, ionized isotopes are extracted through the high-resolution mass separator and delivered to ISAC experimental apparatuses. Figure adapted from [161].

5.5 The magnesium isotopic chain

The magnesium isotopes were selectively ionized with the use of the TRILIS ion source [170]. A schematic of the TRILIS ion source is depicted in Fig. 5.9. Ionization takes place by applying a resonant two or three step ionization scheme. This allows us to unambiguously identify whether the beam contains Mg isotopes as resonant ionization can be interrupted by blocking one of the three laser beams. A comparison of the composition of the RIB with all lasers unblocked and with one of the lasers blocked can be seen in Fig 5.10.

The mass values of $^{31-33}$Mg are all measured to a precision of 3 keV by previous TITAN [57] and MISTRAL [104, 171] measurement campaigns. Our results agree within two sigma with the measured values. ^{34}Mg has been previously measured to a precision of 29 keV at TITAN [57]. The AME-2020 quotes a 7 keV precision, due to the precisely known Q_{β^-} energy [264] from beta-decay spectroscopy. Our result improves the precision from 7 keV to 3.7 keV and agrees within two sigma with the AME value.

In contrast to $^{31-34}$Mg, ^{35}Mg had not been previously measured in a Penning trap. Jurado et al. [133] measured the isotope using TOF mass spectrometry at GANIL with a precision of 180 keV. Due to an almost 2 MeV discrepancy from a previous mass measurement [198], its overall precision quoted at the AME2020 is

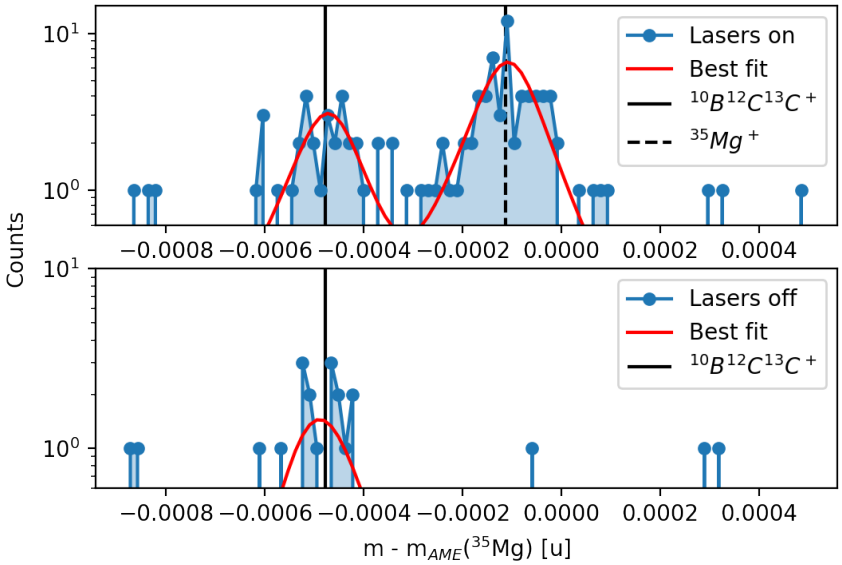

Figure 5.10: Laser on/off comparison for $^{35}Mg^+$. The top plot shows the the mass spectrum with lasers on while the bottom plot shows the mass spectrum with lasers off. The two plots contain different amounts of statistics.

270 keV.

After both the 2021 and 2022 measurement campaigns, we were able to collect a total of 120 counts of ^{35}Mg. The presence of ^{35}Mg was verified by comparing the mass spectrum with and without laser ionization of Mg, as can be seen in Fig. 5.10. This measurement, allowed us to determine the mass of ^{35}Mg to a precision of 6.4 keV, almost a 50-fold improvement from its previous mass precision. Our mass value is 106.3 keV lower than the one in AME2020 [264].

The comparison between the literature values and the results of this work for the Mg isotopic chain can be seen in Fig. 5.11.

The mass measurement of ^{36}Mg was attempted in the 2022 TITAN measurement campaign. In the AME2020 evaluation [264], the mass of ^{36}Mg is determined by combining the measurements published in [133, 228, 229] and the reported ME value is 20380(690) keV.

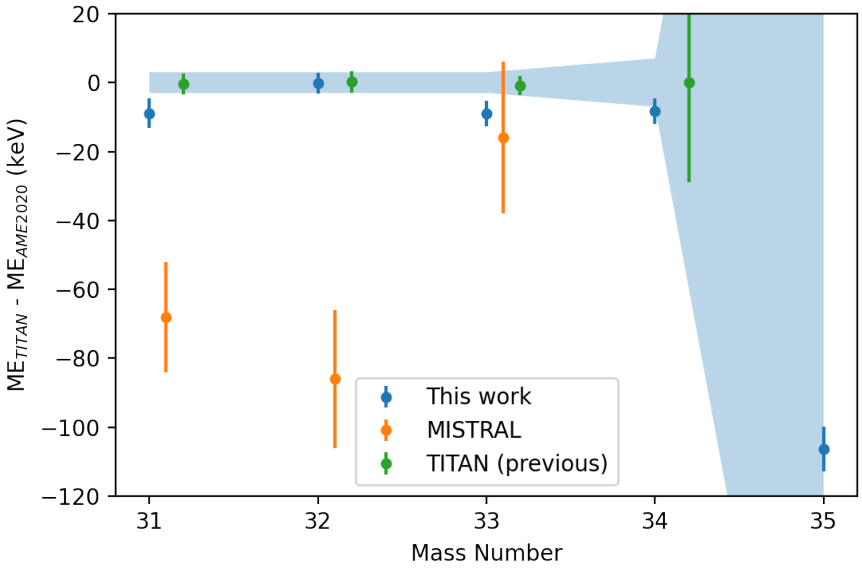

Figure 5.11: Deviation from AME2020 [264] for the Mg masses measured in this experiment (blue). Previous mass values from MISTRAL [104] are plotted in orange, while previous TITAN [57] results are plotted in green. Both the MISTRAL and the previous TITAN results are depicted at a positive offset from the integer mass number for easier comparison with the results of this work. The light blue colored area corresponds to the AME2020 mass uncertainty.

Mass Number	ME (keV)	unc. (keV)	ME_{AME} (keV)	$unc._{AME}$ (keV)
31	-3130.9	4.3	-3122	3
32	-829.2	3.0	-829	3
33	4954.0	3.7	4963	3
34	8314.8	3.7	8323	7
35	15533.7	6.4	15640	270

Table 5.4: Mass Excess values of the Mg isotopes measured in this work. The last two columns correspond to the literature values from AME2020 [264].

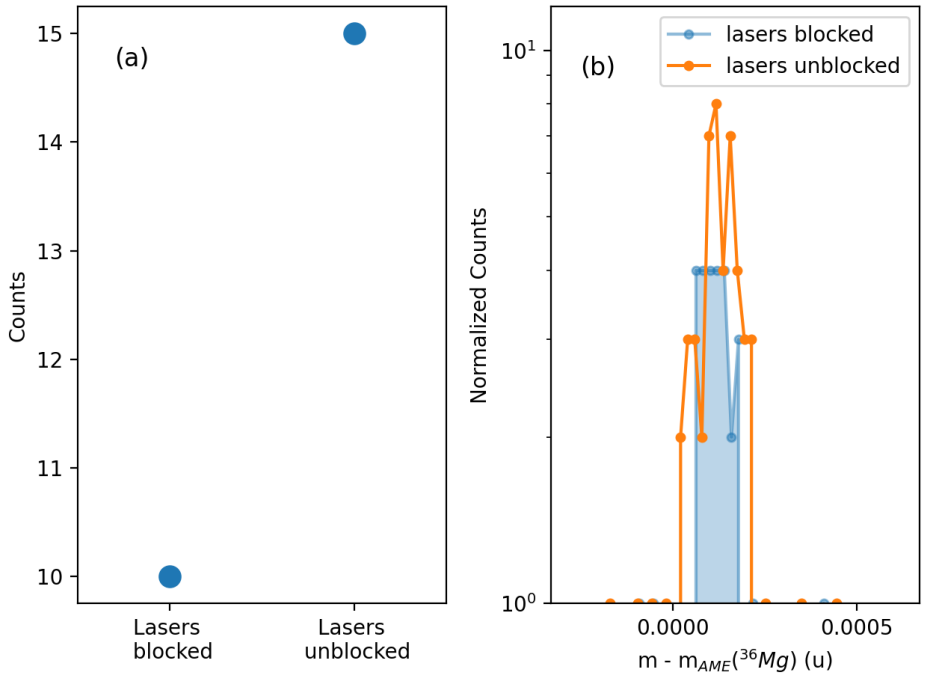

Figure 5.12: (a) Count rate comparison for lasers blocked/unblocked settings for ^{36}Mg. (b) The ^{36}Mg candidate peak under different laser settings.

During the TITAN measurement campaign, a peak of $ME = 20496.8(7.7)$ keV was detected which is within one sigma of the AME2020 [264] mass value for ^{36}Mg and therefore could potentially correspond to ^{36}Mg. In the following, the origin of the detected peak is investigated.

Lasers on/off effect

Measurements with lasers blocked and lasers unblocked were compared to determine if the peak under question corresponds to laser-ionized species, specifically ^{36}Mg. As can be seen in Fig. 5.12 (a) there is a 1/3 count rate difference between lasers on and lasers off measurements. However, there is a consistent peak that is formed in both cases as can be seen in Fig. 5.12 (b).

A comparison with the laser effect for ^{35}Mg (Fig. 5.10), where there is almost an order of magnitude reduction in count rate when the laser beam is blocked,

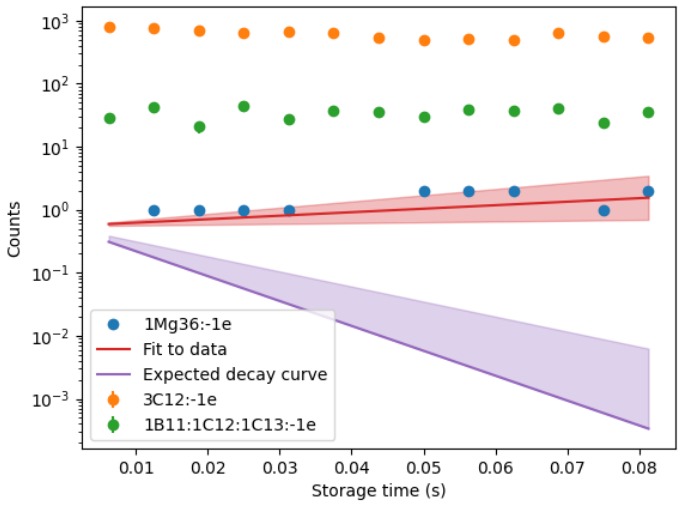

Figure 5.13: Count rate for all species in the mass spectrum of ^{36}Mg as a function of the storage time. The red band corresponds to the fit uncertainty while the purple band depicts the influence of the uncertainty of the half-life of ^{36}Mg on the estimated count rate.

supports the argument that the peak in question does not belong to ^{36}Mg.

Storage time measurement

^{36}Mg has a half-life of 7.6^{+5}_{-8} ms [246]. Therefore, its existence in the TITAN MR-TOF MS could be verified by storing it in the MR-TOF MS RFQ injection trap for different storage times and comparing the count rate for each storage time. If it would be delivered and stored, we would expect an exponential decay of the measured rate as a function of the storage time, with a decay constant equal to $-\ln 2/t_{1/2}$, where $t_{1/2}$ the half-life or ^{36}Mg. The count rate of the peaks that were detected at 36 u as a function of the storage time can be seen in Fig 5.13.

The rate of ^{36}Mg remains consistent with storage time. An exponential fit to the Mg counts indicates a positive decay constant with a 1.5σ confidence level supporting the idea that the measured isotope is not decaying within the measurement timescale. Inconsistencies of the ISAC rate interfering with the storage time mea-

surement can be excluded by observing the rate of the $^{11}B^{12}C^{13}C^{+}$ molecule which was delivered from ISAC. Since the rate of this stable molecule remains constant there were no significant rate fluctuations during the measurement.

The expected decay rate based on the reported half-life of ^{36}Mg [246] can be seen in Fig. 5.13 in purple. The purple band represents the positive 1σ uncertainty of the half-life. The experimental and literature decay constants deviate by more than 10σ and therefore, we conclude that the detected peak does not correspond to ^{36}Mg.

Alternative explanation for the observed peak

There are three singly charged molecules with mass that matches the peak of question within the achieved precision (7.7 keV):

- $^{1}H^{6}Li^{12}C^{17}O^{+}$
- $^{1}H_{3}^{7}Li^{26}Mg^{+}$
- $^{10}Be_{2}^{16}O^{+}$

If the observed peak corresponds to $^{1}H^{6}Li^{12}C^{17}O^{+}$, then the more abundant $^{1}H^{7}Li^{12}C^{16}O^{+}$ should also appear at the mass spectrum, as ^{16}O is 2,500 times more abundant than ^{17}O [264]. Due to the lack of $^{1}H^{7}Li^{12}C^{16}O^{+}$, we can exclude the first molecule.

On the other hand, $^{1}H_{3}^{7}Li^{26}Mg^{+}$ is the most abundant at mass 36 u but ^{24}Mg is eight times more abundant than ^{26}Mg and therefore $^{1}H_{3}^{7}Li^{24}Mg^{+}$ at mass 34 u would be expected. However, for both $^{1}H_{3}^{7}Li^{24}Mg^{+}$ at 34 u and $^{1}H_{3}^{7}Li^{25}Mg^{+}$ at 35 u, $(m_{Mg^{+}} - m_{molecule})/m_{Mg^{+}} > 2000$ and therefore the two molecules are not transported through the ISAC mass separator. For this reason, we cannot exclude $^{1}H_{3}^{7}Li^{26}Mg^{+}$ as the identity of the peak in question.

In other TITAN experiments we have seen Be ions binding with oxygen to form BeO molecules, thus making $^{10}Be_{2}^{16}O^{+}$ another possible candidate. As a result, it is inconclusive whether the peak stems from ^{36}Mg. It is more likely that it belongs to $^{1}H_{3}^{7}Li^{26}Mg^{+}$ or $^{10}Be_{2}^{16}O^{+}$.

In conclusion, the two Mg, Na experimental campaigns enabled us to reduce the uncertainties of ^{34,35}Mg and ^{31,33}Na to values below 10 keV. The derived ME

values and their comparison with literature values can be found in Tables 5.4, 5.3 for the Mg and Na isotopes respectively. In addition, a double peak with a similar mass value to ^{32}Na suggests that we measured a previously unknown 117.6(8.4) keV isomer of ^{32}Na. Finally, the presence of ^{36}Mg in the experimental data was investigated, ultimately pointing towards the absence of ^{36}Mg in the data.

5.6 Discussion of Results

With the analysis completed, final mass values and uncertainties can be assigned and a number of secondary values can be derived. A key value in nuclear structure is the two-neutron separation energy. The two neutron separation energy can be determined using Eq. 2.1:

$$S_{2n} = BE(N,Z) - BE(N-2,Z) \tag{5.8}$$

where $BE(N,Z)$ is the binding energy of a nucleus with Z protons and N neutrons. The new values are plotted along with the literature values in Fig. 5.14.

The TITAN results are in good agreement with the well-known literature values [264] ($N = 19-22$ for Mg and $N = 20$ for Na). For the neutron numbers where the S_{2n} is not precisely known from literature ($N = 23$ for Mg and $N = 21-22$ for Na), the TITAN result reveals an increase in stability, as indicated by the higher two-neutron separation values, in agreement with the extended deformation beyond the $N = 20$ island on inversion [54]. The following two sections discuss the impact of the result on the southern border of the island of inversion and further explore the observation of a new isomer for ^{32}Na.

5.6.1 The $N = 20$ island of inversion

Evidence of the island of inversion through mass measurements can be observed through the empirical shell gap, as discussed in Chapter 2. The empirical shell gap is given by:

$$\Delta_{2n} = S_{2n}(N,Z) - S_{2n}(N+2,Z) \tag{5.9}$$

Fig. 5.15 shows the empirical shell gap for the $N = 20$ isotones, where the result of this work is plotted in red. The precisely determined mass value for ^{33}Na, now

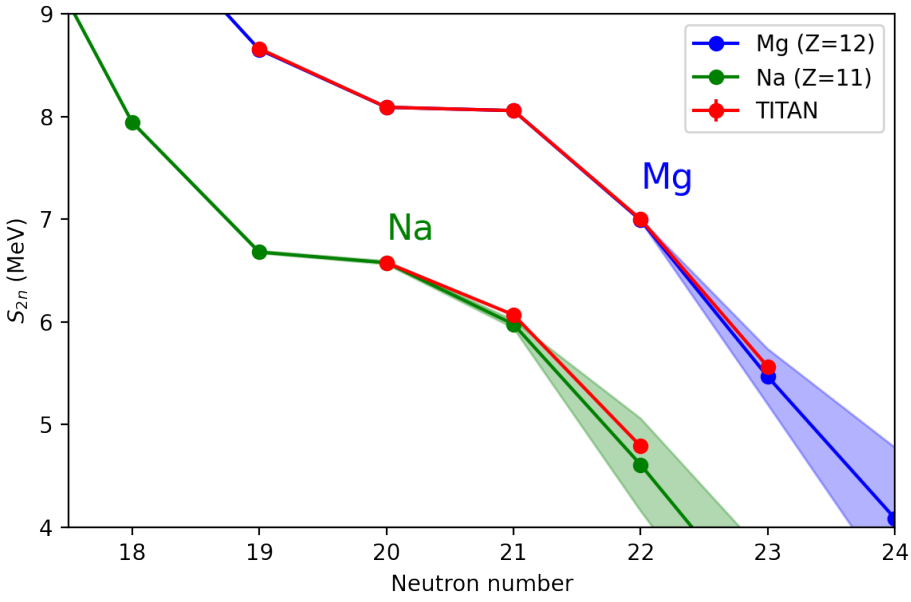

Figure 5.14: Two-neutron separation values in the island of inversion. The results of this work are plotted in red. The colored bands show the uncertainty of the two-neutron separation derived from literature values [264].

gives clear evidence of an increase in Δ_{2n}. As can be seen in Fig. 5.15, typical neutron magic nuclei demonstrate an empirical shell gap of 4-5 MeV. However, for $Z \leq 15$, the empirical shell gap starts to drop and reaches a value of $\sim$ 1 MeV for Mg, which demonstrates that $N = 20$ is no longer a magic number. For the Na isotopes ($Z = 11$), the literature values result in a 1 MeV increase compared to Mg as can be seen in Fig. 5.15 (right). However, the uncertainty of this value was previously dominated by the uncertainty in the mass of ^{33}Na. Our improved mass uncertainty shows that the empirical shell gap increases by 688(9) keV compared to Mg and thus suggests that the maximum quenching occurs at $Z = 12$. As a result, we can conclude that the quenching of the $N = 20$ shell closure starts to weaken for $Z \leq 11$ resulting in a gradual resurrection of magicity at N = 20.

This result is critical in determining the southern border of the island of inversion which still remains hidden. Christian et al. [62] suggest that the fluorine

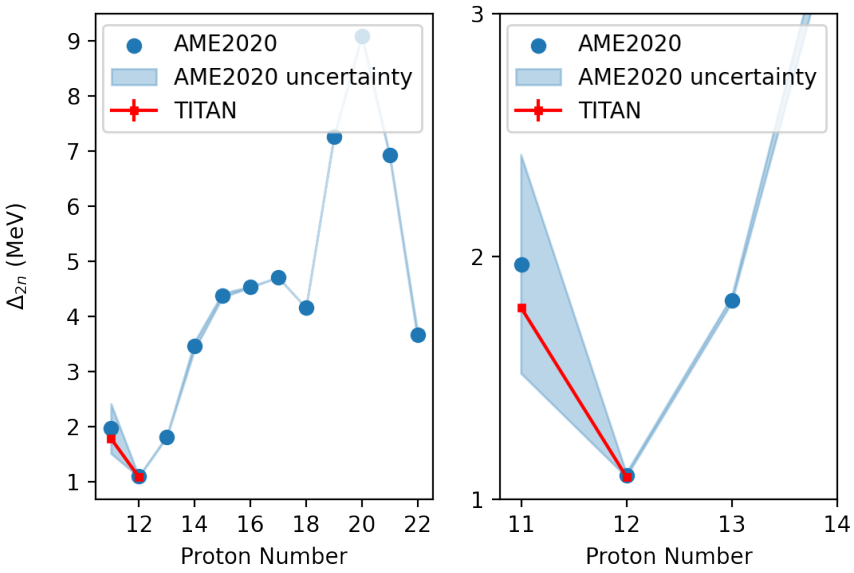

Figure 5.15: Values of the empirical shell gap for the $N = 20$ isotones. The result of this work is plotted in red.

isotopes lie at the limit of the island of inversion. However, more recent studies [220] support that the island of inversion extends beyond the fluorine isotopes and thus challenge the magicity of ^{28}O. Our result, suggests that there is a gradual regain of magicity for $Z \leq 11$ which indicates that the island of inversion may not extend to the neutron dripline.

Fig. 5.16 compares the experimental empirical shell gap with ab-initio theory calculations [250]. Although the precision of theoretical ab initio calculations is limited to $\sim 5\%$ [249], some conclusions can be drawn from the overall trend of the ab-initio results. In two regions the experimental data significantly deviate from the theoretical predictions and therefore are of high interest. The first is at $Z = 20$, where it can be observed that the ab intio calculations overpredict the magicity of the doubly magic ^{40}Ca, possibly due to the theory not taking into account a shell-diminishing effect. The second area of interest is the island of inversion (Z $\leq$ 13), where the ab-initio result reproduces the drop in the empirical shell gap but does not capture the increase for $Z = 11$, as observed in the experiment. The

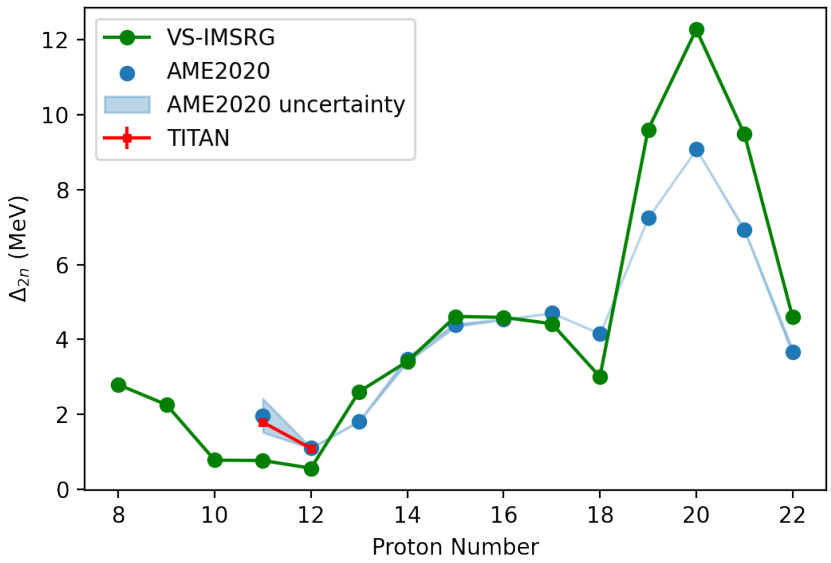

Figure 5.16: Experimental empirical shell gap along with theoretical values derived from ab initio calculations.

discrepancy with the experimental values becomes more prominent at the theoretical two-neutron separation energies in Fig. 5.17. Although theory and experiment agree for $N \leq 18$ and $N \geq 23$, the ab-initio theoretical model shows the opposite trend in the island of inversion. This discrepancy can be either the result of a phenomenon that has not been taken into account in the theoretical calculations or the result of including a phenomenon that is not present in the physical system. Both scenarios point towards the need for more accurate microscopic calculations in the region.

5.6.2 New isomer of Na

It has recently been suggested [109] that there is an isomeric state of ^{32}Na based on theoretical calculations performed with the Monte Carlo Shell Model (MCSM) method [109]. Tripathi and collaborators [259] provide tentative spin assignments for ^{32}Na. Using MCSM calculations, they find that the ground state of ^{32}Na could

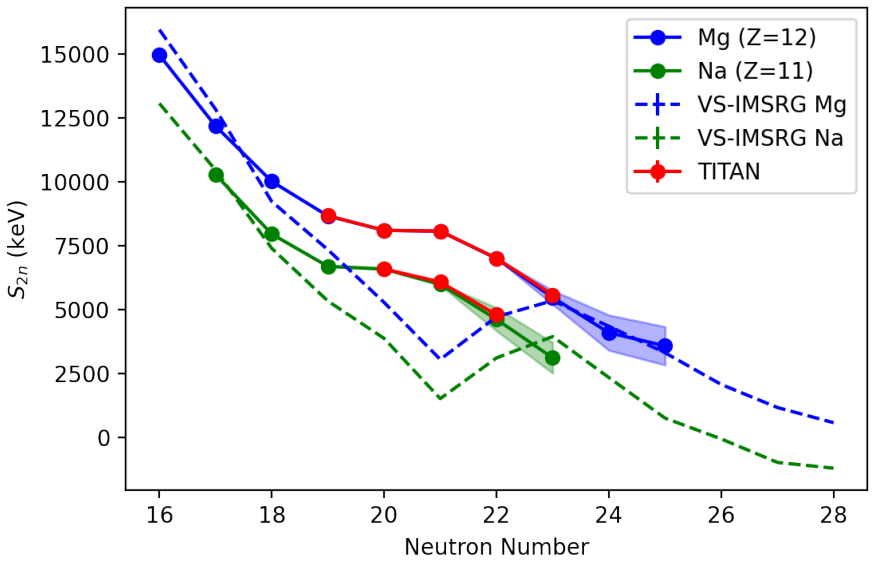

Figure 5.17: Theoretical and experimental two neutron separation energies of Mg and Na isotopes near the island of inversion. The results of this work are represented with red data points, while the theoretical results are depicted with dashed lines.

be either a 3^- or a 0^-. In a deformed nucleus, such as ^{32}Na, and due to the fact that the two states lie very close to each other, they suggest that it could give rise to a long-lived isomer that would decay with an electromagnetic transition.

This interpretation agrees with our experimental finding of a previously unknown isomer of ^{32}Na with an excitation energy of $\sim$ 120 keV. In addition, the literature mass value of ^{32}Na comes from a previous TITAN mass measurement using the Penning Trap [103]. The experimental conditions, specifically the excitation time used in that measuement did not provide for enough resolution to separate a potential 120 keV isomeric state and hence, it is not in disagreement with our present result.

At this point, we suggest that the extra peak in the ^{32}Na spectrum is assigned to be a long-lived isomeric state of ^{32}Na, the first to be discovered in the Na isotopes within the island of inversion.

Chapter 6

Exploring the limits of existence of heavy proton-rich nuclei

6.1 Network calculations using the AME algorithm

The Atomic Mass Evaluation (AME) was first created in the 1950s to meet the demand for a complete and reliable database that contained all experimentally measured masses. The first evaluation was published in 1960 in Nuclear Physics [92] and it is since being updated and improved almost every 4 years. The latest evaluation of mass data was published in 2020 [264], and is referred to as AME2020.

6.1.1 General aspects of the AME procedure

The Atomic Mass evaluation is derived from a large reaction network containing experimental mass values and decay energies. The experimental masses are the quantity of interest while the decay energies are the links between these masses. Nuclei in the network are divided into two categories: primary and secondary. The primary nuclei are the ones that can be accessed through more than one link to other nuclei while secondary are those that are determined by a single link. The links can be any type of decay (alpha, beta, EC, proton decay etc.) as long as their decay energy is experimentally measured. Direct mass measurements can act both as primary or secondary data depending on the number of known links between

them and their neighbours [264].

To achieve greater calculation efficiency, the secondary data are separated from the primary ones and removed from the network calculation. What remains is an over-determined system of linear equations that are connecting the properties of primary nuclei:

$$\mathbf{K}\,|m\rangle = |E\rangle \tag{6.1}$$

where $\mathbf{K}$ is the connectivity matrix, $|m\rangle$ are the masses that are being adjusted and $|E\rangle$ is the array of the decay energies. The entered masses m originate both from direct measurement methods (the measurement quantity is the inertial mass) or from indirect ones (the measurement quantity is a reaction Q-value from which the mass is determined) and they are usually entered in form of ratios m/m_{ref}, where m_{ref} is the mass of a reference isotope measured with the same method and system as the IOI. The inclusion of mass ratios instead of absolute masses allows the update of masses whose reference value is improved or changed in the future. This system of equations (eq. 6.1) is solved using least-squares minimization, while the equations entering the minimization are weighed based on the precision of their parameters.

One critical factor of the mass adjustment procedure is to maintain the "smoothness" of the mass surface. The mass surface can be visualized as surface plot where N and Z are on the X and Y axes while the mass is on the Z-axis. Due to nuclear pairing, this surface plot is in reality 4 surface plots running in parallel to each other, on four 'elevation levels' : a) a contour of even-even nuclei, which has the lowest mass values, b) a contour of odd-odd nuclei, which has the highest mass values and c,d) two contours of even-odd and odd-even nuclei that have intermediate mass values. The behaviour of these contours as a function of Z and N is smooth except for the points of sudden change in nuclear structure such as shell closures or deformation. This has two very interesting consequences:

- It allows for predictions of unknown masses based on the regularity of the mass surface. These predictions are useful in areas where there are no sudden nuclear structure changes as they give a guideline to the experimentalists for what mass to expect.

- Consistent experimental deviation from the predicted masses indicates the

emergence of a nuclear structure effect that was not expected in the framework of the current theories. This effect can be detected in the AME evaluation by sharp unaccounted changes in the otherwise smooth mass surface.

6.1.2 A special case

A special area in the nuclear chart and the AME network is that of proton-rich nuclei around $A = 170$. This area is dominated by long alpha chains that span more than 10 atomic numbers (Z) as well as by observed one-proton emitters. While alpha decay and proton decay energies have been well measured, the masses of the isotopes participating in these reactions often remain unknown, due to difficulties in their production as well as due to their short half-lives. This can be envisioned as a chain of nuclei that "floats" in the mass space. If at least the mass of one of these nuclei is experimentally measured, the reaction chain becomes anchored and all the masses can now be determined, as the energies connecting the involved nuclei are known.

The reactions that contribute to the chains in this area of the nuclear chart are β^+ decays, EC, alpha decays and proton decays. Therefore, the reaction links can be calculated as:

$$m(Z,A) - m(Z-1,A) = Q_{EC}/c^2 \tag{6.2}$$

$$m(Z,A) - m(Z-2,A-4) = Q_{\alpha}/c^2 + m(^4He) \tag{6.3}$$

$$-m(Z,A) + m(Z-1,A-1) = S_p/c^2 - m(^1H) \tag{6.4}$$

where $m(Z,A)$ the atomic mass of the parent nucleus, $m(Z-1,A)$, $m(Z-2,A-4)$, $m(Z-1,A-1)$ the atomic masses of the daughter nuclei, $m(^4He)$ and $m(^1H)$ the helium and hydrogen masses related to the emitted alphas and protons respectively and Q_{EC}, Q_{α}, S_p the Q-values and proton separation energies of the reactions. Decays to long-lived isomeric states are also considered if the excitation energies of those states are known.

6.1.3 Anchoring reaction chains with TITAN mass measurements

In order to provide anchor points for the "floating" chains of nuclei mentioned in the previous section, a mass measurement campaign was carried out. For the

experiment, the masses of the neutron-deficient $^{150-157}$Yb isotopes were measured with the TITAN MR-TOF MS [29]. These seven masses give access to six reaction chains, using the AME algorithm, three of which contain more than nine isotopes each.

A schematic of the reaction network can be seen in Fig. 6.1. Isotopes with the same color belong to the same reaction network and they are connected by EC, proton emission, or alpha decay as can be seen in the insert of Fig. 6.1. The anchors are depicted with diamonds while known proton emitters are depicted with x-symbols.

Previous to the TITAN mass measurements and the present network calculation, the masses of the isotopes in the reaction chain starting from ^{179}Pb (yellow) were known to a precision of 80 keV [264], the ones in the reaction chain starting from ^{172}Hg (pink) were known to a precision of 150 keV [264], while those in the chain starting from ^{173}Hg (blue) were never anchored and thus their masses were only extrapolated. In addition to these three long and largely unknown reaction chains, the measured masses of $^{150,151,156-157}$Yb anchor smaller reaction chains. The masses in the reaction chains starting from ^{156,157}Yb (brown) have an average uncertainty of 10 keV [264] while those in the reaction chain starting from ^{151}Lu are unknown and thus extrapolated.

The results of the network calculation using the mass measurements of $^{150-157}$Yb can be seen in the first two columns of Table A.1. The anchors that were used in this study from [29] are noted with an asterisk while values accompanied by the # symbols in the columns $ME_{AME2020}$ and its uncertainty $(unc.(keV))$ represent AME2020 extrapolations [264]. In total, considering all the Yb isotopes entered in the connection network, we were able to determine the mass of 11 new ground states and improve the precision of 9 other ground-state masses by more than a factor of 2 in the region between $Z = 71$ and $Z = 82$.

The deviation between the results of AME2020 and the present network calculation can be seen in Fig. 6.2. The green area represents the AME2020 uncertainty. The black data points correspond to masses the uncertainty of which was improved in this work while the red ones correspond to masses that were never measured before. Isotopes that demostrate similar deviations from their AME2020 mass values belong to the same reaction chain and their deviation is a result of the deviation

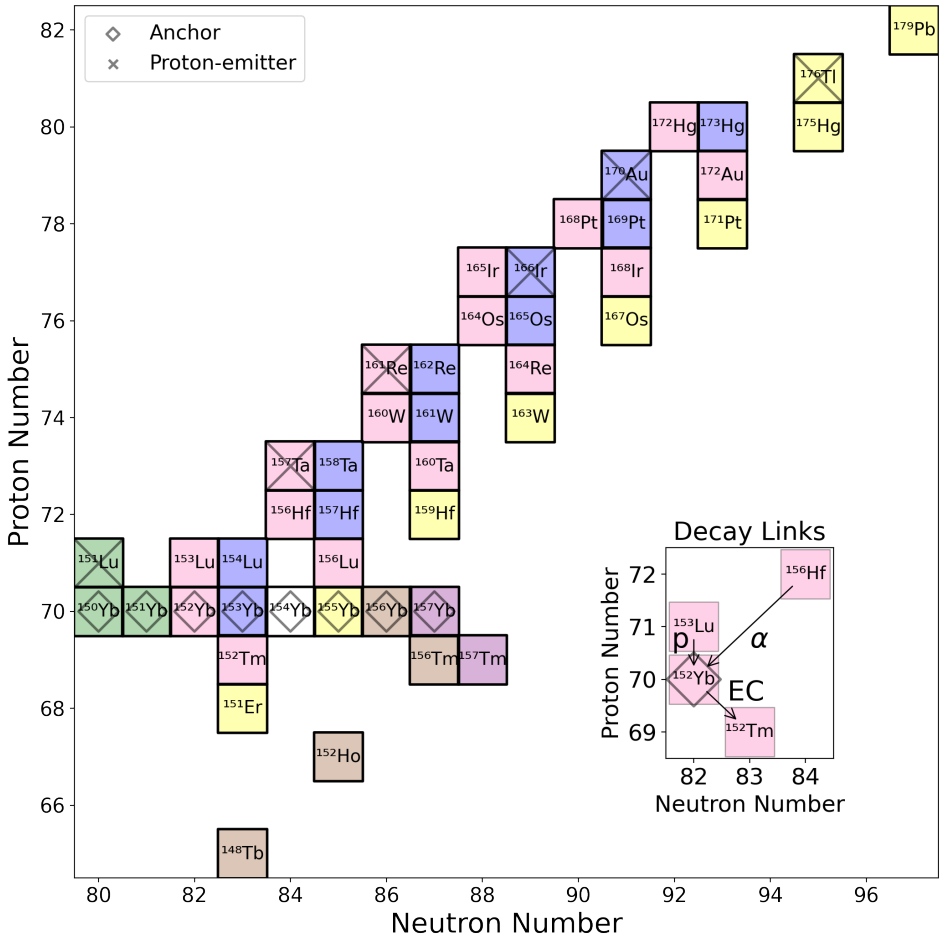

Figure 6.1: Connection diagram of all isotopes determined in this work, shown as a function of neutron (x-axis) and proton number (y-axis); all isotopes that share the same color (chains) are connected by known Q_α, Q_β or S_p. The masses of these isotopes are determined using known decay energies and the AME algorithm. The anchors of the chains are represented with diamonds, while one-proton emitters are marked with x-symbols. The insert shows an example of how nuclei link to ^{152}Yb.

in the mass of their common anchor from its literature value. Although there is a ~ 200 keV deviation for the masses related to the anchors ^{150,151,152}Yb, none of the masses deviates more than 1.5σ from it's previous measurement or prediction.

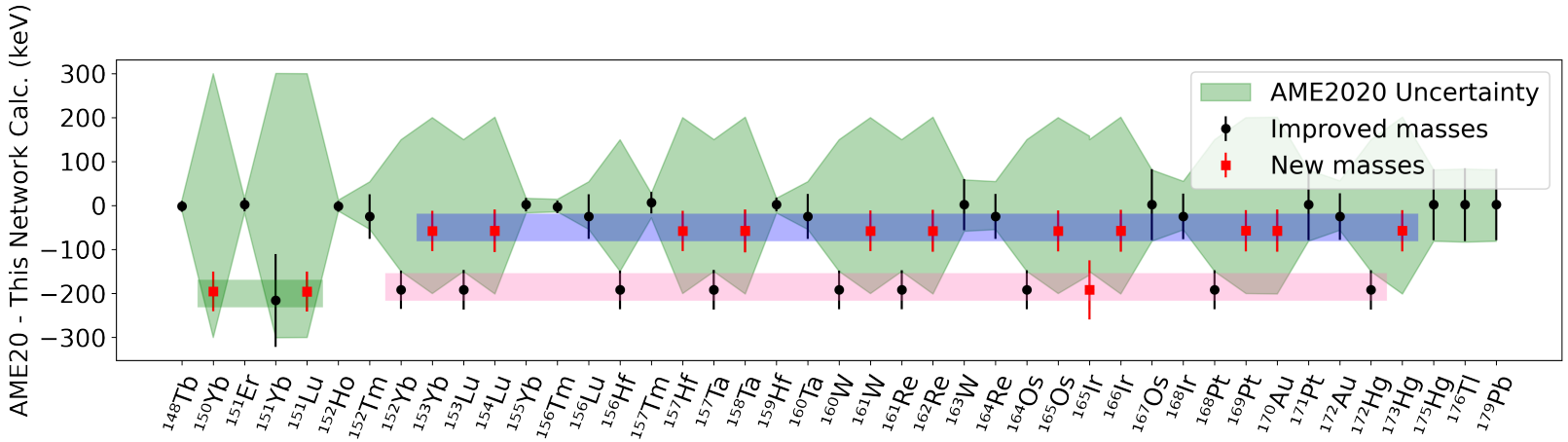

Figure 6.2: Comparison between AME2020 and the masses determined in this work. The green area indicates the AME2020 uncertainty. Nuclides with similar deviations belong to a common alpha chain and their deviation arises from the deviation in the mass of the alpha chain anchor. The mass values of the three alpha chains that deviate from AME2020 the most are grouped in a same-colored rectangles.

6.2 Evaluation of experimental results and comparisons with theory predictions

In the following sections, the mass excess values $ME = m - A$, where m is the atomic mass and A is the mass number, were used to calculate one and two-proton separation energies in order to locate the proton driplines. Based on the position of the two-proton dripline, the occurrence of heavy two-proton emitters is investigated. In addition, from the two-proton separation energies of the Lu isotopes the existence of the $N = 82$ shell closure in the vicinity of proton-rich nuclei is explored along with the possible appearance of Thomas-Ehrman shifts [64].

6.2.1 Driplines

The one- and two-proton separation energies are calculated based on Eq. 2.7 and 2.9. The list of the final results can be seen in the Appendix, in Table A.1. Figure 6.3, shows the overlap between the literature values and the results of this work for the one proton-separation energy.

Similarly with the ME deviations depicted in Fig. 6.2, a deviation in the anchor triggers a consistent deviation across a chain of nuclei as can be seen in Fig. 6.3 (bottom) for the isotopes belonging to the ^{152}Yb chain. In addition, the improvement in the precision of the S_p of the anchor, results in similar improvements in the presicion of the S_p of the other members of the chain.

Since the one-proton separation energies are one of the main inputs in the network calculation, this figure, mainly serves as a consistency check for the results to follow.

Fig. 6.4, compares the literature values with the results of this work for the two-proton separation energies. The individual results for each elements can be found below:

Ytterbium

The new mass measurement results allow for the calculation of S_{2p} for $N = 80$ and $N = 83$ for the first time since previously the masses of ^{150,153}Yb were unknown. In addition the precision of the S_{2p} for $N = 81$ was improved and that for $N = 82$ was derived for the first time from direct mass measurements.

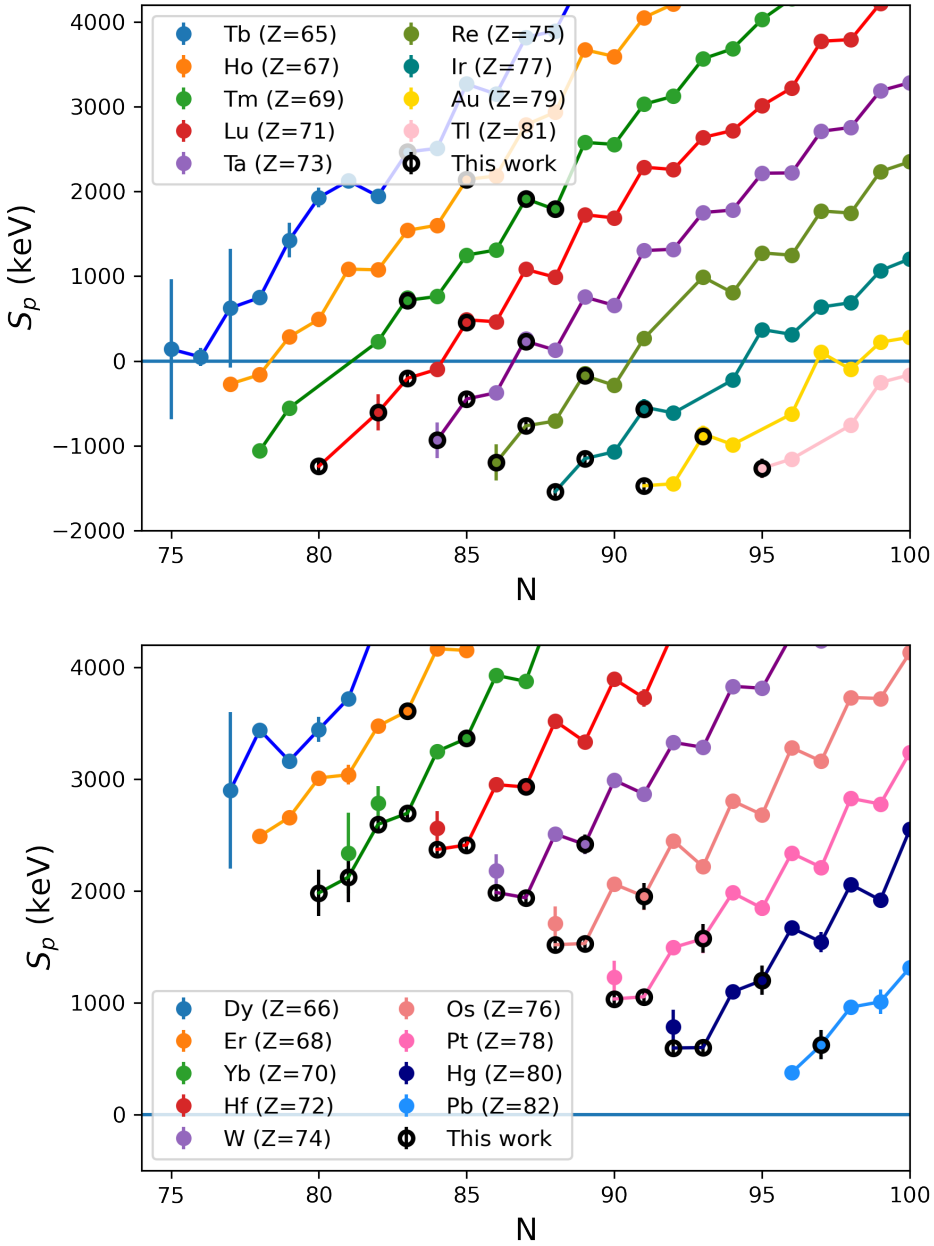

Figure 6.3: One-proton separation energy as a function of neutron number N for odd-Z nuclei (top) and even-Z ones (bottom). The results of this work are represented with black data points while all other data points were calculated using the AME2020. All data-points have been calculated using existent or new mass values and Eq. 6.4.

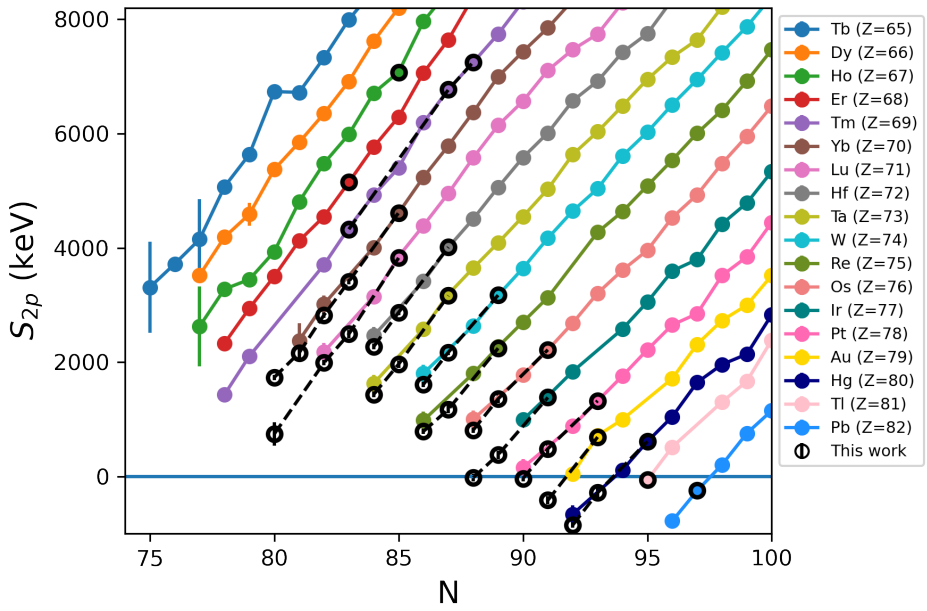

Figure 6.4: Two-proton separation energy as a function of neutron number N for elements of atomic numbers $Z = 65 - 82$. The colored data-points indicate two-proton separation energies derived from the literature mass values while the black data-points represent the results of this work.

Lutetium

Because of the known proton decay energy and EC decay energy of ^{151}Lu, its mass and its two-proton separation energy has been calculated. It is the lowest Lu-S_{2p} identified so far, only 742(205) keV above the two-proton dripline.

Iridium

The two-proton separation energy was determined for the first time for ^{165,167}Ir. As can be seen in Fig. 6.5, the two-proton separation energy of ^{165}Ir is found to be consistent with zero (-21(70) keV). Currently, the decay energy used in the network calculation is extrapolated rather than experimentally determined (#) and thus further confirmation is needed.

Platinum

The two-proton separation energy of ^{168}Pt was found to be -35(48) keV thus confirming it as the first possibly two-proton unbound Platinum isotope.

Gold

The first two-proton unbound gold isotope (^{170}Au) was determined. Its separation energy is -417(71) keV.

Mercury

The uncertainty of the two-proton separation energy of the two-proton unbound ^{172}Hg was improved to 48 keV from 150 keV [264] and the two-proton separation energy of the two-proton unbound ^{173}Hg was determined for the first time.

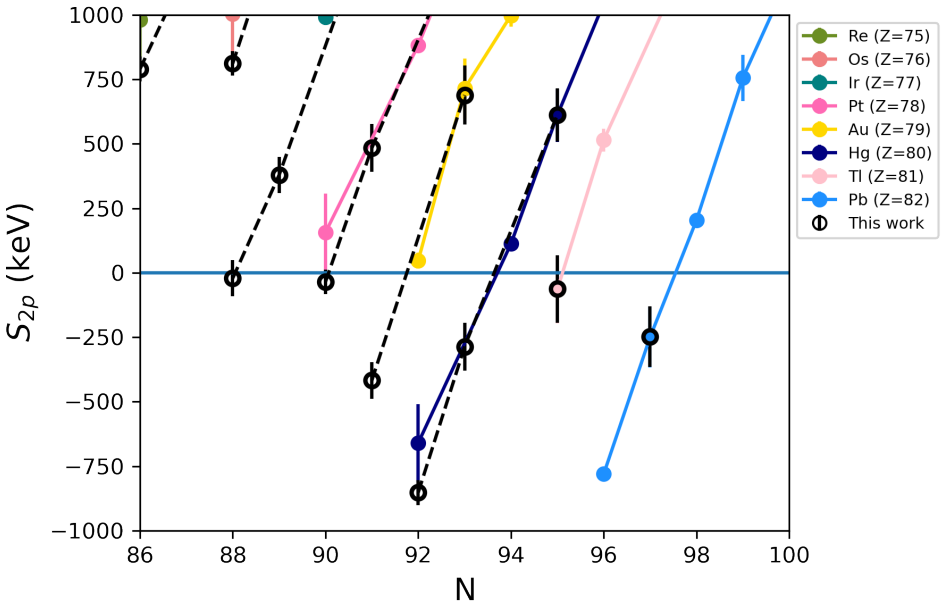

Figure 6.5: Zoomed in version of Fig. 6.4, showing the two-proton dripline for $Z = 75 - 82$.

In summary, seven two-proton unbound nuclei were found in this work, three

of which were determined for the first time (^{165}Ir, ^{170}Au and ^{173}Hg) while the two-proton dripline was located from $Z = 77$ to $Z = 82$. A color-coded perspective of the two-proton separation surface can be seen in Figure 6.6. The color corresponds to the magnitude and sign of the S_{2p}: positive S_{2p} are depicted with red-orange while negative ones are depicted with blue. The two-proton dripline can be seen by the transition from orange to blue for $Z = 77 - 82$. The results of this work are depicted with black outline while the other depicted two-proton separation energies are from AME2020 literature values.

Overlayed with the results of this work and the literature S_{2p} values, are theoretical two-proton dripline calculations of mean field and beyond mean field models using Skyrme and Gogny interactions. Overall, the theoretical driplines agree with the experimental results. Notably the Gogny interaction consistently predicts the dripline one to two neutron numbers further from the Skyrme predictions.

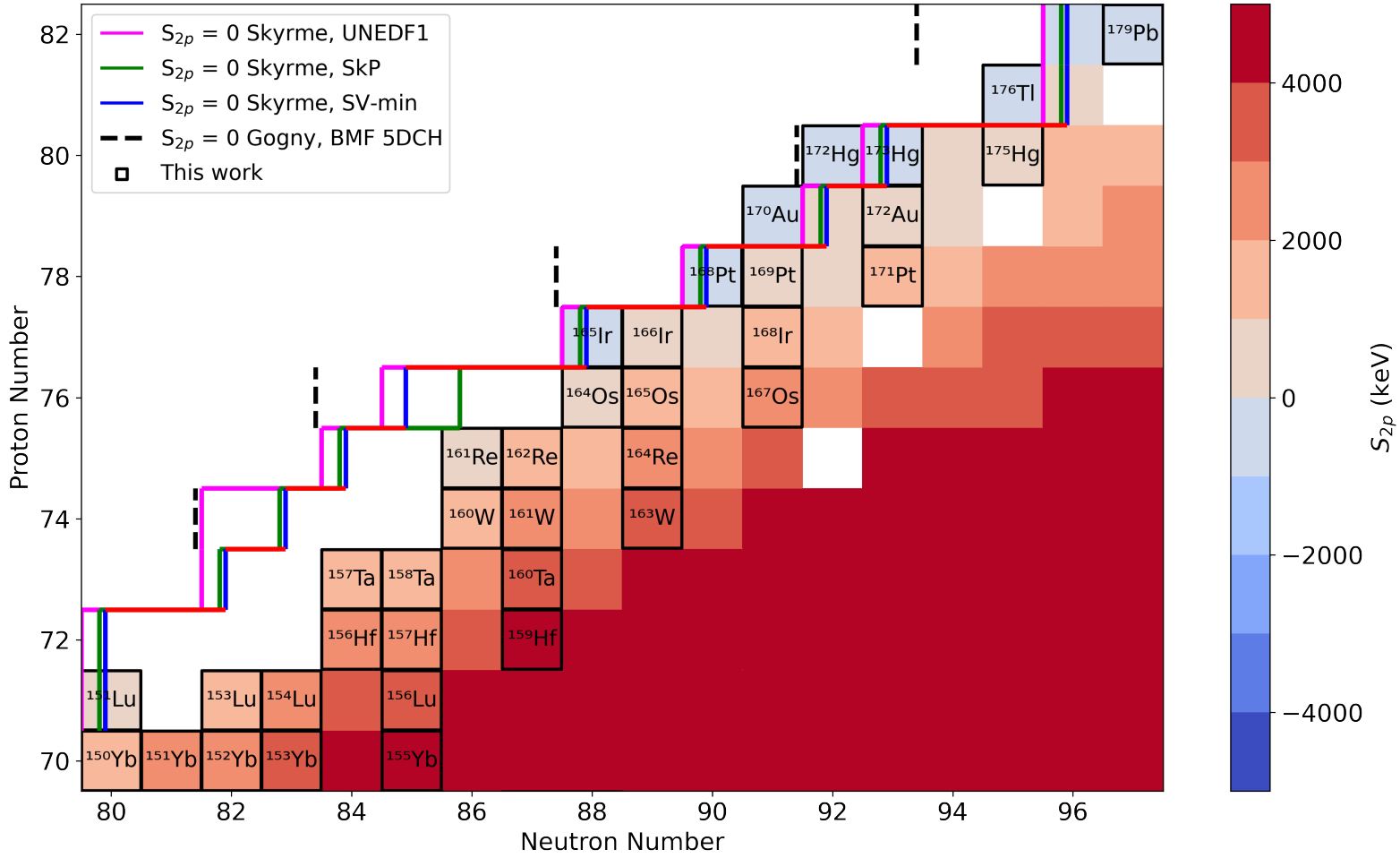

Figure 6.6: Nuclear chart plot of the region between Yb and Pb. The color code indicates the two proton separation energies of the isotopes from the latest Atomic Mass Evaluation and from this work. The dark squares indicate isotopes the masses of which were determined in this work. The theoretical two-proton driplines [4, 70, 88] are plotted with solid and dashed lines.

6.2.2 Two-proton emitters

Now that we have determined a number of two-proton unbound nuclei ($S_{2p} < 0$), we can search for potential two-proton emission candidates. The two-proton unbound nuclides found in this work are summarized in Table 6.1. Out of those, only the ones with $S_p > 0$ can be considered to be two-proton emission candidates since one-proton emission is forbidden.

Isotope	N	Z	S_{2p} (keV)	S_p (keV)	$t_{1/2}$ (ms)
^{165}Ir	88	77	-21(70)	-1541(80)	unknown
^{168}Pt	90	78	-35(48)	1035(48)	2.02(10)
^{170}Au	91	79	-417(71)	-1472(67)	0.29^{+5}_{-4}
^{172}Hg	92	80	-852(48)	596(49)	0.231(9)
^{173}Hg	93	80	-287(93)	600(71)	0.80(8)
^{176}Tl	95	81	-63(131)	-1265(116)	5.2^{+30}_{-14}
^{179}Pb	97	82	-247(117)	626(131)	3.5^{+14}_{-8}

Table 6.1: Two-proton unbound nuclides found in this work. The last column contains the decay half-lives of the nuclides found in literature [264].

Therefore, the two-proton unbound nuclei: ^{168}Pt, ^{172}Hg, ^{173}Hg and ^{179}Pb could potentially be two-proton emitters. However, as mentioned in Chapter 2, two-proton emission is in strong competition with alpha decay in this area of the nuclear chart. Hence, the fact that the aforementioned nuclei satisfy the energy requirements of two-proton emission doesn't guarantee this particular decay mode. The last column of Table 6.1 shows the measured half-lives of the two-proton unbound nuclei. Since there has been no observed two-proton emission for these nuclei, the half-lives are derived by alpha or single proton decay. In order for ^{168}Pt, ^{172}Hg, ^{173}Hg and ^{179}Pb to be considered a candidate for two-proton emission, the partial half-life for two-proton emission needs to be comparable with that of the alpha decay.

We can estimate the two-proton emission partial half-lives of the nuclides by using the Geiger-Nuttal law (following the procedure in [169]):

$$log t_{1/2} = 2.032(Z_d^{0.8} + l^{0.25})Q_{2p}^{-1/2} - 26.832 \tag{6.5}$$

where Z_d is the atomic number of the daughter nucleus, l is the angular momentum

quantum number and $Q_{2p} = -S_{2p}$ is the decay energy of the two-protons. For heavy nuclei ($A \geq 100$), we can make the assumption $Z_d^{0.8} >> l^{0.25}$ and therefore, we can approximate the partial half-life as:

$$logt_{1/2} = 2.032 Z_d^{0.8} Q_{2p}^{-1/2} - 26.832 \tag{6.6}$$

Based on Table 6.1, the alpha decay partial half-lives of ^{168}Pt, ^{172}Hg, ^{173}Hg and ^{179}Pb are of the order of 1 ms. In order for the two-proton decay to occur concurrently with alpha decay, the Q_{2p} of the 2p-decay must be:

$$Q_{2p} \geq \left(\frac{2.032 Z_d^{0.8}}{23.832} \right)^2 \tag{6.7}$$

Figure 6.7 shows the required Q-value values for non-suppressed two-proton emission based on Eq. 6.7 with blue. The Q_{2p} values derived in this work are shown in black. In comparison, the Q_{2p} values of low-Z two-proton emitters [169] are shown with orange data points.

As it can be seen in Fig. 6.7, two-proton emission would not occur concurrently with alpha decay for nuclides with $Z_d \sim 80$ unless $Q_{2p} \sim 8MeV$. Since the Q_{2p}-values determined in this work are significantly lower (see Table 6.1), we conclude that two-proton emission in ^{168}Pt, ^{172}Hg, ^{173}Hg and ^{179}Pb is suppressed in favour of alpha decay.

6.2.3 N=82 shell closure in proton-rich Lutetium isotopes

As mentioned in Chapter 2, $N = 82$ is one of the shell closures determined by the nuclear shell model. As seen in $N = 20$ and $N = 28$, such shell closures can disappear [269] when approaching the limits of nuclear existence. In this section, the newly determined mass excess values are used to investigate whether the $N = 82$ shell closure shows signs of change or quenching on the proton-rich side of the valley of stability.

The masses of ^{151,153}Lu allow for the first time the experimental determination of S_{2n} for $N = 82$, while the mass of ^{153}Lu allows the improvement in the precision of the S_{2n} value of ^{156}Lu. The new values can be found in Table 6.2.

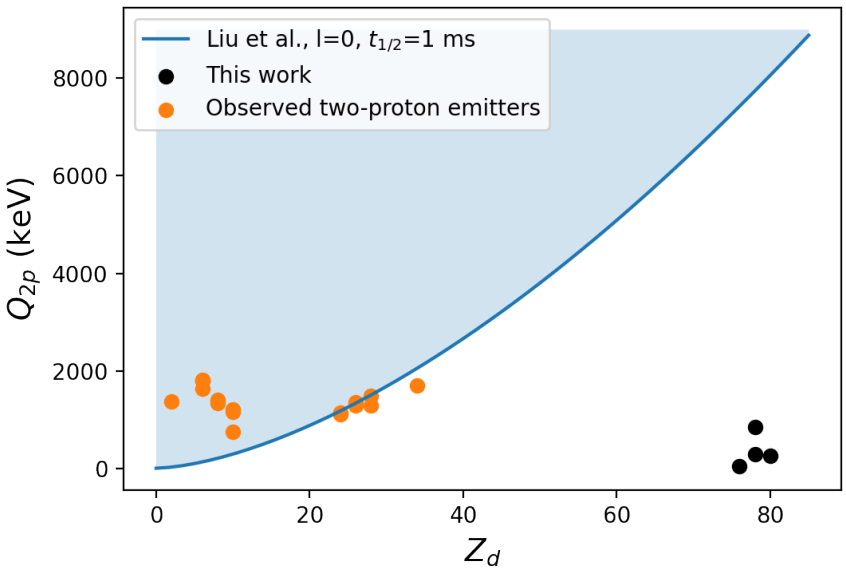

Figure 6.7: Two proton decay energy as a function of the atomic number of the daughter nucleus required to observe a two-proton decay of a nucleus with $l = 0$ and $t_{1/2} = 1$ ms based on the Geiger-Nuttal law. The blue area represents the Q_{2p} space where two-proton decay is allowed while the white area represents the space where it is forbidden. The results of this work are depicted in black while known light two-proton emitters are depicted in orange.

	S_{2n} (MeV)	unc (MeV)
^{153}Lu	24.22	0.06
^{156}Lu	20.21	0.07

Table 6.2: Two-neutron separation energies for the Lu isotopes.

As can be seen from the blue dashed line in Figure 6.8, the two-neutron separation energy of the magic ^{153}Lu at $N = 82$ is significantly higher than those for Lu with $N > 83$, consistently with other isotopes in the $N = 82$ shell closure. Thus we conclude that the $N = 82$ shell closure persists for proton-rich Lu-isotopes near the proton-dripline.

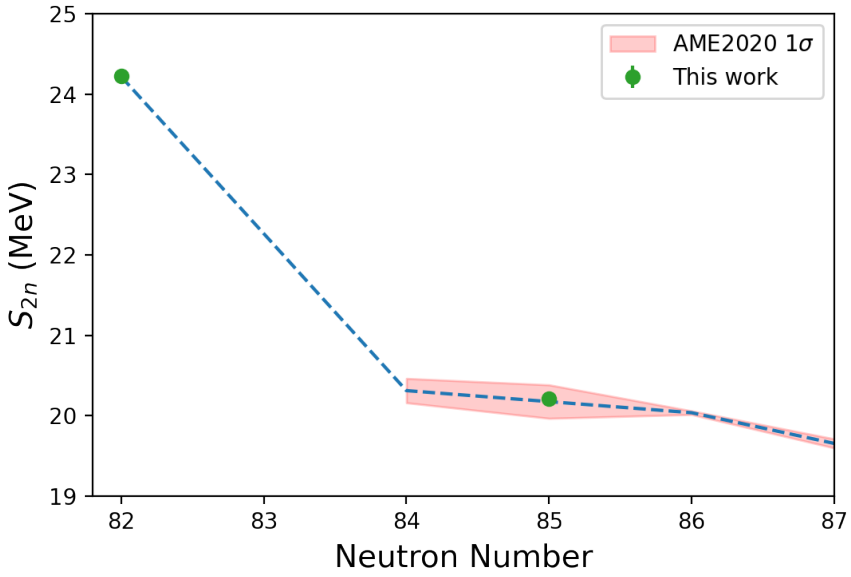

Figure 6.8: Two-neutron separation energy for the Lutetium isotopes near the proton-dripline. The red band represents the literature values and their uncertainties while the data points represent the results of this work. The blue dashed line is a combination of the present results with literature and it demonstrates the persistence of the $N = 82$ shell closure. There is no data-point for N=83 as the mass of ^{152}Lu remains unknown.

6.2.4 Thomas-Ehrman shifts

The determination of masses allows the calculation of one-proton separation energies which can in turn aid in the search of Thomas-Ehrman shifts in heavy nuclei. As can be seen in Figure 6.3, there is a linear dependence between S_p and N for:

- Even-even nuclei
- Odd-odd nuclei
- Even-odd nuclei
- Odd-even nuclei

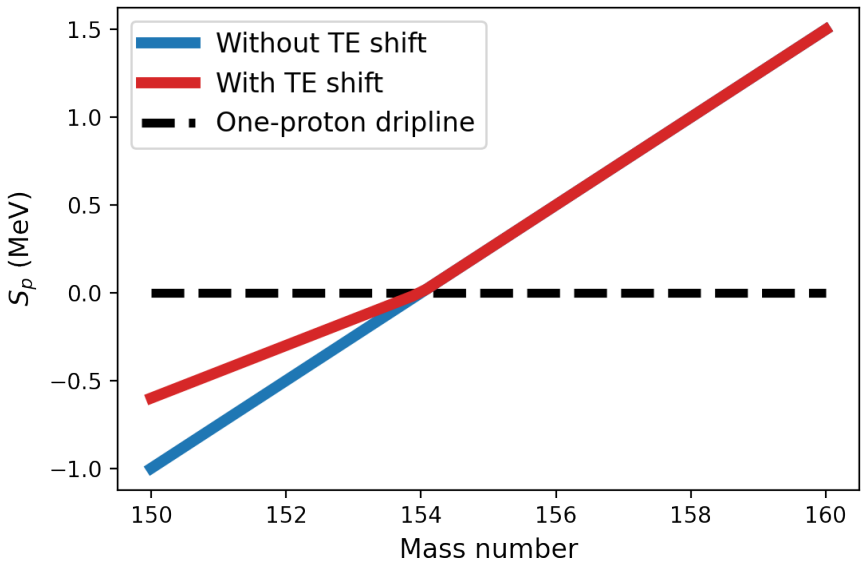

Figure 6.9: Schematic representation of the one proton-separation energy as a function of the mass number with and without the presence of a Thomas-Ehrman shift.

therefore, the procedure described in Novikov et al. [193], can be simplified to:

$$S_p = aN + b \tag{6.8}$$

where a and b are fit parameters and N is the neutron number. Eq. (6.8) is used to separately fit one-proton separation energies of proton-bound and proton-unbound nuclides. A Thomas-Erhman shift would be present if the slope of the fitted line for the proton-unbound nuclei is smaller than the one for the proton-bound ones, as shown in the schematic of Fig. 6.9. This effect would indicate an increase in nuclear stability past the proton dripline.

After obtaining the slopes a and their uncertainty δa for the bound and unbound data sets, a metric can be defined, indicating a possible kink between proton-bound and proton-unbound fitted lines that would reveal a Thomas-Ehrman shift:

$$M = a_+ - a_- \tag{6.9}$$

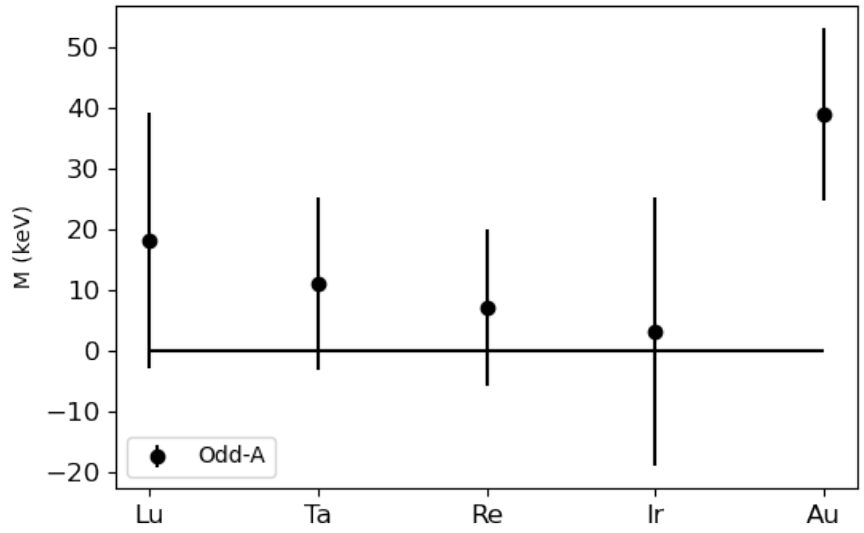

Figure 6.10: Plot of the TE shift metric M for different isotopic chains. Values consistent with zero indicate the absence of TE shifts while values different from zero can arise from the presence of TE shifts.

where a_+ and a_- are the slopes of the proton-bound and proton-unbound nuclides, respectively.

The results can be seen in Fig. 6.10 for each of the odd-Z elements; Lu, Ta, Re, Ir and Au. Only fits with odd-A are shown since there were not enough data from proton unbound even-A nuclides available to perform reliable fits. For Lu there there is only one unbound even-A Lu isotope with known S_p while even-A Ta, Ir and Au isotopes there are only two proton-unbound nuclei in each case. The errorbars correspond to the uncertainties δM_+ and δM_- added quadratically, where δM_+ is the uncertainty derived from the fit of the proton-bound nuclei and δM_- is the one derived from the fit of the proton-unbound nuclei.

Based on the results depicted in Fig. 6.10, there is a noticeable (2σ) discrepancy in the slope of proton-bound and proton-unbound odd-A Au isotopes, which is attributed to a Thomas-Ehrman shift. In addition, the presence of Thomas-Ehrman shifts for Au nuclei agrees with the expectation that odd-A, proton-unbound Au iso-

topes with low spin ($J^{\pi} = 1/2^{+}$) are more likely to show shifts compared to higher spin isotopes like the odd-A, proton-unbound Lu isotopes ($J^{\pi} = 11/2^{-}$) or the even-A Re isotopes ($J^{\pi} = 2^{-}$). However, measurements of more proton-unbound isotopes of the mentioned species are required for a conclusive result.

Chapter 7

Cryogenic upgrade of the TITAN Penning Trap

Nuclear structure studies are often the motivation for mass spectrometry of exotic (radioactive) isotopes. However, mass measurements also provide answers to different scientific questions such as the origin of heavy elements in the universe [236] or provide critical input to questions related to Physics Beyond the Standard Model (PBSM) [90]. The required precision of the measurements relies on the type of the question being asked. Thus the choice of mass spectrometer best suited depends on the specific kinds of science investigations. TITAN's research program revolves around the following three major topics, with the the quantity in parenthesis corresponding to the typical relative precision required for a meaningful scientific result:

- Nuclear structure ($\delta m/m \leq 10^{-6}$). As shown in Chapter 2, a mass uncertainty lower than 50 keV is necessary to reveal shell effects and to resolve low-lying isomers, resulting in $\delta m/m \sim 10^{-6}$ for an isotope of mass 50 u.
- Nuclear Astrophysics ($\delta m/m \leq 10^{-7} - 10^{-6}$). Astrophysical network calculations [184] show that in order to compare the observed star abundances with the calculated abundances produced by astrophysical models, mass uncertainties must be sufficiently small. In the case of heavy element nucleosynthesis via the r-process [236], uncertainties smaller than 100 keV [184] are required. If the mass uncertainties of the isotopes participating in the

process is larger than 100 keV, the different model predictions agree within their uncertainty and different r-process conditions or sites (such as neutron star merger [137] versus core-collapse supernovae [93]) cannot be differentiated through comparisons with the abundance data [184]. This results in a minimum required precision of $\delta m/m \sim 10^{-6}$ for an isotope of mass 100 u. In addition, if low-lying isomeric states (such as ^{166}Ho^{m}, with $E_m = 6$ keV), called astromers, participate in the astrophysical process of interest, a higher precision of $\delta m/m \leq 10^{-7}$ is required in order for the effect of these states to be resolved from that of their ground states.

- Fundamentral Symmetries ($\delta m/m \leq 10^{-8}$). Mass measurements aiming at probing the Standard Model of Particle Physics require uncertainties ranging from a few eV (for probing the neutrino mass [185]) to a few hundred eV (for testing the unitarity of the CKM matrix [145]). Consequently, relative mass precisions of $\delta m/m \sim 10^{-8}$ are needed for an isotope of mass 50 u.

The present chapter focuses on the technical requirements to address the last two research fields with TITAN. It discusses recent activities and improvements of the experimental system in the framework of this work, to enable TITAN to achieve the required conditions.

7.1 Nuclear Astrophysics

Nuclear Physics plays a significant role in Astrophysics to explain the nucleosynthesis in stars [207] and in explosive environments such as X-ray bursts [67, 235], novae [132], supernovae [236], or neutron star mergers [236]. Nucleosynthesis of elements heavier than iron is considered to take place through four nuclear processes: the slow neutron capture (s) process [216], the intermediate neutron capture (i) process [60], the rapid neutron capture (r) process [16] and the rapid proton capture (rp) process [235]. Figure 7.1 shows the path of these processes in the nuclear chart.

The production of half of the elements heavier than iron ($Z > 26$) is attributed to the r-process [236] (green arrow in Fig. 7.1). However, the site at which the r-process takes place in the universe remains an open question. After the detection of

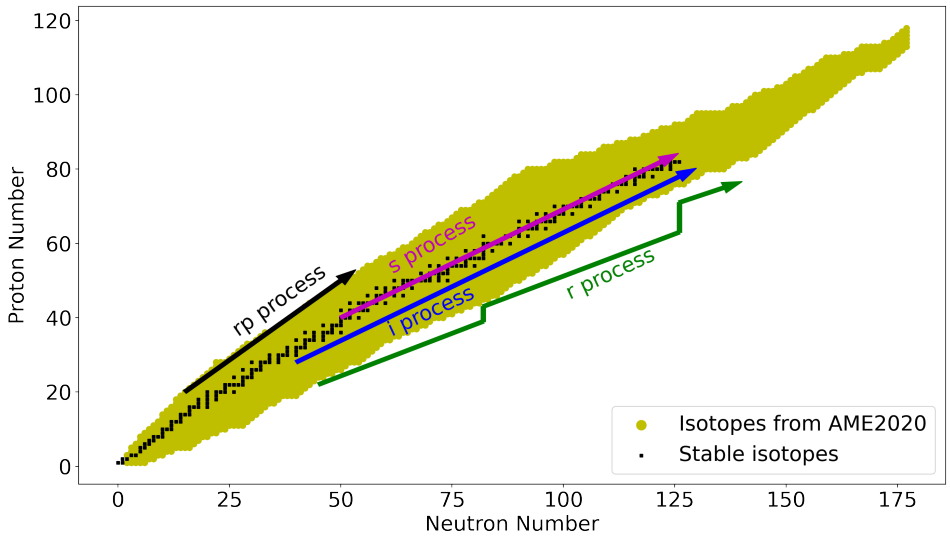

Figure 7.1: Nuclear chart with the four main mechanisms of creating heavy elements in the Universe. The flow of these processes is shown with arrows.

gravitational waves from LIGO and VIRGO [168] and the detection of the kilonova [15] that followed, it has been verified that r-process elements can be produced in neutron star merger events [137], thus making them a suitable site candidate for the r-process. However, many details of the conditions under which the r-process takes place still remain unknown. For this reason, simulations play an important role as they allow comparisons with observational data. More specifically, as can be seen in Fig. 7.2, the observed solar and star abundances of elements in general, are compared with the simulated abundances based on models and using nuclear data as inputs. However, the precision of the simulated results is currently limited by nuclear data uncertainties such as mass uncertainties [184] and reaction rates' uncertainties [183]. It is important to note that, the need for better precision does not demand the precise measurement of all nuclides in the r-process path. Sensitivity studies [183] provide a list of nuclei, for which the current mass precision affects the simulated solar abundances the most.

The position of these nuclei in the nuclear chart correlates with nuclear shell closures ($N = 82, 128$, $Z = 50$). In the framework of Nuclear Astrophysics, nuclei

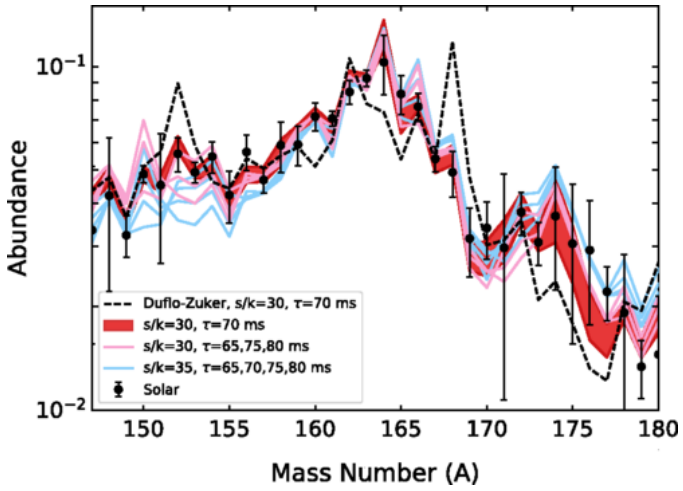

Figure 7.2: r-process solar abundances for $m = [145, 180]$ u in comparison to abundance values calculated using theoretical models. Figure taken from [196].

with neutron or proton numbers corresponding to closed shells are often referred to as waiting points [16]. Due to their increased stability, hence longer nuclear decay half-lives, they slow down the rapid neutron capture process thus increasing the probability of photo-disintegration or beta decay [16]. Therefore, whether or not a nucleus is a waiting point can play a decisive role in the r-process path. Measuring the mass of these nuclei with high precision ($\delta m/m \leq 10^{-6}$), determines their binding energy and in combination with beta-decay half-lives it allows to determine whether a particular nucleus constitutes a waiting point.

Another important parameter that introduces uncertainties in r-process network calculations is the existence of so-called astromers [262]. Astromers are isomeric states of nuclei with half-lives comparable to the half-life of the ground state. As a result, their existence can change the assumed population of the ground state and ultimately alter the r-process path by redirecting the mass flow of the r-process to different reaction channels [263]. As the astromers can have low-lying excitation energies ($E \leq 10$ keV for example for ^{166}Ho, ^{130}Sb and ^{121}Sn [263]), higher mass precision is required ($\delta m/m \leq 10^{-7}$).

In the past, the TITAN MPET carried out r-process studies in a number of cam-

paigns investigating the masses of neutron rich Cd [160] and In [23] isotopes, searching for isomers and astromers by utilising HCI.

CryoMPET is designed to perform mass measurements of ground states and isomers with higher charge states and longer excitation times thus allowing for higher precision and resolution of low-lying isomeric states that are currently not possible with the MR-TOF MS or MPET.

7.2 Fundamental Symmetries

The Standard Model (SM) of Particle Physics [255] describes the fundamental particles and their interactions (except for gravity). The fundamental particles (fermions) consist of three generations of quarks (up-down, charm-strange, top-bottom) and three generations of leptons (electron-electron neutrino, muon-muon neutrino, tau-tau neutrino) as shown in Fig. 7.3. These particles interact by exchanging gauge bosons which act as the force carriers and according to the SM these are: the gluon (g), the photon (γ), the Z-boson and the W-bosons. In addition to the four interaction bosons, there is the Higgs boson (H) which is responsible for the mass of the fermions [53] and the $W^{\pm}$, Z_0 bosons. Over the years, the SM has been repeatedly verified with the pinnacle of the experimental efforts being the discovery of the Higgs boson in 2012 [19]. Nevertheless, we know that the SM is incomplete, as is for example demonstrated by the non-zero mass of the neutrinos [99], and the exploration of its limits and deficiencies, the so-called models of Physics Beyond the Standard Model (PBSM), is of high importance.

High precision mass measurements can contribute in the search for PBSM. One of the active areas of mass measurement research concerning PBSM is the determination of the mass of the electron-neutrino ν_e. Although the SM predicts all neutrinos to be massless, observed flavour oscillations [99, 178] require neutrinos to have a non-zero mass in order for flavour oscillations to occur. To date, the upper limit of the mass of the electron neutrino is $m < 0.8$ eV/c^2 and is derived from studies of the beta decay of tritium with KATRIN [138]. In this experiment, the mass of the neutrino is being determined by mapping out the endpoint of the beta-decay energy spectrum. However, due to the difficulty of determining a sub-eV mass from the energy spectrum, given the background signals induced by the emit-

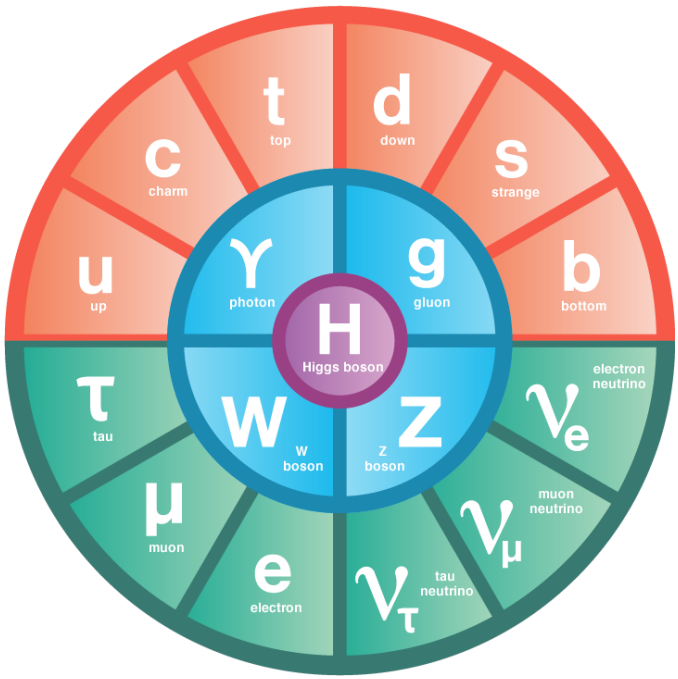

Figure 7.3: Schematic of the particles in the SM. Particles shown in orange correspond to quarks, particles shown in green show leptons while those in blue show the four interaction bosons. The Higgs boson is shown in purple. Figure taken from [5].

ted electrons, high precision Q-value measurements from Penning traps can play a significant role in the determination of systematic effects for the KATRIN experiment [185] or can investigate the Q-values of other candidates for the neutrino mass such as ^{163}Ho [87].

Another possible PBSM model that can be investigated using Penning Traps is the non-unitarity of the Cabbibo-Kobayashi-Maskawa (CKM) matrix. The CKM matrix [145] represents the transformation of the mass eigenstates of some quarks (dsb) to their weak eigenstates $(d's'b')$ that participate in the weak interaction. The predecessor of the CKM matrix was a 2x2 matrix that included the Cabbibo angle [49] and was introduced to explain the mixing of quark flavours in kaon decays [112]. In order to explain the CP violation Kobayashi and Maskawa [145] extended to the Cabibbo matrix by one dimension which was later verified by the

discovery of the third generation of quarks (top-bottom). For the description to be complete, the CKM matrix needs to be unitary. However, the existence of a fourth generation of quarks or a non-SM contribution in the weak interaction, such as a scalar or tensor current, could result in discrepancies from unitarity [115]. This would require the extension of the Standard Model and hence requires PBSM.

The unitarity of the CKM matrix is often tested using the top row elements of the 3x3 matrix, due to experimental access and corresponding precision, as [115]:

$$|V_{ud}|^2 + |V_{us}|^2 + |V_{ub}|^2 = 1 + \Delta_{PBSM} \tag{7.1}$$

where V_{ud} is measured through Super-Allowed (SA) beta decays [115], V_{us} is measured through kaon decays [255] and V_{ub} is measured via baryon decays [255]. The sum of squares defined in Eq. 7.1, currently equals $0.9985(6)$ [115], which corresponds to a 2.4σ tension with unitarity. Therefore, it is important to investigate whether this deviation Δ_{PBSM} is a result of PBSM or one of underestimated uncertainties.

Mass measurements can aid this effort by providing high precision Q-values of Super-Allowed (SA) decays that enter the calculation of the SA Ft value. The Ft value [115] is determined as:

$$Ft = ft(1+\delta_R')(1+\delta_{NS}-\delta_C) \tag{7.2}$$

where δ_R, δ_{NS} and δ_C are theoretical corrections, t is the partial half-life of a particular SA decay and f is the statistical rate function which is proportional to Q^5, where Q is the Q-value of the SA decay. The V_{ud} matrix element can be calculated using Eq. 7.2 as:

$$|V_{ud}|^2 = \frac{K}{2G_F^2(1+\Delta)} \cdot \frac{1}{Ft} \tag{7.3}$$

where $K/(\hbar c)^6 = 8,120.27648(26) \cdot 10^{-10}\ GeV^{-4}s$ is the vector coupling constant for the semileptonic weak interactions [115], Δ is a transition-dependent correction, G_F is the weak interaction constant and Ft is the corrected ft value. In addition, high precision Q-value measurements can indirectly contribute by providing benchmarks for the theoretical corrections that enter the Ft values [174].

Previously, the TITAN MPET contributed to studies of Fundamental Symmetries

using HCI in order to reach unprecedented precisions in short measurement times and for isotopes with short $t_{1/2}$ ($t_{1/2} < 100$ ms) [91]. CryoMPET is designed to store ions of higher charge states and thus further improve the precision achievable in MPET.

7.3 The Cryogenic Measurement Penning Trap (CryoMPET)

The TITAN MR-TOF MS has been used for Nuclear Astrophysics studies [202, 218] but the available precision is currently systematically limited to $\delta m/m \sim 10^{-7}$ thus requiring investigations regarding Fundamental Symmetries and most investigations regarding Nuclear Astrophysics to be performed by MPET. MPET typically achieved a relative precision of $\delta m/m \sim 10^{-8}$ [90, 154]. The room-temperature MPET along with its measurement principle has been described in Chapters 3 and 4.

Uniquely distinguished from all other on-line Penning Traps, the TITAN MPET has access to HCI of radioactive species, charge-bred via the TITAN EBIT [159]. This allows reaching higher precisions because as q increases so does ν_c, while $\delta\nu_c$ remains constant, due to the Fourier limit for a finite excitation period T_{exc}:

$$\frac{\delta m}{m} \sim \frac{\delta \nu_c}{\nu_c} \propto \frac{m}{qBT_{exc}\sqrt{N}} \tag{7.4}$$

where m is the mass of the ion, q is the charge state of the ion, B is the magnetic field, T_{exc} is the excitation time applied to the ions and N is the number of detected particles. Therefore by measuring ions with $q = 10e$, where e is the electron charge, compared to ions with $q = 1e$, the measurement precision can increase by an order of magnitude assuming everything else remains constant.

This principle has been demonstrated for many cases (see for example: [23, 90]) using the TITAN facility with HCI. However, the increase in the ion's charge state poses a challenge due to the increased likelihood of the HCI to interact and charge exchange with their environment [165]. This would lead to a charge state reduction from q to $q-n$, where n is the number of successful charge exchanges, where an electron is transfered from a reactant to the HCI. This is not a dynamic

process of observation, hence it is not possible to excite the ion as X^{q+} and then continue with $X^{(q-n)+}$ after the charge exchange, limiting experiments to the same charge state at the beginning and at the end of the excitation cycle. As a result, the excitation time T_{exc} has to be adjusted so that the probability of charge exchange interactions is minimal, which negatively affects the precision gained by utilising higher charge states q as seen in Eq. 7.4. In addition, the TITAN EBIT has been recently upgraded to a kinetic energy of E_{e-kin} = 65 keV for the electron beams [96], allowing for the production of higher charge states. Since the electron transfer cross section increases with charge state, higher charge states have a higher likelihood of charge exchange. Therefore, the increase in q for precision cannot be efficiently taken advantage of with the existing MPET, as it does not meet the vacuum requirements.

While the design of CryoMPET had been finalized, part of this work describes the assembly and commissioning, including improvements of the system. This section starts with a brief description of the design of CryoMPET (more information can be found in [163]) and continues with the description of the assembly, improvements and commissioning at room temperature and at cryogenic temperatures. In addition, feasibility studies and the implementation of the PI-ICR technique are carried out, details of which can be found in Appendix B.

7.3.1 Description of CryoMPET

To increase the achievable storage times in MPET and to make full use of the charge states reachable using the electron beam energy upgrade of EBIT [52], MPET has been upgraded to perform at cryogenic temperatures [163]. According to simulations [163], operation of the trap at 20 K, will result in a pressure of 10^{-12} Torr, three-orders of magnitude lower than the pressure reached for the room-temperature MPET. Under such pressure, 1 s storage times of up to hydrogen-like (only one electron left in the atomic shell) medium mass nuclei can be achieved with less that 10% probability of charge exchange with the background gas [163], significantly extending the available storage times.

In the CryoMPET system, the cooling to cryogenic temperatures ($T \sim 2-20$ K) is achieved by absorbing molecules on the trap surfaces: a process called cryo-

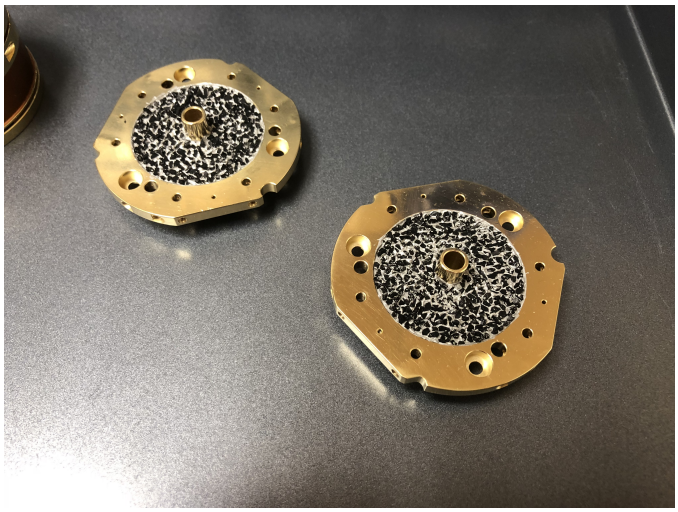

Figure 7.4: Tube electrodes of the Penning trap system with the activated charcoal for cryo-absorption. The activated charcoal is attached using a layer of the MCT 3715-2SE adhesive from MicroCoat Technologies.

absorption (1) and cryo-condensation (2). For (1), gasses are absorbed by a material of high porosity due to its large surface area which allows for efficient adsorption, where the adhesion of molecules to a surface is achieved through covalent bonds and Van der Waals interactions. In the case of CryoMPET, the material used is a plant based (coconut) activated charcoal [56]. Activated charcoal is a common material for cryo-absorption because of its high porosity and easy availability. This material has been applied on six trap surfaces: behind the two end-cap electrodes and on both sides of the two tube electrodes. The tube electrodes coated with the activated charcoal can be seen in Fig. 7.4.

Cryo-condensation, is achieved by the freeze-out of heavy ($m > 15$ u) gas molecules on the trap's surface. In order to achieve this, the trap surface is continuously cooled using a closed-cycle cryocooler. The cryocooler consists of a compressor and an expander (or cold-head) and it operates using the Gifford-McMahon refrigeration cycle [106]: The compressor compresses room-temperature He gas, which is then transferred to the cold-head. There, due to the larger volume, the room-temperature He-gas expands and cools down. Finally the cold He-gas passes through the regeneration material removing heat from the system. The process

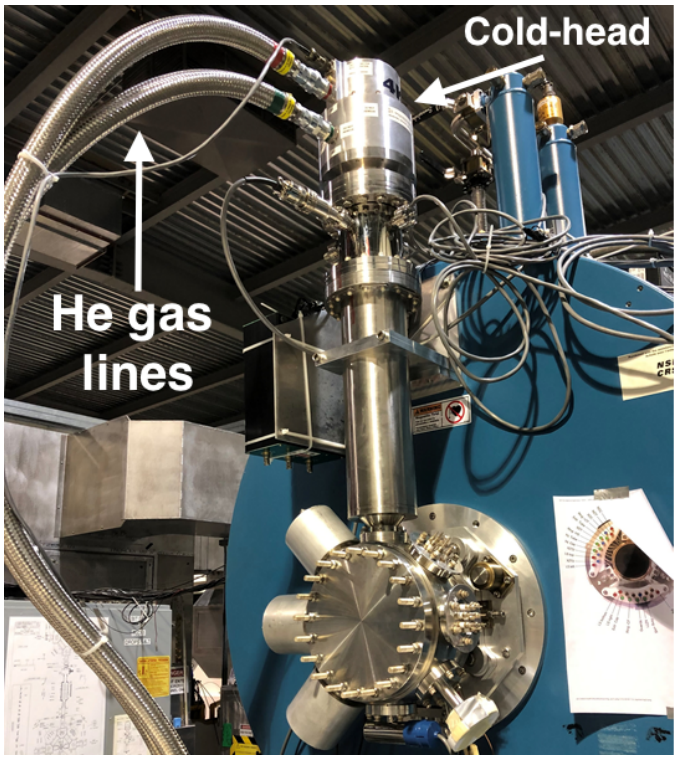

Figure 7.5: Picture of CryoMPET's cold-head connected to the He-lines coming from the compressor. The blue cylinder is the housing of the 3.7 Tesla superconducting magnet.

is continuously repeated. The cold-head provides two cooling stages. According to the manufacturer, without load, a minimum temperature of 20 K and 2.5 K can be achieved in the first and second stages respectively. The reason for using cryo-absorbents in the trap system is because cryo-condensation is not sufficient to freeze-out molecules of $m < 15$ u, such as H_2 and N_2, at a 20 K temperature environment, as demonstrated in [163].

Due to space constraints, the cold-head is placed outside the superconducting magnet (Figure 7.5), and it is coupled to the trap electrodes with a 12.7 mm diameter copper rod. The thermal coupling efficiency is impacted by the diameter of the rod and therefore high-purity copper (99.99995% elemental purity) was used to increase thermal transport efficiency based on simulations reported in [163]. The

purity of the material minimizes heat transmission losses which is critical given the distance (70 cm) between the cold-head and the trap. All the sufaces that are directly coupled to the cryocooler (cold surfaces) are isolated from room-temperature environment with a copper shield attached to the first stage of the cryocooler. To compensate for thermal expansion and related stress, both the trap and the shield are not fixed in place but are allowed to move on three ceramic rods along the axial direction. This avoids mechanical tension from thermal stress during cooldown and warmup due to different expansion behavior of the various materials.

A comparison between the trap electrodes of room temperature MPET and CryoMPET can be seen in Figure 7.6. The bottom picture shows CryoMPET surrounded by its thermal shield and connected to the rod that leads to the cryocooler. In addition, one of the ceramic rods can be seen.

For temperature diagnostics, the system is equipped with three temperature sensors: one Silicon Diode sensor (SiD) attached to the first stage of the cryocooler, one Cernox sensor mounted on the second stage of the cryocooler and a second Cernox sensor attached to the trap electrodes. Cernox sensors were chosen due to their independence of their orientation in the magnetic field [2]. SiD sensors, can have up to $\Delta T/T = -400\%$ [3] deviation due to magnetic fields if placed parallel to the magnetic field lines of a 4 Tesla magnet. In addition, the setup is equipped with two heaters, one attached to the trap electrodes and one on the cryocooler, allowing for the regeneration of the cryo-absorbent, by performing thermal cycles, to prevent saturation. The trap electrodes with the heater and the sensor installed can be seen in Fig. 7.7.

7.3.2 First assembly and installation

CryoMPET was assembled for the first time as part of this thesis. A picture of the assembled trap structure can be seen in Fig. 7.8. Its wiring scheme can be seen in Fig. 7.9. Post-assembly, the trap was heated to 120 ^{o}C for two weeks, in order to accelerate outgassing of the mechanical components and to remove molecular contaminants. This process achieves and maintains a UHV environment, typically on a pressure level of $P \sim 10^{-9}$ Torr.

The composition of molecular species at different stages of the baking proce-

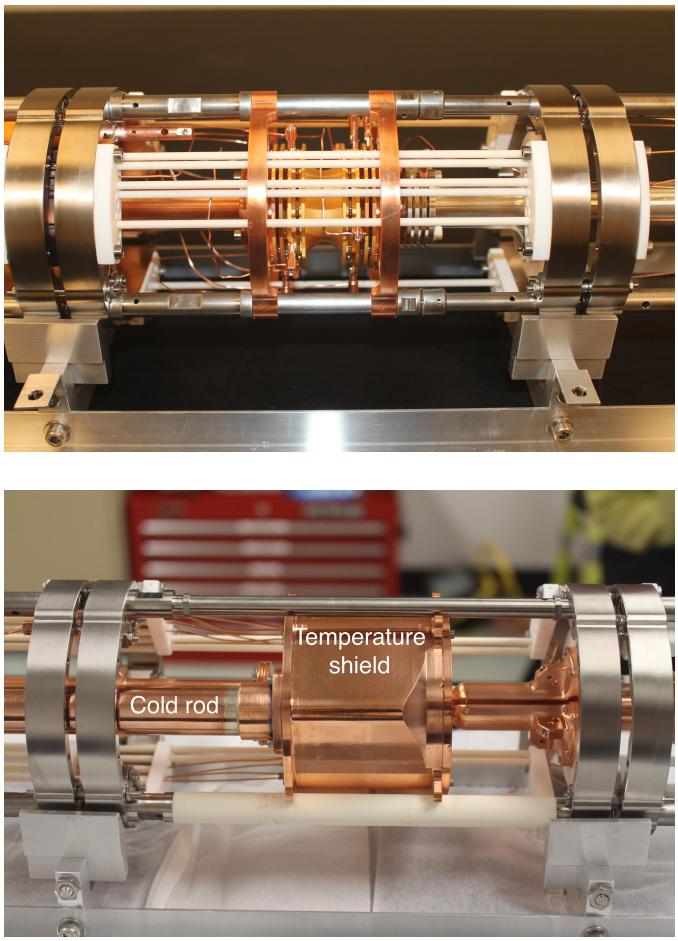

Figure 7.6: The top photo shows the MPET system. The Penning trap electrodes are located at the center and can be distinguished by their gold-plating. The botton photo shows CryoMPET. The trap electrodes are located inside the copper thermal shield shown in the picture. On the left side of the thermal shield, part of the copper rod can be seen, which connects the trap electrodes to the cryocooler.

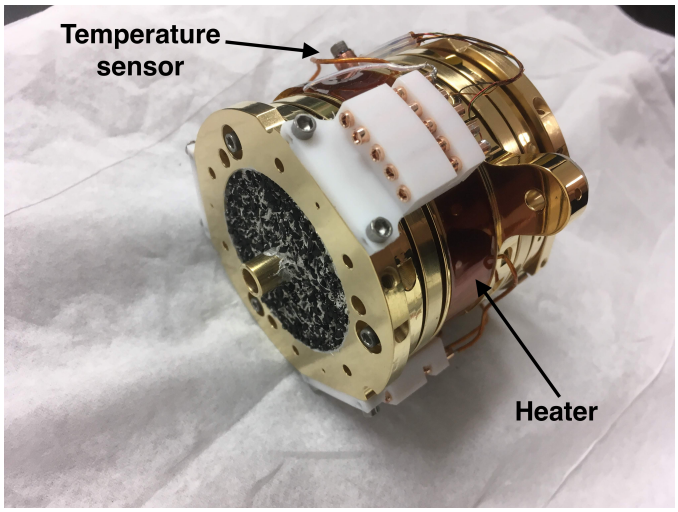

Figure 7.7: Picture of CryoMPET with the temperature sensor and the heater installed. The activated charcoal and the wiring of the individual electrodes can be seen.

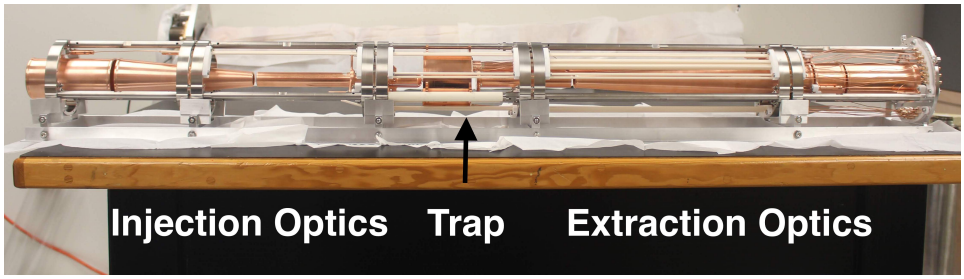

Figure 7.8: The trap assembly prior to being placed in vacuum. The trap electrodes are enclosed in its thermal shield. The injection and extraction beam optics are attached on the left and right of the trap electrodes.

dure was monitored by a Residual Gas Analyzer (RGA). The results of the RGA can be seen in Fig. 7.10. Before the baking of the system the measured partial pressures of the largest ratio molecules in the spectrum (H_2, H_2O, N_2, CO_2) were of the order of 10^{-7} Torr. Due to a large outgassing rate, at the beginning of the baking process large partial pressure readings (up to 10^{-5} Torr) are found, followed by a gradual reduction over the course of the two week process. After the baking the trap system was cooled down to room temperature, and the only molecules detected were H_2,

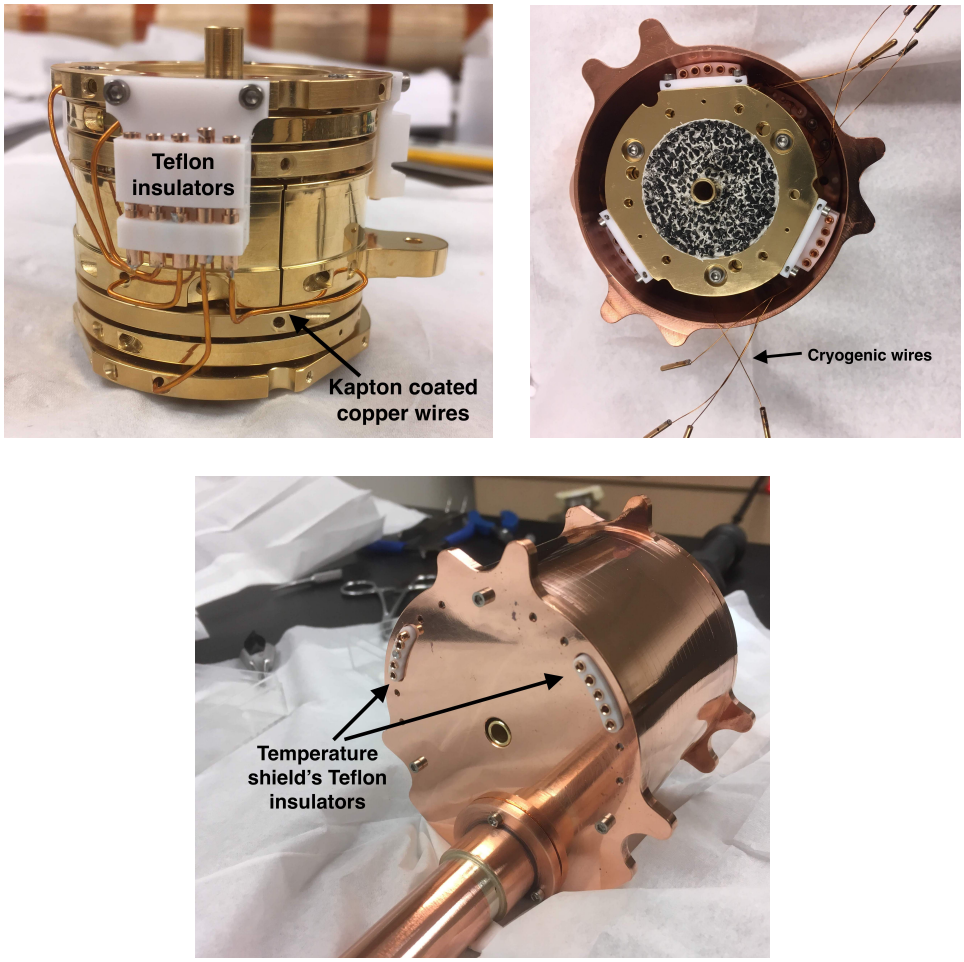

Figure 7.9: Photos of the trap system wiring connections. The trap electrodes are connected to wires on the teflon insulators (top left). The wires (top right) are connected to bare copper wires that run along the extraction optics electrodes using teflon insulators located on the shield (bottom).

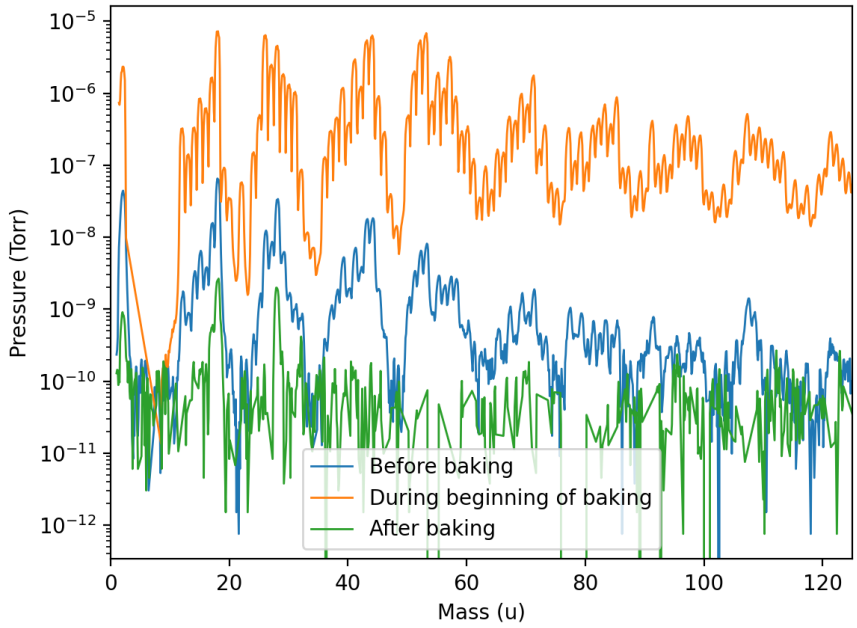

Figure 7.10: Pressure as a function of mass in CryoMPET before, during and after baking at 120°C for two weeks. Different peaks correspond to molecules of different mass. The molecular background that remains after baking corresponds to H_2, H_2O and N_2.

H_2O, N_2 and their partial pressure values were more than an order of magnitude lower than those before the baking process, as shown in Fig. 7.10. After baking, the trap system was installed in the TITAN beamline, minimizing exposure to air during the process.

7.3.3 Improvements and modifications

The goal of the first installation of the trap system was to demonstrate that ions can be trapped and manipulated at cryogenic temperatures. During this process, it was found that the cryocooler can effectively cool the trap, reaching a final temperature of $T_{trap} = 32$ K. However, there were a series of aspects that required further investigation and development, in order to ensure that CryoMPET could reach its

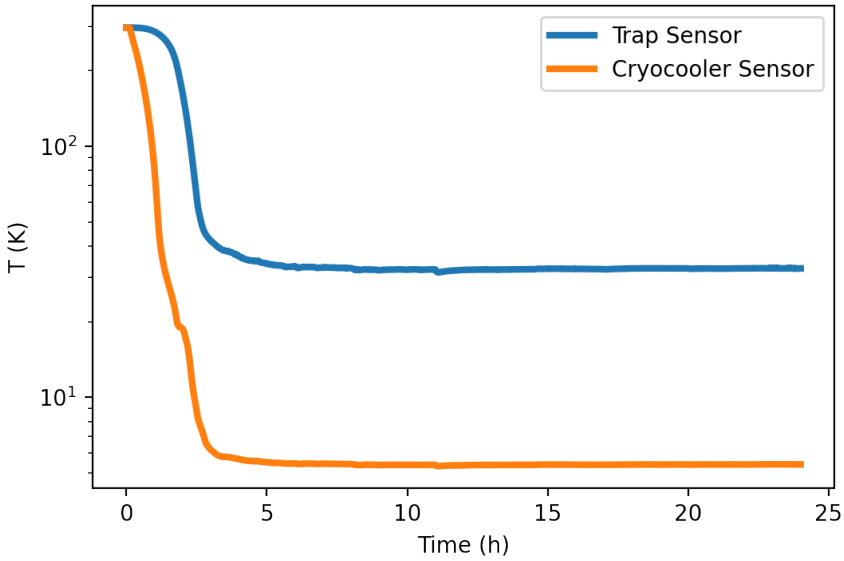

Figure 7.11: Temperature profiles as a function of time of the trap (blue) and the first stage of the cryocooler (orange) during cool-down.

scientific goals and meet design specifications. The present section describes the actions taken, in the framework of this thesis, towards achieving the specified operation conditions of CryoMPET.

During commissioning of the setup, the trap was cooled down to verify functions and to test the equipment with the goal to meet specifications. At the time, the system was equipped with two SiD temperature sensors: one connected to the trap electrodes and one connected to the first stage of the cryocooler. The temperature readings of these sensors during the cool-down process as a function of time can be seen in Fig. 7.11. Although the sensor at the first stage of the cryocooler shows a final temperature of 5 K, the sensor at the trap electrodes indicates a temperature not below 32 K.

Even though the achieved temperature measured at the trap section was only 12 K above the specified temperature, this results in residual molecular species (mostly N_2) present in the trap system as shown in the simulations performed in [163]. The analysis of the system performance for this test led to the following

hypotheses:

- Incorrect sensor readout. As mentioned previously, SiD sensors can have up to $\Delta T/T = -400\%$ [3] if placed parallel to the magnetic field.
- Insufficient contact between the sensors and the cold surface leading to false readouts.
- Poor heat transmission from the cryocooler to the trap.
- Physical contact between the two cooling stages and therefore reduced thermal insulation.

To investigate the first two possibilities, the SiD sensors located in the strong magnetic field were replaced with sensors (Cernox [2]) which have a significantly smaller magnetic field dependence ($\Delta T/T < 0.5\%$ [2]) in a 4 Tesla field. In addition, the new sensors were equipped with the so-called CU packaging [1], a configuration where the sensor has been soldered on a copper bobbin and can easily and securely be attached to the experimental equipment thus ensuring the sensor being in strong mechanical and thermal contact with the cold surface. The mechanical drawing including the two new Cernox sensors attached to the second stage of the cryocooler and to the trap electrodes can be seen in Fig. 7.12 (middle and right).

Another possible reason why the trap did not reach 20 K could be due to poor heat transmission, between the cryocooler and the trap electrodes using a 70 cm long rod. As it is impossible to reduce the length of the rod, as a heat-loss mitigation measure, both the rod and the shield were gold plated and polished to increase heat reflectivity.

Finally, due to the vibrations of the cryocooler and the softness of the material of the cold finger, the possibility of physical contact between the shield and the cold stage, which would constitute a thermal bridge, guiding the cold-flow away from the trap, was investigated. No evidence of contact was found. However, a SiD sensor was added to the shield of the cryocooler (see Fig. 7.12 (left)) to allow continuous monitoring.

[1] https://www.lakeshore.com/packaging/packagessi

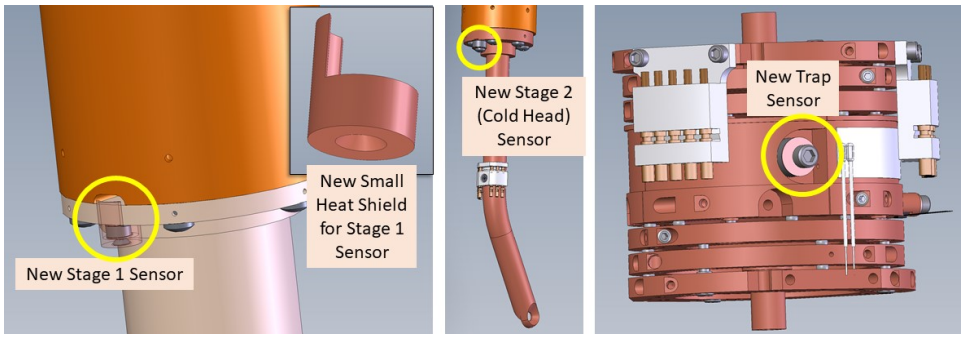

Figure 7.12: The three CryoMPET sensors: the SiD shield sensor (left), the Cernox cryocooler sensor (middle) and the trap Cernox sensor (right).

With the implementation of these modifications, the trap was re-assembled and installed in the summer of 2021. The next two sections describe the commissioning of CryoMPET at room and at cryogenic temperatures. More information about technical aspects of the commissioning can be found in Appendix C.

7.3.4 CryoMPET room temperature commissioning using stable isotopes

After the final installation, the complete trap system was operated without the cryocooler, to ensure that all components were properly functioning prior to cooldown. This phase of commissioning is called room temperature commissioning. Technical details of the process are described in detail in Appendix C, while only the key results of the process are described here.

$^{39}K^{+}$ ions were delivered to CryoMPET to test various ion optics elements as well as the Penning trap RF excitation system. A commissioning sequence of excitation schemes was established starting from dipole resonances. The excitation of ions with magnetron and reduced cyclotron frequencies was achieved. Figure 7.13 shows the dipole ToF resonance for $^{39}K^{+}$ ions excited for $t_{exc} = 100$ ms for different RF amplitudes. Because RF voltages are now applied to the segmented Ring electrode, the necessary RF amplitude for dipole excitations is smaller by a factor of ≈ 20, compared to the previous design, where the excitations were applied to the Guard electrode instead. The Ring electrode is closer to the trapped ions and hence smaller RF amplitudes are used.

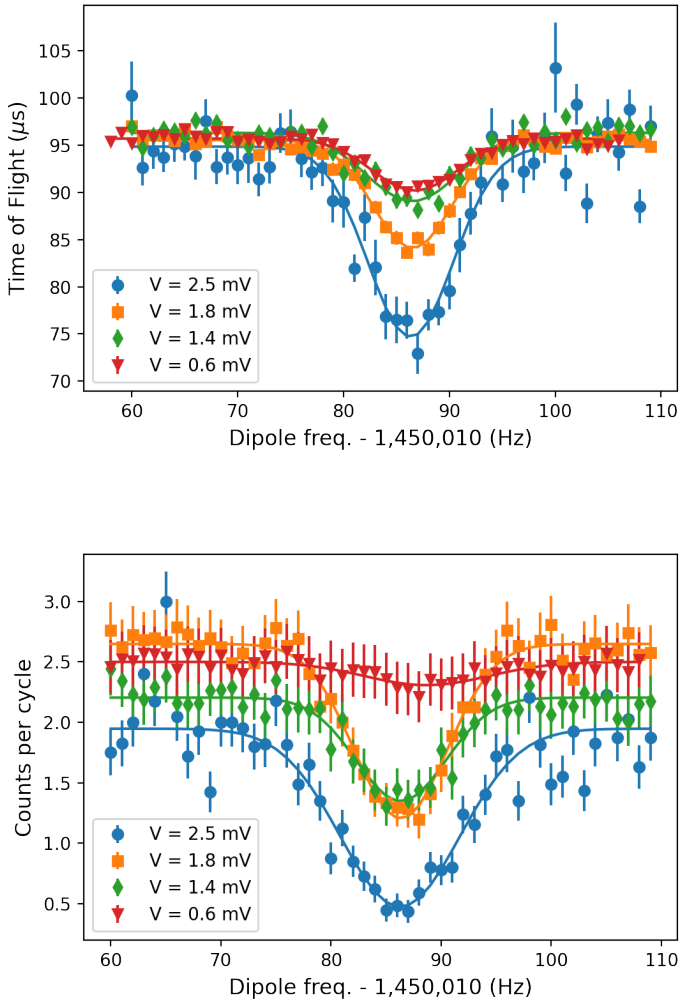

Figure 7.13: Dipole resonances for different V_{RF} and $t_{exc} = 100$ ms. The upper figure shows the Time-of-Flight as a function of the applied frequency. The resonant frequency corresponds the the frequency for which the Time-of-Flight of the ions is minimal. The lower plot shows the count rate as a function of the applied frequency. For large enough amplitudes, resonant ions gain sufficient energy to cause them to hit the trap walls and disappear.

In addition, quadrupole RF-pulses were successfully applied during room temperature commissioning of CryoMPET. For TOF resonances with quadrupole pulses, the ions need to be prepared in a pure magnetron eigenmotion. At TITAN this is achieved using the Lorentz Steerer electrodes, the principle of which was described in Chapter 4.

Ion storage lifetime studies

CryoMPET operated at room temperature can be used as a regular mass spectrometer, however, the time for which ions can be stored is limited, due to the achievable vacuum conditions. To accommodate for cooling and temperature diagnostics, a number of different materials have been introduced, which were designed for optimal operation at cryogenic temperatures. However, they do not perform optimally at at room temperature, and hence they deteriorate the vacuum conditions. As the electrode geometry design had to balance the openings into the trap structure to be as small as possible to minimize radiation heating, and also to be as big as possible to achieve maximal vacuum pumping via conventional turbo-molecular pumps, outgased molecules are difficult to remove. As a consequence, the final pressure at room temperature leads to the trapped ions undergoing collisions with background molecules at an increased rate than before. The ions that undergo collisions lose some of their energy while those that don't undergo collisions are able to maintain their energy. This mix of ions with reduced energy and those that have preserved their initial energy, increases the ions' overall TOF spread as a function of the storage time, as can be seen in Fig. 7.14 and compromises the TOF resonance shape.

Figure 7.15, shows the evolution of a TOF resonance over three eigenmotion conversion periods for a t_{exc} = 500 ms excitation of $^{39}K^{+}$ ions in room temperature CryoMPET. The resonances are fitted with a Gaussian function:

$$\mathrm{ToF} = -Ae^{-(x-b)^2/2\sigma^2} + c \tag{7.5}$$

where A, b, σ, c are fit parameters. The FWHM of a 500 ms excitation should be [76]:

$$FWHM \simeq \frac{0.9}{0.5} = 1.8 \text{ Hz} \tag{7.6}$$

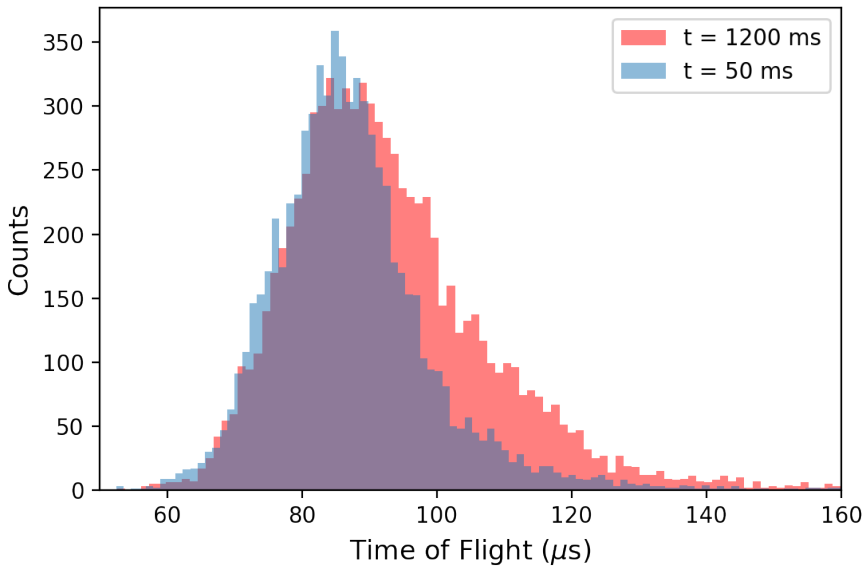

Figure 7.14: Beam profile for $^{39}K^{+}$ ions stored for 50 ms (blue) and 1200 ms (red) at room temperature in CryoMPET. The data were recorded at the MPET MCP. The difference in the shape of the two distributions comes from collisions with background gas in MPET.

and therefore $\sigma = FWHM/2.355 = 0.8$ Hz. The results reveal that after one full conversion (t_{exc} = 500 ms), the width of the ToF resonance is $\sigma = 0.9$ Hz, while for two (t_{exc} = 1 s) and three (t_{exc} = 1.5 s) conversions the σ becomes 1.3 Hz and 1.6 Hz respectively, indicating damping due to collisions with the background gas.

In addition, the baseline of the TOF resonance is shifting to higher TOF values as a function of the storage time. This is consistent with the increase in the average TOF due to collisions that is depicted in Fig. 7.14.

7.3.5 CryoMPET operation at cryogenic temperatures

As a next step, the trap system was cooled down. The commissioning confirmed that the trap could be operated at 22 K, achieving design goals [163]. A comparison between the previous and the current temperature curves during cool-down can be seen in Figure 7.16.

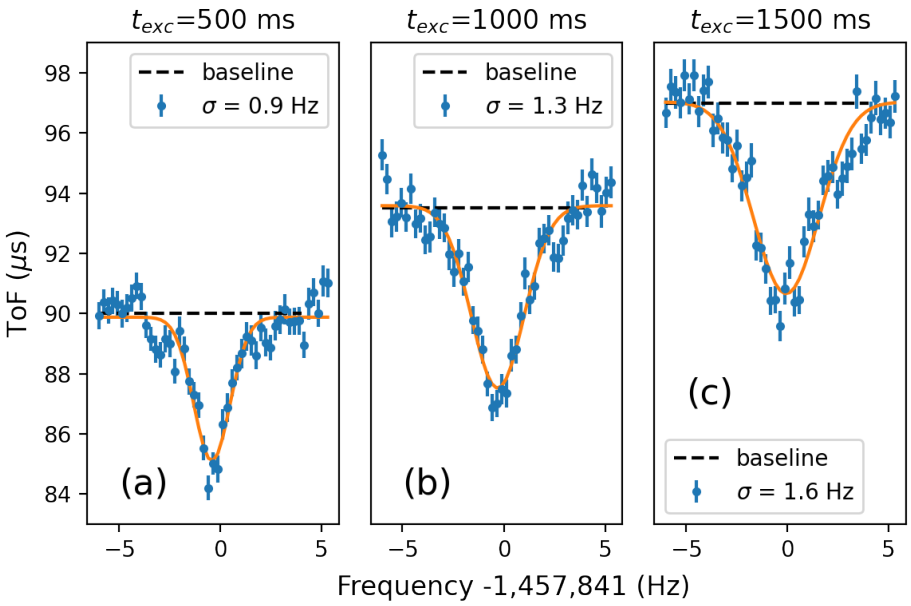

Figure 7.15: Gaussian fits of a 500 ms resonance after (a) one, (b) two, and (c) three conversion periods respectively. The baseline is indicated by a dashed horizontal line.

The improvement was achieved by improving radiation reflection after gold plating the cold finger and the shield. An additional element was to replace the previous sensors and carrying out the temperature readings using Cernox sensors. However, unlike the SiD sensors previously used, Cernox sensors are prone to a larger short term fluctuations, resulting in an increased noise level of the reading signal as can be seen in Fig 7.16.

Two experiments were carried out and Figure 7.17 shows an optimized TOF resonance, in terms of maximum TOF-effect and minimum damping, achieved for a $t_{exc} = 500$ ms excitation with the trap at room temperature. In comparison, a 500 ms TOF-resonance performed with the trap at 22 K is plotted in the same figure. To investigate the vacuum conditions in the trap and to confirm the design goals, resonance comparison studies were performed. The two TOF resonances are fitted

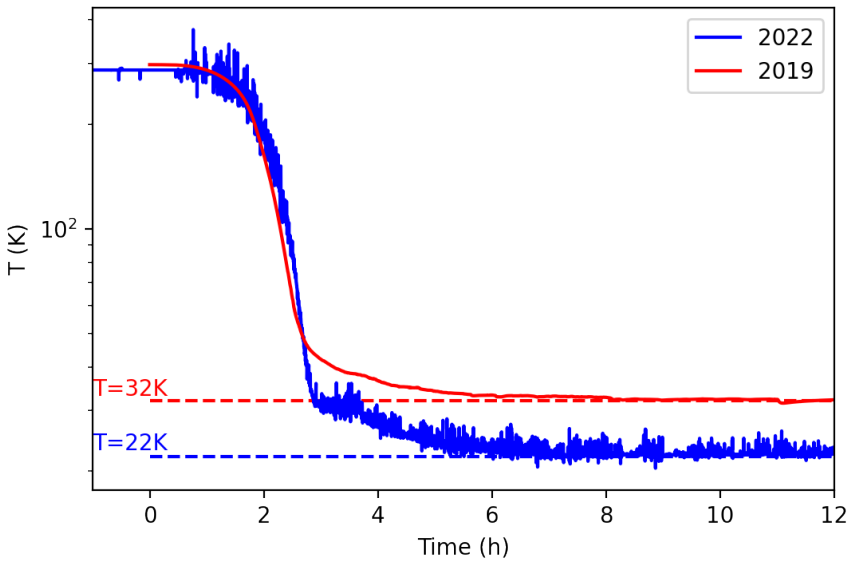

Figure 7.16: Temperature curves for the cool-down process as a function of time before (2019) and after the trap upgrades (2022).

with the following fitting function [156]:

$$\mathrm{ToF}_{fit} = \int_{z_0}^{z_f} \left(\frac{m}{2[E_0 - qV(z) - \mu(\omega_{RF})B(z)]} \right)^{1/2} dz \tag{7.7}$$

which takes into account collisions with background gas by introducing a damping force $\vec{F} = -\delta m\vec{u}$ in the calculation of the ion's kinetic energy. The ion's radial kinetic energy enters Function 7.7 through the magnetic moment of the ions $\vec{\mu}(\omega_{RF}) = (E_r(\omega_{RF})/B)\hat{e}_z$. The damping coefficient of the damping force depends on the pressure p and the temperature T of the background gas according to:

$$\delta = \frac{q}{m}\frac{1}{M_{ion}}\frac{p/p_N}{T/T_N} \tag{7.8}$$

where M_{ion} is the reduced ion mobility of the ions, p_N is the normal pressure and T_N is the normal temperature. For the resonance at $T = 300$ K, a damping parameter $\delta = 4.61(11)s^{-1}$ is found, while for the cold trap (T = 22 K), the damping coef-

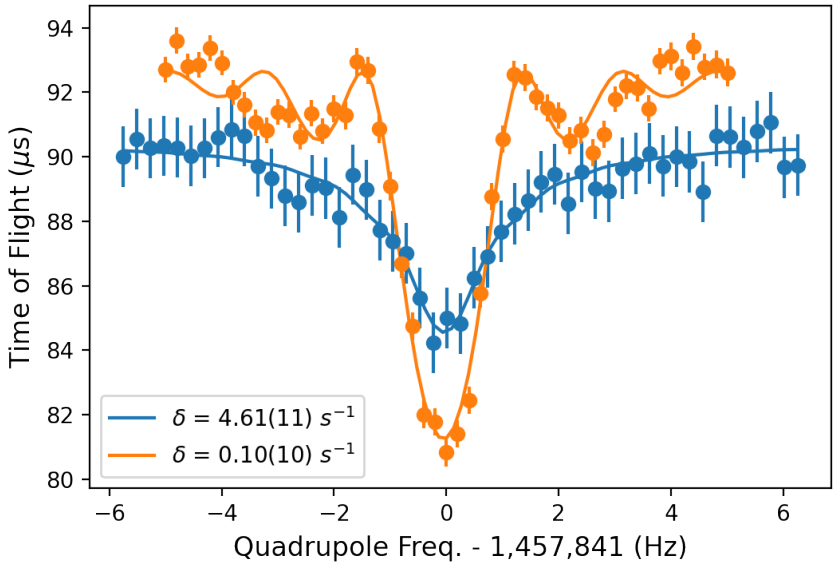

Figure 7.17: ToF resonances of ^{39}K ions at 300 K (blue) and 22 K (orange). The lines indicate fits to the data. For details see text.

ficient is $\delta = 0.10(10)s^{-1}$. A quantitative estimate for the pressure improvement can be derived from these parameters in combination with Eq. 7.8. The reduced ion mobility can be calculated from [14]:

$$M_{ion} = \frac{3e}{16N_0}\left(\frac{2\pi}{\mu kT}\right)^{1/2}\frac{1}{\Omega} \tag{7.9}$$

where e is the electron charge, $N_0 = 2.5 \cdot 10^{25}m^{-3}$ is the number density of an ideal gas, k is the Boltzman constant, $\mu = m_{ion}m_{gas}/(m_{ion}+m_{gas})$ is the reduced mass and

$$\Omega \approx \pi\left(\frac{d_{ion}+d_{gas}}{2}\right)^2 \tag{7.10}$$

is the cross section, where $d = 0.120415405(m[u])^{1/3}$ is the ion or gas atom/-molecule diameter [14].

An average d_{gas} and m_{gas} can be estimated from the composition of gases measured in CryoMPET. Recent background measurements using an RGA [221]

showed that in the room temperature CryoMPET, the dominant molecular contributions belong to H_2, H_2O and N_2 with an approximately equal concentration, while in CryoMPET at 22 K, the only molecular contribution belongs to N_2. With these considerations, the pressure ratio at 22 K versus 300 K results to:

$$\frac{p(22K)}{p(300K)} = 4 \cdot 10^{-3} \tag{7.11}$$

Moreover, as can be seen in Fig. 7.17, where the damping coefficients derived from fitting Eq. 7.7 to the data are displayed in the legend, the damping factor for the resonance at cryogenic conditions is consistent with zero within one sigma and therefore the pressure ratio can be orders of magnitude smaller. In conclusion, our results are in good agreement with the design expectation [163].

At this point, the TITAN MPET upgrade to CryoMPET is complete: a cryogenic Penning trap designed to perform precision mass measurements on short-lived charge bred ions. A key requirement was to improve the pressure by cryo-absorption and cryo-condensation and achieve storage times on the order of 1 s. The trap was assembled and tested. After the first installation, a number of tests were performed leading to additional improvements and optimizations, based on observations, calculations and simulations. With these improvements, it was verified that CryoMPET met specifications and that the system's performance was satisfactory. Commissioning of the trap at room and cryogenic temperatures was performed confirming at-specification performance of CryoMPET in reducing collisions with background gases and enabling the required excitation and storage times for singly charged ions.

Chapter 8

Conclusions

Advances in theoretical and experimental nuclear physics have allowed probing nuclear structure to an unprecedented level. However, the clarity reached also leads to new questions, such as new shell closures [247] and quenched shell closures [182], as expected when improving resolution to finer and finer details. New magic numbers as well as the disappearance of well-established magic numbers have been one of the central focus points of modern nuclear structure research both experimentally (for example [182, 247]) and theoretically [54].

In this thesis, two distinct regions in the chart of nuclei were investigated through approaches to test and benchmark state-of-the-art nuclear theory at extremes. Both studies were carried out with the TITAN MR-TOF MS mass measurement system, currently the leading device in the world for fast measurements while suppressing co-produced background contamination. In the first study, the N = 20 shell quenching was closely investigated via precision mass measurements. Specifically the mass of ^{33}Na was determined directly for the first time. The binding energy of the ^{33}Na nucleus compared to that of other nuclei in the region of the quenched shell closure indicates a recovery of the magic shell towards the neutron dripline. In addition, a new isomeric state at an excitation energy of 117.6(8.4) keV was discovered for the deformed odd-odd ^{32}Na nucleus. This finding gives new insight into the island of inversion. The second study focuses on exploring the limits of existence of heavy neutron-deficient nuclei. The investigation was done using a combination of experimental mass measurements and decay energies, incorpo-

rated in the AME algorithm [264]. The results are the two-proton dripline between iridium and lead and investigations towards the existence of Thomas-Ehrman shifts and heavy two-proton emitters.

In addition to the online experimental studies, significant technical developments and improvements of the TITAN system were performed. This thesis describes the design, assembly and commissioning of TITAN's next generation Penning trap. TITAN's new Penning trap operates at cryogenic temperatures to achieve sufficiently low pressure to store HCI for high precision mass measurements. A significant decrease in interactions with background gas has been observed for singly charged ions and the trap is in a state to receive HCI when they become available, after the TITAN charge breeder is re-commissioned. Finally, simulations and technical upgrades have been performed and are described in this thesis towards the implementation of the PI-ICR technique at TITAN, taking full advantage of HCI at cryogenic temperatures. The commissioning is ongoing but is not part of this thesis.

The upgrade of the TITAN Penning trap to CryoMPET will allow measurements with the potential to improve the achievable precision by an order of magnitude, for equal observation time or corresponding nuclear half-lives. Moreover, with the additional ongoing upgrades of TITAN EBIT for charge breeding and the completion of the PI-ICR detection technique, TITAN will be able to take full advantage of Advanced Rare Isotope Laboratory (ARIEL), the world's most powerful ISOL-isotope production facility. This will make TITAN the leading mass measurement facility for the foreseable future.

Bibliography

[1] Isac yield database. https://mis.triumf.ca/science/planning/yield/beam. → pages xx, 69

[2] Cernox temperature sensor specifications, lakeshore. https://www.lakeshore.com/products/categories/specification/temperature-products/cryogenic-temperature-sensors/cernox, . → pages 145, 151

[3] Dt-670 silicon diode specifications, lakeshore. https://www.lakeshore.com/products/categories/specification/temperature-products/cryogenic-temperature-sensors/dt-670-silicon-diodes, . → pages 145, 151

[4] Mass Explorer. http://massexplorer.frib.msu.edu. → pages xxvi, 126

[5] The Standard Model of Particle Physics, Symmetry Magazine. https://www.symmetrymagazine.org/standard-model/. → pages xxvii, 139

[6] MIDAS Data Aquisition software. https://daq00.triumf.ca/MidasWiki/index.php/Main_Page#Documentation. → page 218

[7] H. G. Dehmelt, Bibliographical, 1990. URL https://www.nobelprize.org/prizes/physics/1989/dehmelt/biographical/. → page 43

[8] *Lenses: Basic Optics*, pages 1–43. Springer Berlin Heidelberg, Berlin, Heidelberg, 2008. ISBN 978-3-540-71925-0. doi:10.1007/978-3-540-71925-0_1. URL https://doi.org/10.1007/978-3-540-71925-0_1. → page 214

[9] Searching for new phenomena with profile likelihood ratio tests. *Nat Rev Phys*, 2:245–252, 2020. doi:https://doi.org/10.1038/s42254-020-0169-5. → page 99

[10] F. Ames, P. Bricault, H. Heggen, P. Kunz, J. Lassen, A. Mjøs, S. Raeder, and A. Teigelhöfer. Ion source developments for the production of radioactive isotope beams at TRIUMF. *Review of Scientific Instruments*, 85 (2), 12 2013. ISSN 0034-6748. doi:10.1063/1.4833926. URL https://doi.org/10.1063/1.4833926. 02B912. → page 31

[11] C. Amole, G. Andresen, M. Ashkezari, M. Baquero-Ruiz, W. Bertsche, P. Bowe, E. Butler, A. Capra, P. Carpenter, C. Cesar, S. Chapman, M. Charlton, A. Deller, S. Eriksson, J. Escallier, J. Fajans, T. Friesen, M. Fujiwara, D. Gill, A. Gutierrez, J. Hangst, W. Hardy, R. Hayano, M. Hayden, A. Humphries, J. Hurt, R. Hydomako, C. Isaac, M. Jenkins, S. Jonsell, L. Jørgensen, S. Kerrigan, L. Kurchaninov, N. Madsen, A. Marone, J. McKenna, S. Menary, P. Nolan, K. Olchanski, A. Olin, B. Parker, A. Povilus, P. Pusa, F. Robicheaux, E. Sarid, D. Seddon, S. Seif El Nasr, D. Silveira, C. So, J. Storey, R. Thompson, J. Thornhill, D. Wells, D. van der Werf, J. Wurtele, and Y. Yamazaki. The alpha antihydrogen trapping apparatus. *Nuclear Instruments and Methods in Physics Research Section A: Accelerators, Spectrometers, Detectors and Associated Equipment*, 735:319–340, 2014. ISSN 0168-9002. doi:https://doi.org/10.1016/j.nima.2013.09.043. URL https://www.sciencedirect.com/science/article/pii/S0168900213012771. → page 43

[12] I. Angeli and K. Marinova. Table of experimental nuclear ground state charge radii: An update. *Atomic Data and Nuclear Data Tables*, 99(1): 69–95, 2013. ISSN 0092-640X. doi:https://doi.org/10.1016/j.adt.2011.12.006. URL https://www.sciencedirect.com/science/article/pii/S0092640X12000265. → pages xvi, 7

[13] S. Aoyama, N. Itagaki, K. Katō, and K. Ikeda. Thomas-ehrman effect on $s_{1/2}$ and $p_{1/2}$ resonance states in $^{10}\mathrm{C}+p$. *Phys. Rev. C*, 57:975–977, Feb 1998. doi:10.1103/PhysRevC.57.975. URL https://link.aps.org/doi/10.1103/PhysRevC.57.975. → pages xvii, 20, 21

[14] A. D. Appelhans and D. A. Dahl. Simion ion optics simulations at atmospheric pressure. *International Journal of Mass Spectrometry*, 244(1): 1–14, 2005. ISSN 1387-3806. doi:https://doi.org/10.1016/j.ijms.2005.03.010. URL https://www.sciencedirect.com/science/article/pii/S1387380605001089. → page 158

[15] I. Arcavi, D. Howell, D. Kasen, et al. Energetic eruptions leading to a peculiar hydrogen-rich explosion of a massive star. *Nature*, 551, 2017. doi:https://doi.org/10.1038/nature24030. → page 136

[16] M. Arnould, S. Goriely, and K. Takahashi. The r-process of stellar nucleosynthesis: Astrophysics and nuclear physics achievements and mysteries. *Physics Reports*, 450(4):97–213, 2007. ISSN 0370-1573. doi:https://doi.org/10.1016/j.physrep.2007.06.002. URL https://www.sciencedirect.com/science/article/pii/S0370157307002438. → pages 135, 137

[17] K. Asahi and K. Matsuta. Nuclear electromagnetic moments. -nmr and its applications. *Nuclear Physics A*, 693(1):63–76, 2001. ISSN 0375-9474. doi:https://doi.org/10.1016/S0375-9474(01)00361-X. URL https://www.sciencedirect.com/science/article/pii/S037594740100361X. Radioactive Nuclear Beams. → page 14

[18] P. Ascher, L. Daudin, M. Flayol, M. Gerbaux, S. Grévy, M. Hukkanen, A. Husson, A. de Roubin, P. Alfaurt, B. Blank, K. Blaum, B. Lachacinski, D. Lunney, E. M. Ramirez, S. Naimi, S. Perard, and B. Thomas. PIPERADE: A double Penning trap for mass separation and mass spectrometry at DESIR/SPIRAL2. *Nuclear Instruments and Methods in Physics Research Section A: Accelerators, Spectrometers, Detectors and Associated Equipment*, 1019:165857, 2021. ISSN 0168-9002. doi:https://doi.org/10.1016/j.nima.2021.165857. URL https://www.sciencedirect.com/science/article/pii/S0168900221008421. → pages 34, 44

[19] ATLAS collaboration. Observation of a new particle in the search for the Standard Model Higgs boson with the ATLAS detector at the LHC. *Physics Letters B*, 716(1):1–29, 2012. ISSN 0370-2693. doi:https://doi.org/10.1016/j.physletb.2012.08.020. URL https://www.sciencedirect.com/science/article/pii/S037026931200857X. → page 138

[20] T. Aumann, W. Bartmann, O. Boine-Frankenheim, et al. PUMA, antiProton unstable matter annihilation. *Eur. Phys. J. A*, 58, 2022. doi:https://doi.org/10.1140/epja/s10050-022-00713-x. URL https://link.springer.com/article/10.1140/epja/s10050-022-00713-x. → page 43

[21] S. Ayet San Andrés, C. Hornung, J. Ebert, W. R. Plass, T. Dickel, H. Geissel, C. Scheidenberger, J. Bergmann, F. Greiner, E. Haettner, C. Jesch, W. Lippert, I. Mardor, I. Miskun, Z. Patyk, S. Pietri, A. Pihktelev, S. Purushothaman, M. P. Reiter, A.-K. Rink, H. Weick, M. I. Yavor, S. Bagchi, V. Charviakova, P. Constantin, M. Diwisch, A. Finlay, S. Kaur, R. Knöbel, J. Lang, B. Mei, I. D. Moore, J.-H. Otto, I. Pohjalainen, A. Prochazka, C. Rappold, M. Takechi, Y. K. Tanaka, J. S. Winfield, and X. Xu. High-resolution, accurate multiple-reflection time-of-flight mass spectrometry for short-lived, exotic nuclei of a few events in their ground and low-lying isomeric states. *Phys. Rev. C*, 99:064313, Jun 2019. doi:10.1103/PhysRevC.99.064313. URL https://link.aps.org/doi/10.1103/PhysRevC.99.064313. → pages 35, 42, 90

[22] G. M. B. Franzke, H. Geissel. Mass and lifetime measurements of exotic nuclei in storage rings. *Mass Spectrometry Reviews*, 27:428–469, 2008. doi:https://doi.org/10.1002/mas.20173. URL https://analyticalsciencejournals.onlinelibrary.wiley.com/doi/abs/10.1002/mas.20173. → page 34

[23] C. Babcock, R. Klawitter, E. Leistenschneider, D. Lascar, B. R. Barquest, A. Finlay, M. Foster, A. T. Gallant, P. Hunt, B. Kootte, Y. Lan, S. F. Paul, M. L. Phan, M. P. Reiter, B. Schultz, D. Short, C. Andreoiu, M. Brodeur, I. Dillmann, G. Gwinner, A. A. Kwiatkowski, K. G. Leach, and J. Dilling. Mass measurements of neutron-rich indium isotopes toward the $N = 82$ shell closure. *Phys. Rev. C*, 97:024312, Feb 2018. doi:10.1103/PhysRevC.97.024312. URL https://link.aps.org/doi/10.1103/PhysRevC.97.024312. → pages 83, 138, 141

[24] S. Baker and R. D. Cousins. Clarification of the use of CHI-square and likelihood functions in fits to histograms. *Nuclear Instruments and Methods in Physics Research*, 221(2):437–442, 1984. ISSN 0167-5087. doi:https://doi.org/10.1016/0167-5087(84)90016-4. URL https://www.sciencedirect.com/science/article/pii/0167508784900164. → page 92

[25] G. C. Ball, G. Hackman, and R. Krücken. The TRIUMF-ISAC facility: two decades of discovery with rare isotope beams. *Physica Scripta*, 91(9): 093002, jul 2016. doi:10.1088/0031-8949/91/9/093002. URL https://dx.doi.org/10.1088/0031-8949/91/9/093002. → pages 32, 66, 68

[26] B. Bastin, S. Grévy, D. Sohler, O. Sorlin, Z. Dombrádi, N. L. Achouri, J. C. Angélique, F. Azaiez, D. Baiborodin, R. Borcea, C. Bourgeois, A. Buta,

A. Bürger, R. Chapman, J. C. Dalouzy, Z. Dlouhy, A. Drouard, Z. Elekes, S. Franchoo, S. Iacob, B. Laurent, M. Lazar, X. Liang, E. Liénard, J. Mrazek, L. Nalpas, F. Negoita, N. A. Orr, Y. Penionzhkevich, Z. Podolyák, F. Pougheon, P. Roussel-Chomaz, M. G. Saint-Laurent, M. Stanoiu, I. Stefan, F. Nowacki, and A. Poves. Collapse of the $N = 28$ Shell Closure in ^{42}Si. *Phys. Rev. Lett.*, 99:022503, Jul 2007. doi:10.1103/PhysRevLett.99.022503. URL https://link.aps.org/doi/10.1103/PhysRevLett.99.022503. → page 13

[27] P. Baumann, A. Huck, G. Klotz, A. Knipper, G. Walter, G. Marguier, H. Ravn, C. Richard-Serre, A. Poves, and J. Retamosa. 34Si: A new doubly magic nucleus? *Physics Letters B*, 228(4):458–462, 1989. ISSN 0370-2693. doi:https://doi.org/10.1016/0370-2693(89)90974-X. URL https://www.sciencedirect.com/science/article/pii/037026938990974X. → page 14

[28] D. Beck, K. Blaum, G. Bollen, P. Delahaye, S. George, C. Guénaut, F. Herfurth, A. Herlert, D. Lunney, L. Schweikhard, and C. Yazidjian. Electric and magnetic field optimization procedure for Penning trap mass spectrometers. *Nuclear Instruments and Methods in Physics Research Section A: Accelerators, Spectrometers, Detectors and Associated Equipment*, 598(2):635–641, 2009. ISSN 0168-9002. doi:https://doi.org/10.1016/j.nima.2008.09.019. URL https://www.sciencedirect.com/science/article/pii/S0168900208013909. → page 60

[29] S. Beck, B. Kootte, I. Dedes, T. Dickel, A. A. Kwiatkowski, E. M. Lykiardopoulou, W. R. Plaß, M. P. Reiter, C. Andreoiu, J. Bergmann, T. Brunner, D. Curien, J. Dilling, J. Dudek, E. Dunling, J. Flowerdew, A. Gaamouci, L. Graham, G. Gwinner, A. Jacobs, R. Klawitter, Y. Lan, E. Leistenschneider, N. Minkov, V. Monier, I. Mukul, S. F. Paul, C. Scheidenberger, R. I. Thompson, J. L. Tracy, M. Vansteenkiste, H.-L. Wang, M. E. Wieser, C. Will, and J. Yang. Mass Measurements of Neutron-Deficient Yb Isotopes and Nuclear Structure at the Extreme Proton-Rich Side of the $N = 82$ Shell. *Phys. Rev. Lett.*, 127:112501, Sep 2021. doi:10.1103/PhysRevLett.127.112501. URL https://link.aps.org/doi/10.1103/PhysRevLett.127.112501. → pages xxi, 41, 79, 117

[30] S. Berryman. Democritus. In *The Stanford Encyclopedia of Philosophy*. Metaphysics Research Lab, Stanford University, 2023. → page 1

[31] H. A. Bethe and R. F. Bacher. Nuclear Physics A. Stationary States of Nuclei. *Rev. Mod. Phys.*, 8:82–229, Apr 1936. doi:10.1103/RevModPhys.8.82. URL https://link.aps.org/doi/10.1103/RevModPhys.8.82. → page 2

[32] S. Bethke. Determination of the qcd coupling α_s. *Journal of Physics G: Nuclear and Particle Physics*, 26(7):R27, jul 2000. doi:10.1088/0954-3899/26/7/201. URL https://dx.doi.org/10.1088/0954-3899/26/7/201. → page 8

[33] K. Blaum, H. Kracke, S. Kreim, A. Mooser, C. Mrozik, W. Quint, C. C. Rodegheri, B. Schabinger, S. Sturm, S. Ulmer, A. Wagner, J. Walz, and G. Werth. g-factor experiments on simple systems in Penning traps*. *Journal of Physics B: Atomic, Molecular and Optical Physics*, 42(15): 154021, jul 2009. doi:10.1088/0953-4075/42/15/154021. URL https://dx.doi.org/10.1088/0953-4075/42/15/154021. → page 43

[34] K. Blaum, S. Eliseev, and S. Goriely. *Masses of Exotic Nuclei*, pages 1–38. Springer Nature Singapore, Singapore, 2020. ISBN 978-981-15-8818-1. doi:10.1007/978-981-15-8818-1_101-1. URL https://doi.org/10.1007/978-981-15-8818-1_101-1. → pages 43, 45

[35] Y. Blumenfeld, T. Nilsson, and P. V. Duppen. Facilities and methods for radioactive ion beam production. *Physica Scripta*, 2013(T152):014023, Jan 2013. doi:10.1088/0031-8949/2013/T152/014023. URL https://dx.doi.org/10.1088/0031-8949/2013/T152/014023. → pages xvii, 31

[36] G. Bollen, P. Dabkiewicz, P. Egelhof, et al. First absolute mass measurements of short-lived isotopes. *Hyperfine Interactions*, 38:793–802, 1987. doi:https://doi.org/10.1007/BF02394875. URL https://link.springer.com/article/10.1007/BF02394875. → page 44

[37] G. Bollen, H. J. Kluge, T. Otto, G. Savard, and H. Stolzenberg. Ramsey technique applied in a Penning trap mass spectrometer, Aug 1992. → pages 52, 54

[38] F. Bosch and Y. A. Litvinov. Mass and lifetime measurements at the experimental storage ring of GSI. *International Journal of Mass Spectrometry*, 349-350:151–161, 2013. ISSN 1387-3806. doi:https://doi.org/10.1016/j.ijms.2013.04.025. URL https://www.sciencedirect.com/science/article/pii/S1387380613001528. 100 years of Mass Spectrometry. → page 34

[39] N. E. Bradbury and R. A. Nielsen. Absolute values of the electron mobility in hydrogen. *Phys. Rev.*, 49:388–393, Mar 1936. doi:10.1103/PhysRev.49.388. URL https://link.aps.org/doi/10.1103/PhysRev.49.388. → page 223

[40] P. Bricault, M. Dombsky, A. Dowling, and M. Lane. High power target developments at ISAC. *Nuclear Instruments and Methods in Physics Research Section B: Beam Interactions with Materials and Atoms*, 204: 319–324, 2003. ISSN 0168-583X. doi:https://doi.org/10.1016/S0168-583X(03)00504-4. URL https://www.sciencedirect.com/science/article/pii/S0168583X03005044. 14th International Conference on Electromagnetic Isotope Separators and Techniques Related to their Applications. → pages 66, 67

[41] P. Bricault, F. Ames, T. Achtzehn, M. Dombsky, F. Labrecque, J. Lassen, J.-P. Lavoie, and N. Lecesne. An overview on TRIUMF's developments on ion source for radioactive beams (invited). *Review of Scientific Instruments*, 79(2):02A908, 2008. doi:10.1063/1.2801344. URL https://aip.scitation.org/doi/abs/10.1063/1.2801344. → page 68

[42] P. Bricault, F. Ames, M. Dombsky, et al. Rare isotope beams at ISAC—target and ion source systems. *Hyperfine Interact*, 225:25–49, 2014. doi:https://doi.org/10.1007/s10751-013-0880-z. URL https://link.springer.com/article/10.1007/s10751-013-0880-z. → pages 31, 68, 89

[43] P. G. Bricault. Thick target for high-power isol facilities. *Nuclear Instruments and Methods in Physics Research Section B: Beam Interactions with Materials and Atoms*, 376:3–7, 2016. ISSN 0168-583X. doi:https://doi.org/10.1016/j.nimb.2016.03.024. URL https://www.sciencedirect.com/science/article/pii/S0168583X16002275. Proceedings of the XVIIth International Conference on Electromagnetic Isotope Separators and Related Topics (EMIS2015), Grand Rapids, MI, U.S.A., 11-15 May 2015. → page 67

[44] M. Brodeur. *First direct mass measurement of the two and four neutron halos 6He and 8He using the TITAN Penning trap mass spectrometer*. PhD thesis, University of British Columbia, 2010. URL https://open.library.ubc.ca/collections/ubctheses/24/items/1.0069970. → pages 60, 226

[45] M. Brodeur, V. Ryjkov, T. Brunner, S. Ettenauer, A. Gallant, V. Simon, M. Smith, A. Lapierre, R. Ringle, P. Delheij, M. Good, D. Lunney, and J. Dilling. Verifying the accuracy of the TITAN Penning-trap mass spectrometer. *International Journal of Mass Spectrometry*, 310:20–31, 2012. ISSN 1387-3806. doi:https://doi.org/10.1016/j.ijms.2011.11.002. URL https://www.sciencedirect.com/science/article/pii/S1387380611004568. → pages 59, 60, 83

[46] L. S. Brown and G. Gabrielse. Geonium theory: Physics of a single electron or ion in a Penning trap. *Rev. Mod. Phys.*, 58:233–311, Jan 1986. doi:10.1103/RevModPhys.58.233. URL https://link.aps.org/doi/10.1103/RevModPhys.58.233. → page 46

[47] T. Brunner, M. Smith, M. Brodeur, S. Ettenauer, A. Gallant, V. Simon, A. Chaudhuri, A. Lapierre, E. Mané, R. Ringle, M. Simon, J. Vaz, P. Delheij, M. Good, M. Pearson, and J. Dilling. TITAN's digital RFQ ion beam cooler and buncher, operation and performance. *Nuclear Instruments and Methods in Physics Research Section A: Accelerators, Spectrometers, Detectors and Associated Equipment*, 676:32–43, 2012. ISSN 0168-9002. doi:https://doi.org/10.1016/j.nima.2012.02.004. URL https://www.sciencedirect.com/science/article/pii/S0168900212001398. → pages xxi, 68, 70, 71, 72, 89

[48] C. D. Bruzewicz, J. Chiaverini, R. McConnell, and J. M. Sage. Trapped-ion quantum computing: Progress and challenges. *Applied Physics Reviews*, 6, 2019. doi:https://doi.org/10.1063/1.5088164. URL https://aip.scitation.org/doi/10.1063/1.5088164. → page 43

[49] N. Cabibbo. Unitary symmetry and leptonic decays. *Phys. Rev. Lett.*, 10: 531–533, Jun 1963. doi:10.1103/PhysRevLett.10.531. URL https://link.aps.org/doi/10.1103/PhysRevLett.10.531. → page 139

[50] P. Campbell, I. Moore, and M. Pearson. Laser spectroscopy for nuclear structure physics. *Progress in Particle and Nuclear Physics*, 86:127–180, 2016. ISSN 0146-6410. doi:https://doi.org/10.1016/j.ppnp.2015.09.003. URL https://www.sciencedirect.com/science/article/pii/S0146641015000915. → page 14

[51] X. Campi, H. Flocard, A. Kerman, and S. Koonin. Shape transition in the neutron rich sodium isotopes. *Nuclear Physics A*, 251(2):193–205, 1975.

ISSN 0375-9474. doi:https://doi.org/10.1016/0375-9474(75)90065-2. URL https://www.sciencedirect.com/science/article/pii/0375947475900652. → page 12

[52] J. D. Cardona, K. Dietrich, I. Mukul, J. Dilling, G. Gwinner, O. Kester, and A. A. Kwiatkowski. Simulations of a new electron gun for the TITAN EBIT. *Journal of Physics: Conference Series*, 2244(1):012075, apr 2022. doi:10.1088/1742-6596/2244/1/012075. URL https://dx.doi.org/10.1088/1742-6596/2244/1/012075. → pages 80, 142

[53] M. Carena and H. Haber. Higgs boson theory and phenomenology. *Progress in Particle and Nuclear Physics*, 50(1):63–152, 2003. ISSN 0146-6410. doi:https://doi.org/10.1016/S0146-6410(02)00177-1. URL https://www.sciencedirect.com/science/article/pii/S0146641002001771. → page 138

[54] E. Caurier, F. Nowacki, and A. Poves. Merging of the islands of inversion at $N = 20$ and $N = 28$. *Phys. Rev. C*, 90:014302, Jul 2014. doi:10.1103/PhysRevC.90.014302. URL https://link.aps.org/doi/10.1103/PhysRevC.90.014302. → pages 16, 109, 160

[55] E. Chabanat, P. Bonche, P. Haensel, J. Meyer, and R. Schaeffer. A Skyrme parametrization from subnuclear to neutron star densities Part II. Nuclei far from stabilities. *Nuclear Physics A*, 635(1):231–256, 1998. ISSN 0375-9474. doi:https://doi.org/10.1016/S0375-9474(98)00180-8. URL https://www.sciencedirect.com/science/article/pii/S0375947498001808. → page 28

[56] N. Chada, J. Romanos, R. Hilton, G. Suppes, J. Burress, and P. Pfeifer. Activated carbon monoliths for methane storage. In *APS March Meeting Abstracts*, volume 2012 of *APS Meeting Abstracts*, page W33.012, Feb. 2012. → page 143

[57] A. Chaudhuri, C. Andreoiu, T. Brunner, U. Chowdhury, S. Ettenauer, A. T. Gallant, G. Gwinner, A. A. Kwiatkowski, A. Lennarz, D. Lunney, T. D. Macdonald, B. E. Schultz, M. C. Simon, V. V. Simon, and J. Dilling. Evidence for the extinction of the $N = 20$ neutron-shell closure for ^{32}Mg from direct mass measurements. *Phys. Rev. C*, 88:054317, Nov 2013. doi:10.1103/PhysRevC.88.054317. URL https://link.aps.org/doi/10.1103/PhysRevC.88.054317. → pages xxiv, 14, 87, 103, 105

[58] A. Chaudhuri, C. Andreoiu, M. Brodeur, et al. TITAN: an ion trap for accurate mass measurements of ms-half-life nuclides. *Appl. Phys. B*, 114: 99–105, 2014. doi:https://doi.org/10.1007/s00340-013-5618-8. URL https://www.sciencedirect.com/science/article/pii/0168583X9195108P. → page 81

[59] P. Chauveau, P. Delahaye, G. De France, S. El Abir, J. Lory, Y. Merrer, M. Rosenbusch, L. Schweikhard, and R. Wolf. PILGRIM, a Multi-Reflection Time-of-Flight Mass Spectrometer for Spiral2-S3 at GANIL. *Nuclear Instruments and Methods in Physics Research Section B: Beam Interactions with Materials and Atoms*, 376:211–215, 2016. ISSN 0168-583X. doi:https://doi.org/10.1016/j.nimb.2016.01.025. URL https://www.sciencedirect.com/science/article/pii/S0168583X16000732. Proceedings of the XVIIth International Conference on Electromagnetic Isotope Separators and Related Topics (EMIS2015), Grand Rapids, MI, U.S.A., 11-15 May 2015. → page 34

[60] A. Choplin, L. Siess, and S. Goriely. The intermediate neutron capture process. I. Development of the i-process in low-metallicity low-mass AGB stars. *Astronomy & Astrophysics*, 648, 2021. doi:10.1051/0004-6361/202040170. → page 135

[61] P. Choudhary and P. C. Srivastava. Ab initio no-core shell model study of neutron-rich 18,19,20C isotopes. *Nuclear Physics A*, 1029:122565, 2023. ISSN 0375-9474. doi:https://doi.org/10.1016/j.nuclphysa.2022.122565. URL https://www.sciencedirect.com/science/article/pii/S0375947422001890. → page 25

[62] G. Christian, N. Frank, S. Ash, T. Baumann, D. Bazin, J. Brown, P. A. DeYoung, J. E. Finck, A. Gade, G. F. Grinyer, A. Grovom, J. D. Hinnefeld, E. M. Lunderberg, B. Luther, M. Mosby, S. Mosby, T. Nagi, G. F. Peaslee, W. F. Rogers, J. K. Smith, J. Snyder, A. Spyrou, M. J. Strongman, M. Thoennessen, M. Warren, D. Weisshaar, and A. Wersal. Exploring the Low-Z Shore of the Island of Inversion at $N = 19$. *Phys. Rev. Lett.*, 108: 032501, Jan 2012. doi:10.1103/PhysRevLett.108.032501. URL https://link.aps.org/doi/10.1103/PhysRevLett.108.032501. → pages 14, 110

[63] I. D. Clark. *isotopesstableStable isotopes*, pages 588–592. Springer Netherlands, Dordrecht, 1998. ISBN 978-1-4020-4496-0. doi:10.1007/1-4020-4496-8_295. URL https://doi.org/10.1007/1-4020-4496-8_295. → pages 3, 5

[64] E. Comay, I. Kelson, and A. Zidon. The Thomas – Ehrman shift across the proton dripline. *Phys. Lett. B*, 210:31–34, 1988. → pages 20, 23, 121

[65] M. K. Craddock, E. W. Blackmore, G. Dutto, C. J. Kost, G. H. Mackenzie, and P. Schmor. Improvements to the beam properties of the triumf cyclotron. *IEEE Transactions on Nuclear Science*, 24(3):1615–1617, 1977. doi:10.1109/TNS.1977.4329028. → page 66

[66] H. L. Crawford, V. Tripathi, J. M. Allmond, B. P. Crider, R. Grzywacz, S. N. Liddick, A. Andalib, E. Argo, C. Benetti, S. Bhattacharya, C. M. Campbell, M. P. Carpenter, J. Chan, A. Chester, J. Christie, B. R. Clark, I. Cox, A. A. Doetsch, J. Dopfer, J. G. Duarte, P. Fallon, A. Frotscher, T. Gaballah, T. J. Gray, J. T. Harke, J. Heideman, H. Heugen, R. Jain, T. T. King, N. Kitamura, K. Kolos, F. G. Kondev, A. Laminack, B. Longfellow, R. S. Lubna, S. Luitel, M. Madurga, R. Mahajan, M. J. Mogannam, C. Morse, S. Neupane, A. Nowicki, T. H. Ogunbeku, W.-J. Ong, C. Porzio, C. J. Prokop, B. C. Rasco, E. K. Ronning, E. Rubino, T. J. Ruland, K. P. Rykaczewski, L. Schaedig, D. Seweryniak, K. Siegl, M. Singh, S. L. Tabor, T. L. Tang, T. Wheeler, J. A. Winger, and Z. Xu. Crossing $N = 28$ Toward the Neutron Drip Line: First Measurement of Half-Lives at FRIB. *Phys. Rev. Lett.*, 129:212501, Nov 2022. doi:10.1103/PhysRevLett.129.212501. URL https://link.aps.org/doi/10.1103/PhysRevLett.129.212501. → pages 14, 17, 87

[67] R. H. Cyburt et al. Dependence of X-ray burst models on Nuclear reaction rates. *The Astrophysics Journal*, 830(2):55, 2016. doi:https://doi.org/10.3847/0004-637X/830/2/55. URL https://iopscience.iop.org/article/10.3847/0004-637X/830/2/55. → page 135

[68] D. A. Dahl. SIMION for the personal computer in reflection. *International Journal of Mass Spectrometry*, 200(1):3–25, 2000. ISSN 1387-3806. doi:https://doi.org/10.1016/S1387-3806(00)00305-5. URL https://www.sciencedirect.com/science/article/pii/S1387380600003055. Volume 200: The state of the field as we move into a new millenium. → page 212

[69] J. Dechargé and D. Gogny. Hartree-Fock-Bogolyubov calculations with the $D1$ effective interaction on spherical nuclei. *Phys. Rev. C*, 21:1568–1593, Apr 1980. doi:10.1103/PhysRevC.21.1568. URL https://link.aps.org/doi/10.1103/PhysRevC.21.1568. → pages 27, 29

[70] J. P. Delaroche, M. Girod, J. Libert, H. Goutte, S. Hilaire, S. Péru, N. Pillet, and G. F. Bertsch. Structure of even-even nuclei using a mapped collective Hamiltonian and the D1S Gogny interaction. *Phys. Rev. C*, 81:014303, Jan 2010. doi:10.1103/PhysRevC.81.014303. URL https://link.aps.org/doi/10.1103/PhysRevC.81.014303. → pages xxvi, 126

[71] C. Détraz, D. Guillemaud, G. Huber, R. Klapisch, M. Langevin, F. Naulin, C. Thibault, L. C. Carraz, and F. Touchard. Beta decay of $^{27-32}$Na and their descendants. *Phys. Rev. C*, 19:164–176, Jan 1979. doi:10.1103/PhysRevC.19.164. URL https://link.aps.org/doi/10.1103/PhysRevC.19.164. → page 12

[72] T. Dickel, W. Plaß, A. Becker, U. Czok, H. Geissel, E. Haettner, C. Jesch, W. Kinsel, M. Petrick, C. Scheidenberger, A. Simon, and M. Yavor. A high-performance multiple-reflection time-of-flight mass spectrometer and isobar separator for the research with exotic nuclei. *Nuclear Instruments and Methods in Physics Research Section A: Accelerators, Spectrometers, Detectors and Associated Equipment*, 777:172–188, 2015. ISSN 0168-9002. doi:https://doi.org/10.1016/j.nima.2014.12.094. URL https://www.sciencedirect.com/science/article/pii/S0168900214015629. → page 40

[73] S. Diebold. *Development and Testing of Instrumentation for Space-Based Ultraviolet and X-Ray Astronomy*. PhD thesis, 01 2015. → pages xxx, 217

[74] J. Dilling, D. Ackermann, J. Bernard, et al. The SHIPTRAP project: A capture and storage facility at GSI for heavy radionuclides from SHIP. *Hyperfine Interactions*, 127:491–496, 2000. doi:https://doi.org/10.1023/A:1012638322226. URL https://link.springer.com/article/10.1023/A:1012638322226. → pages 34, 44, 52, 66

[75] J. Dilling, P. Bricault, M. Smith, and H.-J. Kluge. The proposed TITAN facility at ISAC for very precise mass measurements on highly charged short-lived isotopes, journal = Nuclear Instruments and Methods in Physics Research Section B: Beam Interactions with Materials and Atoms. 204: 492–496, 2003. ISSN 0168-583X. doi:https://doi.org/10.1016/S0168-583X(02)02118-3. URL https://www.sciencedirect.com/science/article/pii/S0168583X02021183. 14th International Conference on Electromagnetic Isotope Separators and Techniques Related to their Applications. → pages 34, 44, 66, 87

[76] J. Dilling, K. Blaum, M. Brodeur, and S. Eliseev. Penning-trap mass measurements in atomic and nuclear physics. *Annual Review of Nuclear and Particle Science*, 68(1):45–74, 2018. doi:10.1146/annurev-nucl-102711-094939. URL https://doi.org/10.1146/annurev-nucl-102711-094939. → pages xix, 44, 52, 57, 58, 154

[77] I. Dillmann, K.-L. Kratz, A. Wöhr, O. Arndt, B. A. Brown, P. Hoff, M. Hjorth-Jensen, U. Köster, A. N. Ostrowski, B. Pfeiffer, D. Seweryniak, J. Shergur, and W. B. Walters. $N = 82$ Shell Quenching of the Classical *r*-Process "Waiting-Point" Nucleus ^{130}Cd. *Phys. Rev. Lett.*, 91:162503, Oct 2003. doi:10.1103/PhysRevLett.91.162503. URL https://link.aps.org/doi/10.1103/PhysRevLett.91.162503. → page 13

[78] P. Doornenbal, H. Scheit, N. Aoi, S. Takeuchi, K. Li, E. Takeshita, H. Wang, H. Baba, S. Deguchi, N. Fukuda, H. Geissel, R. Gernhäuser, J. Gibelin, I. Hachiuma, Y. Hara, C. Hinke, N. Inabe, K. Itahashi, S. Itoh, D. Kameda, S. Kanno, Y. Kawada, N. Kobayashi, Y. Kondo, R. Krücken, T. Kubo, T. Kuboki, K. Kusaka, M. Lantz, S. Michimasa, T. Motobayashi, T. Nakamura, T. Nakao, K. Namihira, S. Nishimura, T. Ohnishi, M. Ohtake, N. A. Orr, H. Otsu, K. Ozeki, Y. Satou, S. Shimoura, T. Sumikama, M. Takechi, H. Takeda, K. N. Tanaka, K. Tanaka, Y. Togano, M. Winkler, Y. Yanagisawa, K. Yoneda, A. Yoshida, K. Yoshida, and H. Sakurai. Spectroscopy of ^{32}Ne and the "island of inversion". *Phys. Rev. Lett.*, 103:032501, Jul 2009. doi:10.1103/PhysRevLett.103.032501. URL https://link.aps.org/doi/10.1103/PhysRevLett.103.032501. → page 14

[79] P. Doornenbal, H. Scheit, N. Kobayashi, N. Aoi, S. Takeuchi, K. Li, E. Takeshita, Y. Togano, H. Wang, S. Deguchi, Y. Kawada, Y. Kondo, T. Motobayashi, T. Nakamura, Y. Satou, K. N. Tanaka, and H. Sakurai. Exploring the "island of inversion" by in-beam γ-ray spectroscopy of the neutron-rich sodium isotopes ^{31,32,33}Na. *Phys. Rev. C*, 81:041305, Apr 2010. doi:10.1103/PhysRevC.81.041305. URL https://link.aps.org/doi/10.1103/PhysRevC.81.041305.

[80] P. Doornenbal, H. Scheit, S. Takeuchi, N. Aoi, K. Li, M. Matsushita, D. Steppenbeck, H. Wang, H. Baba, H. Crawford, C. R. Hoffman, R. Hughes, E. Ideguchi, N. Kobayashi, Y. Kondo, J. Lee, S. Michimasa, T. Motobayashi, H. Sakurai, M. Takechi, Y. Togano, R. Winkler, and K. Yoneda. In-Beam γ-Ray Spectroscopy of ^{34,36,38}Mg: Merging the N=20 and N=28 Shell Quenching. *Phys. Rev. Lett.*, 111:212502, Nov 2013.

doi:10.1103/PhysRevLett.111.212502. URL https://link.aps.org/doi/10.1103/PhysRevLett.111.212502. → pages 16, 88

[81] P. Doornenbal, H. Scheit, S. Takeuchi, Y. Utsuno, N. Aoi, K. Li, M. Matsushita, D. Steppenbeck, H. Wang, H. Baba, E. Ideguchi, N. Kobayashi, Y. Kondo, J. Lee, S. Michimasa, T. Motobayashi, T. Otsuka, H. Sakurai, M. Takechi, Y. Togano, and K. Yoneda. Low-Z shore of the "island of inversion" and the reduced neutron magicity toward ^{28}O. *Phys. Rev. C*, 95:041301, Apr 2017. doi:10.1103/PhysRevC.95.041301. URL https://link.aps.org/doi/10.1103/PhysRevC.95.041301. → page 14

[82] J. B. Ehrman. On the Displacement of Corresponding Energy Levels of ^{13}C and ^{13}N. *Phys. Rev.*, 81:412–416, Feb 1951. doi:10.1103/PhysRev.81.412. URL https://link.aps.org/doi/10.1103/PhysRev.81.412. → page 21

[83] Z. Elekes, Z. Dombrádi, A. Saito, N. Aoi, H. Baba, K. Demichi, Z. Fülöp, J. Gibelin, T. Gomi, H. Hasegawa, N. Imai, M. Ishihara, H. Iwasaki, S. Kanno, S. Kawai, T. Kishida, T. Kubo, K. Kurita, Y. Matsuyama, S. Michimasa, T. Minemura, T. Motobayashi, M. Notani, T. Ohnishi, H. J. Ong, S. Ota, A. Ozawa, H. K. Sakai, H. Sakurai, S. Shimoura, E. Takeshita, S. Takeuchi, M. Tamaki, Y. Togano, K. Yamada, Y. Yanagisawa, and K. Yoneda. Proton inelastic scattering studies at the borders of the "island of inversion": The ^{30,31}Na and ^{33,34}Mg case. *Phys. Rev. C*, 73:044314, Apr 2006. doi:10.1103/PhysRevC.73.044314. URL https://link.aps.org/doi/10.1103/PhysRevC.73.044314. → page 14

[84] S. Eliseev, M. Block, A. Chaudhuri, F. Herfurth, H.-J. Kluge, A. Martin, C. Rauth, and G. Vorobjev. Octupolar excitation of ions stored in a Penning trap mass spectrometer—A study performed at SHIPTRAP. *International Journal of Mass Spectrometry*, 262(1):45–50, 2007. ISSN 1387-3806. doi:https://doi.org/10.1016/j.ijms.2006.10.003. URL https://www.sciencedirect.com/science/article/pii/S1387380606004623. → page 53

[85] S. Eliseev, K. Blaum, M. Block, C. Droese, M. Goncharov, E. Minaya Ramirez, D. A. Nesterenko, Y. N. Novikov, and L. Schweikhard. Phase-Imaging Ion-Cyclotron-Resonance Measurements for Short-Lived Nuclides. *Phys. Rev. Lett.*, 110:082501, Feb 2013. doi:10.1103/PhysRevLett.110.082501. URL https://link.aps.org/doi/10.1103/PhysRevLett.110.082501. → pages 55, 56, 211

[86] S. Eliseev, K. Blaum, M. Block, et al. A phase-imaging technique for cyclotron-frequency measurements. *Appl. Phys. B*, 114:107–128, 2014. doi:https://doi.org/10.1007/s00340-013-5621-0. URL https://link.springer.com/article/10.1007/s00340-013-5621-0. → pages 56, 211

[87] S. Eliseev, K. Blaum, M. Block, S. Chenmarev, H. Dorrer, C. E. Düllmann, C. Enss, P. E. Filianin, L. Gastaldo, M. Goncharov, U. Köster, F. Lautenschläger, Y. N. Novikov, A. Rischka, R. X. Schüssler, L. Schweikhard, and A. Türler. Direct Measurement of the Mass Difference of ^{163}Ho and ^{163}Dy solves the Q-Value Puzzle for the Neutrino Mass Determination. *Phys. Rev. Lett.*, 115:062501, Aug 2015. doi:10.1103/PhysRevLett.115.062501. URL https://link.aps.org/doi/10.1103/PhysRevLett.115.062501. → page 139

[88] J. Erler, N. Birge, M. Kortelainen, W. Nazarewicz, E. Olsen, A. M. Perhac, and M. Stoitsov. The limits of the nuclear landscape. *Nature*, 486:509–512, 2012. doi:https://doi.org/10.1038/nature11188. URL https://www.nature.com/articles/nature11188. → pages xvii, xxvi, 5, 14, 17, 28, 126

[89] T. Eronen, V. S. Kolhinen, V. V. Eloma, et al. JYFLTRAP: a Penning trap for precision mass spectroscopy and isobaric purification. *Eur. Phys. J. A*, 48, 2012. doi:https://doi.org/10.1140/epja/i2012-12046-1. URL https://link.springer.com/article/10.1140/epja/i2012-12046-1. → pages 34, 44

[90] S. Ettenauer, M. C. Simon, A. T. Gallant, T. Brunner, U. Chowdhury, V. V. Simon, M. Brodeur, A. Chaudhuri, E. Mané, C. Andreoiu, G. Audi, J. R. C. López-Urrutia, P. Delheij, G. Gwinner, A. Lapierre, D. Lunney, M. R. Pearson, R. Ringle, J. Ullrich, and J. Dilling. First use of high charge states for mass measurements of short-lived nuclides in a penning trap. *Phys. Rev. Lett.*, 107:272501, Dec 2011. doi:10.1103/PhysRevLett.107.272501. URL https://link.aps.org/doi/10.1103/PhysRevLett.107.272501. → pages 54, 66, 79, 83, 134, 141

[91] S. Ettenauer et al. First Use of High Charge States for Mass Measurements of Short-Lived Nuclides in a Penning Trap. *Phys. Rev. Lett.*, 107:272501, Dec 2011. doi:10.1103/PhysRevLett.107.272501. URL https://link.aps.org/doi/10.1103/PhysRevLett.107.272501. → page 141

[92] F. Everling, L. König, J. Mattauch, and A. Wapstra. Relative nuclidic masses. *Nuclear Physics*, 18:529–569, 1960. ISSN 0029-5582. doi:https://doi.org/10.1016/0029-5582(60)90423-5. URL

https://www.sciencedirect.com/science/article/pii/0029558260904235. → page 114

[93] K. Farouqi, K. L. Kratz, B. Pfeiffer, T. Rauscher, F. K. Thielemann, and J. W. Truran. Charged-particle and Neutron-capture Processes in the High-entropy Wind of Core-collapse Supernovae. , 712(2):1359–1377, Apr. 2010. doi:10.1088/0004-637X/712/2/1359. → page 135

[94] H. T. Fortune. The puzzle of ^{32}Mg. *Phys. Rev. C*, 84:024327, Aug 2011. doi:10.1103/PhysRevC.84.024327. URL https://link.aps.org/doi/10.1103/PhysRevC.84.024327. → page 14

[95] M. Foster. *An Upgrade of the TITAN-EBIT High Voltage Operation for Investigations into Decay Rate Modifications by Highly Charged Ions*. PhD thesis, University of Surrey, Physics Department, 2017. URL https://titan.triumf.ca/research/publications/MFoster_Dissertation2017.pdf. → page 80

[96] M. Foster, K. Leach, I. Dillmann, C. Babcock, M. Good, A. Kwiatkowski, A. Lennarz, J. Dilling, E. Leistenschneider, R. Klawitter, C. Andreoiu, T. Brunner, and D. Frekers. Decay Spectroscopy Of Highly Charged Radioactive Ions With Titan At TRIUMF. *PoS*, INPC2016:097, 2017. doi:10.22323/1.281.0097. → page 142

[97] J. Fridmann, I. Wiedenhöver, A. Gade, et al. 'Magic' nucleus 42Si. *Nature*, 435:922–924, 2005. doi:https://doi.org/10.1038/nature03619. URL https://www.nature.com/articles/nature03619. → page 13

[98] M. Froese, C. Champagne, J. Crespo López-Urrutia, et al. A high-current electron beam ion trap as an on-line charge breeder for the high precision mass measurement TITAN experiment. *Hyperfine Interact*, 173:85–92, 2006. doi:https://doi.org/10.1007/s10751-007-9546-z. URL https://link.springer.com/article/10.1007/s10751-007-9546-z. → page 80

[99] Y. Fukuda, T. Hayakawa, E. Ichihara, K. Inoue, K. Ishihara, H. Ishino, Y. Itow, T. Kajita, J. Kameda, S. Kasuga, K. Kobayashi, Y. Kobayashi, Y. Koshio, M. Miura, M. Nakahata, S. Nakayama, A. Okada, K. Okumura, N. Sakurai, M. Shiozawa, Y. Suzuki, Y. Takeuchi, Y. Totsuka, S. Yamada, M. Earl, A. Habig, E. Kearns, M. D. Messier, K. Scholberg, J. L. Stone, L. R. Sulak, C. W. Walter, M. Goldhaber, T. Barszczxak, D. Casper, W. Gajewski, P. G. Halverson, J. Hsu, W. R. Kropp, L. R. Price, F. Reines, M. Smy, H. W. Sobel, M. R. Vagins, K. S. Ganezer, W. E. Keig, R. W.

Ellsworth, S. Tasaka, J. W. Flanagan, A. Kibayashi, J. G. Learned, S. Matsuno, V. J. Stenger, D. Takemori, T. Ishii, J. Kanzaki, T. Kobayashi, S. Mine, K. Nakamura, K. Nishikawa, Y. Oyama, A. Sakai, M. Sakuda, O. Sasaki, S. Echigo, M. Kohama, A. T. Suzuki, T. J. Haines, E. Blaufuss, B. K. Kim, R. Sanford, R. Svoboda, M. L. Chen, Z. Conner, J. A. Goodman, G. W. Sullivan, J. Hill, C. K. Jung, K. Martens, C. Mauger, C. McGrew, E. Sharkey, B. Viren, C. Yanagisawa, W. Doki, K. Miyano, H. Okazawa, C. Saji, M. Takahata, Y. Nagashima, M. Takita, T. Yamaguchi, M. Yoshida, S. B. Kim, M. Etoh, K. Fujita, A. Hasegawa, T. Hasegawa, S. Hatakeyama, T. Iwamoto, M. Koga, T. Maruyama, H. Ogawa, J. Shirai, A. Suzuki, F. Tsushima, M. Koshiba, M. Nemoto, K. Nishijima, T. Futagami, Y. Hayato, Y. Kanaya, K. Kaneyuki, Y. Watanabe, D. Kielczewska, R. A. Doyle, J. S. George, A. L. Stachyra, L. L. Wai, R. J. Wilkes, and K. K. Young. Evidence for oscillation of atmospheric neutrinos. *Phys. Rev. Lett.*, 81:1562–1567, Aug 1998. doi:10.1103/PhysRevLett.81.1562. URL https://link.aps.org/doi/10.1103/PhysRevLett.81.1562. → page 138

[100] G. G. Mass defect curve and nuclear constitution. *Proc. R. Soc. Lond.*, 126: 632–644, 1930. doi:https://doi.org/10.1098/rspa.1930.0032. URL https://royalsocietypublishing.org/doi/10.1098/rspa.1930.0032. → page 2

[101] A. Gade, P. Adrich, D. Bazin, M. D. Bowen, B. A. Brown, C. M. Campbell, J. M. Cook, S. Ettenauer, T. Glasmacher, K. W. Kemper, S. McDaniel, A. Obertelli, T. Otsuka, A. Ratkiewicz, K. Siwek, J. R. Terry, J. A. Tostevin, Y. Utsuno, and D. Weisshaar. Spectroscopy of ^{36}Mg: Interplay of normal and intruder configurations at the neutron-rich boundary of the "island of inversion". *Phys. Rev. Lett.*, 99:072502, Aug 2007. doi:10.1103/PhysRevLett.99.072502. URL https://link.aps.org/doi/10.1103/PhysRevLett.99.072502. → page 14

[102] A. T. Gallant, J. C. Bale, T. Brunner, U. Chowdhury, S. Ettenauer, A. Lennarz, D. Robertson, V. V. Simon, A. Chaudhuri, J. D. Holt, A. A. Kwiatkowski, E. Mané, J. Menéndez, B. E. Schultz, M. C. Simon, C. Andreoiu, P. Delheij, M. R. Pearson, H. Savajols, A. Schwenk, and J. Dilling. New precision mass measurements of neutron-rich calcium and potassium isotopes and three-nucleon forces. *Phys. Rev. Lett.*, 109:032506, Jul 2012. doi:10.1103/PhysRevLett.109.032506. URL https://link.aps.org/doi/10.1103/PhysRevLett.109.032506. → page 83

[103] A. T. Gallant, M. Alanssari, J. C. Bale, C. Andreoiu, B. R. Barquest,

U. Chowdhury, J. Even, A. Finlay, D. Frekers, G. Gwinner, R. Klawitter, B. Kootte, A. A. Kwiatkowski, D. Lascar, K. G. Leach, E. Leistenschneider, A. Lennarz, A. J. Mayer, D. Short, R. Thompson, M. Wieser, D. Lunney, and J. Dilling. Mass determination near $N = 20$ for Al and Na isotopes. *Phys. Rev. C*, 96:024325, Aug 2017. doi:10.1103/PhysRevC.96.024325. URL https://link.aps.org/doi/10.1103/PhysRevC.96.024325. → pages 14, 88, 101, 102, 113

[104] C. Gaulard, G. Audi, C. Bachelet, D. Lunney, M. de Saint Simon, C. Thibault, and N. Vieira. Accurate mass measurements of 26Ne, 26–30Na, 29–33Mg performed with the Mistral spectrometer. *Nuclear Physics A*, 766:52–73, 2006. ISSN 0375-9474. doi:https://doi.org/10.1016/j.nuclphysa.2005.12.007. URL https://www.sciencedirect.com/science/article/pii/S0375947405012431. → pages xxiv, 103, 105

[105] H. Geissel, P. Armbruster, K. Behr, A. Brünle, K. Burkard, M. Chen, H. Folger, B. Franczak, H. Keller, O. Klepper, B. Langenbeck, F. Nickel, E. Pfeng, M. Pfützner, E. Roeckl, K. Rykaczewski, I. Schall, D. Schardt, C. Scheidenberger, K.-H. Schmidt, A. Schröter, T. Schwab, K. Sümmerer, M. Weber, G. Münzenberg, T. Brohm, H.-G. Clerc, M. Fauerbach, J.-J. Gaimard, A. Grewe, E. Hanelt, B. Knödler, M. Steiner, B. Voss, J. Weckenmann, C. Ziegler, A. Magel, H. Wollnik, J. Dufour, Y. Fujita, D. Vieira, and B. Sherrill. The GSI projectile fragment separator (FRS): a versatile magnetic system for relativistic heavy ions. *Nuclear Instruments and Methods in Physics Research Section B: Beam Interactions with Materials and Atoms*, 70(1):286–297, 1992. ISSN 0168-583X. doi:https://doi.org/10.1016/0168-583X(92)95944-M. URL https://www.sciencedirect.com/science/article/pii/0168583X9295944M. → page 32

[106] W. E. Gifford. The Gifford-McMahon Cycle. In *Advances in Cryogenic Engineering*, pages 152–159, Boston, MA, 1966. Springer US. ISBN 978-1-4757-0522-5. → page 143

[107] J. Giovinazzo, B. Blank, M. Chartier, S. Czajkowski, A. Fleury, M. J. Lopez Jimenez, M. S. Pravikoff, J.-C. Thomas, F. de Oliveira Santos, M. Lewitowicz, V. Maslov, M. Stanoiu, R. Grzywacz, M. Pfützner, C. Borcea, and B. A. Brown. Two-Proton Radioactivity of ^{45}Fe. *Phys. Rev. Lett.*, 89:102501, Aug 2002. doi:10.1103/PhysRevLett.89.102501. URL https://link.aps.org/doi/10.1103/PhysRevLett.89.102501. → page 19

[108] V. Goldansky. On neutron-deficient isotopes of light nuclei and the phenomena of proton and two-proton radioactivity. *Nucl. Phys.*, 19:482, 1960. doi:https://doi.org/10.1016/0029-5582(60)90258-3. URL https://www.sciencedirect.com/science/article/pii/0029558260902583. → pages 19, 20

[109] T. J. Gray, J. M. Allmond, Z. Xu, T. T. King, R. S. Lubna, H. L. Crawford, V. Tripathi, B. P. Crider, R. Grzywacz, S. N. Liddick, A. O. Macchiavelli, T. Miyagi, A. Poves, A. Andalib, E. Argo, C. Benetti, S. Bhattacharya, C. M. Campbell, M. P. Carpenter, J. Chan, A. Chester, J. Christie, B. R. Clark, I. Cox, A. A. Doetsch, J. Dopfer, J. G. Duarte, P. Fallon, A. Frotscher, T. Gaballah, J. T. Harke, J. Heideman, H. Huegen, J. D. Holt, R. Jain, N. Kitamura, K. Kolos, F. G. Kondev, A. Laminack, B. Longfellow, S. Luitel, M. Madurga, R. Mahajan, M. J. Mogannam, C. Morse, S. Neupane, A. Nowicki, T. H. Ogunbeku, W. J. Ong, C. Porzio, C. J. Prokop, B. C. Rasco, E. K. Ronning, E. Rubino, T. J. Ruland, K. P. Rykaczewski, L. Schaedig, D. Seweryniak, K. Siegl, M. Singh, A. E. Stuchbery, S. L. Tabor, T. L. Tang, T. Wheeler, J. A. Winger, and J. L. Wood. Microsecond isomer at the n=20 island of shape inversion observed at frib, 2023. → page 112

[110] D. J. Griffiths and D. F. Schroeter. *Introduction to Quantum Mechanics*. Cambridge University Press, 3rd edition, 2018. doi:10.1017/9781316995433. → page 19

[111] J. Grund, M. Asai, K. Blaum, M. Block, S. Chenmarev, C. Düllmann, K. Eberhardt, S. Lohse, Y. Nagame, S. Nagy, P. Naubereit, J. van de Laar, F. Schneider, T. Sato, N. Sato, D. Simonovski, K. Tsukada, and K. Wendt. First online operation of TRIGA-TRAP. *Nuclear Instruments and Methods in Physics Research Section A: Accelerators, Spectrometers, Detectors and Associated Equipment*, 972:164013, 2020. ISSN 0168-9002. doi:https://doi.org/10.1016/j.nima.2020.164013. URL https://www.sciencedirect.com/science/article/pii/S0168900220304617. → page 66

[112] F. Halzen and A. D. Martin. *Quarks and Leptones: An Introductory Course in Modern Particle Physics*. Wiley, New York, NY, 1991. → pages 8, 139

[113] A. Hamaker, G. Bollen, M. Eibach, et al. SIPT - An ultrasensitive mass spectrometer for rare isotopes. . *Hyperfine Interact*, 240, 2019. doi:https://doi.org/10.1007/s10751-019-1576-9. URL https://link.springer.com/article/10.1007/s10751-019-1576-9. → page 59

[114] R. Han, X. Li, W. Jiang, Z. Li, H. Hua, S. Zhang, C. Yuan, D. Jiang, Y. Ye, J. Li, Z. Li, F. Xu, Q. Chen, J. Meng, J. Wang, C. Xu, Y. Sun, C. Wang, H. Wu, C. Niu, C. Li, C. He, W. Jiang, P. Li, H. Zang, J. Feng, S. Chen, Q. Liu, X. Chen, H. Xu, Z. Hu, Y. Yang, P. Ma, J. Ma, S. Jin, Z. Bai, M. Huang, Y. Zhou, W. Ma, Y. Li, X. Zhou, Y. Zhang, G. Xiao, and W. Zhan. Northern boundary of the "island of inversion" and triaxiality in 34si. *Physics Letters B*, 772:529–533, 2017. ISSN 0370-2693. doi:https://doi.org/10.1016/j.physletb.2017.07.007. URL https://www.sciencedirect.com/science/article/pii/S0370269317305543. → page 101

[115] J. C. Hardy and I. S. Towner. Superallowed $0^+ \to 0^+$ nuclear β decays: 2020 critical survey, with implications for V_{ud} and ckm unitarity. *Phys. Rev. C*, 102:045501, Oct 2020. doi:10.1103/PhysRevC.102.045501. URL https://link.aps.org/doi/10.1103/PhysRevC.102.045501. → page 140

[116] M. Harlander, M. Brownnutt, W. Hänsel, and R. Blatt. Trapped-ion probing of light-induced charging effects on dielectrics. *New Journal of Physics*, 12 (9):093035, sep 2010. doi:10.1088/1367-2630/12/9/093035. URL https://dx.doi.org/10.1088/1367-2630/12/9/093035. → page 64

[117] O. Haxel, J. H. D. Jensen, and H. E. Suess. On the "magic numbers" in nuclear structure. *Phys. Rev.*, 75:1766–1766, Jun 1949. doi:10.1103/PhysRev.75.1766.2. URL https://link.aps.org/doi/10.1103/PhysRev.75.1766.2. → pages 6, 9, 24

[118] F. Herfurth, J. Dilling, A. Kellerbauer, G. Bollen, S. Henry, H.-J. Kluge, E. Lamour, D. Lunney, R. Moore, C. Scheidenberger, S. Schwarz, G. Sikler, and J. Szerypo. A linear radiofrequency ion trap for accumulation, bunching, and emittance improvement of radioactive ion beams. *Nuclear Instruments and Methods in Physics Research Section A: Accelerators, Spectrometers, Detectors and Associated Equipment*, 469(2): 254–275, 2001. ISSN 0168-9002. doi:https://doi.org/10.1016/S0168-9002(01)00168-1. URL https://www.sciencedirect.com/science/article/pii/S0168900201001681. → pages 39, 72, 73

[119] H. Heylen, M. De Rydt, G. Neyens, M. L. Bissell, L. Caceres, R. Chevrier, J. M. Daugas, Y. Ichikawa, Y. Ishibashi, O. Kamalou, T. J. Mertzimekis, P. Morel, J. Papuga, A. Poves, M. M. Rajabali, C. Stödel, J. C. Thomas, H. Ueno, Y. Utsuno, N. Yoshida, and A. Yoshimi. High-precision quadrupole moment reveals significant intruder component in $^{33}_{13}\mathrm{Al}_{20}$

ground state. *Phys. Rev. C*, 94:034312, Sep 2016. doi:10.1103/PhysRevC.94.034312. URL https://link.aps.org/doi/10.1103/PhysRevC.94.034312. → page 14

[120] P. Himpe, G. Neyens, D. Balabanski, G. Bélier, D. Borremans, J. Daugas, F. de Oliveira Santos, M. De Rydt, K. Flanagan, G. Georgiev, M. Kowalska, S. Mallion, I. Matea, P. Morel, Y. Penionzhkevich, N. Smirnova, C. Stodel, K. Turzó, N. Vermeulen, and D. Yordanov. g factors of 31,32,33Al: Indication for intruder configurations in the 33Al ground state. *Physics Letters B*, 643(5):257–262, 2006. ISSN 0370-2693. doi:https://doi.org/10.1016/j.physletb.2006.10.026. URL https://www.sciencedirect.com/science/article/pii/S0370269306013219. → pages 14, 88

[121] P. Himpe, G. Neyens, D. Balabanski, G. Bélier, J. Daugas, F. de Oliveira Santos, M. De Rydt, K. Flanagan, I. Matea, P. Morel, Y. Penionzhkevich, L. Perrot, N. Smirnova, C. Stodel, J. Thomas, N. Vermeulen, D. Yordanov, Y. Utsuno, and T. Otsuka. g factor of the exotic N=21 isotope 34Al: probing the N=20 and N=28 shell gaps at the border of the "island of inversion". *Physics Letters B*, 658(5):203–208, 2008. ISSN 0370-2693. doi:https://doi.org/10.1016/j.physletb.2007.11.017. URL https://www.sciencedirect.com/science/article/pii/S037026930701369X. → page 14

[122] S. Hofmann, W. Reisdorf, G. Münzenberg, F. Heßberger, J. Schneider, and P. Armbruster. Proton radioactivity of 151 Lu. *Zeitschrift für Physik A Atoms and Nuclei*, 305(2):111–123, 1982. → page 18

[123] G. Huber, F. Touchard, S. Büttgenbach, C. Thibault, R. Klapisch, H. T. Duong, S. Liberman, J. Pinard, J. L. Vialle, P. Juncar, and P. Jacquinot. Spins, magnetic moments, and isotope shifts of $^{21-31}$Na by high resolution laser spectroscopy of the atomic D_1 line. *Phys. Rev. C*, 18:2342–2354, Nov 1978. doi:10.1103/PhysRevC.18.2342. URL https://link.aps.org/doi/10.1103/PhysRevC.18.2342. → page 12

[124] R. W. Ibbotson, T. Glasmacher, B. A. Brown, L. Chen, M. J. Chromik, P. D. Cottle, M. Fauerbach, K. W. Kemper, D. J. Morrissey, H. Scheit, and M. Thoennessen. Quadrupole collectivity in ^{32,34,36,38}Si and the $N = 20$ shell closure. *Phys. Rev. Lett.*, 80:2081–2084, Mar 1998. doi:10.1103/PhysRevLett.80.2081. URL https://link.aps.org/doi/10.1103/PhysRevLett.80.2081. → page 14

[125] H. Iwasaki, T. Motobayashi, H. Sakurai, K. Yoneda, T. Gomi, N. Aoi, N. Fukuda, Z. Fülöp, U. Futakami, Z. Gacsi, Y. Higurashi, N. Imai, N. Iwasa, T. Kubo, M. Kunibu, M. Kurokawa, Z. Liu, T. Minemura, A. Saito, M. Serata, S. Shimoura, S. Takeuchi, Y. Watanabe, K. Yamada, Y. Yanagisawa, and M. Ishihara. Large collectivity of 34Mg. *Physics Letters B*, 522(3):227–232, 2001. ISSN 0370-2693. doi:https://doi.org/10.1016/S0370-2693(01)01244-8. URL https://www.sciencedirect.com/science/article/pii/S0370269301012448. → page 14

[126] C. Izzo. *Mass measurements of neutron-rich cobalt isotopes and the development of a single ion Penning trap mass spectrometer for rare isotopes*. PhD thesis, 2018. → page 58

[127] A. Jacobs. *Collision induced dissociation and mass spectrometry with the TITAN Multiple-Reflection Time-of-Flight Mass-Spectrometer*. PhD thesis, University of British Columbia, 2019. URL https://open.library.ubc.ca/collections/ubctheses/24/items/1.0380561. → pages xviii, 37, 38, 42, 78

[128] O. Jagutzki, V. Mergel, K. Ullmann-Pfleger, L. Spielberger, U. Spillmann, R. Dörner, and H. Schmidt-Böcking. A broad-application microchannel-plate detector system for advanced particle or photon detection tasks: large area imaging, precise multi-hit timing information and high detection rate. *Nuclear Instruments and Methods in Physics Research Section A: Accelerators, Spectrometers, Detectors and Associated Equipment*, 477(1):244–249, 2002. ISSN 0168-9002. doi:https://doi.org/10.1016/S0168-9002(01)01839-3. URL https://www.sciencedirect.com/science/article/pii/S0168900201018393. 5th Int. Conf. on Position-Sensitive Detectors. → pages xxx, 215, 216

[129] C. Jesch. *The multiple-reflection time-of-flight isobar separator for TITAN and direct mass measurements at the FRS Ion Catcher*. PhD thesis, Justus-Liebig-Universitat, 2016. URL http://geb.uni-giessen.de/geb/volltexte/2016/12096. → page 75

[130] L. Jing, M. Du, K. Wei, and W. G. Hurley. A health monitoring method for bond wires in igbt modules based on voltage ringing characteristics. *IEEE Transactions on Electron Devices*, 66(9):3953–3960, 2019. doi:10.1109/TED.2019.2931445. → page 42

[131] J. T. Johnson, I. J. Carrick, G. S. Eakins, and S. A. McLuckey. Simultaneous isolation of nonadjacent m/z ions using mirror switching in an electrostatic linear ion trap. *Anal. Chem.*, 91, 2019. ISSN 12574–12580. doi:https://doi.org/10.1021/acs.analchem.9b03560. URL https://pubs.acs.org/doi/abs/10.1021/acs.analchem.9b03560. → page 41

[132] J. José, M. Hernanz, and C. Iliadis. Nucleosynthesis in classical novae. *Nuclear Physics A*, 777:550–578, 2006. ISSN 0375-9474. doi:https://doi.org/10.1016/j.nuclphysa.2005.02.121. URL https://www.sciencedirect.com/science/article/pii/S0375947405002708. Special Isseu on Nuclear Astrophysics. → page 135

[133] B. Jurado, H. Savajols, W. Mittig, N. Orr, P. Roussel-Chomaz, D. Baiborodin, W. Catford, M. Chartier, C. Demonchy, Z. Dlouhý, A. Gillibert, L. Giot, A. Khouaja, A. Lépine-Szily, S. Lukyanov, J. Mrazek, Y. Penionzhkevich, S. Pita, M. Rousseau, and A. Villari. Mass measurements of neutron-rich nuclei near the N=20 and 28 shell closures. *Physics Letters B*, 649(1):43–48, 2007. ISSN 0370-2693. doi:https://doi.org/10.1016/j.physletb.2007.04.006. URL https://www.sciencedirect.com/science/article/pii/S0370269307004339. → pages 88, 103, 104

[134] R. Kanungo. Shell closures in the N and Z=40–60 region for neutron and proton-rich nuclei. *Physics Letters B*, 649(1):31–34, 2007. ISSN 0370-2693. doi:https://doi.org/10.1016/j.physletb.2007.03.044. URL https://www.sciencedirect.com/science/article/pii/S0370269307003930. → page 13

[135] R. Kanungo, C. Nociforo, A. Prochazka, Y. Utsuno, T. Aumann, D. Boutin, D. Cortina-Gil, B. Davids, M. Diakaki, F. Farinon, H. Geissel, R. Gernhäuser, J. Gerl, R. Janik, B. Jonson, B. Kindler, R. Knöbel, R. Krücken, M. Lantz, H. Lenske, Y. Litvinov, K. Mahata, P. Maierbeck, A. Musumarra, T. Nilsson, T. Otsuka, C. Perro, C. Scheidenberger, B. Sitar, P. Strmen, B. Sun, I. Szarka, I. Tanihata, H. Weick, and M. Winkler. Structure of 33Mg sheds new light on the N=20 island of inversion. *Physics Letters B*, 685(4):253–257, 2010. ISSN 0370-2693. doi:https://doi.org/10.1016/j.physletb.2010.02.008. URL https://www.sciencedirect.com/science/article/pii/S0370269310001693. → page 14

[136] J. Karthein. Precision mass measurements using the phase-imaging

ion-cyclotron-resonance detection technique, 2017. URL https://cds.cern.ch/record/2300223. Presented 2017. → page 56

[137] D. Kasen, B. Metzger, J. Barnes, et al. Origin of the heavy elements in binary neutron-star mergers from a gravitational-wave event. *Nature*, 551, 2017. doi:https://doi.org/10.1038/nature24453. → pages 135, 136

[138] KATRIN Collaboration. Direct neutrino-mass measurement with sub-electronvolt sensitivity. *Nature Physics*, 18:160–166, 2022. doi:https://doi.org/10.1038/s41567-021-01463-1. → page 138

[139] Y. Kawase, K. Okano, M. Shibata, and A. Taniguchi. Fluorination method for the surface ionization of sr and ba with a helium-jet type isol. *Nuclear Instruments and Methods in Physics Research Section B: Beam Interactions with Materials and Atoms*, 70(1):146–149, 1992. ISSN 0168-583X. doi:https://doi.org/10.1016/0168-583X(92)95923-F. URL https://www.sciencedirect.com/science/article/pii/0168583X9295923F. → page 68

[140] J. Ketelaer, J. Krämer, D. Beck, K. Blaum, M. Block, K. Eberhardt, G. Eitel, R. Ferrer, C. Geppert, S. George, F. Herfurth, J. Ketter, S. Nagy, D. Neidherr, R. Neugart, W. Nörtershäuser, J. Repp, C. Smorra, N. Trautmann, and C. Weber. TRIGA-SPEC: A setup for mass spectrometry and laser spectroscopy at the research reactor TRIGA Mainz. *Nuclear Instruments and Methods in Physics Research Section A: Accelerators, Spectrometers, Detectors and Associated Equipment*, 594(2): 162–177, 2008. ISSN 0168-9002. doi:https://doi.org/10.1016/j.nima.2008.06.023. URL https://www.sciencedirect.com/science/article/pii/S0168900208008693. → pages 34, 44

[141] R. Kirchner. Review of isol target–ion-source systems. *Nuclear Instruments and Methods in Physics Research Section B: Beam Interactions with Materials and Atoms*, 204:179–190, 2003. ISSN 0168-583X. doi:https://doi.org/10.1016/S0168-583X(02)01900-6. URL https://www.sciencedirect.com/science/article/pii/S0168583X02019006. 14th International Conference on Electromagnetic Isotope Separators and Techniques Related to their Applications. → page 68

[142] R. Klawitter, A. Bader, M. Brodeur, U. Chowdhury, A. Chaudhuri, J. Fallis, A. T. Gallant, A. Grossheim, A. A. Kwiatkowski, D. Lascar, K. G. Leach, A. Lennarz, T. D. Macdonald, J. Pearkes, S. Seeraji, M. C. Simon, V. V.

Simon, B. E. Schultz, and J. Dilling. Mass measurements of neutron-rich Rb and Sr isotopes. *Phys. Rev. C*, 93:045807, Apr 2016. doi:10.1103/PhysRevC.93.045807. URL https://link.aps.org/doi/10.1103/PhysRevC.93.045807. → page 83

[143] H. Kluge and G. Bollen. Isoltrap: A tandem penning trap mass spectrometer for radioactive isotopes. *Hyperfine Interactions*, 81:15–26, 1993. doi:https://doi.org/10.1007/BF00567247. URL https://link.springer.com/article/10.1007/BF00567247. → pages 44, 66

[144] P. Klüpfel, P.-G. Reinhard, T. J. Bürvenich, and J. A. Maruhn. Variations on a theme by skyrme: A systematic study of adjustments of model parameters. *Phys. Rev. C*, 79:034310, Mar 2009. doi:10.1103/PhysRevC.79.034310. URL https://link.aps.org/doi/10.1103/PhysRevC.79.034310. → page 28

[145] M. Kobayashi and T. Maskawa. CP-Violation in the Renormalizable Theory of Weak Interaction. *Progress of Theoretical Physics*, 49(2): 652–657, 02 1973. ISSN 0033-068X. doi:10.1143/PTP.49.652. URL https://doi.org/10.1143/PTP.49.652. → pages 135, 139

[146] N. Kobayashi, T. Nakamura, Y. Kondo, J. A. Tostevin, Y. Utsuno, N. Aoi, H. Baba, R. Barthelemy, M. A. Famiano, N. Fukuda, N. Inabe, M. Ishihara, R. Kanungo, S. Kim, T. Kubo, G. S. Lee, H. S. Lee, M. Matsushita, T. Motobayashi, T. Ohnishi, N. A. Orr, H. Otsu, T. Otsuka, T. Sako, H. Sakurai, Y. Satou, T. Sumikama, H. Takeda, S. Takeuchi, R. Tanaka, Y. Togano, and K. Yoneda. Observation of a *p*-wave one-neutron halo configuration in ^{37}Mg. *Phys. Rev. Lett.*, 112:242501, Jun 2014. doi:10.1103/PhysRevLett.112.242501. URL https://link.aps.org/doi/10.1103/PhysRevLett.112.242501. → page 88

[147] N. Kobayashi, T. Nakamura, Y. Kondo, J. A. Tostevin, N. Aoi, H. Baba, R. Barthelemy, M. A. Famiano, N. Fukuda, N. Inabe, M. Ishihara, R. Kanungo, S. Kim, T. Kubo, G. S. Lee, H. S. Lee, M. Matsushita, T. Motobayashi, T. Ohnishi, N. A. Orr, H. Otsu, T. Sako, H. Sakurai, Y. Satou, T. Sumikama, H. Takeda, S. Takeuchi, R. Tanaka, Y. Togano, and K. Yoneda. One-neutron removal from ^{29}Ne: Defining the lower limits of the island of inversion. *Phys. Rev. C*, 93:014613, Jan 2016. doi:10.1103/PhysRevC.93.014613. URL https://link.aps.org/doi/10.1103/PhysRevC.93.014613. → page 14

[148] V. Kolhinen, S. Kopecky, T. Eronen, U. Hager, J. Hakala, J. Huikari, A. Jokinen, A. Nieminen, S. Rinta-Antila, J. Szerypo, and J. Äystö. JYFLTRAP: a cylindrical Penning trap for isobaric beam purification at IGISOL. *Nuclear Instruments and Methods in Physics Research Section A: Accelerators, Spectrometers, Detectors and Associated Equipment*, 528(3): 776–787, 2004. ISSN 0168-9002. doi:https://doi.org/10.1016/j.nima.2004.05.029. URL https://www.sciencedirect.com/science/article/pii/S0168900204009854. → page 66

[149] M. Kortelainen, T. Lesinski, J. Moré, W. Nazarewicz, J. Sarich, N. Schunck, M. V. Stoitsov, and S. Wild. Nuclear energy density optimization. *Phys. Rev. C*, 82:024313, Aug 2010. doi:10.1103/PhysRevC.82.024313. URL https://link.aps.org/doi/10.1103/PhysRevC.82.024313. → page 28

[150] M. Kowalska, D. T. Yordanov, K. Blaum, P. Himpe, P. Lievens, S. Mallion, R. Neugart, G. Neyens, and N. Vermeulen. Nuclear ground-state spins and magnetic moments of ^{27}Mg, ^{29}Mg, and ^{31}Mg. *Phys. Rev. C*, 77:034307, Mar 2008. doi:10.1103/PhysRevC.77.034307. URL https://link.aps.org/doi/10.1103/PhysRevC.77.034307. → page 14

[151] K. S. Krane. *Introductory nuclear physics*. Wiley, New York, NY, 1988. URL https://cds.cern.ch/record/359790. → pages 1, 2, 5, 7, 9, 19

[152] M. Kretzschmar. The ramsey method in high-precision mass spectrometry with penning traps: Theoretical foundations. *International Journal of Mass Spectrometry*, 264(2):122–145, 2007. ISSN 1387-3806. doi:https://doi.org/10.1016/j.ijms.2007.04.002. URL https://www.sciencedirect.com/science/article/pii/S1387380607001649. → page 52

[153] A. Kwiatkowski, G. Bollen, M. Redshaw, R. Ringle, and S. Schwarz. Isobaric beam purification for high precision penning trap mass spectrometry of radioactive isotope beams with swift. *International Journal of Mass Spectrometry*, 379:9–15, 2015. ISSN 1387-3806. doi:https://doi.org/10.1016/j.ijms.2014.09.016. URL https://www.sciencedirect.com/science/article/pii/S1387380614004011. → page 49

[154] A. A. Kwiatkowski, T. Brunner, J. D. Holt, A. Chaudhuri, U. Chowdhury, M. Eibach, J. Engel, A. T. Gallant, A. Grossheim, M. Horoi, A. Lennarz,

T. D. Macdonald, M. R. Pearson, B. E. Schultz, M. C. Simon, R. A. Senkov, V. V. Simon, K. Zuber, and J. Dilling. New determination of double-β-decay properties in ^{48}Ca: High-precision $Q_{\beta\beta}$-value measurement and improved nuclear matrix element calculations. *Phys. Rev. C*, 89:045502, Apr 2014. doi:10.1103/PhysRevC.89.045502. URL https://link.aps.org/doi/10.1103/PhysRevC.89.045502. → pages 83, 141

[155] A. A. Kwiatkowski, C. Andreoiu, J. C. Bale, A. Chaudhuri, U. Chowdhury, S. Malbrunot-Ettenauer, A. T. Gallant, A. Grossheim, G. Gwinner, A. Lennarz, T. D. Macdonald, T. J. M. Rauch, B. E. Schultz, S. Seeraji, M. C. Simon, V. V. Simon, D. Lunney, A. Poves, and J. Dilling. Observation of a crossover of S_{2n} in the island of inversion from precision mass spectrometry. *Phys. Rev. C*, 92:061301, Dec 2015. doi:10.1103/PhysRevC.92.061301. URL https://link.aps.org/doi/10.1103/PhysRevC.92.061301. → pages 14, 88

[156] M. König, G. Bollen, H.-J. Kluge, T. Otto, and J. Szerypo. Quadrupole excitation of stored ion motion at the true cyclotron frequency. *International Journal of Mass Spectrometry and Ion Processes*, 142(1): 95–116, 1995. ISSN 0168-1176. doi:https://doi.org/10.1016/0168-1176(95)04146-C. URL https://www.sciencedirect.com/science/article/pii/016811769504146C. → pages xix, 49, 50, 53, 54, 62, 157, 211

[157] J. Ladislas Wiza. Microchannel plate detectors. *Nuclear Instruments and Methods*, 162(1):587–601, 1979. ISSN 0029-554X. doi:https://doi.org/10.1016/0029-554X(79)90734-1. URL https://www.sciencedirect.com/science/article/pii/0029554X79907341. → page 217

[158] J. M. Lafferty. *Foundations of Vacuum Science and Technology*. Wiley Sons, 1998. → page 63

[159] A. Lapierre, M. Brodeur, T. Brunner, S. Ettenauer, A. Gallant, V. Simon, M. Good, M. Froese, J. Crespo López-Urrutia, P. Delheij, S. Epp, R. Ringle, S. Schwarz, J. Ullrich, and J. Dilling. The TITAN EBIT charge breeder for mass measurements on highly charged short-lived isotopes—First online operation, journal = Nuclear Instruments and Methods in Physics Research Section A: Accelerators, Spectrometers, Detectors and Associated Equipment. 624(1):54–64, 2010. ISSN 0168-9002. doi:https://doi.org/10.1016/j.nima.2010.09.030. URL

https://www.sciencedirect.com/science/article/pii/S0168900210020231. → pages 80, 141

[160] D. Lascar, R. Klawitter, C. Babcock, E. Leistenschneider, S. R. Stroberg, B. R. Barquest, A. Finlay, M. Foster, A. T. Gallant, P. Hunt, J. Kelly, B. Kootte, Y. Lan, S. F. Paul, M. L. Phan, M. P. Reiter, B. Schultz, D. Short, J. Simonis, C. Andreoiu, M. Brodeur, I. Dillmann, G. Gwinner, J. D. Holt, A. A. Kwiatkowski, K. G. Leach, and J. Dilling. Precision mass measurements of $^{125-127}$Cd isotopes and isomers approaching the $N = 82$ closed shell. *Phys. Rev. C*, 96:044323, Oct 2017. doi:10.1103/PhysRevC.96.044323. URL https://link.aps.org/doi/10.1103/PhysRevC.96.044323. → pages 83, 138

[161] J. Lassen, R. Li, M. Mostamand, A. Gacsbaranyi, P. Kunz, C. Babcock, D. Bishop, A. Teigelhöfer, F. Ames, and A. Gottberg. Developments at triumf's laser resonance ionization ion source multi-element operation. *Nuclear Instruments and Methods in Physics Research Section B: Beam Interactions with Materials and Atoms*, 541:137–140, 2023. ISSN 0168-583X. doi:https://doi.org/10.1016/j.nimb.2023.04.055. URL https://www.sciencedirect.com/science/article/pii/S0168583X23001933. → pages xxiv, 89, 103

[162] K. Leach, A. Grossheim, A. Lennarz, T. Brunner, J. Crespo López-Urrutia, A. Gallant, M. Good, R. Klawitter, A. Kwiatkowski, T. Ma, T. Macdonald, S. Seeraji, M. Simon, C. Andreoiu, J. Dilling, and D. Frekers. The TITAN in-trap decay spectroscopy facility at TRIUMF. *Nuclear Instruments and Methods in Physics Research Section A: Accelerators, Spectrometers, Detectors and Associated Equipment*, 780:91–99, 2015. ISSN 0168-9002. doi:https://doi.org/10.1016/j.nima.2014.12.118. URL https://www.sciencedirect.com/science/article/pii/S0168900215001023. → page 66

[163] E. Leistenschneider. *Dawning of nuclear magicity in N = 32 seen through precision mass spectrometry*. PhD thesis, University of British Columbia, 2019. URL https://open.library.ubc.ca/collections/ubctheses/24/items/1.0383355. → pages xvii, xix, 25, 35, 53, 64, 83, 142, 144, 150, 155, 159

[164] E. Leistenschneider, M. P. Reiter, S. Ayet San Andrés, B. Kootte, J. D. Holt, P. Navrátil, C. Babcock, C. Barbieri, B. R. Barquest, J. Bergmann, J. Bollig, T. Brunner, E. Dunling, A. Finlay, H. Geissel, L. Graham, F. Greiner, H. Hergert, C. Hornung, C. Jesch, R. Klawitter, Y. Lan, D. Lascar, K. G.

Leach, W. Lippert, J. E. McKay, S. F. Paul, A. Schwenk, D. Short, J. Simonis, V. Somà, R. Steinbrügge, S. R. Stroberg, R. Thompson, M. E. Wieser, C. Will, M. Yavor, C. Andreoiu, T. Dickel, I. Dillmann, G. Gwinner, W. R. Plaß, C. Scheidenberger, A. A. Kwiatkowski, and J. Dilling. Dawning of the $N = 32$ Shell Closure Seen through Precision Mass Measurements of Neutron-Rich Titanium Isotopes. *Phys. Rev. Lett.*, 120:062503, Feb 2018. doi:10.1103/PhysRevLett.120.062503. URL https://link.aps.org/doi/10.1103/PhysRevLett.120.062503. → page 34

[165] E. Leistenschneider, A. Kwiatkowski, and J. Dilling. Vacuum requirements for penning trap mass spectrometry with highly charged ions. *Nuclear Instruments and Methods in Physics Research Section B: Beam Interactions with Materials and Atoms*, 463:496–498, 2020. ISSN 0168-583X. doi:https://doi.org/10.1016/j.nimb.2019.03.047. URL https://www.sciencedirect.com/science/article/pii/S0168583X19301673. → pages 83, 141

[166] A. Lennarz, A. Grossheim, K. G. Leach, M. Alanssari, T. Brunner, A. Chaudhuri, U. Chowdhury, J. R. Crespo López-Urrutia, A. T. Gallant, M. Holl, A. A. Kwiatkowski, J. Lassen, T. D. Macdonald, B. E. Schultz, S. Seeraji, M. C. Simon, C. Andreoiu, J. Dilling, and D. Frekers. In-trap spectroscopy of charge-bred radioactive ions. *Phys. Rev. Lett.*, 113:082502, Aug 2014. doi:10.1103/PhysRevLett.113.082502. URL https://link.aps.org/doi/10.1103/PhysRevLett.113.082502. → page 80

[167] M. Lewitowicz. The SPIRAL2 Project and experiments with high-intensity rare isotope beams. *Journal of Physics: Conference Series*, 312(5):052014, sep 2011. doi:10.1088/1742-6596/312/5/052014. URL https://dx.doi.org/10.1088/1742-6596/312/5/052014. → page 32

[168] LIGO-VIRGO collaboration. GW170817: Observation of Gravitational Waves from a Binary Neutron Star Inspiral. *Phys. Rev. Lett.*, 119:161101, Oct 2017. doi:10.1103/PhysRevLett.119.161101. URL https://link.aps.org/doi/10.1103/PhysRevLett.119.161101. → page 136

[169] H.-M. Liu, Y.-T. Zou, X. Pan, J.-L. Chen, B. He, and X.-H. Li. New geiger-nuttall law for two-proton radioactivity *. *Chinese Physics C*, 45(2): 024108, feb 2021. doi:10.1088/1674-1137/abd01e. URL https://dx.doi.org/10.1088/1674-1137/abd01e. → pages 127, 128

[170] Y. Liu, J. R. Beene, T. Gottwald, C. C. Havener, C. Mattolat, J. Lassen, K. Wendt, and C. R. Vane. Resonant ionization laser ion source for

radioactive ion beams. *AIP Conference Proceedings*, 1099(1):141–145, 2009. doi:10.1063/1.3119999. URL https://aip.scitation.org/doi/abs/10.1063/1.3119999. → pages 31, 68, 103

[171] D. Lunney, G. Audi, C. Gaulard, et al. High-precision masses of 29-33Mg and the N = 20 shell "closure". *Eur. Phys. J. A*, 28:129–138, 2006. doi:https://doi.org/10.1140/epja/i2005-10281-13. URL https://link.springer.com/article/10.1140/epja/i2005-10281-1. → pages 87, 103

[172] E. Lykiardopoulou, C. Izzo, E. Leistenschneider, et al. Towards high precision mass measurements of Highly Charged Ions using the Phase-Imaging Ion-Cyclotron-Resonance technique at TITAN. *Hyperfine Interact*, 241(37), 2020. doi:https://doi.org/10.1007/s10751-020-1705-5. URL https://link.springer.com/article/10.1007/s10751-020-1705-5. → page 212

[173] M. Madurga, J. M. Christie, Z. Xu, R. Grzywacz, A. Poves, T. King, A. Chester, J. Farr, I. Fletcher, J. Heideman, D. Hoskins, A. Laminack, S. Liddick, S. Neupane, S. Peng, A. L. Richard, K. Sieg, P. Wagenknecht, and R. Yokoyama. New isomeric transition in ^{36}Mg: Bridging the N=20 and N=28 islands of inversion, 2023. → page 17

[174] S. Malbrunot-Ettenauer et al. Penning trap mass measurements utilizing highly charged ions as a path to benchmark isospin-symmetry breaking corrections in ^{74}Rb. *Phys. Rev. C*, 91:045504, Apr 2015. doi:10.1103/PhysRevC.91.045504. URL https://link.aps.org/doi/10.1103/PhysRevC.91.045504. → page 140

[175] E. Matthias, B. Olsen, D. A. Shirley, J. E. Templeton, and R. M. Steffen. Theory of nuclear magnetic resonance detected by nuclear radiations. *Phys. Rev. A*, 4:1626–1658, Oct 1971. doi:10.1103/PhysRevA.4.1626. URL https://link.aps.org/doi/10.1103/PhysRevA.4.1626. → page 14

[176] M. G. Mayer. Nuclear Configurations in the Spin-Orbit Coupling Model. I. Empirical Evidence. *Phys. Rev.*, 78:16–21, Apr 1950. doi:10.1103/PhysRev.78.16. URL https://link.aps.org/doi/10.1103/PhysRev.78.16. → pages 9, 12, 24

[177] E. Meissner. *Schweizer Bauzeitung*, 72:9598, 1918. → page 70

[178] S. Mertens. Direct neutrino mass experiments. *Journal of Physics: Conference Series*, 718, 2016. doi:10.1088/1742-6596/718/2/022013.

URL https://iopscience.iop.org/article/10.1088/1742-6596/718/2/022013. → page 138

[179] S. Michimasa, Y. Yanagisawa, K. Inafuku, N. Aoi, Z. Elekes, Z. Fülöp, Y. Ichikawa, N. Iwasa, K. Kurita, M. Kurokawa, T. Machida, T. Motobayashi, T. Nakamura, T. Nakabayashi, M. Notani, H. J. Ong, T. K. Onishi, H. Otsu, H. Sakurai, M. Shinohara, T. Sumikama, S. Takeuchi, K. Tanaka, Y. Togano, K. Yamada, M. Yamaguchi, and K. Yoneda. Quadrupole collectivity in island-of-inversion nuclei ^{28,30}Ne and ^{34,36}Mg. *Phys. Rev. C*, 89:054307, May 2014. doi:10.1103/PhysRevC.89.054307. URL https://link.aps.org/doi/10.1103/PhysRevC.89.054307. → page 14

[180] W. Mittig, H. Savajols, D. Baiborodin, et al. Shape coexistence and the n = 20 shell closure far from stability by inelastic scattering. *Eur Phys J A*, 15: 157–160, 2002. doi:https://doi.org/10.1140/epja/i2001-10245-5. URL https://link.springer.com/article/10.1140/epja/i2001-10245-5. → page 14

[181] T. Miyagi, S. R. Stroberg, P. Navrátil, K. Hebeler, and J. D. Holt. Converged ab initio calculations of heavy nuclei. *Phys. Rev. C*, 105: 014302, Jan 2022. doi:10.1103/PhysRevC.105.014302. URL https://link.aps.org/doi/10.1103/PhysRevC.105.014302. → page 25

[182] T. Motobayashi, Y. Ikeda, K. Ieki, M. Inoue, N. Iwasa, T. Kikuchi, M. Kurokawa, S. Moriya, S. Ogawa, H. Murakami, S. Shimoura, Y. Yanagisawa, T. Nakamura, Y. Watanabe, M. Ishihara, T. Teranishi, H. Okuno, and R. Casten. Large deformation of the very neutron-rich nucleus 32mg from intermediate-energy coulomb excitation. *Physics Letters B*, 346(1):9–14, 1995. ISSN 0370-2693. doi:https://doi.org/10.1016/0370-2693(95)00012-A. URL https://www.sciencedirect.com/science/article/pii/037026939500012A. → pages 14, 88, 160

[183] M. Mumpower, R. Surman, G. McLaughlin, and A. Aprahamian. The impact of individual nuclear properties on r-process nucleosynthesis. *Progress in Particle and Nuclear Physics*, 86:86–126, 2016. ISSN 0146-6410. doi:https://doi.org/10.1016/j.ppnp.2015.09.001. URL https://www.sciencedirect.com/science/article/pii/S0146641015000897. → page 136

[184] M. R. Mumpower, R. Surman, D.-L. Fang, M. Beard, P. Möller, T. Kawano, and A. Aprahamian. Impact of individual nuclear masses on *r*-process abundances. *Phys. Rev. C*, 92:035807, Sep 2015.

doi:10.1103/PhysRevC.92.035807. URL https://link.aps.org/doi/10.1103/PhysRevC.92.035807. → pages 134, 135, 136

[185] E. G. Myers, A. Wagner, H. Kracke, and B. A. Wesson. Atomic masses of tritium and helium-3. *Phys. Rev. Lett.*, 114:013003, Jan 2015. doi:10.1103/PhysRevLett.114.013003. URL https://link.aps.org/doi/10.1103/PhysRevLett.114.013003. → pages 135, 139

[186] W. D. Myers and W. J. Swiatecki. The macroscopic approach to nuclear masses and deformations. *Annual Review of Nuclear and Particle Science*, 32(1):309–334, 1982. doi:10.1146/annurev.ns.32.120182.001521. URL https://doi.org/10.1146/annurev.ns.32.120182.001521. → page 3

[187] P. Navrátil and B. R. Barrett. No-core shell-model calculations with starting-energy-independent multivalued effective interactions. *Phys. Rev. C*, 54:2986–2995, Dec 1996. doi:10.1103/PhysRevC.54.2986. URL https://link.aps.org/doi/10.1103/PhysRevC.54.2986. → page 25

[188] P. Navrátil, V. G. Gueorguiev, J. P. Vary, W. E. Ormand, and A. Nogga. Structure of $a = 10 - -13$ nuclei with two- plus three-nucleon interactions from chiral effective field theory. *Phys. Rev. Lett.*, 99:042501, Jul 2007. doi:10.1103/PhysRevLett.99.042501. URL https://link.aps.org/doi/10.1103/PhysRevLett.99.042501. → page 25

[189] D. Nesterenko, T. Eronen, Z. Ge, et al. Study of radial motion phase advance during motion excitations in a Penning trap and accuracy of JYFLTRAP mass spectrometer. *Eur. Phys. J. A*, 57, 2021. doi:https://doi.org/10.1140/epja/s10050-021-00608-3. URL https://link.springer.com/article/10.1140/epja/s10050-021-00608-3. → page 56

[190] L. Neufcourt, Y. Cao, S. A. Giuliani, W. Nazarewicz, E. Olsen, and O. B. Tarasov. Quantified limits of the nuclear landscape. *Phys. Rev. C*, 101: 044307, Apr 2020. doi:10.1103/PhysRevC.101.044307. URL https://link.aps.org/doi/10.1103/PhysRevC.101.044307. → page 20

[191] G. Neyens. Nuclear magnetic and quadrupole moments for nuclear structure research on exotic nuclei. *Reports on Progress in Physics*, 66(7): 1251, jul 2003. doi:10.1088/0034-4885/66/7/501. URL https://dx.doi.org/10.1088/0034-4885/66/7/501. → page 12

[192] G. Neyens, M. Kowalska, D. Yordanov, K. Blaum, P. Himpe, P. Lievens, S. Mallion, R. Neugart, N. Vermeulen, Y. Utsuno, and T. Otsuka.

Measurement of the spin and magnetic moment of ^{31}Mg: Evidence for a strongly deformed intruder ground state. *Phys. Rev. Lett.*, 94:022501, Jan 2005. doi:10.1103/PhysRevLett.94.022501. URL https://link.aps.org/doi/10.1103/PhysRevLett.94.022501. → page 14

[193] Y. Novikov, F. Attallah, F. Bosch, M. Falch, H. Geissel, M. Hausmann, T. Kerscher, O. Klepper, H.-J. Kluge, C. Kozhuharov, Y. Litvinov, K. Löbner, G. Münzenberg, Z. Patyk, T. Radon, C. Scheidenberger, A. Wapstra, and H. Wollnik. Mass mapping of a new area of neutron-deficient suburanium nuclides. *Nuclear Physics A*, 697(1):92–106, 2002. ISSN 0375-9474. doi:https://doi.org/10.1016/S0375-9474(01)01233-7. URL https://www.sciencedirect.com/science/article/pii/S0375947401012337. → pages 20, 21, 22, 23, 131

[194] S. Nummela, P. Baumann, E. Caurier, P. Dessagne, A. Jokinen, A. Knipper, G. Le Scornet, C. Miehé, F. Nowacki, M. Oinonen, Z. Radivojevic, M. Ramdhane, G. Walter, and J. Äystö. Spectroscopy of ^{34,35}Si by β decay: $sd-fp$ shell gap and single-particle states. *Phys. Rev. C*, 63: 044316, Mar 2001. doi:10.1103/PhysRevC.63.044316. URL https://link.aps.org/doi/10.1103/PhysRevC.63.044316. → page 14

[195] E. Olsen, M. Pfützner, N. Birge, M. Brown, W. Nazarewicz, and A. Perhac. Landscape of two-proton radioactivity. *Phys. Rev. Lett.*, 110:222501, May 2013. doi:10.1103/PhysRevLett.110.222501. URL https://link.aps.org/doi/10.1103/PhysRevLett.110.222501. → page 20

[196] R. Orford, N. Vassh, J. A. Clark, G. C. McLaughlin, M. R. Mumpower, G. Savard, R. Surman, A. Aprahamian, F. Buchinger, M. T. Burkey, D. A. Gorelov, T. Y. Hirsh, J. W. Klimes, G. E. Morgan, A. Nystrom, and K. S. Sharma. Precision mass measurements of neutron-rich neodymium and samarium isotopes and their role in understanding rare-earth peak formation. *Phys. Rev. Lett.*, 120:262702, Jun 2018. doi:10.1103/PhysRevLett.120.262702. URL https://link.aps.org/doi/10.1103/PhysRevLett.120.262702. → pages xxvii, 137

[197] R. Orford, J. Clark, G. Savard, A. Aprahamian, F. Buchinger, M. Burkey, D. Gorelov, J. Klimes, G. Morgan, A. Nystrom, W. Porter, D. Ray, and K. Sharma. Improving the measurement sensitivity of the Canadian Penning Trap mass spectrometer through PI-ICR. *Nuclear Instruments and Methods in Physics Research Section B: Beam Interactions with Materials and Atoms*, 463:491–495, 2020. ISSN 0168-583X.

doi:https://doi.org/10.1016/j.nimb.2019.04.016. URL https://www.sciencedirect.com/science/article/pii/S0168583X19302009. → pages 56, 59

[198] N. Orr, W. Mittig, L. Fifield, M. Lewitowicz, E. Plagnol, Y. Schutz, Z. Wen Long, L. Bianchi, A. Gillibert, A. Belozyorov, S. Lukyanov, Y. Penionzhkevich, A. Villari, A. Cunsolo, A. Foti, G. Audi, C. Stephan, and L. Tassan-Got. New mass measurements of neutron-rich nuclei near N=20. *Physics Letters B*, 258(1):29–34, 1991. ISSN 0370-2693. doi:https://doi.org/10.1016/0370-2693(91)91203-8. URL https://www.sciencedirect.com/science/article/pii/0370269391912038. → page 103

[199] T. Otsuka, T. Suzuki, R. Fujimoto, H. Grawe, and Y. Akaishi. Evolution of nuclear shells due to the tensor force. *Phys. Rev. Lett.*, 95:232502, Nov 2005. doi:10.1103/PhysRevLett.95.232502. URL https://link.aps.org/doi/10.1103/PhysRevLett.95.232502. → pages 12, 13

[200] A. Ozawa, T. Kobayashi, T. Suzuki, K. Yoshida, and I. Tanihata. New Magic Number, $N = 16$, near the Neutron Drip Line. *Phys. Rev. Lett.*, 84: 5493–5495, Jun 2000. doi:10.1103/PhysRevLett.84.5493. URL https://link.aps.org/doi/10.1103/PhysRevLett.84.5493. → page 13

[201] S. F. Paul. emgfit - Fitting of time-of-flight mass spectra with hyper-EMG models, Dec. 2020. URL https://doi.org/10.5281/zenodo.4731019. → pages 90, 92, 99

[202] S. F. Paul, J. Bergmann, J. D. Cardona, K. A. Dietrich, E. Dunling, Z. Hockenbery, C. Hornung, C. Izzo, A. Jacobs, A. Javaji, B. Kootte, Y. Lan, E. Leistenschneider, E. M. Lykiardopoulou, I. Mukul, T. Murböck, W. S. Porter, R. Silwal, M. B. Smith, J. Ringuette, T. Brunner, T. Dickel, I. Dillmann, G. Gwinner, M. MacCormick, M. P. Reiter, H. Schatz, N. A. Smirnova, J. Dilling, and A. A. Kwiatkowski. Mass measurements of $^{60–63}$Ga reduce x-ray burst model uncertainties and extend the evaluated $t = 1$ isobaric multiplet mass equation. *Phys. Rev. C*, 104:065803, Dec 2021. doi:10.1103/PhysRevC.104.065803. URL https://link.aps.org/doi/10.1103/PhysRevC.104.065803. → page 141

[203] M. Pfũtzner, E. Badura, C. Bingham, B. Blank, M. Chartier, H. Geissel, J. Giovinazzo, L. V. Grigorenko, R. Grzywacz, M. Hellström, Z. Janas, J. Kurcewicz, A. S. Lalleman, C. Mazzocchi, I. Mukha, G. Mũnzenberg, C. Plettner, E. Roeckl, K. P. Rykaczewski, K. Schmidt, R. S. Simon,

M. Stanoiu, and J.-C. Thomas. First evidence for the two-proton decay of ^{45}Fe. *The European Physical Journal A - Hadrons and Nuclei*, 14(3): 279–285, Jul 2002. ISSN 1434-601X. doi:10.1140/epja/i2002-10033-9. URL https://doi.org/10.1140/epja/i2002-10033-9. → page 19

[204] W. R. Plaß, T. Dickel, U. Czok, H. Geissel, M. Petrick, K. Reinheimer, C. Scheidenberger, and M. I.Yavor. Isobar separation by time-of-flight mass spectrometry for low-energy radioactive ion beam facilities. *Nuclear Instruments and Methods in Physics Research Section B: Beam Interactions with Materials and Atoms*, 266(19):4560–4564, 2008. ISSN 0168-583X. doi:https://doi.org/10.1016/j.nimb.2008.05.079. URL https://www.sciencedirect.com/science/article/pii/S0168583X08007763. Proceedings of the XVth International Conference on Electromagnetic Isotope Separators and Techniques Related to their Applications. → page 34

[205] W. R. Plaß, T. Dickel, and C. Scheidenberger. Multiple-reflection time-of-flight mass spectrometry. *International Journal of Mass Spectrometry*, 349-350:134–144, 2013. ISSN 1387-3806. doi:https://doi.org/10.1016/j.ijms.2013.06.005. URL https://www.sciencedirect.com/science/article/pii/S138738061300239X. 100 years of Mass Spectrometry. → pages 66, 75

[206] W. Porter. *The northern shore of the N = 40 island of inversion through precision mass measurements and developments towards phase-imaging ion-cyclotron-resonance at the TITAN MPET*. PhD thesis, University of British Columbia, 2021. URL https://open.library.ubc.ca/collections/ubctheses/24/items/1.0401807. → pages xviii, 41, 95

[207] N. Prantzos and S. Ekström. *Stellar Nucleosynthesis*, pages 1584–1592. Springer Berlin Heidelberg, Berlin, Heidelberg, 2011. ISBN 978-3-642-11274-4. doi:10.1007/978-3-642-11274-4_1084. URL https://doi.org/10.1007/978-3-642-11274-4_1084. → page 135

[208] B. V. Pritychenko, T. Glasmacher, B. A. Brown, P. D. Cottle, R. W. Ibbotson, K. W. Kemper, L. A. Riley, and H. Scheit. First observation of an excited state in the neutron-rich nucleus ^{31}Na. *Phys. Rev. C*, 63:011305, Dec 2000. doi:10.1103/PhysRevC.63.011305. URL https://link.aps.org/doi/10.1103/PhysRevC.63.011305. → page 14

[209] S. Purushothaman, S. Ayet San Andrés, J. Bergmann, T. Dickel, J. Ebert, H. Geissel, C. Hornung, W. Plaß, C. Rappold, C. Scheidenberger,

Y. Tanaka, and M. Yavor. Hyper-EMG: A new probability distribution function composed of Exponentially Modified Gaussian distributions to analyze asymmetric peak shapes in high-resolution time-of-flight mass spectrometry. *International Journal of Mass Spectrometry*, 421:245–254, 2017. ISSN 1387-3806. doi:https://doi.org/10.1016/j.ijms.2017.07.014. URL https://www.sciencedirect.com/science/article/pii/S1387380616302913. → page 91

[210] S. Péru and M. Martini. Mean field based calculations with the Gogny force: Some theoretical tools to explore the nuclear structure. *Eur. Phys. J. A*, 50, 2014. doi:https://doi.org/10.1140/epja/i2014-14088-7. URL https://link.springer.com/article/10.1140/epja/i2014-14088-7. → pages 3, 29

[211] I. I. Rabi, S. Millman, P. Kusch, and J. R. Zacharias. The molecular beam resonance method for measuring nuclear magnetic moments. the magnetic moments of $_3Li^6$, $_3Li^7$ and $_9F^{19}$. *Phys. Rev.*, 55:526–535, Mar 1939. doi:10.1103/PhysRev.55.526. URL https://link.aps.org/doi/10.1103/PhysRev.55.526. → page 52

[212] S. Raeder, H. Heggen, J. Lassen, F. Ames, D. Bishop, P. Bricault, P. Kunz, A. Mjøs, and A. T. 1. An ion guide laser ion source for isobar-suppressed rare isotope beams. *Rev Sci Instrum.*, 2014. → page 89

[213] N. F. Ramsey. A new molecular beam resonance method. *Phys. Rev.*, 76: 996–996, Oct 1949. doi:10.1103/PhysRev.76.996. URL https://link.aps.org/doi/10.1103/PhysRev.76.996. → pages xix, 50, 52

[214] N. F. Ramsey. A molecular beam resonance method with separated oscillating fields. *Phys. Rev.*, 78:695–699, Jun 1950. doi:10.1103/PhysRev.78.695. URL https://link.aps.org/doi/10.1103/PhysRev.78.695. → page 52

[215] H. Ravn. Experiments with intense secondary beams of radioactive ions. *Physics Reports*, 54(3):201–259, 1979. ISSN 0370-1573. doi:https://doi.org/10.1016/0370-1573(79)90045-0. URL https://www.sciencedirect.com/science/article/pii/0370157379900450. → pages 31, 32

[216] R. Reifarth. The s-process - overview and selected developments. *Journal of Physics: Conference Series*, 202, 2020. doi:10.1088/1742-6596/202/1/012022. → page 135

[217] M. Reiter, S. A. S. Andrés, J. Bergmann, T. Dickel, J. Dilling, A. Jacobs, A. Kwiatkowski, W. Plaß, C. Scheidenberger, D. Short, C. Will, C. Babcock, E. Dunling, A. Finlay, C. Hornung, C. Jesch, R. Klawitter, B. Kootte, D. Lascar, E. Leistenschneider, T. Murböck, S. Paul, and M. Yavor. Commissioning and performance of TITAN's Multiple-Reflection Time-of-Flight Mass-Spectrometer and isobar separator. *Nuclear Instruments and Methods in Physics Research Section A: Accelerators, Spectrometers, Detectors and Associated Equipment*, 1018:165823, 2021. ISSN 0168-9002. doi:https://doi.org/10.1016/j.nima.2021.165823. URL https://www.sciencedirect.com/science/article/pii/S0168900221008081. → pages xxi, 36, 70, 74, 75, 76, 78, 89, 97

[218] M. P. Reiter, S. Ayet San Andrés, S. Nikas, J. Lippuner, C. Andreoiu, C. Babcock, B. R. Barquest, J. Bollig, T. Brunner, T. Dickel, J. Dilling, I. Dillmann, E. Dunling, G. Gwinner, L. Graham, C. Hornung, R. Klawitter, B. Kootte, A. A. Kwiatkowski, Y. Lan, D. Lascar, K. G. Leach, E. Leistenschneider, G. Martínez-Pinedo, J. E. McKay, S. F. Paul, W. R. Plaß, L. Roberts, H. Schatz, C. Scheidenberger, A. Sieverding, R. Steinbrügge, R. Thompson, M. E. Wieser, C. Will, and D. Welch. Mass measurements of neutron-rich gallium isotopes refine production of nuclei of the first *r*-process abundance peak in neutron-star merger calculations. *Phys. Rev. C*, 101:025803, Feb 2020. doi:10.1103/PhysRevC.101.025803. URL https://link.aps.org/doi/10.1103/PhysRevC.101.025803. → page 141

[219] J. Repp, C. Böhm, J. Crespo López-Urrutia, et al. PENTATRAP: a novel cryogenic multi-Penning-trap experiment for high-precision mass measurements on highly charged ions. *Appl. Phys. B*, 107:983–996, 2012. doi:https://doi.org/10.1007/s00340-011-4823-6. URL https://link.springer.com/article/10.1007/s00340-011-4823-6. → page 79

[220] A. Revel, O. Sorlin, F. M. Marqués, Y. Kondo, J. Kahlbow, T. Nakamura, N. A. Orr, F. Nowacki, J. A. Tostevin, C. X. Yuan, N. L. Achouri, H. Al Falou, L. Atar, T. Aumann, H. Baba, K. Boretzky, C. Caesar, D. Calvet, H. Chae, N. Chiga, A. Corsi, H. L. Crawford, F. Delaunay, A. Delbart, Q. Deshayes, Z. Dombrádi, C. A. Douma, Z. Elekes, P. Fallon, I. Gašparić, J.-M. Gheller, J. Gibelin, A. Gillibert, M. N. Harakeh, W. He, A. Hirayama, C. R. Hoffman, M. Holl, A. Horvat, A. Horváth, J. W. Hwang, T. Isobe, N. Kalantar-Nayestanaki, S. Kawase, S. Kim, K. Kisamori, T. Kobayashi, D. Körper, S. Koyama, I. Kuti, V. Lapoux, S. Lindberg, S. Masuoka, J. Mayer, K. Miki, T. Murakami, M. Najafi,

K. Nakano, N. Nakatsuka, T. Nilsson, A. Obertelli, F. de Oliveira Santos, H. Otsu, T. Ozaki, V. Panin, S. Paschalis, D. Rossi, A. T. Saito, T. Saito, M. Sasano, H. Sato, Y. Satou, H. Scheit, F. Schindler, P. Schrock, M. Shikata, Y. Shimizu, H. Simon, D. Sohler, L. Stuhl, S. Takeuchi, M. Tanaka, M. Thoennessen, H. Törnqvist, Y. Togano, T. Tomai, J. Tscheuschner, J. Tsubota, T. Uesaka, Z. Yang, M. Yasuda, and K. Yoneda. Extending the southern shore of the island of inversion to ^{28}F. *Phys. Rev. Lett.*, 124:152502, Apr 2020. doi:10.1103/PhysRevLett.124.152502. URL https://link.aps.org/doi/10.1103/PhysRevLett.124.152502. → pages 14, 111

[221] A. Ridley. Penning traps and pressure: The path to higher precision nuclear mass measurements through highly charged ions. Master's thesis, University of Surrey, 2023. → page 158

[222] R. Ringle, G. Bollen, D. Lawton, et al. The LEBIT 9.4 T Penning trap system. *Eur. Phys. J. A*, 25, 2005. doi:https://doi.org/10.1140/epjad/i2005-06-132-y. → pages 52, 64, 66

[223] R. Ringle, G. Bollen, A. Prinke, J. Savory, P. Schury, S. Schwarz, and T. Sun. A "lorentz" steerer for ion injection into a penning trap. *International Journal of Mass Spectrometry*, 263(1):38–44, 2007. ISSN 1387-3806. doi:https://doi.org/10.1016/j.ijms.2006.12.008. URL https://www.sciencedirect.com/science/article/pii/S1387380606005781. → page 83

[224] R. Ringle, G. Bollen, P. Schury, S. Schwarz, and T. Sun. Octupolar excitation of ion motion in a Penning trap—A study performed at LEBIT. *International Journal of Mass Spectrometry*, 262(1):33–44, 2007. ISSN 1387-3806. doi:https://doi.org/10.1016/j.ijms.2006.10.009. URL https://www.sciencedirect.com/science/article/pii/S1387380606004738. → page 53

[225] R. Ringle, G. Bollen, A. Prinke, J. Savory, P. Schury, S. Schwarz, and T. Sun. The LEBIT 9.4T Penning trap mass spectrometer. *Nuclear Instruments and Methods in Physics Research Section A: Accelerators, Spectrometers, Detectors and Associated Equipment*, 604(3):536–547, 2009. ISSN 0168-9002. doi:https://doi.org/10.1016/j.nima.2009.03.207. URL https://www.sciencedirect.com/science/article/pii/S0168900209006901. → pages 34, 44, 83

[226] J. Ringuette and Z. Hockenbery. EBIT Simulator for Ionization. https://github.com/TITANCollaboration/ebitsim. → pages xxii, 82

[227] M. Rosenbusch, M. Wada, S. Chen, A. Takamine, S. Iimura, D. Hou, W. Xian, S. Yan, P. Schury, Y. Hirayama, Y. Ito, H. Ishiyama, S. Kimura, T. Kojima, J. Lee, J. Liu, S. Michimasa, H. Miyatake, J. Moon, M. Mukai, S. Naimi, S. Nishimura, T. Niwase, T. Sonoda, Y. Watanabe, and H. Wollnik. The new MRTOF mass spectrograph following the ZeroDegree spectrometer at RIKEN's RIBF facility. *Nuclear Instruments and Methods in Physics Research Section A: Accelerators, Spectrometers, Detectors and Associated Equipment*, 1047:167824, 2023. ISSN 0168-9002. doi:https://doi.org/10.1016/j.nima.2022.167824. URL https://www.sciencedirect.com/science/article/pii/S0168900222011160. → pages 41, 42

[228] F. Sarazin, H. Savajols, W. Mittig, F. Nowacki, N. A. Orr, Z. Ren, P. Roussel-Chomaz, G. Auger, D. Baiborodin, A. V. Belozyorov, C. Borcea, E. Caurier, Z. Dlouhý, A. Gillibert, A. S. Lalleman, M. Lewitowicz, S. M. Lukyanov, F. de Oliveira, Y. E. Penionzhkevich, D. Ridikas, H. Sakuraï, O. Tarasov, and A. de Vismes. Shape Coexistence and the $N = 28$ Shell Closure Far from Stability. *Phys. Rev. Lett.*, 84: 5062–5065, May 2000. doi:10.1103/PhysRevLett.84.5062. URL https://link.aps.org/doi/10.1103/PhysRevLett.84.5062. → page 104

[229] F. Sarazin, W. Savajols, H.and Mittig, et al. Shape Coexistence and the N=28 Shell Closure Far from Stability. *Hyperfine Interactions*, 132: 147–152, 2001. doi:https://doi.org/10.1023/A:1011912400725. URL https://link.springer.com/article/10.1023/A:1011912400725. → page 104

[230] H. Savajols. The SPEG Mass Measurement Program at GANIL. *Hyperfine Interactions*, 132:243–252, 2001. doi:https://doi.org/10.1023/A:1011964401634. URL https://link.springer.com/article/10.1023/A:1011964401634. → pages 87, 89

[231] G. Savard. Large radio-frequency gas catchers and the production of radioactive nuclear beams. *Journal of Physics: Conference Series*, 312(5): 052004, sep 2011. doi:10.1088/1742-6596/312/5/052004. URL https://dx.doi.org/10.1088/1742-6596/312/5/052004. → page 32

[232] G. Savard, S. Becker, G. Bollen, H.-J. Kluge, R. Moore, T. Otto, L. Schweikhard, H. Stolzenberg, and U. Wiess. A new cooling technique for heavy ions in a penning trap. *Physics Letters A*, 158(5):247–252, 1991.

ISSN 0375-9601. doi:https://doi.org/10.1016/0375-9601(91)91008-2. URL https://www.sciencedirect.com/science/article/pii/0375960191910082. → page 43

[233] G. Savard, R. Barber, C. Boudreau, et al. The Canadian Penning Trap Spectrometer at Argonne. *Hyperfine Interactions*, 132:221–228, 2001. doi:https://doi.org/10.1023/A:1011986930931. URL https://link.springer.com/article/10.1023/A:1011986930931. → page 44

[234] D. Schardt. Direct proton decay of 147 Tm. In *Heavy-Ion Collisions*, pages 256–266. Springer, 1982. → page 18

[235] H. Schatz. The importance of nuclear masses in the astrophysical rp-process. *International Journal of Mass Spectrometry*, 251(2):293–299, 2006. ISSN 1387-3806. doi:https://doi.org/10.1016/j.ijms.2006.02.014. URL https://www.sciencedirect.com/science/article/pii/S1387380606001187. ULTRA-ACCURATE MASS SPECTROMETRY AND RELATED TOPICS Dedicated to H.-J. Kluge on the occasion of his 65th birthday anniversary. → page 135

[236] H. Schatz. Nuclear masses in astrophysics. *International Journal of Mass Spectrometry*, 349-350:181–186, 2013. ISSN 1387-3806. doi:https://doi.org/10.1016/j.ijms.2013.03.016. URL https://www.sciencedirect.com/science/article/pii/S1387380613001073. 100 years of Mass Spectrometry. → pages 134, 135

[237] P. Schury, M. Wada, Y. Ito, F. Arai, S. Naimi, T. Sonoda, H. Wollnik, V. Shchepunov, C. Smorra, and C. Yuan. A high-resolution multi-reflection time-of-flight mass spectrograph for precision mass measurements at RIKEN/SLOWRI. *Nuclear Instruments and Methods in Physics Research Section B: Beam Interactions with Materials and Atoms*, 335:39–53, 2014. ISSN 0168-583X. doi:https://doi.org/10.1016/j.nimb.2014.05.016. URL https://www.sciencedirect.com/science/article/pii/S0168583X1400559X. → pages 34, 66

[238] S. Sels, F. M. Maier, M. Au, P. Fischer, C. Kanitz, V. Lagaki, S. Lechner, E. Leistenschneider, D. Leimbach, E. M. Lykiardopoulou, A. A. Kwiatkowski, T. Manovitz, Y. N. Vila Gracia, G. Neyens, P. Plattner, S. Rothe, L. Schweikhard, M. Vilen, R. N. Wolf, and S. Malbrunot-Ettenauer. Doppler and sympathetic cooling for the

investigation of short-lived radioactive ions. *Phys. Rev. Res.*, 4:033229, Sep 2022. doi:10.1103/PhysRevResearch.4.033229. URL https://link.aps.org/doi/10.1103/PhysRevResearch.4.033229. → pages xviii, 39, 40

[239] B. Sherrill, D. Morrissey, J. Nolen, and J. Winger. The A1200 projectile fragment separator. *Nuclear Instruments and Methods in Physics Research Section B: Beam Interactions with Materials and Atoms*, 56-57:1106–1110, 1991. ISSN 0168-583X. doi:https://doi.org/10.1016/0168-583X(91)95108-P. URL https://www.sciencedirect.com/science/article/pii/0168583X9195108P. → page 32

[240] K. Shimada, H. Ueno, G. Neyens, K. Asahi, D. Balabanski, J. Daugas, M. Depuydt, M. De Rydt, L. Gaudefroy, S. Grévy, Y. Hasama, Y. Ichikawa, D. Kameda, P. Morel, T. Nagatomo, L. Perrot, C. Stodel, J.-C. Thomas, Y. Utsuno, W. Vanderheijden, N. Vermeulen, P. Vingerhoets, E. Yagi, K. Yoshida, and A. Yoshimi. Erosion of N=20 shell in Al33 investigated through the ground-state electric quadrupole moment. *Physics Letters B*, 714(2):246–250, 2012. ISSN 0370-2693. doi:https://doi.org/10.1016/j.physletb.2012.07.030. URL https://www.sciencedirect.com/science/article/pii/S0370269312007708. → page 14

[241] D. Short. *Nuclear isobar separation for Penning trap mass measurements at TRIUMF*. PhD thesis, Simon Fraser University, 2018. URL https://summit.sfu.ca/item/18495. → pages xxiii, 93

[242] V. V. Simon, T. Brunner, U. Chowdhury, B. Eberhardt, S. Ettenauer, A. T. Gallant, E. Mané, M. C. Simon, P. Delheij, M. R. Pearson, G. Audi, G. Gwinner, D. Lunney, H. Schatz, and J. Dilling. Penning-trap mass spectrometry of highly charged, neutron-rich Rb and Sr isotopes in the vicinity of $\mathbf{A} \approx \mathbf{100}$. *Phys. Rev. C*, 85:064308, Jun 2012. doi:10.1103/PhysRevC.85.064308. URL https://link.aps.org/doi/10.1103/PhysRevC.85.064308. → page 83

[243] T. Skyrme. The effective nuclear potential. *Nuclear Physics*, 9(4):615–634, 1958. ISSN 0029-5582. doi:https://doi.org/10.1016/0029-5582(58)90345-6. URL https://www.sciencedirect.com/science/article/pii/0029558258903456. → pages 3, 24, 27

[244] M. Smith, M. Brodeur, T. Brunner, S. Ettenauer, A. Lapierre, R. Ringle, V. L. Ryjkov, F. Ames, P. Bricault, G. W. F. Drake, P. Delheij, D. Lunney, F. Sarazin, and J. Dilling. First penning-trap mass measurement of the exotic halo nucleus ^{11}Li. *Phys. Rev. Lett.*, 101:202501, Nov 2008. doi:10.1103/PhysRevLett.101.202501. URL https://link.aps.org/doi/10.1103/PhysRevLett.101.202501. → page 81

[245] M. J. Smith. *A mass measurement of the short-lived halo nucleus 11Li with the TITAN Penning trap spectrometer*. PhD thesis, University of British Columbia, 2008. URL https://open.library.ubc.ca/collections/ubctheses/24/items/1.0066362. → page 70

[246] K. Steiger. *Decay spectroscopy of neutron-rich nuclei around ^{37}Al*. PhD thesis, 2013. → pages 107, 108

[247] D. Steppenbeck, S. Takeuchi, N. Aoi, et al. Evidence for a new nuclear 'magic number' from the level structure of 54Ca. *Nature*, 502:207–210, 2013. doi:https://doi.org/10.1038/nature12522. URL https://www.nature.com/articles/nature12522. → pages 13, 160

[248] G. Sterman. Quantum chromodynamics. In J.-P. Françoise, G. L. Naber, and T. S. Tsun, editors, *Encyclopedia of Mathematical Physics*, pages 144–153. Academic Press, Oxford, 2006. ISBN 978-0-12-512666-3. doi:https://doi.org/10.1016/B0-12-512666-2/00293-5. URL https://www.sciencedirect.com/science/article/pii/B0125126662002935. → pages 8, 24

[249] J. Stone and P.-G. Reinhard. The skyrme interaction in finite nuclei and nuclear matter. *Progress in Particle and Nuclear Physics*, 58(2):587–657, 2007. ISSN 0146-6410. doi:https://doi.org/10.1016/j.ppnp.2006.07.001. URL https://www.sciencedirect.com/science/article/pii/S0146641006000627. → pages 27, 28, 111

[250] S. R. Stroberg, J. D. Holt, A. Schwenk, and J. Simonis. Ab initio limits of atomic nuclei. *Phys. Rev. Lett.*, 126:022501, Jan 2021. doi:10.1103/PhysRevLett.126.022501. URL https://link.aps.org/doi/10.1103/PhysRevLett.126.022501. → pages 3, 24, 111

[251] S. Sturm, I. Arapoglou, A. Egl, et al. The ALPHATRAP experiment. *Eur. Phys. J. Spec. Top.*, 227:1425–1491, 2019.

doi:https://doi.org/10.1140/epjst/e2018-800225-2. URL https://link.springer.com/article/10.1140/epjst/e2018-800225-2. → pages 43, 56

[252] T. Suda. Present status of the RIKEN Radioactive Ion Beam Factory, RIBF. *Journal of Physics: Conference Series*, 267(1):012008, jan 2011. doi:10.1088/1742-6596/267/1/012008. URL https://dx.doi.org/10.1088/1742-6596/267/1/012008. → page 32

[253] D. Suzuki, H. Iwasaki, D. Beaumel, L. Nalpas, E. Pollacco, M. Assié, H. Baba, Y. Blumenfeld, N. De Séréville, A. Drouart, S. Franchoo, A. Gillibert, J. Guillot, F. Hammache, N. Keeley, V. Lapoux, F. Maréchal, S. Michimasa, X. Mougeot, I. Mukha, H. Okamura, H. Otsu, A. Ramus, P. Roussel-Chomaz, H. Sakurai, J.-A. Scarpaci, O. Sorlin, I. Stefan, and M. Takechi. Breakdown of the $Z = 8$ Shell Closure in Unbound ^{12}**O** and its Mirror Symmetry. *Phys. Rev. Lett.*, 103:152503, Oct 2009. doi:10.1103/PhysRevLett.103.152503. URL https://link.aps.org/doi/10.1103/PhysRevLett.103.152503. → page 13

[254] N. Takigawa. *Fundamentals of nuclear physics*. Springer, 2017. → page 27

[255] M. Tanabashi et al. Review of Particle Physics. *Phys. Rev. D*, 98:030001, Aug 2018. doi:10.1103/PhysRevD.98.030001. URL https://link.aps.org/doi/10.1103/PhysRevD.98.030001. → pages 138, 140

[256] C. Thibault, R. Klapisch, C. Rigaud, A. M. Poskanzer, R. Prieels, L. Lessard, and W. Reisdorf. Direct measurement of the masses of ^{11}Li and $^{26-32}$Na with an on-line mass spectrometer. *Phys. Rev. C*, 12:644–657, Aug 1975. doi:10.1103/PhysRevC.12.644. URL https://link.aps.org/doi/10.1103/PhysRevC.12.644. → page 12

[257] M. Thoennessen. Plans for the facility for rare isotope beams. *Nuclear Physics A*, 834(1):688c–693c, 2010. ISSN 0375-9474. doi:https://doi.org/10.1016/j.nuclphysa.2010.01.125. URL https://www.sciencedirect.com/science/article/pii/S0375947410001260. The 10th International Conference on Nucleus-Nucleus Collisions (NN2009). → page 32

[258] R. G. Thomas. An Analysis of the Energy Levels of the Mirror Nuclei, ^{13}C and ^{13}N. *Phys. Rev.*, 88:1109–1125, Dec 1952. doi:10.1103/PhysRev.88.1109. URL https://link.aps.org/doi/10.1103/PhysRev.88.1109. → page 21

[259] V. Tripathi, S. L. Tabor, P. Bender, C. R. Hoffman, S. Lee, K. Pepper, M. Perry, P. F. Mantica, J. M. Cook, J. Pereira, J. S. Pinter, J. B. Stoker, D. Weisshaar, Y. Utsuno, and T. Otsuka. Excited intruder states in ^{32}Mg. *Phys. Rev. C*, 77:034310, Mar 2008. doi:10.1103/PhysRevC.77.034310. URL https://link.aps.org/doi/10.1103/PhysRevC.77.034310. → pages 101, 102, 112

[260] N. Vieira, G. Audi, Z. Djouadi, H. Doubre, C. Gaulard, S. Henry, D. Lunney, M. de Saint Simon, C. Thibault, and G. Bollen. Mistral. In J. Äystö, P. Dendooven, A. Jokinen, and M. Leino, editors, *Exotic Nuclei and Atomic Masses*, pages 21–24, Berlin, Heidelberg, 2003. Springer Berlin Heidelberg. ISBN 978-3-642-55560-2. → page 87

[261] M. Vogel. *Particle Confinement in Penning Traps*. Springer Cham, 2018. doi:https://doi.org/10.1007/978-3-319-76264-7. → page 49

[262] M. G. W. et al. Astromers: Nuclear Isomers in Astrophysics. *The Astrophysics Journal*, 252. doi:10.3847/1538-4365/abc41d. URL https://iopscience.iop.org/article/10.3847/1538-4365/abc41d/meta. → page 137

[263] M. G. W. et al. Astromers in the Radioactive Decay of r-process. *The Astrophysics Journal Letters*, 913, 2021. doi:10.3847/2041-8213/abfb74. URL https://iopscience.iop.org/article/10.3847/2041-8213/abfb74/meta. → page 137

[264] M. Wang, W. Huang, F. Kondev, G. Audi, and S. Naimi. The AME 2020 atomic mass evaluation (II). Tables, graphs and references. *Chinese Physics C*, 45(3):030003, Mar 2021. doi:10.1088/1674-1137/abddaf. URL https://doi.org/10.1088/1674-1137/abddaf. → pages xiv, xvi, xvii, xxiv, xxv, 6, 16, 18, 101, 102, 103, 104, 105, 106, 108, 109, 110, 114, 115, 117, 124, 127, 161, 209

[265] E. K. Warburton, J. A. Becker, and B. A. Brown. Mass systematics for A=29-44 nuclei: The deformed A∼32 region. *Phys. Rev. C*, 41:1147–1166, Mar 1990. doi:10.1103/PhysRevC.41.1147. URL https://link.aps.org/doi/10.1103/PhysRevC.41.1147. → page 12

[266] S. Weinberg. Nuclear forces from chiral lagrangians. *Physics Letters B*, 251(2):288–292, 1990. ISSN 0370-2693. doi:https://doi.org/10.1016/0370-2693(90)90938-3. URL https://www.sciencedirect.com/science/article/pii/0370269390909383. → page 24

[267] F. Wienholtz, D. Beck, K. Blaum, et al. Masses of exotic calcium isotopes pin down nuclear forces. *Nature*, 498:346–349, 2013. doi:https://doi.org/10.1038/nature12226. URL https://www.nature.com/articles/nature12226. → page 13

[268] F. Wienholtz, S. Kreim, M. Rosenbusch, L. Schweikhard, and R. Wolf. Mass-selective ion ejection from multi-reflection time-of-flight devices via a pulsed in-trap lift. *International Journal of Mass Spectrometry*, 421: 285–293, 2017. ISSN 1387-3806. doi:https://doi.org/10.1016/j.ijms.2017.07.016. URL https://www.sciencedirect.com/science/article/pii/S1387380617301987. → page 41

[269] B. H. Wildenthal and W. Chung. Collapse of the conventional shell-model ordering in the very-neutron-rich isotopes of na and mg. *Phys. Rev. C*, 22: 2260–2262, Nov 1980. doi:10.1103/PhysRevC.22.2260. URL https://link.aps.org/doi/10.1103/PhysRevC.22.2260. → page 128

[270] B. H. Wildenthal and W. Chung. Collapse of the conventional shell-model ordering in the very-neutron-rich isotopes of Na and Mg. *Phys. Rev. C*, 22: 2260–2262, Nov 1980. doi:10.1103/PhysRevC.22.2260. URL https://link.aps.org/doi/10.1103/PhysRevC.22.2260. → pages 12, 87

[271] K. Wimmer, T. Kröll, R. Krücken, V. Bildstein, R. Gernhäuser, B. Bastin, N. Bree, J. Diriken, P. Van Duppen, M. Huyse, N. Patronis, P. Vermaelen, D. Voulot, J. Van de Walle, F. Wenander, L. M. Fraile, R. Chapman, B. Hadinia, R. Orlandi, J. F. Smith, R. Lutter, P. G. Thirolf, M. Labiche, A. Blazhev, M. Kalkühler, P. Reiter, M. Seidlitz, N. Warr, A. O. Macchiavelli, H. B. Jeppesen, E. Fiori, G. Georgiev, G. Schrieder, S. Das Gupta, G. Lo Bianco, S. Nardelli, J. Butterworth, J. Johansen, and K. Riisager. Discovery of the shape coexisting 0^+ state in ^{32}Mg by a two neutron transfer reaction. *Phys. Rev. Lett.*, 105:252501, Dec 2010. doi:10.1103/PhysRevLett.105.252501. URL https://link.aps.org/doi/10.1103/PhysRevLett.105.252501. → page 14

[272] R. Wolf, D. Beck, K. Blaum, C. Böhm, C. Borgmann, M. Breitenfeldt, F. Herfurth, A. Herlert, M. Kowalska, S. Kreim, D. Lunney, S. Naimi, D. Neidherr, M. Rosenbusch, L. Schweikhard, J. Stanja, F. Wienholtz, and K. Zuber. On-line separation of short-lived nuclei by a multi-reflection time-of-flight device. *Nuclear Instruments and Methods in Physics Research Section A: Accelerators, Spectrometers, Detectors and Associated Equipment*, 686:82–90, 2012. ISSN 0168-9002.

doi:https://doi.org/10.1016/j.nima.2012.05.067. URL https://www.sciencedirect.com/science/article/pii/S016890021200575X. → page 34

[273] H. Wollnik. 1 - gaussian optics and transfer matrices. In H. Wollnik, editor, *Optics of Charged Particles*, pages 1–26. Academic Press, 1987. ISBN 978-0-12-762130-2. doi:https://doi.org/10.1016/B978-0-12-762130-2.50004-2. URL https://www.sciencedirect.com/science/article/pii/B9780127621302500042. → page 36

[274] H. Wollnik. History of mass measurements in time-of-flight mass analyzers. *International Journal of Mass Spectrometry*, 349-350:38–46, 2013. ISSN 1387-3806. doi:https://doi.org/10.1016/j.ijms.2013.04.023. URL https://www.sciencedirect.com/science/article/pii/S1387380613001504. 100 years of Mass Spectrometry. → page 37

[275] J. Wouters, D. Vieira, H. Wollnik, G. Butler, R. Kraus, and K. Vaziri. The Time-Of-Flight Isochronous (TOFI) spectrometer for direct mass measurements of exotic light nuclei. *Nuclear Instruments and Methods in Physics Research Section B: Beam Interactions with Materials and Atoms*, 26(1):286–293, 1987. ISSN 0168-583X. doi:https://doi.org/10.1016/0168-583X(87)90765-8. URL https://www.sciencedirect.com/science/article/pii/0168583X87907658. → page 87

[276] Z. Xu, H. Heylen, K. Asahi, F. Boulay, J. Daugas, R. de Groote, W. Gins, O. Kamalou, Koszorús, M. Lykiardopoulou, T. Mertzimekis, G. Neyens, H. Nishibata, T. Otsuka, R. Orset, A. Poves, T. Sato, C. Stodel, J. Thomas, N. Tsunoda, Y. Utsuno, M. Vandebrouck, and X. Yang. Nuclear moments of the low-lying isomeric 1+ state of 34Al: Investigation on the neutron 1p1h excitation across N=20 in the island of inversion. *Physics Letters B*, 782:619–626, 2018. ISSN 0370-2693. doi:https://doi.org/10.1016/j.physletb.2018.06.009. URL https://www.sciencedirect.com/science/article/pii/S037026931830457X. → page 14

[277] Y. Yanagisawa, M. Notani, H. Sakurai, M. Kunibu, H. Akiyoshi, N. Aoi, H. Baba, K. Demichi, N. Fukuda, H. Hasegawa, Y. Higurashi, M. Ishihara, N. Iwasa, H. Iwasaki, T. Gomi, S. Kanno, M. Kurokawa, Y. Matsuyama, S. Michimasa, T. Minemura, T. Mizoi, T. Nakamura, A. Saito, M. Serata,

S. Shimoura, T. Sugimoto, E. Takeshita, S. Takeuchi, K. Ue, K. Yamada, K. Yoneda, and T. Motobayashi. The first excited state of 30Ne studied by proton inelastic scattering in reversed kinematics. *Physics Letters B*, 566 (1):84–89, 2003. ISSN 0370-2693. doi:https://doi.org/10.1016/S0370-2693(03)00802-5. URL https://www.sciencedirect.com/science/article/pii/S0370269303008025. → page 14

[278] D. T. Yordanov, M. Kowalska, K. Blaum, M. De Rydt, K. T. Flanagan, P. Lievens, R. Neugart, G. Neyens, and H. H. Stroke. Spin and magnetic moment of ^{33}Mg: Evidence for a negative-parity intruder ground state. *Phys. Rev. Lett.*, 99:212501, Nov 2007. doi:10.1103/PhysRevLett.99.212501. URL https://link.aps.org/doi/10.1103/PhysRevLett.99.212501. → page 14

[279] D. T. Yordanov, M. L. Bissell, K. Blaum, M. De Rydt, C. Geppert, M. Kowalska, J. Krämer, K. Kreim, A. Krieger, P. Lievens, T. Neff, R. Neugart, G. Neyens, W. Nörtershäuser, R. Sánchez, and P. Vingerhoets. Nuclear charge radii of $^{21-32}$Mg. *Phys. Rev. Lett.*, 108:042504, Jan 2012. doi:10.1103/PhysRevLett.108.042504. URL https://link.aps.org/doi/10.1103/PhysRevLett.108.042504. → page 14

[280] W. Younes, D. M. Gogny, and J.-F. Berger. *Hartree-Fock-Bogoliubov Theory*, pages 3–40. Springer International Publishing, Cham, 2019. ISBN 978-3-030-04424-4. doi:10.1007/978-3-030-04424-4_1. URL https://doi.org/10.1007/978-3-030-04424-4_1. → pages 24, 27

[281] Y. H. Zhang, Y. A. Litvinov, T. Uesaka, and H. S. Xu. Storage ring mass spectrometry for nuclear structure and astrophysics research. *Physica Scripta*, 91. → page 34

Appendix A

Table of AME calculation results

Table A.1 contains the results of the AME [264] network calculation described in Chapter 6. The first two column show the resulted Mass Excess (ME) values and their uncertainty and the next two columns display the literature values from AME2020 [264]. The last four columns show the one and two-proton separation energies and their uncertainties, calculated using the ME values of columns 1, 2 and literature values [264] when needed.

Isotope	ME (keV)	unc. (keV)	ME$_{AME2020}$ (keV)	unc. (keV)	S_p (keV)	unc. (keV)	S_{2p} (keV)	unc. (keV)
^{148}Tb	-70535	12	-70537	12	2467	13	7995	14
^{150}Yb*	-38635	45	-38830#	300#	1983	205	1733	46
^{151}Er	-58268	15	-58266	17	3611	21	5152	18
^{151}Yb*	-41326	106	-41542	300	2124	222	2162	109
^{151}Yb^{m}*	-40617	49						
^{151}Lu	-30105	45	-30300#	300#	-1241	64	742	205
^{151}Lu^{m}	-30048	45	-30244#	300#				
^{152}Ho	-63603	12	-63605	13	2139	13	7074	14
^{152}Tm	-51695	51	-51720	54	716	53	4327	53
^{152}Yb*	-46079	44	-46270	150	2596	48	2825	47
^{153}Yb*	-47102	46	-47160#	200#	2696	68	3412	48
^{153}Lu	-38184	45	-38375	150	-606	63	1990	49
^{153}Lu^{m}	-38104	45	-38296	150				
^{154}Lu	-39609	48	-39667#	201#	-204	66	2492	70
^{154}Lu^{m}	-39547	48	-39604#	201#				
^{155}Yb*	-50505	16	-50503	17	3366	21	4616	18
^{156}Tm	-56831	14	-56834	14	1911	15	6770	16
^{156}Lu	-43675	51	-43700	54	459	53	3825	53
^{156}Hf	-37628	44	-37820	150	2371	48	2273	47
^{156}Hf^{m}	-35669	44	-35861	150				
^{157}Tm	-58716	24	-58709	28	1793	34	7253	30
^{157}Hf	-38797	46	-38855#	200#	2412	68	2871	48
^{157}Ta	-29404	45	-29596	150	-935	63	1437	49
^{157}Ta^{m}	-29382	45	-29574	150				
^{157}Ta^{n}	-27811	45	-28003	150				
^{158}Ta	-31061	48	-31118#	201#	-448	66	1964	70
^{158}Ta^{m}	-30919	48	-30977#	201#				
^{158}Ta^{n}	-28253	49	-28311#	201#				
^{159}Hf	-42855	16	-42853	17	2931	22	4012	19
^{160}Ta	-35799	51	-35824	54	233	53	3164	53
^{160}W	-29137	44	-29329	150	1987	48	1613	47
^{161}W	-30449	46	-30507#	200#	1940	69	2178	49
^{161}Re	-20651	44	-20843	150	-1197	62	790	48
^{161}Re^{m}	-20527	44	-20719	150				
^{162}Re	-22395	47	-22453#	201#	-765	66	1175	70
^{162}Re^{m}	-22220	48	-22278#	201#				
^{163}W	-34910	58	-34908	58	2418	86	3172	63
^{164}Re	-27447	51	-27472	55	-174	78	2244	81
^{164}Os	-20233	44	-20425	150	1519	48	811	48
^{165}Os	-21689	46	-21747#	200#	1531	69	1357	74
^{165}Ir	-11403#	67#	-11595#	158#	-1541	80	-21	70
^{165}Ir^{m}	-11223	45	-11415	150				
^{166}Ir	-13248	47	-13306#	201#	-1152	66	379	70
^{166}Ir^{m}	-13077	48	-13134#	201#				
^{167}Os	-26501	81	-26499	81	1952	120	2217	85
^{168}Ir	-18641	52	-18666	55	-571	96	1382	102
^{168}Pt	-10818	44	-11010	150	1035	48	-35	48
^{169}Pt	-12407	47	-21464#	200#	1054	70	484	93
^{170}Au	-3646	48	-3703#	201#	-1472	67	-417	71
^{170}Au^{m}	-3366	47	-3424#	201#				
^{171}Pt	-17469	81	-17467	81	1575	130	1323	85
^{172}Au	-9293	53	-9318	56	-886	97	689	115
^{172}Hg	-869	45	-1061	150	596	49	-852	48
^{173}Hg	-2604	47	-2661#	201#	600	71	-287	93
^{175}Hg	-7971	81	-7969	81	1202	130	613	103
^{176}Tl	583	83	585	83	-1265	116	-63	131
^{179}Pb	2050	81	2052	81	626	131	-247	117

Table A.1: Results of the AME network calculation. # signs indicate extrapolated values.

Appendix B

Towards the implementation of the PI-ICR technique at TITAN

The PI-ICR technique [85] (described in Chapter 3) has replaced TOF-ICR in many of the mass measurement facilities that use Penning traps [156], due to the efficiency of the method as well as due to a factor of 40 gain in resolving power [86] that it offers [85].

At TITAN, higher resolving power is achieved by the use of HCI, as described in Chapters 3 and 4. However, an additional advantage can be achieved by combining HCI and PI-ICR reaching even higher precision while maintaining efficiency and half-life limitations. In addition, for measurements of very short-lived or very low-yield isotopes, TITAN can benefit from using PI-ICR due to its non-scanning character (thus requiring fewer total detected counts for a measurement) and due to the fact that shorter excitation times can be used in order to achieve the same precision [85].

In the framework of this thesis, the feasibility and the requirements for implementing the PI-ICR technique at TITAN are investigated. This chapter, starts with the simulations performed to investigate the feasibility and the gain in precision when using PI-ICR with HCI at TITAN. It continues with the technical upgrades performed to transition from the TOF-ICR to the PI-ICR technique.

B.1 Simulations

Simulations[1] of the PI-ICR technique using the CryoMPET experimental apparatus were performed in the ion optics simulation program SIMION [68]. The trap geometry, as defined in Chapter 4, was imported from the Solid-Works technical drawings to achieve best representation of the experimental setup. A schematic of the imported geometry is shown in Fig. B.1.

SIMION [68] is an ion optics software which calculates electric and magnetic field trajectories of charged particles given a set of voltages, magnetic fields and initial particle conditions, such as mass, energy and position. The electric field is calculated by solving the Laplace equation for the simulated geometry using a set of user defined voltage values. Then the trajectories of ions in the determined electric and magnetic field are determined by calculating the Lorentz force on the ions and by solving the ions' equations of motion. In addition, SIMION allows to simulate RF fields, particle collisions, ion trapping and others.

In the present work, ions of mass m = 74 u were created at the center of the trap with an energy spread of 5 eV/q in the axial direction and 0.1 eV/q at the radial direction, where q is the charge state of the simulated ion. The ions were created either at the center of the trap or at a r = 1 mm magnetron radius, as can be seen in Fig. B.1. The charge of the ions varied from q = 1e, where e the electron charge, to q = 37e and the (x,y) positions of each ion were recorded at the z-position of the detector.

The voltage values of the extraction beam elements were optimized for the q = 1 charge state, using least squares minimization, to maximize transmission and resolving power $\nu_c/\Delta\nu_c$, where ν_c the cyclotron frequency. The final voltage values can be seen in Table B.1. The second column of Table B.1 shows the extraction voltages for the TOF-ICR technique. The important difference between the two sets of voltages, lies in the values for XDC ans XZT1. In the case of TOF-ICR, they are zero because the ions need to exit the magnetic field gradient as slowly as possible in order to fully convert their reduced cyclotron frequency and therefore to maximize the TOF effect in the resonance plots. On the contrary, ion extraction for PI-ICR needs to be as fast as possible in order to avoid beam spread and therefore

[1] The following work has been published in [172].

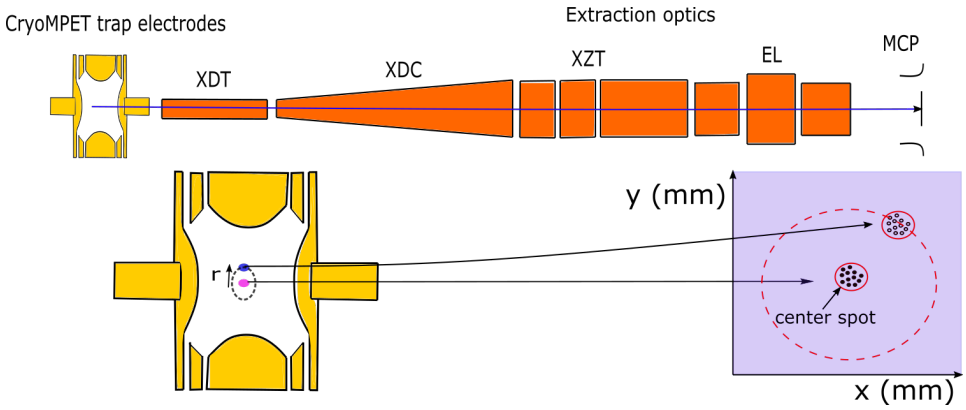

Figure B.1: Top: Schematic of the simulated geometry. Bottom: Schematic showing the two initial position settings of the ions in the trap and their projection to the position-sensitive MCP.

Element	ToF-ICR Voltage (V)	PI-ICR Voltage (V)
XDT	-10	-10
XDC	0	-198
XZT1,3	0	-2142
XZT2	-500	-3010
EL1,3	-20	-3294
EL2	-1200	-550
Extr. Cap Open	0	-26
Extr. Tube open	-60	-37
MCP bias	-2050	-2050

Table B.1: Applied TOF-ICR and Simulated PI-ICR voltages for each extraction electrode of the MPET beamline.

to obtain the maximum spacial resolving power.

Starting with a procedure to optimize the extraction voltages for $q = 1e$, all other charge states (up to 37e) were simulated. The phase-image of ions of different charge states can be seen in Fig B.2. Although all parameters other than the charge state stay the same, the magnification factor, which represents the radius of the position of the ions on the detector compared to their position in the trap:

$$G = \frac{r_{detector}}{r_{trap}} \tag{B.1}$$

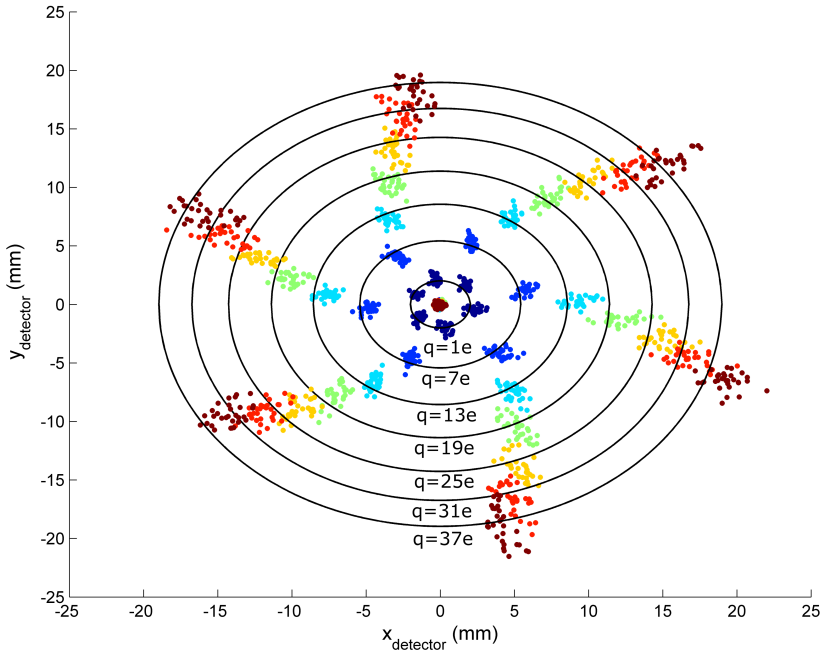

Figure B.2: Simulation of ion spots of different charge states projected on a position sensitive detector. Their simulated magnetron radius at the trap is 1 mm.

increases almost linearly, as a function of the charge state. This effect is related to the Einzel lens [8] (EL1,2,3) of the extraction optics. An Einzel lens is made of three consecutive cylindrical electrodes, at which different voltages are applied. The Einzel lens can have a focusing or defocusing effect depending of the voltage difference between the central tube and the two other ones that are kept at the same voltage. In the present case, we need the Einzel lens to create a defocusing effect at the detector so that the radial position of the ions in the trap is preserved. The force experienced by the ions travelling through the Einzel lens will scale with their charge state q, as

$$\vec{F} = -q\vec{\nabla}V \tag{B.2}$$

which causes the ions of higher charge states to gain a larger radius by the time they reach the detector. As a result, the resolving power of the PI-ICR technique,

as defined in Eq. 3.31, becomes:

$$R_{PI-ICR} = \frac{\pi \nu_+ t_{acc} r_+}{\Delta r_+} \propto \frac{\pi q t_{acc} r_+}{\Delta r_+} \propto \frac{\pi q^2 t_{acc}}{\Delta r_+} \tag{B.3}$$

where ν_+ the reduced cyclotron frequency of the trapped ions.

However, it is not only the radius of the ions that increases with increasing the charge state but also their position spread. Fig B.3 shows the ratio of the radius versus its position spread (1σ of the distribution, assuming a gaussian distribution) as a function of the charge state. From the plot we can estimate the final resolving power to be:

$$R^{final}_{PI-ICR} \propto \pi q^{1+\alpha} t_{acc} \tag{B.4}$$

where $\alpha \simeq 3/2$. Therefore, we conclude that the PI-ICR technique benefits from using HCI by more than a factor q where q is the charge state and that the implementation of the technique is feasible in the CryoMPET setup. However, when considering the charge-breeding of short-lived ions with low production rates, loses due to charge-breeding efficiency and decay loses due to the time required for charge breeding can reduce the gain of combining the PI-ICR and HCI. The use of PI-ICR with highly charged ions or singly charged ions will have to be decided on a case by case basis based on the required precision, the nuclear half-life and the production rate of the studied isotopes.

B.2 Towards the implementation of the PI-ICR technique

After the feasibility studies described in the previous section, the experimental requirements for a possible implementation are discussed:

A new position-sensitive MCP detector (RoentDek DLD40EP [128]) is needed to replace the existing MCP detector installed at the CryoMPET beamline. The new position sensitive MCP is equipped with a delay-line anode which is capable of providing the position information (B.6 (Left)). In addition it uses two MCP plates, with an approx. 40 mm active diameter, stacked in the Chevron configuration. In the Chevron configuration, the MCP channels are angled and form a shallow "V" shape as shown in Fig. B.5. This configuration allows for up to three orders of magnitude larger electron gains compared to MCP plates with straight chan-

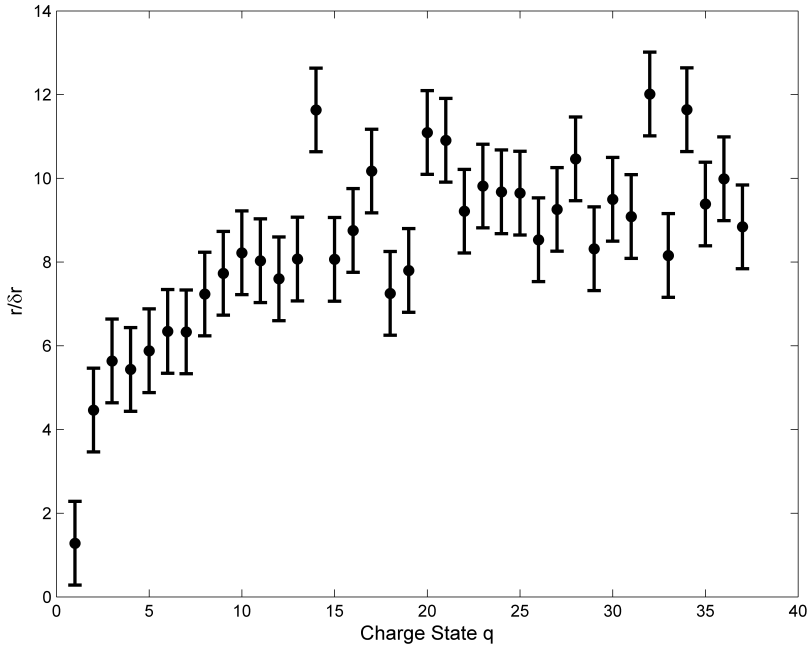

Figure B.3: Simulated ratio of the radius versus the position spread as a function of the charge state. Saturation in the ratio $r/\delta r$ comes from the increase in the size of the ion spots as the ions move close to the electrodes and thus experience changes in the electric field due to mechanical imperfections.

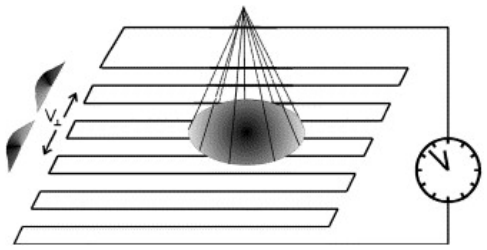

Figure B.4: Schematic of the principle of a position measurement using a delay line anode. As ions hit the delay line wire, one signal travels towards each end of the wire. From the difference in the arrival time between the two signals, the position of the event is reconstructed. Figure taken from [128].

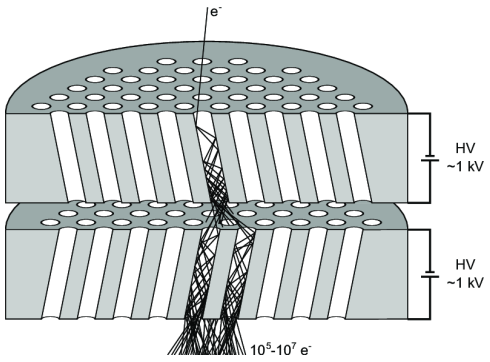

Figure B.5: Schematic of two MCP plates stacked in a Chevron configuration. When a charged particle or photon hits the MCP plates, electrons are produced and accelerated towards the back of the MCP, producing secondary electrons along the way. The signal is summed and amplified at MCP back resulting in charged particle detection. Figure taken from [73].

nels [157]. As ions hit the front MCP plate, secondary electrodes are created and propagated through the MCP apparatus at an approx. 2 kV drift difference. Once they reach the back of the second MCP, the signal is recorded. This signal is an electrical pulse amplified by a pre-amplifier, however it does not provide position information. Employing voltage dividers, the secondary electrons are propagated towards the delay anode located behind the MCP plates. The delay anode consists of a set of two wires that are arranged perpendicularly to each other. Once the secondary electrodes hit the wires, as can be seen in Fig. B.4, additional electrical pulses propagate towards both ends of each wire. The timing difference between the signals at each end of the wire, provides the x and y positions of the ions.

This detector was assembled (Fig. B.6 (Right)) and installed at the beamline in January 2023. In addition to the detector, the following commercial electronic components are being used:

- The FT12-TP signal decoupler, cointaining the HVZ voltage divider. This device takes two SHV input voltages and splits them in six channels: MCP Front, Back, Signal wires, Reference wires, Delay anode and MCP Holder. In addition, it contains six LEMO outputs that provide the signals read from the MCP Front, Back, x_1, x_2, y_1 and y_2. For optimal perfomance, the MCP

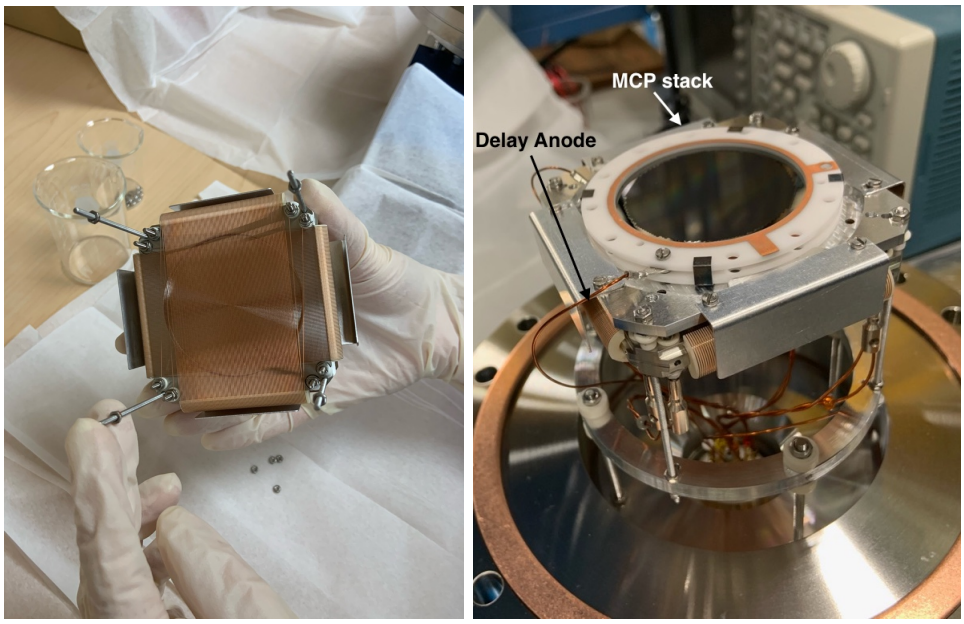

Figure B.6: Left: Picture of the delay-line anode. It is made of two sets of wires that are arranged perpendicular to each other. Right: The assembled MCP. The MCP stack and the delay anode are pointed with arrows.

Front LEMO output has been terminated with a 50 Ω terminator.

- The FAMP1 amplifier that amplifies the signal arriving from the MCP back.
- The Constant Fraction Discriminator (CFD1) that digitizes the amplified signal from the MCP back. The standard used for the output signal is NIM.
- Two ATR19 units for amplification and digitization of the position signals. Each unit has two channels.

The NIM signals from the MCP back and the position channels are used as input to a CAEN Time-to-Digital Converter (TDC) for further processing. The TDC signals are finally read by the MPET DAq which uses the MIDAS Data Acquisition software [6], which is co-developped by TRIUMF and PSI. In MIDAS, the five indepenent signals (MCP-back, x_1, y_1, x_2 and y_2) are treated in two groups. The first only contains the MCP back and it is used as a timing signal for the ions, while the rest give the position information (x,y), if all four signals are in coincidence.

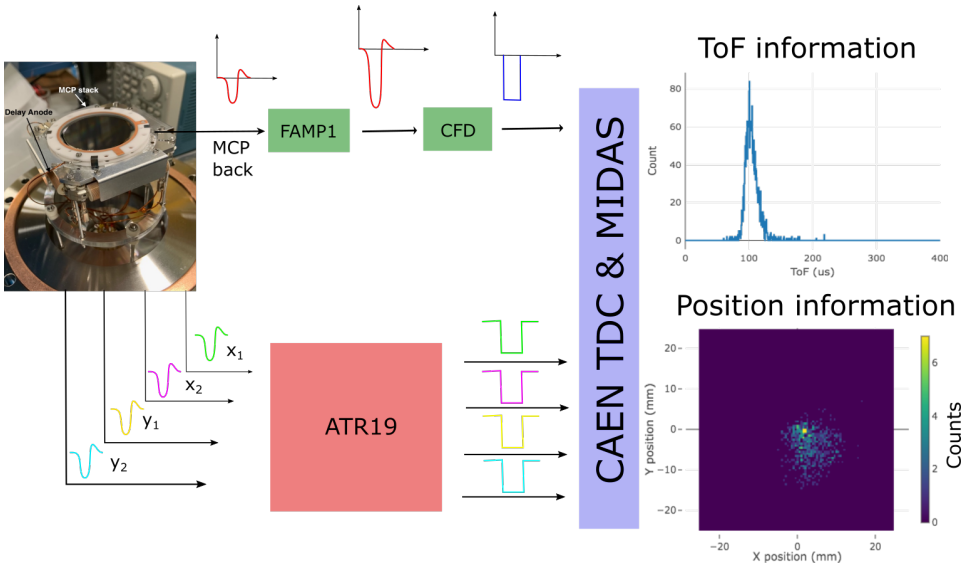

Figure B.7: Schematic of the electronics and the different signals produced by the position sensitive MCP. For details see text.

A visual representation of the electronic components and the shape of the signal in each stage can be seen in Fig. B.7.

All hardware and software upgrades for the implementation of PI-ICR have been completed. Currently, the technique is being tested with the aim to be used in CryoMPET's first experiment with RIB, which is scheduled to take place in September 2023. In this experiment, the Q-value of ^{48}Sc-^{48}Ti will be measured with the aim for a $\delta m/m \sim 10^{-9}$ precision.

Appendix C

Technical details for the commissioning of CryoMPET

During the CryoMPET assembly and commissioning phases, a number of procedures and techniques were developed (such as RF testing, tuning and trapping in CryoMPET etc.) which are necessary when operating the trap. This Chapter provides procedured on how to optimize aspects of CryoMPET and how new devices (such as new RF drivers, LS filters etc) were implemented.

C.1 RF function tests

In the current design of CryoMPET, almost none of the trap electrodes can be accessed for continuity check as well as for investigation of electrical shortcuts. The situation is even more challenging because of the fragility of the cryogenic wires connecting the trap to the shield, which can easily be cut resulting in disconnecting an electrode from its power supply (for more information behind the trap wiring see Fig. 7.9).

A method applied in previous installations which has proven beneficial to systematically confirm the status of trap wires is the “RF test”.

RF tests determine the the voltage pick-up induced by neighbouring electrodes. A sine wave is supplied to one of the trap electrodes using a function generator. The supplied voltage induces a voltage in each neighbouring electrode, the amplitude

	Inj. Tube	Inj. Cap	Guards	Ring +HS	Ring -HS	Ring +CF	Ring -CF	Extr. Cap	Extr. Tube
Inj. Tube		**0.5**	0.3	0.1	0.2	0.1	0.1	0.1	0.1
Inj. Cap	**0.5**		**0.4**	0.1	0.2	0.1	0.1	0.1	0.1
Guards	0.3	**0.4**		**0.3**	**0.3**	**0.2**	**0.4**	**0.5**	0.3
Ring +HS	0.1	0.1	**0.4**		0.1	**0.2**	**0.2**	0.1	0.1
Ring -HS	0.2	0.2	**0.3**	0.1		**0.2**	**0.1**	0.1	0.2
Ring +CF	0.1	0.1	**0.2**	**0.2**	**0.2**		0.1	0.1	0.2
Ring -CF	0.1	0.1	**0.4**	**0.2**	**0.2**	0.1		0.2	0.1
Extr. Cap	0.1	0.2	**0.5**	0.2	0.2	0.2	0.2		**0.4**
Extr. Tube	0.1	0.1	0.3	0.1	0.2	0.2	0.1	**0.4**	

Table C.1: RF-test in vacuum. Measurements are in Volts. The applied voltage in each case is V_{app} = 1 V. Values in bold depict pick-up values of neighbouring electrodes.

of which depends on the distance between the electrodes and can be monitored. Therefore, an unusually large pick-up signal (for example 1 V for a 1 V input signal) can indicate an electrical contact while a suspiciously small signal (for example 0.05 V for a 1 V input signal) can indicate a faulty wire.

This test was performed at various stages of the assembly and installation and the values between different tests were compared for consistency. An example from when the trap was installed in the beamline can be seen in Table C.1.

Overall, there is a $\sim$ 0.1 V pick-up signal regardless of the relative position of the electrodes, possibly coming from the proximity of the wires. However, neighbouring electrodes (Table C.1 values in bold), usually show pick-up voltages significantly higher than the baseline, as for example the case between injection tube and injection cap electrodes where the amplitude of the pick-up signal is 0.5 V. A picture of the trap electrodes and showing which electrodes are closest to each other can be seen in Fig. C.1 The most useful test is by supplying a voltage to the guard electrode and detecting the pick-up signal on all other electrodes. Due to their geometry, the guard electrode induces a significant pick-up signal to all of the trap electrodes and therefore offers a good comparison.

The values of Table C.1, for neigboring electrodes are large enough ($V_{pickup} >$ 0.1 V) to indicate that all the electrodes are still connected but too large ($V_{pickup} <$

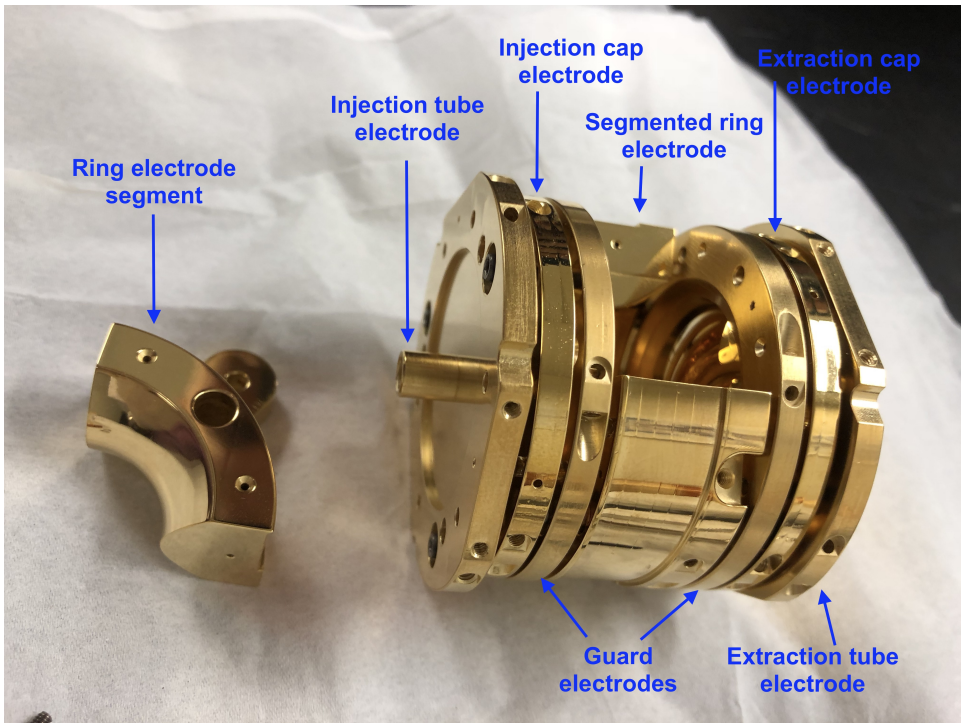

Figure C.1: The CryoMPET trap electrodes.

1 V) to suggest an electrical contact (short).

After the trap was installed in the superconducting magnet bore, pumped down and all the specified checks were performed, $^{39}K^{+}$ ions were tuned through the beamline from the TITAN Ion Source (TIS). The final test of the connectivity of the electrodes was performed by blocking the $^{39}K^{+}$ beam. The beam coming from TIS usually has a kinetic beam energy of 2.2 keV, as described in Chapter 4, and therefore can be blocked by any voltage potential larger than 2.2 kV. The beam was responsive to voltages applied from all injection and extraction electrodes, as indicated by the loss of ions on the detector for applied voltages that surpassed the 2.2 kV threshold. However, the trap voltages cannot be biased to more than 200 V and therefore the beam energy needed to be first reduced using the PLT electrode. With the low-energy beam, all trap electrodes can be biased sufficiently high to reflect the beam, verifying the RF tests.

C.2 Beam Tuning: Selecting ions of interest and optimizing beam energy and position in CryoMPET

A beam of stable alkali ions can be produced by TIS, which is located south of the TITAN RFQ. For delivery of beam to the CryoMPET, the ion source was heated up to 1.15-1.25 A. At the lower current, mostly ^{133}Cs (E_{ion} = 3.84 eV) and ^{85,87}Rb (E_{ion} = 4.18 eV) are ionized while for the higher current, there is additional production of $^{39}K^{+}$ (E_{ion} = 4.34 eV).

Although all alkali ions can be transported and trapped in CryoMPET, $^{39}K^{+}$ is preferred for Penning trap commissioning with TOF-ICR because, due to its lower mass, it results in larger TOF-effects. Selection between Rb, Cs and K ions is accompliced by selecting the switching time of RFQ's pulsed drift tube (PB5) and utilizing the different time it takes for ions of different mass to arrive at that position. The PB5 switches from 1.78 kV to ground thus defining the kinetic energy of the ions to 2.2 keV (the difference between the RFQ bias: 20 kV and the PB5 switch high voltage), provided that the ions of interest are in a field-free region near the center of PB5 when it switches. The beamline ion optical elements are operated such that only ions with an energy of $\sim$ 2.2 keV are transported to CryoMPET and therefore, by selecting the right point for PB5 to switch, the ions of interest can be transported. An example of the selection process can be seen in Fig. C.2, where *Time of Flight* is the time required for the ions to travel from the RFQ to the detector after CryoMPET and *PB5 delay* is the time point when the voltage of PB5 switches in reference to the extraction from the RFQ.

As can be seen in Fig. C.2, potassium ions can be separated from rubidium ions by selecting a PB5 delay $t_{PB5} < 12000$ ns. It is not possible to select between $^{39}K^{+}$ and $^{41}K^{+}$ using the PB5 electrode, as this process does not provide sufficient resolving power. To eliminate $^{41}K^{+}$ during commissioning, a Bradburry-Nilsen (BNG) Gate [39], located approximately 1 m before CryoMPET, was used. A BNG Gate consists of two grids of wires that are located perpendicular to the beam's axis, as can be seen in Fig. C.3. The two sets of wires are supplied by two opposite polarity voltages (ΔV = 300 V), that deflect the ions that pass through the grid (see Fig. C.3 (right)), except for a window of time (usually 10 μs) when the ion of interest is expected (see Fig. C.3 (left)) where the voltage asymmetry is eliminated.

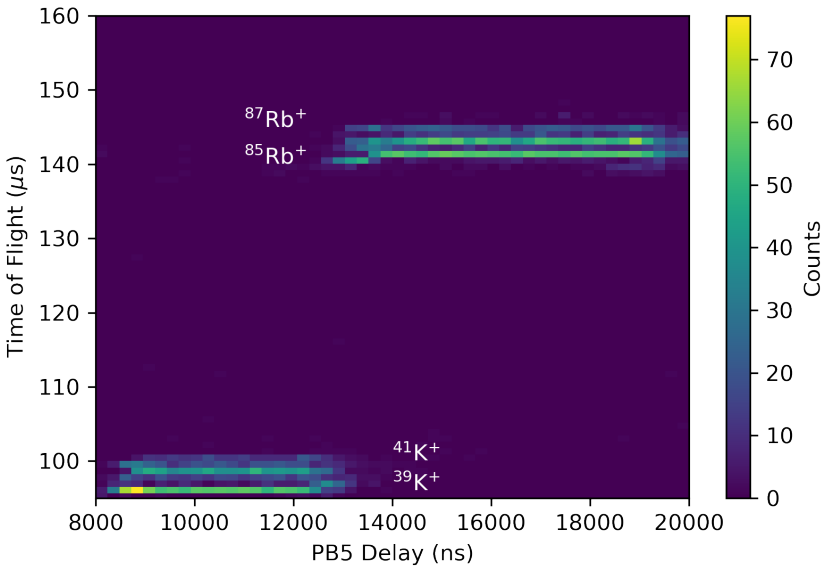

Figure C.2: Plot of the Time of Flight at MPET as a function of the extraction timing from the RFQ. The choice of extraction time determines the species that is transferred to MPET. The species that are available for off-line testing are shown in the figure.

At this point, the voltage difference is set to zero, allowing the ions to pass through.

Similarly to the PB5 delay, the time at which the voltage difference between the BNG wires becomes zero, can be scanned to determine the optimal time. Figure C.4, shows an example of that type of scan. For early BNG switching times there is a setting where only $^{39}K^+$ ions are passing through (blue arrow) while for late times, there is one setting where only $^{41}K^+$ ions (orange arrow) are transmitted.

After the settings for delivery of a clean 2.2 keV $^{39}K^+$ beam have been determined, the beam needs to be slowed down to a few-tens of eV so that it can be trapped in CryoMPET which has a 40 V axial trap depth. This is achieved with a second Pulsed Drift Tube (PLT). The PLT voltage switches from 2 keV to -180 eV, with a pulse duration of 10 ms. The timing of the PLT switching pulse is scanned to find the optimal time, as can be seen in Fig. C.5. When the $^{39}K^+$ ions are slowed down successfully, they arrive in the detector significantly later, and therefore the

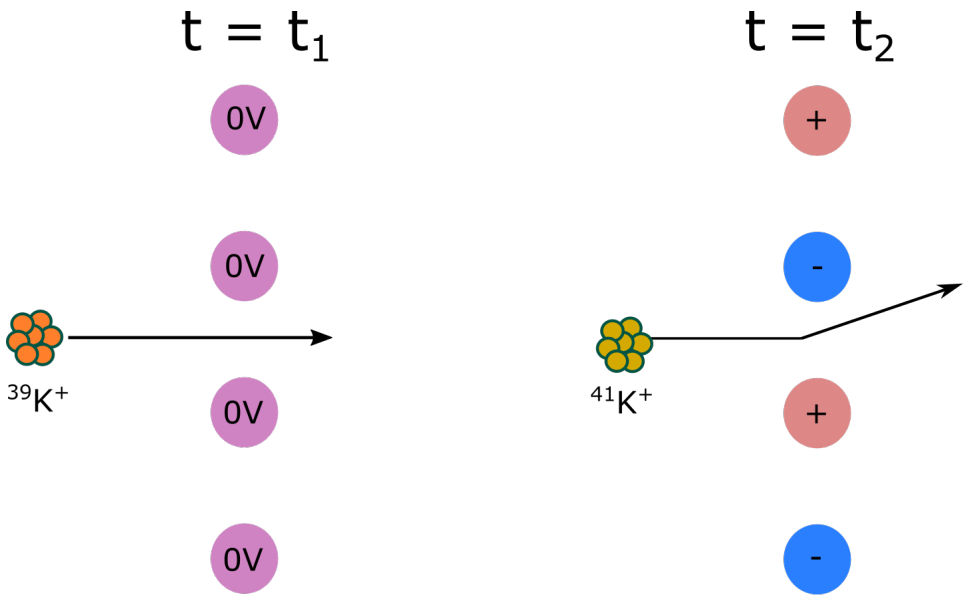

Figure C.3: A schematic of the BNG electrode and its principle. The figure on the left shows the voltage settings under which ions pass through the BNG unaffected. The figure on the right shows the voltage asymmetry that causes the ions that pass through to be reflected and removed from the beam.

count rate in the observation window becomes zero as can be seen in Fig. C.5.

When the ions are slowed down to a few eV, they can be axially trapped in the 40V trap by properly setting the closing time of the trap, as depicted in Fig. C.6. In every measurement cycle, the trap voltages switch between three configurations: i) injection, ii) capture and iii) ejection, which can be seen in Figure C.6.

In order to achieve large TOF effects, the axial energy of the ions should be minimal. This is, as the axial energy determines the baseline of the TOF resonance spectrum. This is achieved by optimizing the PB5 voltage, the PLT high voltage (PLTp) and the capture time in the trap. For the PB5 and PLTp distributions, the optimal value corresponds to the maximum voltage for which there is no loss in counts (see for example red arrow in Fig. C.7) while for the capture time, it is the timing where the TOF of the ions is large while the width of the TOF distribution (σ_{ToF}) is minimum (see for example Fig. C.8). When σ_{ToF} is not minimum, it

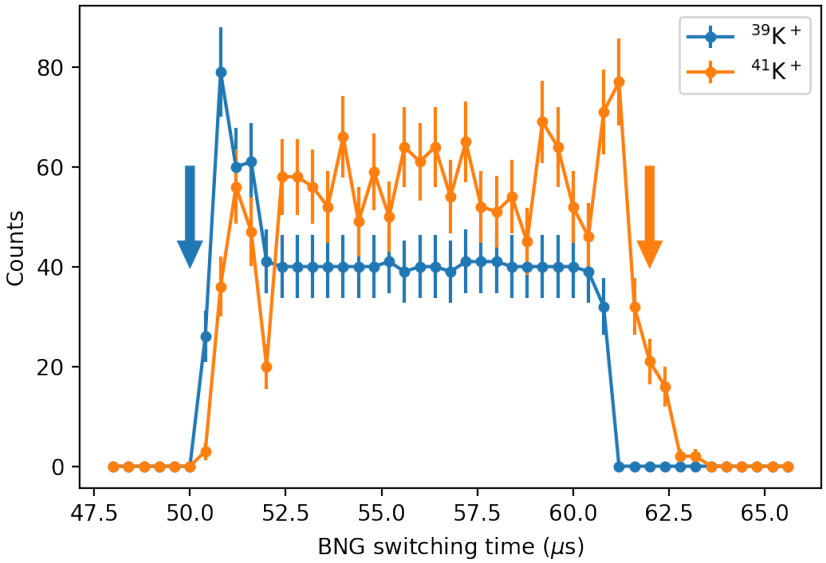

Figure C.4: Scanning of the BNG switching time to select $^{39}K^+$ from $^{41}K^+$. The arrows show the setting where only $^{39}K^+$ (blue) or $^{41}K^+$ (orange) is transported to MPET.

indicates that some the ions experience switching fields resulting in an increase of the their energy spread [44].

C.3 RF excitations in the Penning trap: Integration of the new Phase Splitter electronic system in the CryoMPET DAQ

Mass measurements with TOF-ICR utilize the application of RF excitations that cause the conversion between the ion's eigenmotions.

For MPET, the RF excitations were provided by two Arbitrary Function Generator (AFG): one for dipole and one for quadrupole excitations. The signal of the AFGs was then split by a $0^o/180^o$ splitter to four different signals, with appropriate polarity depending on whether a dipole or quadrupole excitation was applied. After the splitter, the signal was amplified and then mixed with a DC bias before

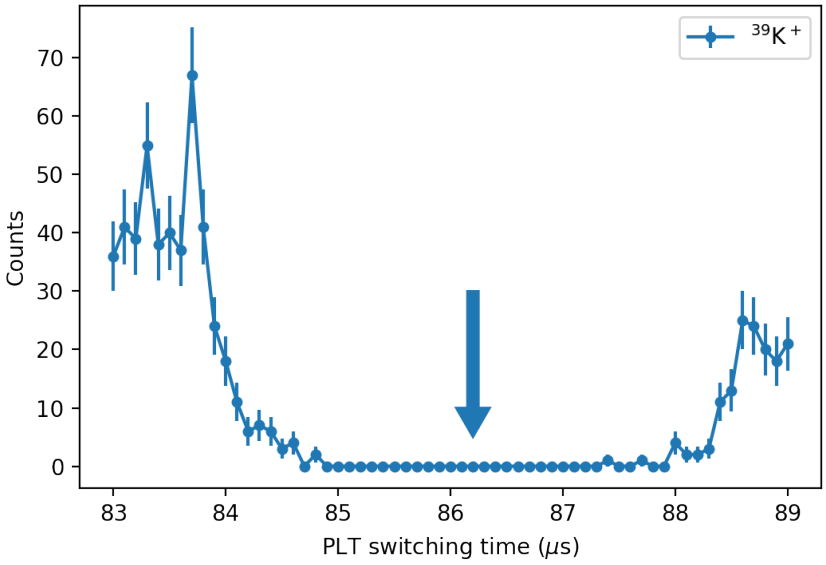

Figure C.5: Scanning of the PLT switching time for $^{39}K^+$ ions. The disappearance of counts indicates the successful energy reduction of the ions. The PLT switching time uses the point in time when the ions are extraction from the RFQ as a reference.

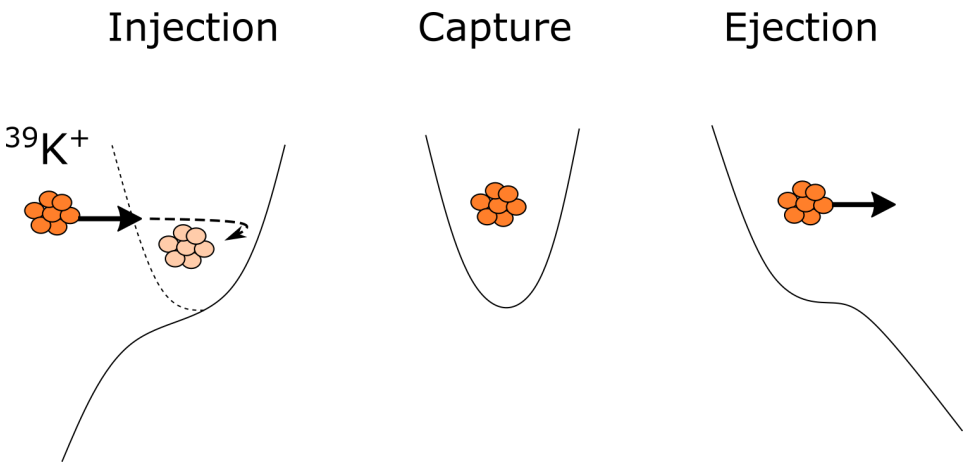

Figure C.6: Trap schematic of the potential during injection, capture and ejection.

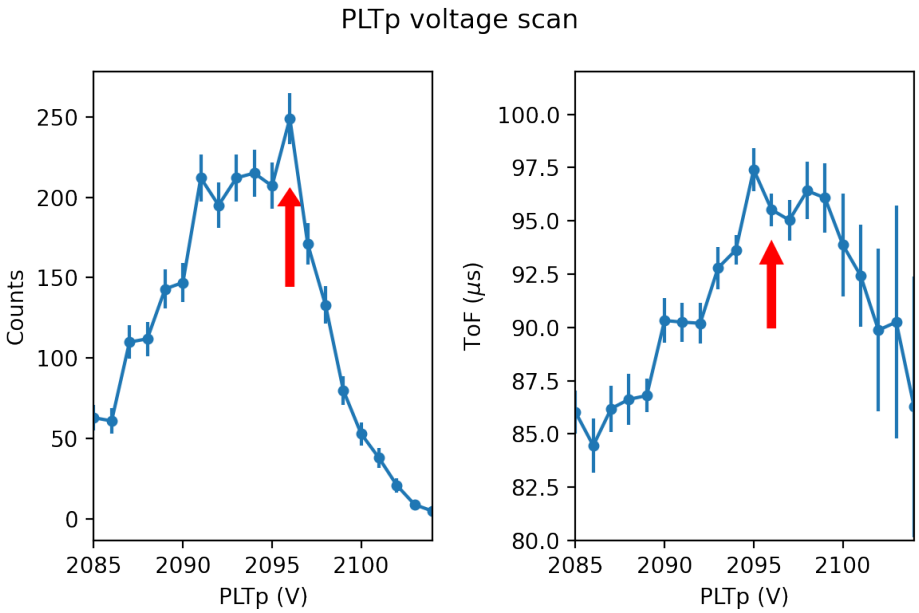

Figure C.7: PLTp voltage scan. Red arrows indicate the optimal voltage settings. The plot on the left shows the distribution of counts as a function of the PLTp voltage while the picture on the right shows the Time-of-Flight as a function of the PLTp voltage.

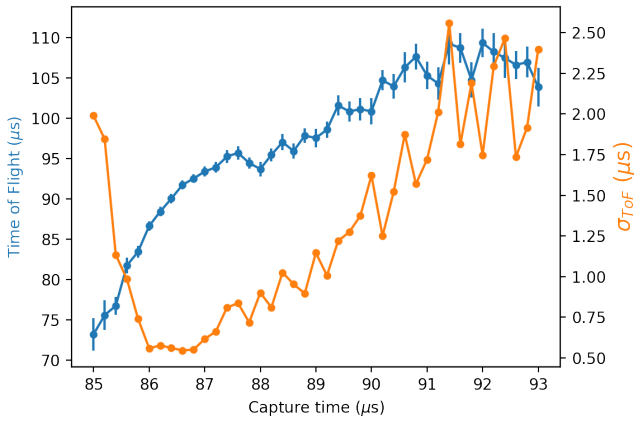

Figure C.8: Capture time scan. The optimal capture time corresponds to a large Time of Flight (blue) and a small σ_{ToF} (orange).

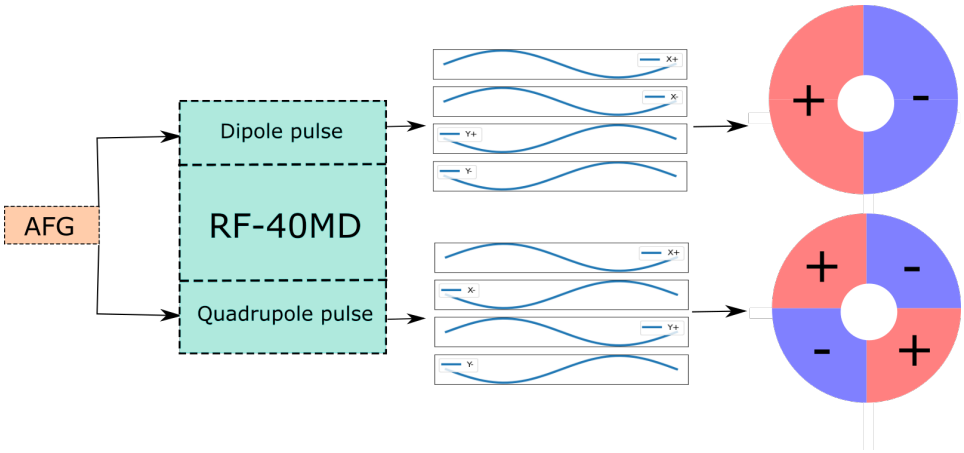

Figure C.9: Schematic of the new RF system for CryoMPET. An arbitrary frequency generator (AFG) produces an RF pulse of chosen frequency and amplitude. The AFG signal is then split and inverted by the RF-40MD module with the option of a dipole or quadrupole pulse. Four signals are produced from the RF-40MD module that are sent to the segmented ring electrode of the trap.

being sent to the segmented guard electrodes.

In CryoMPET, the RF design is significantly changed. The RF pulses are no longer applied to the guard electrode but to the ring electrode instead. This reduces the amplitude required for dipole excitations because the ions are significantly closer to the surface where the RF is applied. However, it requires the central ring electrode to be segmented which can introduce mechanical misalignments. In addition, the compex RF splitting and amplification system has been replaced with the RF-40 MD: A custom made AC drive for ion excitations, manufactured by Stahl Electronics. Unlike the previous system, RF-40 MD performs the splitting, the RF amplification and the DC mixing, thus eliminating the need of additional electronics. It is designed to provide an RF voltage of the range from 0 to 10 V_{pp}, with a frequency range between 5 kHz and 40 MHz. A schematic of the current RF system can be seen in Figure C.9.

Figure C.10, shows a typical LS voltage scan in CryoMPET: the voltage asymmetry of two opposite segments of the LS (in this case LSXP and LSXN) is varied and and the counts and TOF of the ions are recorded. In addition, while the ions are

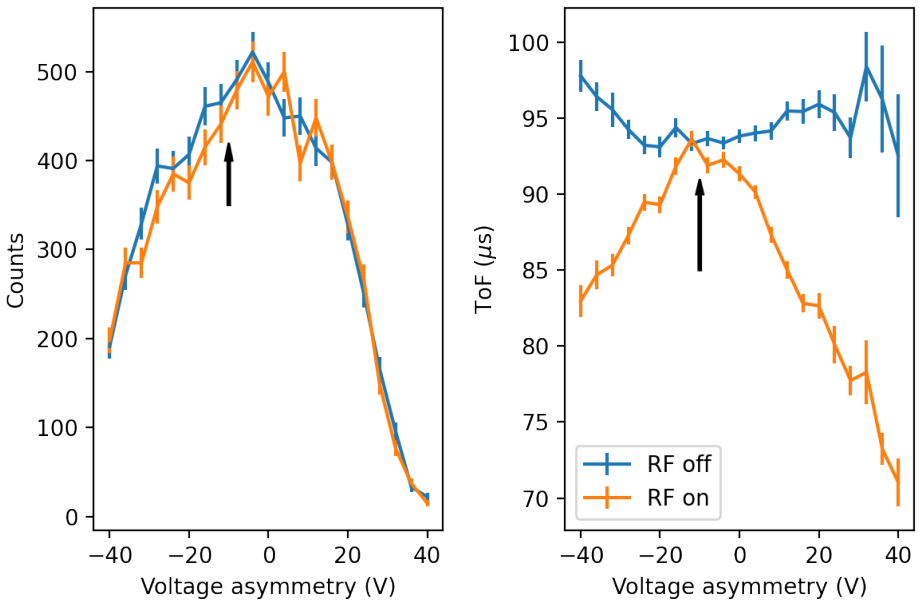

Figure C.10: Lorentz Steerer voltage scan. Voltage assymetry is the voltage difference between two opposite LS electrodes (for example LSXP and LSXN). Left: Count rate as a function of the voltage asymmetry. Right: Time-of-Flight as a function of the voltage asymmetry.

trapped, a quadrupolar RF pulse is applied, on resonance with the ions' cyclotron frequency: $\nu_{RF} = \nu_c$ (orange) or off resonance: $\nu_{RF} \neq \nu_c$ (blue). The LS settings at which the ions are trapped in the center of the trap (without any magnetron motion), can be found by the intersection between the on-resonance TOF pattern and the off-resonance one (see arrow in Fig. C.10). If the ions are in the center of the trap, they have no magnetron energy which can be converted to reduced cyclotron motion and therefore, their time of flight is independent of the applied RF. However, as the ions are placed further and further away from the trap center using the LS voltage asymmetry, their magnetron radius increases. If the RF frequency is on resonance with ν_c the increased magnetron radius converts into a reduced cyclotron radius, and thus the kinetic energy of the ions increases causing them to fly faster to the detector. Therefore, as the voltage asymmetry increases, so does the TOF difference between the on resonance ions and the off resonance ions. A good

setting for a quadrupole resonance is one that maximizes the difference between the TOF for on- and off- resonance.

As mentioned in Chapter 3, the amplitude of the quadrupole pulse required for one full conversion is inversely proportional to the excitation time and it depends on the magnetic field and the trap radius. Due to CryoMPET's new dimensions, a different conversion formula was established.

The TOF of ions experiencing a resonant pulse for t_{exc}= 100 ms can be seen in Figure C.11. For each V_{RF} the amount of magnetron motion that is converted into reduced cyclotron motion varies. Figure C.12, shows the corresponding TOF resonance for three different values of V_{RF}, depicting different amounts of conversion between magnetron and reduced cyclotron motion. The RF amplitude required for a full conversion can be found by looking at the TOF of ions as a function of V_{RF} when $\nu = \nu_c$. The result of such type of study can be seen in Fig. C.11, where the desired V_{RF} can be derived by fitting a damped sine wave

$$ToF = Acos(BV_{RF} + C)e^{-FV_{RF}} + D$$

to the data. The fit can be seen in Fig. C.11 with an orange line and its parameters are:

$$A = 9.1 \pm 0.4\,\mu s$$

$$B = 0.03070 \pm 0.00006\,mV^{-1}$$

$$C = 6.25 \pm 0.04$$

$$D = 85.9 \pm 0.1\,\mu s$$

$$F = 59 \cdot 10^{-5} \pm 6 \cdot 10^{-5}\,mV^{-1}$$

For one full conversion for $t_{exc} = 100$ ms, the RF amplitude required is $V_{RF} = 105 \pm 1$ mV and therefore, the conversion formula for CryoMPET is:

$$V_{RF}T_{RF} = 1.05 \cdot 10^4 mV \cdot ms \tag{C.1}$$

Although this value depends on the magnetic field strength and hence varies

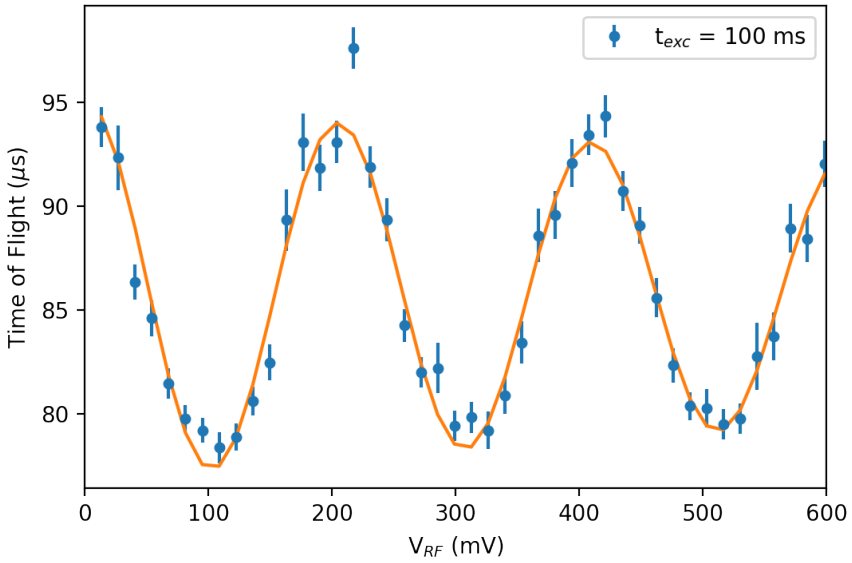

Figure C.11: Time of flight of ions on resonance for different RF voltages. The data are fitted to an damped sine function.

with the field, it provides a starting value and allows in determining the properties of CryoMPET.

C.4 DC electronic filters for the Lorentz Steerer power supplies

During the commissioning of CryoMPET, we found that, with switching the voltage of PLT electrode to slow down the beam energy, the LS power supplies were no longer able to efficiently regulate the voltage applied to the Lorentz Steerers, which are next to the PLT, especially when low ($V < 20$ V) voltages where applied to the Lorentz Steerers. As can be seen in Table C.2, the current read-out for $V_{LS}^{applied} = 0$ was 100 μ A, while the voltage read-out was fluctuating by several volts.

To reduce the induced voltage and current, RC filters were constructed and placed between the power supplies and the LS electrodes (Fig. C.13 (left)). In an RC filter, the capacitor offers a path to ground for any potential unwanted AC

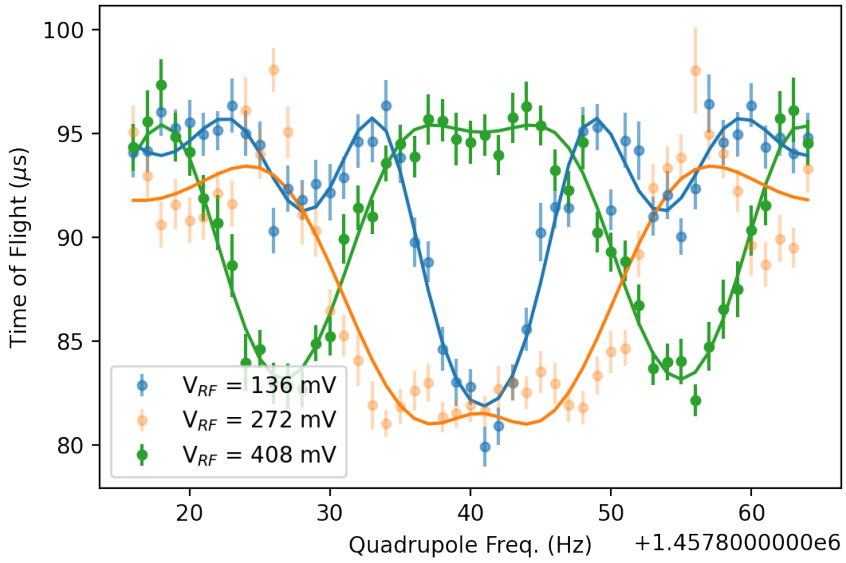

Figure C.12: The time of flight resonance for different conversion times. Solid lines indicate fits to the experimental data.

V_{PLT} (kV)	$V_{LS}^{applied}$ (V)	$\Delta V_{LS}^{readout}$ (V)	$I_{LS}^{readout}$ (μA)
1.8	0	4	100
1.8	-50	0.01	20

Table C.2: Response of LS power supplies when the PLT electrode switches from 1.8 kV to 0 V.

components while it does not affect the DC current that flows from V_{in} to V_{out}. A schematic of the RC filter can be seen in Fig. C.13 (right).

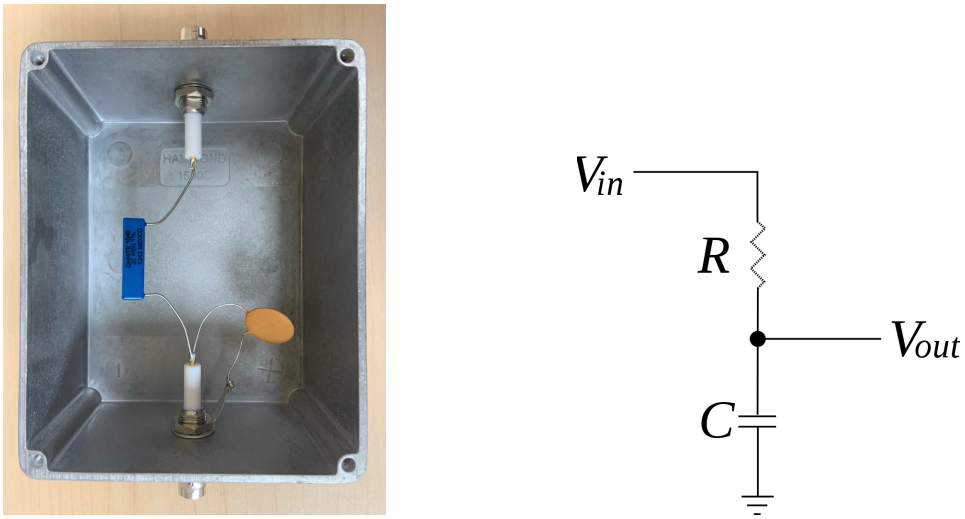

Figure C.13: RC filters for the Lorentz Steerer power supplies. Left: Photo of the assembled RC filters. Right: The circuit schematic of the RC filters.